VOLUME 80 FEBRUARY 12, 1976 / NUMBER 4

JPCHAx

THE JOURNAL OF PHYSICAL CHEMISTRY

PUBLISHED BIWEEKLY BY THE AMERICAN CHEMICAL SOCIETY

Announcing:

Now your J.T. Baker distributor can also ship you things he doesn't have!

How can your Baker distributor ship you things he doesn't have? Easy. He now can immediately contact the Baker Super Service Center and—in almost every instance—have the desired item shipped directly to you within 24 hours. *It's as though your J. T. Baker distributor has just added the largest reagent warehouse in the world to his backyard to serve you.* (To super-serve you.)

Now depend on your nearest Baker distributor for *all* of your laboratory reagent needs. He's listed on the facing page.

And do you have our new 428-page Catalog 750 featuring thousands of Baker quality laboratory chemicals? If not, please use coupon below. Thanks.

J. T. Baker Chemical Co.
222 Red School Lane
Phillipsburg, N.J. 08865

Please forward a copy of your new Catalog 750

Name_____

Title _____

Dept. _____

Organization _____

Address _____

_____ Zip _____

S

Check Baker first!

J.T.Baker®

J. T. Baker Chemical Co.
222 Red School Lane
Phillipsburg, N.J. 08865
201/859-5411

J.T. Baker SUPER SERVICE DISTRIBUTORS

ALABAMA

Sargent-Welch Scientific Co.
Birmingham
205 / 251-5125

ARIZONA

VWR Scientific
Phoenix
602 / 272-3272

VWR Scientific
Tucson
602 / 624-8371

CALIFORNIA

Sargent-Welch Scientific Co.
Anaheim
714 / 772-3550

VWR Scientific
Los Angeles
213 / 265-8123

VWR Scientific
San Diego
714 / 262-0711

VWR Scientific
San Francisco
415 / 469-0100

Curtin-Matheson Scientific Co.
Brisbane
415 / 467-1040

Curtin-Matheson Scientific Co.
Fountain Valley
714 / 963-6761

COLORADO

VWR Scientific
Denver
303 / 388-5651

Sargent-Welch Scientific Co.
Denver
303 / 399-8220

CONNECTICUT

Brand-Nu Laboratories, Inc.
Meriden
203 / 235-7989

DELAWARE

John G. Merkel & Sons
Wilmington
302 / 654-8818

FLORIDA

Curtin-Matheson Scientific Co.
Orlando
305 / 859-8281

GEORGIA

Curtin-Matheson Scientific Co.
Atlanta
404 / 349-3710

VWR Scientific
Atlanta
404 / 351-3872

Estes Surgical Supply Co.
Atlanta
404 / 521-1700

HAWAII

VWR Scientific
Honolulu
808 / 847-1361

ILLINOIS

Sargent-Welch Scientific Co.
Skokie
312 / 267-5300

A. Daigger & Co.
Chicago
312 / 644-9438

LaPine Scientific Co.
Chicago
312 / 735-4700

Macmillan Science Co., Inc.
Chicago
312 / 488-4100

SGA Scientific Inc.
Elk Grove Village
312 / 439-2500

Technical Industrial Products
East Peoria
309 / 694-6226

Wilkens-Anderson Co.
Chicago
312 / 384-4433

Curtin-Matheson Scientific Co.
Elk Grove Village
312 / 439-5880

Rascher & Betzold, Inc.
Chicago
312 / 275-7300

INDIANA

General Medical of Indiana
Indianapolis
317 / 634-8560

KENTUCKY

Preiser Scientific Inc.
Louisville
304 / 343-5515

LOUISIANA

Curtin-Matheson Scientific Co.
New Orleans
504 / 524-0475

MARYLAND

Curtin-Matheson Scientific Co.
Beltsville
301 / 937-5950

VWR Scientific
Baltimore
301 / 796-8500

MASSACHUSETTS

Doe & Ingalls, Inc.
Medford
617 / 391-0090

Curtin-Matheson Scientific Co.
Woburn
617 / 935-8888

Healthco Scientific
Canton
617 / 828-3310

SciChemCo
Everett
617 / 389-7000

VWR Scientific
Newton Upper Falls
617 / 969-0900

MICHIGAN

Curtin-Matheson Scientific Co.
Detroit
313 / 964-0310

Curtin-Matheson Scientific Co.
Midland
517 / 631-9500

Rupp & Bowman Company
Detroit
313 / 491-7000

Sargent-Welch Scientific Co.
Detroit
313 / 931-0337

MINNESOTA

Curtin-Matheson Scientific Co.
Minneapolis
612 / 378-1110

Hawkins Chemical Co.
Minneapolis
612 / 331-6910

Lerlab Supply Co.
Hibbing
218 / 262-3456

Physicians & Hosp. Supply Co.
Scientific & Laboratory Div.
Minneapolis
612 / 333-5251

MISSOURI

Curtin-Matheson Scientific Co.
Kansas City
816 / 561-8780

Curtin-Matheson Scientific Co.
Maryland Heights
314 / 872-8100

MONTANA

Northwest Scientific Co.
Billings
406 / 252-3269

NEW JERSEY

Ace Scientific Supply Co., Inc.
Linden
201 / 925-3300

Amend Drug & Chem. Co., Inc.
Irvington
201 / 926-0333
212 / 228-8920

J. & H. Berge, Inc.
South Plainfield
201 / 561-1234

Beckman Instruments Inc.
Mountainside
201 / 232-7600

Curtin-Matheson Scientific Co.
Wayne
201 / 278-3300

Macalaster Bicknell of N.J., Inc.
Millville
609 / 825-3222

Sargent-Welch Scientific Co.
Springfield
201 / 376-7050

SGA Scientific Inc.
Bloomfield
201 / 748-6600
212 / 267-9451

Seidler Chem. & Supply Co.
Newark
201 / 622-4495

NEW MEXICO

VWR Scientific
Albuquerque
505 / 842-8650

NEW YORK

Albany Laboratories, Inc.
Albany
518 / 434-1747

Ashland Chemical Co.
Binghamton
607 / 723-5455

Berg Chemical Co.
New York
212 / 563-2684

Kem Chemical
Mt. Vernon
914 / 699-3110

New York Lab. Supply Co.
West Hempstead
516 / 538-7790

Riverside Chemical Co.
N. Tonawanda
716 / 692-1350

VWR Scientific
Rochester
716 / 288-5881

NORTH CAROLINA

Carolina Biological Supply Co.
Burlington
919 / 584-0381

OHIO

Curtin-Matheson Scientific Co.
Cincinnati
513 / 671-1200

Curtin-Matheson Scientific Co.
Cleveland
216 / 883-2424

VWR Scientific
Columbus
614 / 445-8281

Sargent-Welch Scientific Co.
Cincinnati
513 / 771-3850

Sargent-Welch Scientific Co.
Garfield Heights, Cleveland
216 / 587-3300

OKLAHOMA

Curtin-Matheson Scientific Co.
Tulsa
918 / 622-1700

Melton Company, Inc.
Labco Scientific Div.
Oklahoma City
405 / 235-3526

OREGON

VWR Scientific
Portland
503 / 225-0400

PENNSYLVANIA

Arthur H. Thomas Company
Philadelphia
215 / 627-5600

Bellevue Surgical Supply Co.
Reading
215 / 376-2991

Bowman-Mell Co., Inc.
Harrisburg
717 / 238-5235

Dolbey Scientific
Philadelphia
215 / 748-8600

Para Scientific Co.
Fairless Hills
609 / 882-4545

Reading Scientific Co.
Reading
215 / 921-0221

Scientific Equipment Co.
Philadelphia
215 / 222-5655

RHODE ISLAND

Eastern Scientific Co.
Providence
401 / 831-4100

TENNESSEE

Durr-Fillauer Surgical
Supplies, Inc.
Chattanooga
615 / 267-1161

Nashville Surgical Supply Co.
Nashville
615 / 255-4601

TEXAS

Curtin-Matheson Scientific Co.
Dallas
214 / 747-2503

Curtin-Matheson Scientific Co.
Houston
713 / 923-1661

Sargent-Welch Scientific Co.
Dallas
214 / 357-9381

Capitol Scientific
Austin
512 / 836-1167

VWR Scientific
Houston
713 / 641-0681

VWR Scientific
El Paso
915 / 778-4225

UTAH

VWR Scientific
Salt Lake City
801 / 328-1112

VIRGINIA

General Medical
Vienna
703 / 938-3500

General Scientific
Richmond
804 / 264-2861

WEST VIRGINIA

Preiser Scientific
Charleston
304 / 343-5515

WASHINGTON

VWR Scientific
Seattle
206 / 447-5811

WISCONSIN

Genetec Hospital Supply Co.
Div. of McKesson & Robbins
Milwaukee
414 / 271-0468

Drake Brothers
Menomonee Falls
414 / 781-2166

J.T.Baker®

Visit us at the Pittsburgh Conference, Booth 405-407-409-411

THE JOURNAL OF

PHYSICAL CHEMISTRY

Published by the
AMERICAN CHEMICAL SOCIETY
BOOKS AND JOURNALS DIVISION
D. H. Michael Bowen, Director

Editorial Department: Charles R. Bertsch, Head; Marianne C. Brogan, Associate Head; Celia B. McFarland, Joseph E. Yurvati, Assistant Editors
Graphics and Production Department: Bacil Guiley, Head
Research and Development Department: Seldon W. Terrant, Head

Advertising Office: Centcom, Ltd., 50 W. State St., Westport, Conn. 06880.

Published biweekly by the American Chemical Society at 20th and Northampton Sts., Easton, Pennsylvania 18042. Second class postage paid at Washington, D.C. and at additional mailing offices.

Editorial Information

Instructions for authors are printed in the first issue of each volume. Please conform to these instructions when submitting manuscripts.

Manuscripts for publication should be submitted to *The Journal of Physical Chemistry*, Department of Chemistry, University of Minnesota, Minneapolis, Minn. 55455. Correspondence regarding **accepted papers and proofs** should be directed to the Editorial Department at the ACS Easton address.

Page charges of $60.00 per page are assessed for papers published in this journal. Ability to pay does not affect acceptance or scheduling of papers.

Bulk reprints or photocopies of individual articles are available. For information write to Business Operations, Books and Journals Division at the ACS Washington address.

Requests for **permission to reprint** should be directed to Permissions, Books and Journals Division at the ACS Washington address. The American Chemical Society and its Editors assume no responsibility for the statements and opinions advanced by contributors.

Subscription and Business Information

1976 Subscription rates—including surface postage

	U.S.	PUAS	Canada, Foreign
Member	$24.00	$29.75	$30.25
Nonmember	96.00	101.75	102.25
Supplementary material	15.00	19.00	20.00

Air mail and air freight rates are available from Membership & Subscription Services, at the ACS Columbus address.

New and renewal subscriptions should be sent with payment to the Office of the Controller at the ACS Washington address. **Changes of address** must include both old and new addresses with ZIP code and a recent mailing label. Send all address changes to the ACS Columbus address. Please allow six weeks for change to become effective. **Claims** for missing numbers will not be allowed if loss was due to failure of notice of change of address to be received in the time specified; if claim is dated (a) North America—more than 90 days beyond issue date, (b) all other foreign—more than 1 year beyond issue date; or if the reason given is "missing from files". Hard copy claims are handled at the ACS Columbus address.

Microfiche subscriptions are available at the same rates but are mailed first class to U.S. subscribers, air mail to the rest of the world. Direct all inquiries to Business Operations, Books and Journals Division, at the ACS Washington address or call (202) 872-4444. **Single issues** in hard copy and/or microfiche are available from Special Issues Sales at the ACS Washington address. Current year $4.75. Back issue rates available from Special Issues Sales. **Back volumes** are available in hard copy and/or microform. Write to Special Issues Sales at the ACS Washington address for further information. **Microfilm** editions of ACS periodical publications are available from volume 1 to the present. For further information, contact Special Issues Sales at the ACS Washington address. **Supplementary material** must be ordered directly from Business Operations, Books and Journals Division, at the ACS Washington address.

Microfiche	U.S.	PUAS, Canada	Other Foreign
Photocopy	$2.50	$3.00	$3.50
1–7 pages	4.00	5.50	7.00
8–20 pages	5.00	6.50	8.00

Orders over 20 pages are available only on microfiche, 4 × 6 in., 24X, negative, silver halide. Orders must state photocopy or microfiche if both are available. Full bibliographic citation including names of all authors and prepayment are required. Prices are subject to change.

American Chemical Society
1155 16th Street, N.W.
Washington, D.C. 20036
(202) 872-4600

Member & Subscription Services
American Chemical Society
P.O. Box 3337
Columbus, Ohio 43210
(614) 421-7230

Editorial Department
American Chemical Society
20th and Northampton Sts.
Easton, Pennsylvania 18042
(215) 258-9111

Notice to Authors last printed in the issue of January 1, 1976

THE JOURNAL OF

PHYSICAL CHEMISTRY

Volume 80, Number 4 February 12, 1976

JPCHAx 80(4) 341–432 (1976)

ISSN 0022-3654

COMMUNICATIONS TO THE EDITOR

■ Supplementary material for this paper is available separately (consult the masthead page for ordering information) it will also appear following the paper in the microfilm edition of this journal.

* In papers with more than one author, the asterisk indicates the name of the author to whom inquiries about the paper should be addressed.

AUTHOR INDEX

THE JOURNAL OF
PHYSICAL CHEMISTRY

VOLUME 80, NUMBER 4 FEBRUARY 12, 1976

Photochemical Ion Formation in Lumiflavin Solutions

S. Gwyn Ballard,* David C. Mauzerall,

The Rockefeller University, New York, New York 10021

and Gordon Tollin

Department of Chemistry, University of Arizona, Tuscon, Arizona 85721 *(Received June 10, 1975)*

We have studied ion formation in pulse-irradiated lumiflavin solutions using both a sensitive photoconductance instrument with a time resolution of 0.3 μs, and conventional flash photolysis with optical detection. Free ions are observed only in solvents of high dielectric constant. Their formation and decay are complex processes influenced by the presence of electron donors and, most dramatically, by solvent pH. Experimental observations are interpreted in terms of a primary ionization process involving electron transfer in a triplet flavin dimer or aggregate, followed by a number of fast proton transfer reactions. Extrinsic electron donors (indoles) undergo electron transfer to a nonaggregated triplet species. An attempt is made to relate the kinetics of species observable through absorbance measurements to those of the ionic species measured conductimetrically. Conductance has been shown to be an extremely sensitive method for studying photochemical ionization, and particularly the acid–base behavior of transient photoproducts. These reactions may be almost invisible to optical detection; the ability of absorbance measurement to detect neutral species, however, makes the two methods highly complementary. The reactions described in this paper occur over an excess acid or base concentration range of a few micromolar, and measurable kinetic changes occur as a resllt of acid/base levels of a few parts per billion.

Introduction

The lowest triplet state of flavin (isoalloxazine) is known to accept electrons from a variety of organic compounds.[1,2] Indole derivatives[3] are of particular importance as donors because of the recent demonstration[4,5] that a tryptophan side chain is part of the coenzyme binding site in certain flavoenzymes (i.e., the flavodoxins). It has been shown that both the flavin singlet[6] and triplet[7] excited states are highly quenched in these proteins, and it is possible that the quenching mechanism involves electron transfer to the indole ring. Flavins have also been implicated in several photobiological phenomena,[8–11] giving additional importance to an understanding of isoalloxazine photochemistry.

Inasmuch as the primary photoproducts of electron transfer from an organic donor to the flavin triplet state will be ion radicals, electrical conductance measurements should provide a useful means of monitoring the photoreaction, provided that solvent conditions permit uncorrelation of the first-formed ion pairs. Furthermore, the flavin radical is known to have a pK near neutrality (8.4 for lumiflavin),[12,13] and so conductance measurements might also reveal proton transfer reactions which occur subsequent to the initial electron transfer. With these considerations in mind we have undertaken a flash photolysis study of the electron transfer reactions between the triplet and ground states of lumiflavin, and also between the lumiflavin triplet state and indole. Optical and conductimetric detection methods were employed. Both organic (acetonitrile, butyronitrile, and dichloromethane) and aqueous solvents were used in order to demonstrate dielectric effects; the former also provide aprotic environments, thereby decreasing the rates of proton transfer reactions such that they become distinct from the primary electron transfer processes. The results of these experiments have provided some new insights into the chemistry of the flavin triplet state, and have demonstrated the utility of electrical measurements in the study of fast protonic equilibria in photochemical reactions. Kinetic conductance techniques have played an important role in the elucidation of a number of photophysical processes involving creation or annihilation of charge carriers. These include electron ejection from mole-

cules,[14–17] thermal and infrared stimulated detrapping of electrons trapped in polarizable matrices[18–21,28] and their recombination with parent cations or scavengers,[22,23] secondary ionization phenomena following pulse radiolysis of fluid solutions,[21,24,28] and ionic photodissociation of charge-transfer complexes.[25–27]

In general these studies have employed relatively crude photoconductance apparatus, consisting essentially of a resistive divider network containing the cell, and polarized by large continuously applied dc voltages. While fields of many kilovolts per centimeter are tolerable in studies of solid samples, this is not the case with solutions. The redox potentials of organic solutes are not likely to be more than a few volts; electrode voltages exceeding these potentials will cause undesirable electrolysis. The apparatus employed in this study avoids large dc polarizing voltages and demonstrates that great sensitivity can be achieved without them, using low-noise operational electronics and signal averaging. An alternative approach is alternating-current conductimetry,[21,28] though this technique has neither the sensitivity nor the speed of the pulsed dc method employed in the present study.

Conductance methods have been very little applied to monophotonic ionization processes[25–27,29,30] which have, however, been studied by various investigators using conventional flash photolysis.[31–33] In such studies the kinetic absorbance and conductance methods nicely compliment each other. Conductance is very much more sensitive, has equally fast response (potentially into the nanosecond region), and is specific for charged species. Absorbance gives more information on the identity of transient products, though some information can also be gained from measurement of ion mobility. Because of the large values of this quantity for H^+ and OH^-, particularly in water, the conductance method is especially suited to the measurement of fast protonic equilibria.

Experimental Section

Acetonitrile and butyronitrile are prepared by two successive distillations of MCB chromatoquality solvent stored over calcium hydride, the first from P_2O_5 and the second from activated Linde 3A molecular sieve. Water is doubly distilled in glass, and dichloromethane (Fischer spectroscopic grade) used without further purification. Indole is purified by recrystallization from methanol–water, followed by vacuum desiccation. Perchloric acid and tetramethylammonium hydroxide (Eastman) are used without purification and added in the form of millimolar solutions in the appropriate solvent by means of a micropipet. Lumiflavin is prepared according to the method described in ref 34. Solutions are prepared at concentrations from 2.5 to 50 μM and vigorously purged with prepurified N_2 gas (Ohio) before irradiation (residual O_2 concentration ca. 0.5 μM).

Conductivity experiments use repetitive 10-ns pulses of uv light (3371 Å) from a Molectron UV1000 nitrogen laser at peak powers up to 1 MW. Irradiated solution volume is 0.2 ml in the center of the conductance cell. The platinum electrodes are polarized at up to 10 V cm^{-1} immediately prior to the laser discharge, the polarizing voltage being maintained throughout the measurement period (up to 100 ms), then reversed for an approximately equal time to minimize solute electrolysis and bulk transport effects. Precise balancing of these two periods holds the dark conductance constant to better than 10^{-10} mho over extended periods of time. Photoionization is measured via the accompanying small change in cell conductance; typical ion drift currents in the present experiments are 10^{-7} to 10^{-9} A, though averaging techniques permit considerably smaller currents to be measured. Approximate detection limit is 10^{-9} M univalent ions of molecular weight 100 with a response time of 300 ns, 10^{-11} M with a response time of 50 μs. Provision is made to compensate the large cell currents involved with aqueous solutions. The apparatus also automatically zero-adjusts before each laser pulse, thereby referring the photoconductance signal to an initial zero baseline without ac coupling. Output is a voltage analogue of the ion drift current. It is digitized, averaged if necessary, and displayed via an X–Y recorder for subsequent analysis. The apparatus also provides a continuous readout of the total dc cell conductance, obtained by sampling immediately before each flash. This permits establishment of standard prephotolysis conditions, and allows continuous monitoring of the extent of irreversible photoionization throughout the experiment. The entire apparatus is contained in an elaborate Faraday cage, with temperature constant to approximately 1 °C. All operational circuitry is powered via stabilized supplies based on Ni–Cd cells, and the digitization and averaging electronics powered via an ultraisolation transformer. Trigger pulses between the laser and the central controller are transmitted through ultrafast optical isolators, to minimize coupling of the laser discharge noise into the signal processing equipment. A block diagram of the conductance apparatus is shown in Figure 1; it is to be described in detail elsewhere.[35] A description of the optical detection flash photolysis instrument is to be found in ref 2.

Results and Discussion

Flash Photolysis with Conductimetric Detection. A. Lumiflavin Photoionization in the Absence of Extrinsic Donors. i. Neutral Solutions. For the purposes of this discussion, neutral solutions are defined as those to which no acid ($HClO_4$) or base (NMe_4OH) has been added. Figure 2 shows the kinetic behavior of conductance of a laser-irradiated 50 μM lumiflavin solution in acetonitrile over the entire time scale from ion formation to complete decay. Details of the rise kinetics are shown in Figure 3, in which the dashed curve represents the response of the instrument to a delta function current input (obtained by substituting a p-i-n photodiode for the conductance cell, and attenuating the laser pulse appropriately). Kinetics of growth of the ion current in the first few tens of microseconds after pulse irradiation are accurately first order, though deviations are observed when indole is present (cf. Figure 8, section B). Amplitude of the ion signal is proportional to the laser power, but $t_{1/2}$ varies neither with laser power nor with lumiflavin concentration over the range 2.5 to 50 μM. Thus, the simplest mechanism compatible with first-order kinetics, namely

$$L_G \xrightarrow{h\nu} L_T \xrightarrow{L_G \text{ excess}} (L^{\cdot+}L^{\cdot-}) \xrightarrow{\text{rapid}} L^{\cdot+} + L^{\cdot-}$$

lumiflavin ground state; lumiflavin triplet state; ion pair; uncorrelated ions

cannot be correct. In acetonitrile and butyronitrile the signal amplitude is a slowly saturating function of $[L_G]$ over the range studied, which cannot be accounted for by optical screening. More linear behavior is seen in water, but the risetime is shorter by a factor of 2, and the signal amplitude

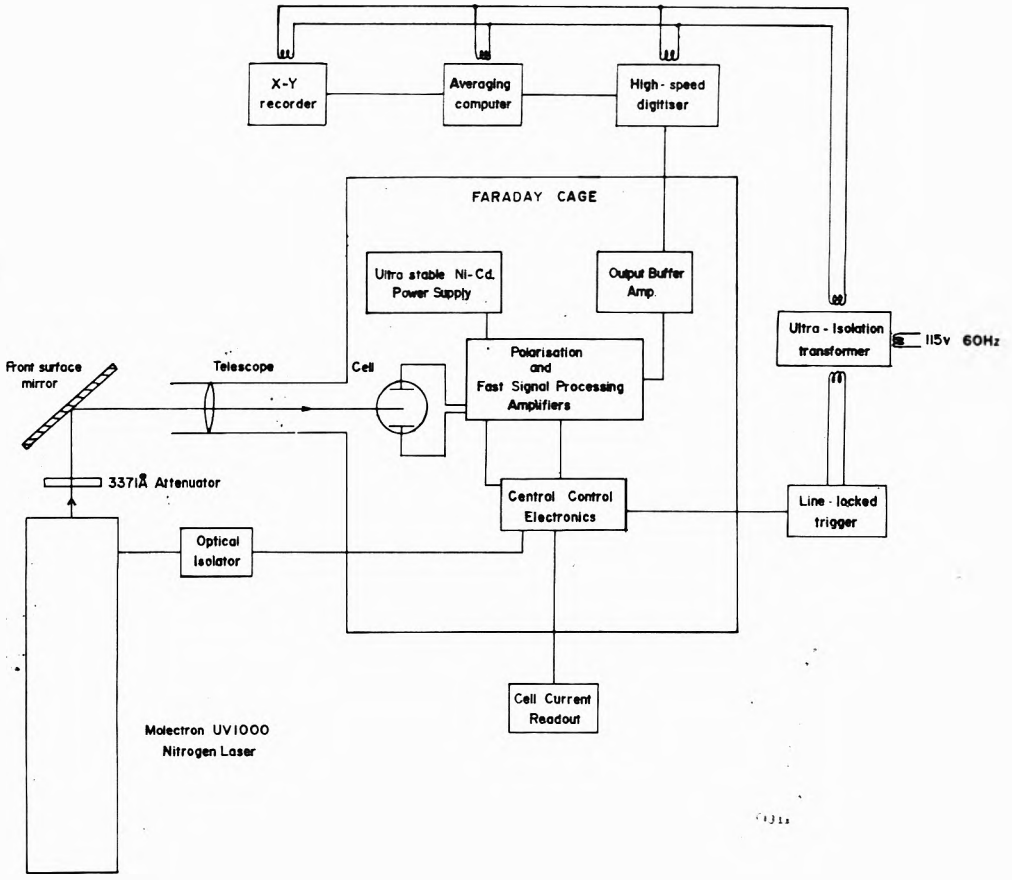

Figure 1. Block diagram of the photoconductance apparatus. The laser is pulsed at approximately 10 Hz, digitization being performed in real-time. A typical data set involves the averaging of 32 or 64 shots at 300-ns resolution or 4 shots at 50-μs resolution.

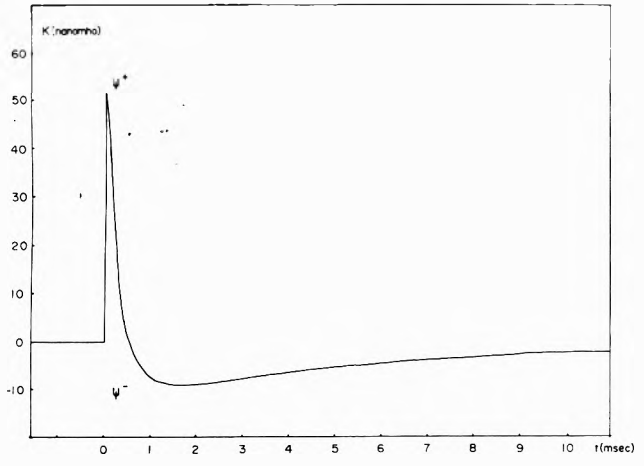

Figure 2. Retrace of photoconductance behavior of 50 μM lumiflavin solution in "neutral" acetonitrile. Data show the average of 4 shots, and is not additionally smoothed. The single-shot signal-to-noise ratio is approximately 50.

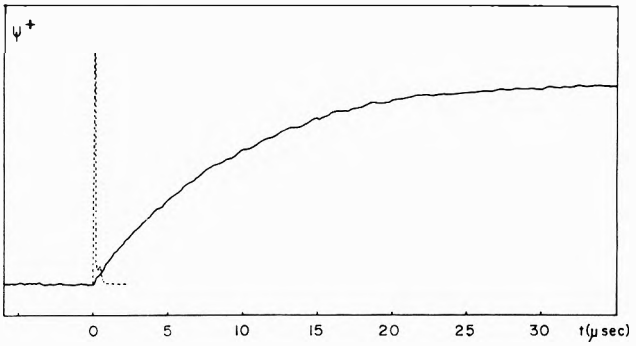

Figure 3. Detail of the radical ion current growth kinetics, average of 32 pulses. The dotted curve is the single-shot response of the instrument to a delta function current input (10-ns laser flash, detected by p-i-n photodiode, response 1 ns).

smaller by a factor of 15 (see Figure 9). No ion formation is seen in dichloromethane.

These observations are interpreted as being due to monophotonic ionization of a preformed dimer or more complex aggregate; oxygen quenching strongly suggests that the species involved is a triplet state. According to this scheme the primary photochemical events can be summarized as

$$(L_G \cdots L_G)_n \xrightarrow{h\nu} (L_T \cdots L_G)_n \xrightarrow{e^- \text{ transfer}}$$

$$(L\cdot^+ L\cdot^-) \xrightarrow[1.3\times10^5 s^{-1}]{k_1} L\cdot^+ + L\cdot^-$$

$$L_G \cdot \xrightarrow{h\nu} L_T$$

(free triplet; does not undergo electron transfer)

Solutions of the flavins in water have been previously shown to contain aggregated species,[36-38] and it seems reasonable to invoke similar species in acetonitrile solutions. We suggest that the dimer or aggregate concentration is in fact considerably lower in water than in acetonitrile or (particularly) butyronitrile due to smaller hydrogen-bonding interactions between the flavin molecules in aqueous systems. If electron transfer occurs only in the aggregated excited flavin, then the variation of signal amplitude butyronitrile > acetonitrile ≫ water appears to have a ready explanation. The observed shorter risetime of ion signal in water implies a more rapid uncorrelation of the ion pairs, presumably due to reduced Coulombic interaction between the radical cation and anion components. The dimer theory is further supported by the fact that although optical flash photolysis shows a triplet species with lifetime over 100 μs (see below), primary photoionization occurs with a $t_{1/2}$ of less than 10 μs. This implies that there must be two triplet state populations, one of which is "free" and accounts for the 100-μs signal in the absorbance measurements, and one which is part of the aggregate and has a much shorter lifetime (because of the electron transfer reaction). Strong additional evidence for two distinct triplet species comes from the behavior of the system in high acid and in the presence of indole, described below. If the aggregate hypothesis is correct in this case, the observation of rapid and abruptly terminated primary photoionization implies a tight aggregate into which the "free" triplet species cannot penetrate significantly. If this were not the case, ion formation would occur over the full 100-μs lifetime of the free triplet. In other words, aggregation appears to be primarily a property of the ground state flavin molecules only.

In a solution of 50 μM lumiflavin, assuming that the triplet yield is 0.5, we estimate that the laser generates approximately 5 μM flavin triplet (both forms). Photogenerated concentrations of $L\cdot^+$ and $L\cdot^-$ can be estimated from the conductance equation

$$c_\pm = 1000K/s\Lambda_\pm$$

where K is the increment of cell conductance (mho) due to photoionization; $c_\pm$ is the corresponding concentrations of radical cation and anion; $\Lambda_\pm = \lambda_{L\cdot^+} + \lambda_{L\cdot^-}$, where $\lambda_{L\cdot^+}$ and $\lambda_{L\cdot^-}$ are the equivalent conductances of $L\cdot^+$ and $L\cdot^-$ at concentration $c_\pm$ in the solvent employed, and at the prevailing temperature. For the purposes of this study the limiting values (i.e., at infinite dilution) are employed, and denoted by $\lambda^0_{L\cdot^+}$ and $\lambda^0_{L\cdot^-}$. s is the cell constant, obtained by calibration with tetraethylammonium perchlorate, whose limiting conductance in acetonitrile is accurately known.[39a]

The equivalent conductances of a large number of ionic species in acetonitrile and many other nonaqueous solvents have been studied and tabulated in the literature. A comprehensive compilation of this data, together with source references and some theoretical discussion is contained in ref 39b. For the purpose of this study, the following limiting equivalent conductances in acetonitrile are used:

Ion	λ^0, mho cm^2 mol^{-1}	Ion	λ^0, mho cm^2 mol^{-1}
$L\cdot^+$	35	H^+	100
$L\cdot^-$	35	OH^-	120

$\lambda^0_{H^+}$ in CH_3CN is taken directly from ref 39b (Appendix 5.12.9, p 678). $\lambda^0_{L\cdot^+}$ and $\lambda^0_{L\cdot^-}$ in CH_3CN are estimated by extrapolation of mobility data for large organic ions to the radii of $L\cdot^+$ and $L\cdot^-$. $\lambda^0_{OH^-}$ in CH_3CN has not been recorded in the literature surveyed. The value employed in this study (120 mho cm^2 mol^{-1}) is estimated on the basis of extrapolation of data for halide anions in acetonitrile to the radius of OH^-. Support for this value is provided by the asymptotic approach to unity of the parameter β (see below and Figure 5).

The observation that the $t_{1/2}$ of the subsequent bimolecular recombination is invariably much greater than the ion current risetime implies that essentially all $L\cdot^+L\cdot^-$ pairs uncorrelate. The conductance equation gives $[L\cdot^+]$ and $[L\cdot^-] = 6.5 \times 10^{-7}$ M when $[L_T] = 5$ μM, indicating that about 13% of the total triplet population is involved in the electron transfer reaction.

Decay of the primary photosignal does not apparently obey simple first- or second-order kinetics, though we have not undertaken rigorous analysis of the observed transients. The $t_{1/2}$ of the decay is approximately 250 μs in the true neutral or slightly basic solutions (50 μM flavin, 500 kW laser) and we attribute it primarily to the process of reverse electron transfer:

$$L\cdot^+ + L\cdot^- \xrightarrow{k_2} 2L_G \qquad \Delta\lambda^0 = -\{\lambda^0_{L\cdot^+} + \lambda^0_{L\cdot^-}\} = -70$$

k_2 can be calcuated from the decay data: at 20 °C it has a value of approximately 6×10^9 M^{-1} s^{-1}. It should be pointed out that if the k_2 reaction were the sole relaxation process, then true second-order kinetics would be seen. The $t_{1/2}$ of the decay does vary approximately as the inverse of the laser power, however, indicating that the k_2 reaction is the dominant process in situations where there is little or no "undershoot" (see below). It appears to correspond to the rapid transient phase in the flash photolysis signal measured at 560 nm (see below). In acidic and basic solutions other processes compete with k_2, resulting in an intriguing kinetic complexity shown in the summary diagram (Figure 4) and described in the section acid–base behavior.

ii. Acid–Base Behavior. An important feature of the so-called neutral solution is that its recovery kinetics show an "undershoot" phase, i.e., the conductance falls below its initial value and undergoes final relaxation in the positive direction. This undershoot is small in the neutral case, but in the presence of acid or base (added as perchloric acid or tetramethylammonium hydroxide) it dominates the conductance kinetics. In suitable conditions several reversals occur (Figure 4). These effects are not explicable purely in terms of the k_2 reaction, but appear to involve alternative pathways of reaction of $L\cdot^+$ and $L\cdot^-$ with excess OH^- or H_3O^+. These reactions are assigned rate constants k_3 and k_4, and both give rise to large negative conductance changes ($\Delta\lambda^0$):

$$L\cdot^+ + OH^- \xrightarrow{k_3 \sim 4\times10^9} L\cdot + H_2O$$
$$\Delta\lambda^0 = -\{\lambda^0_{L\cdot^+} + \lambda^0_{OH^-}\} = -155$$

$$L\cdot^- + H_3O^+ \xrightarrow{k_4 \sim 4\times10^9} LH\cdot + H_2O$$
$$\Delta\lambda^0 = -\{\lambda^0_{L\cdot^-} + \lambda^0_{H_3O^+}\} = -135$$

The dramatic sensitivity of the observed kinetics to acid and base illustrates the responsiveness of the conductimetric method to reactions involving H_3O^+ and OH^-, because of the high mobilities of these ions compared to the large organic radical ions. Partition of $L\cdot^+$ between the k_2 and k_3 reactions is described empirically by the parameter β, and

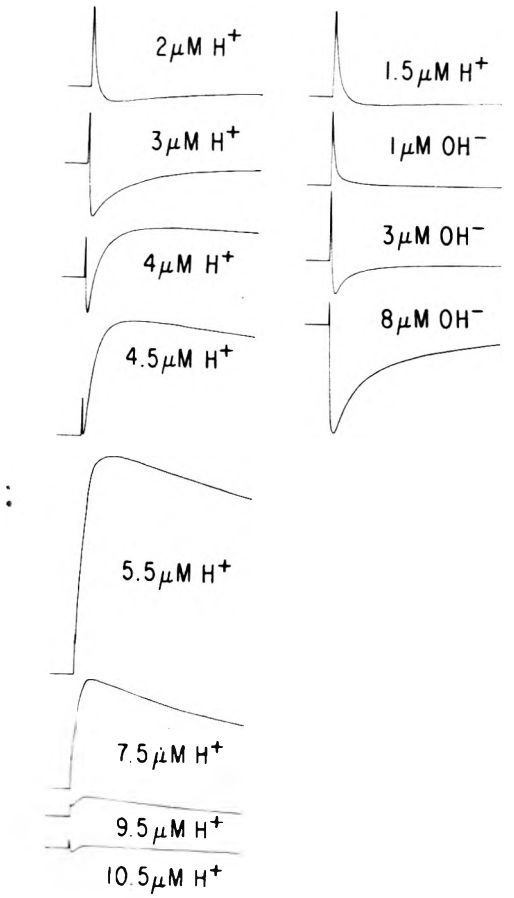

Figure 4. Variation of the secondary conductance behavior of pulse irradiated lumiflavin solutions with acid/base levels of the solvent. The "2 μM H^+" condition corresponds to the data of Figure 3, i.e., complete time scale of each trace is ca. 10 ms.

that of $L\cdot^-$ between k_2 and k_4 by the parameter α. The observed kinetic curves can be resolved into a positive conductance contribution due to k_1 and negative contributions due to k_2 plus k_3 or k_4, each weighted according to the mobilities of the species involved. Decay of the positive component is via k_2 and either k_3 or k_4. Decay of the negative component is more complex. In acid, diversion of a fraction α of $L\cdot^-$ into the k_4 reaction implies that the yield of the k_2 reaction is reduced by the factor $(1 - \alpha)$. Consequently a fraction α of $L\cdot^+$ remains unreacted via k_2, and the final relaxation to the baseline can be attributed to the process

$$L\cdot^+ + LH\cdot \xrightarrow{k_5,\ \text{excess } H_2O} 2L_G + H_3O^+$$

$$\Delta\lambda^0 = +\{\lambda^0_{H_3O^+} - \lambda^0_{L\cdot^+}\}$$

$$\alpha = +65$$

This reaction and others to be described below require that an excess (i.e., greater than a few tens of micromolar) of water be present in the acetonitrile solvent. There are several independent indications that this is a justified assumption. Direct measurement of water content of nitriles prepared by the method employed in this study has been performed by several investigators (e.g., ref 42); in general levels not much less than millimolar are to be expected. We find that the conductivity of freshly prepared acetonitrile increases rapidly on standing in the laboratory atmosphere, and this phenomenon is particularly dramatic in samples pretreated by electrolytic cleaning to reduce water content to a very low level. We attribute this growth of conductivity to absorption of atmospheric water. Finally, deliberate addition of water to ca. 10 mM has no discernable effect on the above kinetics, suggesting that water is already present "in excess".

k_5 has a value of approximately 2×10^9 M^{-1} s^{-1} (calculated from $t_{1/2}$), and an associated positive conductance change precisely that required for reattainment of the baseline. A similar situation exists when base is in excess. In this case a fraction β of $L\cdot^+$ is diverted into the k_3 reaction, resulting in the same fraction of $L\cdot^-$ remaining unreacted via k_2. The final relaxation is now attributed to the process

$$L\cdot^- + L\cdot \xrightarrow{k_6} L_G + L_G^- \xrightarrow[\text{fast}]{H_2O} L_G + OH^-$$

$$\Delta\lambda^0 = (\lambda^0_{OH^-} - \lambda^0_{L\cdot^-})$$

$$\beta = +85$$

in which k_6 has an approximate value of 3×10^9 M^{-1} s^{-1}. It is assumed that water is in sufficient concentration (>100 μM) that the k_6 step is rate limiting. The final rapid regeneration of L_G and OH^- by reaction of L^- with water is associated with a positive conductance change exactly that required to restore the initial conditions. The value of k_5 coincides closely with that determined optically; k_6 was not obtained by conventional flash photolysis, however, because of the difficulty of detecting $L\cdot^-$.

The above scheme (summarized in Figure 6) appears to describe simply and elegantly the remarkable symmetry of the acid and base kinetics. Variation of α and β as a function of solution acid/base levels is shown in Figure 5. In calculating α it is assumed that the amplitude (ψ_0^+) of the initial positive transient is constant in all cases and equal to its value in the limit of slow inversion. The apparent truncation in acidic solutions (Figure 4) is an artifact of the slow digitization timebase employed in recording this data. The equation for ψ_0^+ is

$$\psi_0^+ = \mathbf{k}\{\lambda^0_{L\cdot^+} + \lambda^0_{L\cdot^-}\} = 70\mathbf{k}\ (\mathbf{k}\text{ is a scaling constant}) \quad \text{(i)}$$

The amplitude of the final relaxation phase, and hence the undershoot, is proportional to the extent of the k_5 reaction, and hence to α. The appropriate equation is

$$\psi_0^- = \mathbf{k}\alpha\{\lambda^0_{H_3O^+} - \lambda^0_{L\cdot^+}\} = 65\alpha\mathbf{k} \quad \text{(ii)}$$

Simultaneous solution of (i) and (ii) gives

$$\alpha = 1.08(\psi_0^-/\psi_0^+)_{acid} \quad \text{(iii)}$$

The internal consistency of this simple description can be seen from the fact that the total signal amplitude must be equal to the sum of the k_2 and k_4 components

$$\psi_{total} = \mathbf{k}(1 - \alpha)70 + \mathbf{k}(\alpha)35 \quad \text{(iv)}$$

(iv) clearly equals (i) + (ii). In the calculation of β eq i is still applicable to ψ_0^+. The undershoot is given in base by

$$\psi_0^- = \mathbf{k}\beta\{\lambda^0_{OH^-} - \lambda^0_{L\cdot^-}\} = 85\beta\mathbf{k} \quad \text{(v)}$$

Simultaneous solution of (i) and (v) gives

$$\beta = 0.82(\psi_0^-/\psi_0^+)_{base} \quad \text{(vi)}$$

The above description is adequate for all levels of base up to 10 μM, and for acid up to approximately 1.5 μM. It will be noted that the form of Figure 5 strongly suggests that the so-called "neutral" solution is, in fact, somewhat acidic.

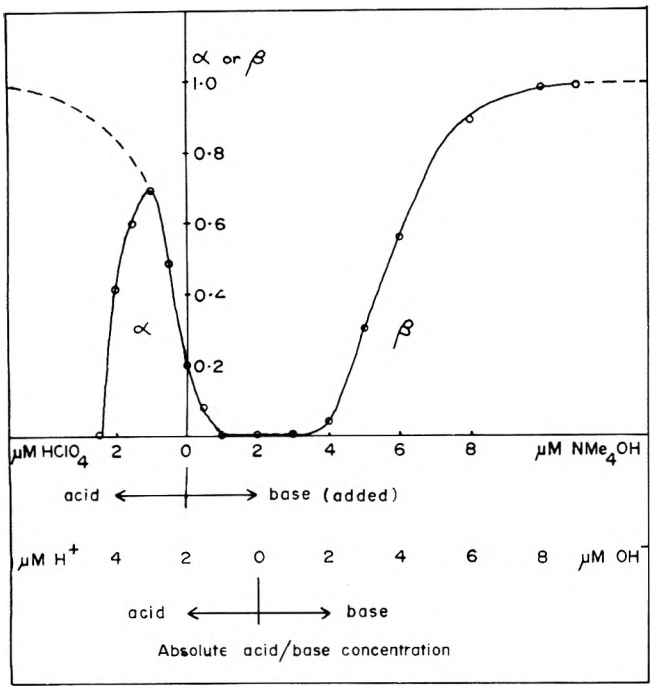

Figure 5. The variation of the parameters α and β (see text) with acid/base levels of the solvent (acetonitrile). The upper acidity scale represents concentrations of $HClO_4$ and NMe_4OH added by micropipet. The lower scale indicates what appears to be the absolute levels of H^+ and OH^-. Dashed portions of the curves are extrapolations based on the proposed proton transfer reactions. Note that β appears to extrapolate to unity, as required by the theory, and that α falls rapidly to zero beyond 3 μM H^+ not because the k_4 reaction is inoperative but because of the growth of the k_7 reaction.

If true neutrality is taken as the midpoint of the trough in Figure 5, then the neutral solution is actually about 2 μM in H^+, possibly due to residual CO_2. The true titration range is then from 4.5 μM H^+ to 8 μM OH^- (lower scale in Figure 6). In high acid (beyond 1.5 μM added $HClO_4$) the situation gets more complicated. Instead of returning to the baseline, the conductance swings positive once more. As additional traces of acid are added this new positive phase increases dramatically, and quickly obliterates the negative transient entirely. The k_1 spike, however, persists. The apparent value of α collapses rapidly to zero, and ceases to be meaningful because the "high acid" positive signal does not involve the k_4 reaction. The kinetic behavior of this signal suggests that it does not arise from any sequential reaction of the species so far discussed. Its risetime is shorter than the decay times of the intermediates involved in processes k_2 through k_6 and the initial positive spike (k_1) does not appear to change appreciably during the growth of the new signal. The maximum value of this phase occurs at approximately 3.5 μM added $HClO_4$ (5.5 μM total H^+), then it declines rapidly to a few percent of this value at 11 μM H^+. Beyond this point only small rapid transients with multiple inversions are seen, and precise measurement becomes difficult because of the large background conductivity. From Figure 7 it can be seen that not only does the size of the signal increase with acid concentration up to 3.5 μM, but the risetime varies inversely as $[H^+]$. The final relaxation is now very slow (at 2 μM $HClO_4$ the $t_{1/2}$ is in excess of 100 ms) and cannot be measured accurately with the present equipment.

Absorption spectrum measurements clearly show that in the "high acid" condition acetonitrile solutions of lumiflavin are partially protonated in the ground state. Thus, a possible mechanism for generating the large positive signal in high acid is a reaction of L_GH^+ with the "free" triplet, also protonated, according to the scheme

$$L_GH^+ + L_TH^+ \xrightarrow{k_7} LH\cdot + LH\cdot^{2+} \xrightarrow{H_2O,\ fast} LH\cdot + L\cdot^+ + H_3O^+$$

$$\Delta\lambda^0 = \{\lambda^0_{H_3O^+} - \lambda^0_{LH^+}\} = +65 \text{ per mol}$$

The pK of the lumiflavin triplet state has recently been determined to be 4.4 in aqueous solution.[40] It is not unreasonable, therefore, to assume protonation under the present conditions. The oxidized doubly positive species $LH\cdot^{2+}$, formed by electron transfer between the protonated flavin triplet and singlet molecules, is expected to lose a proton rapidly to water, making k_7 rate determining.

The signal maximum at 3.5 μM added acid corresponds to the conversion of 1.9 μM LH^+ to H_3O^+, and illustrates the ability of the conductance method to reveal reactions in which no change of charge occurs. The observed effect is entirely due to mobility differences. The diminution of the signal at higher acid can be attributed to the protonation of LH· or the reversal of the $LH\cdot^{2+} + H_2O \rightarrow L\cdot^+ + H_3O^+$ reaction. The rise kinetics are approximately pseudo first order due to the excess of L_GH^+ over L_TH^+, and the linear variation of $(t_{1/2})^{-1}$ with added H^+ implies that $[L_GH^+]$ increases linearly with $[H^+]$. Exact assignment of a rate constant for the reaction is not possible, however, since $[L_GH^+]$ is not known. If we assume that it is equal to $[H^+]$, then k_7 assumes a value of approximately 4×10^8 M^{-1} s^{-1}. Because $[L_GH^+]$ is necessarily less than $[H^+]$, k_7 is certain to be somewhat larger than the above value, though probably less than 1×10^9. This is slower than the other electron transfer reactions described in this study, presumably because both participants in the reaction carry a positive charge. The nonlinear variation of the amplitude of the k_7 component with added $[H^+]$ (Figure 7) is consistent with the requirement that both participating species be protonated. The $(t_{1/2})^{-1}$ vs. $[H^+]$ plot extrapolates to zero at $[H^+]$ = 1.5 μM, indicating that the k_7 reaction begins to develop at this point. The signal amplitude (ϕ^+) also appears to extrapolate to zero at the same point, though measurement in this region is difficult because of the presence of the ψ^- component described previously.

The slow final relaxation to the baseline in the "high acid" solution is attributed to the sequence

$$LH\cdot + L\cdot^+ \xrightarrow{k_5} L_GH^+ + L_G \qquad (\Delta\lambda^0 = 0)$$

followed by

$$L_G + H_3O^+ \xrightarrow{\text{slow, } k_8} L_GH^+ + H_2O \qquad (\Delta\lambda^0 = -65)$$

k_5 has already been assigned a value of 2×10^9 M^{-1} s^{-1}, so the first reaction cannot possibly be the rate-determining step in this sequence. We are forced to the conclusion that the process responsible for the observed very slow kinetics is the reprotonation of L_G. Even in 10 μM acid only a small fraction of L_G can be protonated (from purely stoichiometric considerations), so the final relaxation kinetics are expected to be pseudo first order, and relatively insensitive to $[H^+]$, the minority component. The $t_{1/2}$ is indeed apparently independent of $[H^+]$ and has a value of approximately 100 ms. Furthermore, $[L_G]$ can be assumed to be roughly constant at 45 μM, so that $k_8 \sim 1.5 \times 10^5$, i.e., very much

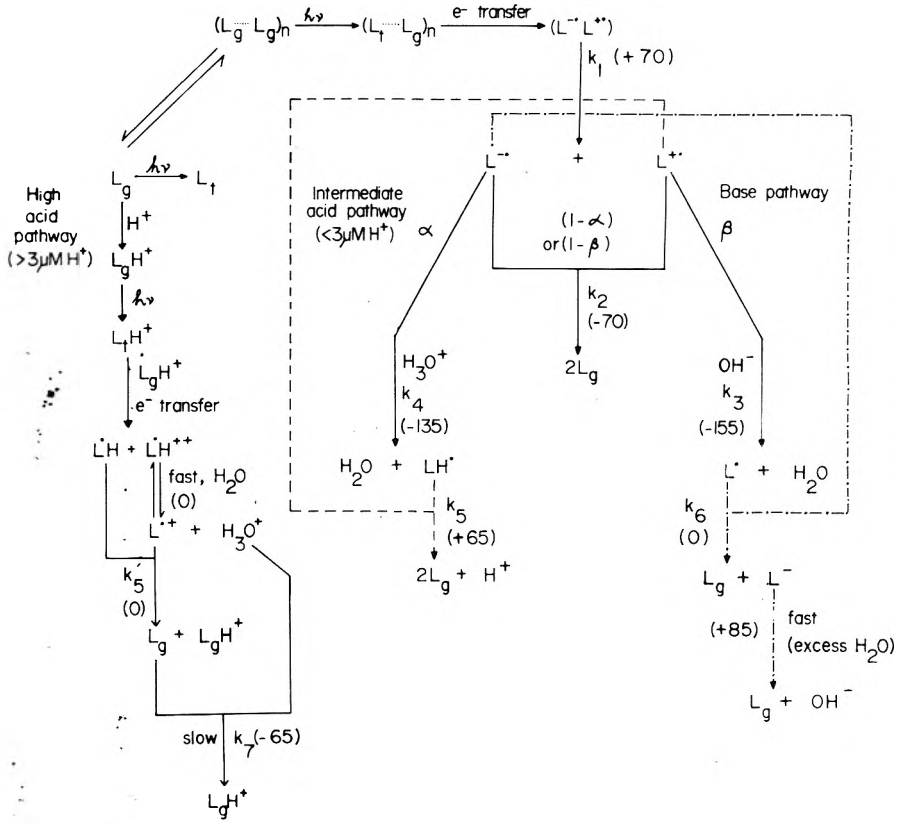

Figure 6. Summary of the primary electron transfer and secondary proton transfer reactions in pulse irradiated lumiflavin solutions in acetonitrile in the absence of indole. Rate constants are summarized in Table I.

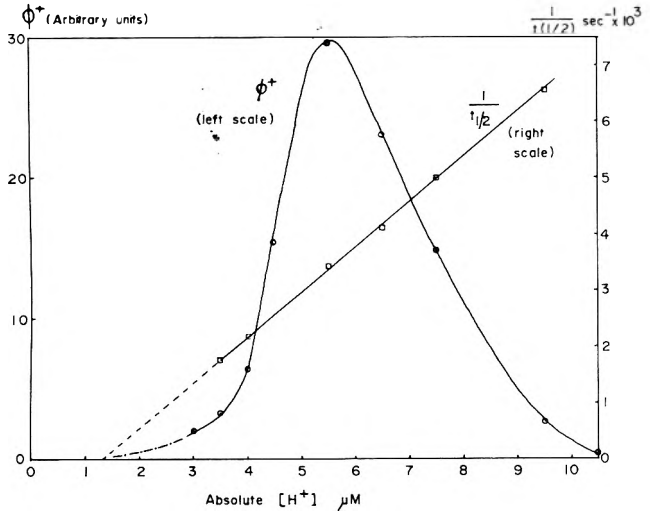

Figure 7. Kinetic behavior and amplitude of the positive "high acid" transient (attributed to k_7 and subsequent reactions) as a function of $[H^+]$.

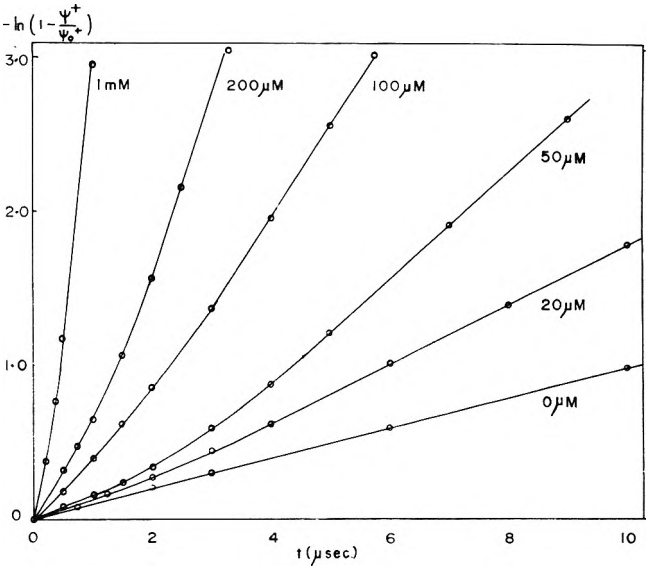

Figure 8. First-order (semilogarithmic) plots of the kinetics of growth of ion current in the presence of various concentrations of indole. At low indole concentrations the behavior is accurately first order. At higher concentrations deviations are seen in the first few microseconds, possibly due to participation of additional indole molecules in the radical ion uncorrelation process.

slower than diffusion controlled. We know of no independent estimate of this rate constant, but feel it is not incompatible with the weak basicity of the lumiflavin ground state.

B. Lumiflavin Photoionization in the Presence of Indole. i. Neutral Solutions. The effects of indole on the photochemical ionization of lumiflavin were studied at concentrations up to 250 μM by addition of the necessary volume of a stock solution of the donor in the appropriate solvent to the lumiflavin solution. Figure 8 shows a family of first-order plots of risetime data obtained from 50 μM solutions of lumiflavin in acetonitrile, doped with various concentrations of indole. The risetime (from slopes of linear regions of Figure 8 data) decreases linearly with increasing indole concentration, indicating that in contrast to the undoped flavin, ion formation in the presence of indole involves a bimolecular reaction between free triplet (L_T') and excess donor:

$$L_T' + I \xrightarrow{k_9} L\cdot^- + I\cdot^+$$

for which k_9, obtained from the data of Figure 8, is approximately 3×10^6 M^{-1} s^{-1}. Similar values for k_9 are obtained in butyronitrile and water solvents.

Figure 9 shows the variation of the initial positive signal amplitude with indole concentration in the three solvents employed. We interpret this complex behavior in terms of the k_9 reaction by means of the aggregate hypothesis.

i. In water, where little aggregation occurs, there is little photochemical ionization via k_1. Addition of indole causes the large quantity of free triplet to react via k_9, resulting in a dramatic enhancement of the primary photoconductance signal.

ii. In acetonitrile, the initial increase of conductance with [I] is similarly due to k_9, but further indole quenches the k_1 reaction within the aggregate.

iii. In butyronitrile, where almost all the flavin is thought to be aggregated, the k_9 component is negligible and the only effect of indole is to quench the k_1 reaction. The nature of this quenching is a matter of speculation. We suggest a mechanism in which indole complexes with the ground state flavin, but $I\cdot^+$ and $L\cdot^-$ fail to uncorrelate in the aggregate and rapid back-transfer of the electron occurs.

ii. Acid–Base Behavior in the Presence of Indole. The kinetic features of the secondary proton transfer reactions in the presence of indole are qualitatively similar to those already described for the undoped system. The important difference is that the major radical cation is $I\cdot^+$ rather than $L\cdot^+$; to invoke a similarity between the acid–base properties of these two species does not appear to be unreasonable. In acid solutions (up to 3 μM $HClO_4$) the final decay is found to be first order, in contrast to the approximately second-order behavior when indole is absent. The $t_{1/2}$ of this phase is independent of laser power when indole is present. Absorbance measurements, however, continue to show second-order kinetics even at high indole concentrations. To reconcile these observations we propose that the process associated with k_5 i.e.

$$L\cdot^+ + LH\cdot \xrightarrow{k_5,\ H_2O} 2L_G + H_3O^+$$

is replaced by the sequence

$$I\cdot^+ \xrightarrow{k_{10},\ H_2O\text{excess}} I\cdot + H_3O^+$$

(first-order relaxation of conductance)

followed by

$$I\cdot + LH\cdot \xrightarrow{k_{11}} L_G + I$$

(second-order absorbance decay; $\Delta\lambda^0 = 0$)

In base, second-order kinetics are seen by both methods, with the same $t_{1/2}$, implying that the following mechanism is predominant:

$$I\cdot^+ + OH^- \xrightarrow{k_{12}} I\cdot + H_2O$$

$$I\cdot + L\cdot^- \xrightarrow[H_2O\ \text{excess}]{k_{13}} L_G + I + OH^-$$

Since the k_{12} reaction obeys pseudo-first-order kinetics the observed second-order behavior implies that the k_{13} step is rate determining. The conductance signal corresponds to the eventual net one-electron reduction of $I\cdot^+$. Values for

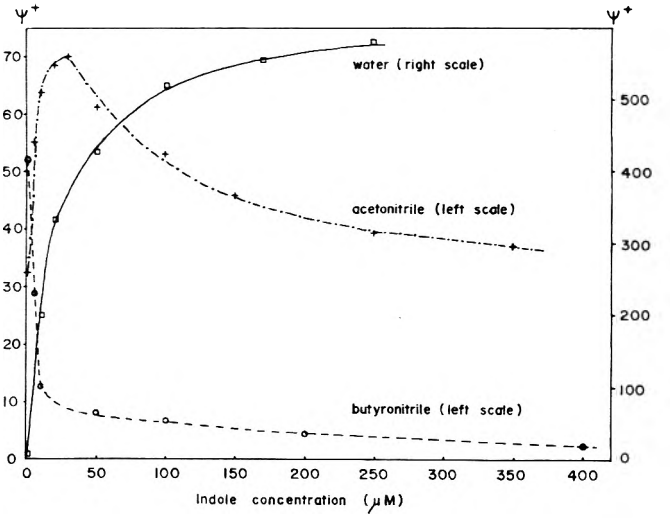

Figure 9. Variation of the amplitude of the primary radical-ion signal as a function of indole concentration in acetonitrile, butyronitrile, and water.

k_{10}, k_{11}, and k_{13} are compiled in Table I. k_{12} cannot easily be assigned, beyond the necessity that it exceed k_{13}.

Flash Photolysis with Optical Detection. i. Neutral Solutions. Flash photolysis experiments with lumiflavin alone in aqueous solution have been reported previously.[2] Both the flavin radical and the triplet species can be observed; the triplet lifetime is approximately 100 μs, and the radical decays via second-order kinetics with a rate constant of 1.5×10^9 M^{-1} s^{-1}. A similar triplet lifetime is seen in the present experiments in acetonitrile. The radical transient, however, is significantly different. Instead of simple second-order kinetics a multiphasic signal is observed (Figure 10). The initial rapid phase has a $t_{1/2}$ of several hundred microseconds; the slow component follows second-order kinetics with rate constant $k = 2 \times 10^9$ M^{-1} s^{-1}. Furthermore, the slow component grows in at a rate which is significantly smaller than the risetime of the flash.

When indole (100 μM) is added to the lumiflavin solution in water the triplet transient can no longer be observed, and the radical transient increases in magnitude. Again, radical decay is second order ($k = 1.4 \times 10^9$ M^{-1} s^{-1}) with no biphasic character. In acetonitrile no triplet can be observed in the presence of indole, and the radical signal is greatly increased (approximately fivefold). Biphasic kinetics are observed and in this case the fast component is much better resolved, because the rate of decay of the second component is much slower in the presence of indole than in the undoped system. The fast decay has a $t_{1/2}$ of approximately 400 μs; the slow phase is second order ($k = 1 \times 10^7$ M^{-1} s^{-1}). No distinct growing-in of the second component is seen in this case, presumably due to the slower decay of the initial transient.

To provide a comparison, an optical flash photolysis experiment was conducted with lumiflavin plus indole (100 μM) in butyronitrile. As with acetonitrile, no triplet transient is observable, the radical decay is biphasic, and no growing-in of the slow component can be seen. The initial fast phase has a decay $t_{1/2}$ identical with that obtained in acetonitrile; the second-order rate constant for the slow component is now 5.2×10^6 M^{-1} s^{-1}. A comparison of these results in terms of the relative proportions of rapid and slow radical decay components is instructive. In water, no biphasic decays are observed. In acetonitrile the fast com-

TABLE I: Rate Constants for Radical Reactions

Reaction	Solvent[a]	k	Method[b]
$L\cdot^+ + L\cdot^- \xrightarrow{k_1} L\cdot^+ + L\cdot^-$	A,B	1.3×10^5 s^{-1}	E
	W	2.6×10^5 s^{-1}	E
$L\cdot^+ + L\cdot^- \xrightarrow{k_2} 2L_G$	A,B	6×10^9 M^{-1} s^{-1}	E,O
$L\cdot^+ + OH^- \xrightarrow{k_3} L\cdot + H_2O$	A	4×10^9 M^{-1} s^{-1}	E
$L\cdot^- + H_3O^+ \xrightarrow{k_4} LH\cdot + H_2O$	A	4×10^9 M^{-1} s^{-1}	E
$LH\cdot + L\cdot^+ \xrightarrow[H_2O]{k_5} 2L_G + H_3O^+$	A	2×10^9 M^{-1} s^{-1}	E
	W	1.5×10^9 M^{-1} s^{-1}	O
$L\cdot^- + L\cdot \xrightarrow{k_6} L_G + L^-$	A	3×10^9 M^{-1} s^{-1}	E
$L_GH^+ + L_TH^+ \xrightarrow{k_7} LH\cdot + LH\cdot^{2+}$	(?) A	$\sim 4 \times 10^8$ M^{-1} s^{-1}	E
$L_G + H_3O^+ \xrightarrow{k_8} LH^+ + H_2O$	A	$\sim 1.5 \times 10^5$ M^{-1} s^{-1}	E
$L_T' + I \xrightarrow{k_9} L\cdot^- + I\cdot^+$	A,B,W	3×10^9 M^{-1} s^{-1}	E
$I\cdot^+ \xrightarrow[H_2O]{k_{10}} I\cdot + H_3O^+$	A	2.2×10^2 s^{-1}	E
$I\cdot + LH\cdot \xrightarrow{k_{11}} I + L_G$	A	1.0×10^7 M^{-1} s^{-1}	O
	B	5.2×10^6 M^{-1} s^{-1}	O
$I\cdot^+ + OH^- \xrightarrow{k_{12}} I\cdot + H_2O$	A	$> 2 \times 10^9$ M^{-1} s^{-1}	E,O
$I\cdot + L\cdot^- + H_2O \xrightarrow{k_{13}} L_G + I + OH^-$	A	2×10^9 M^{-1} s^{-1}	E
	A	1.4×10^9 M^{-1} s^{-1}	O
$LH\cdot + I\cdot^+ \xrightarrow[H_2O]{k_{14}} L_G + I + H_3O^+$	A	1.0×10^7 M^{-1} s^{-1}	E,O

[a] A = acetonitrile, B = butyronitrile, W = water. [b] E = electrical (i.e., conductimetric), O = optical (absorbance).

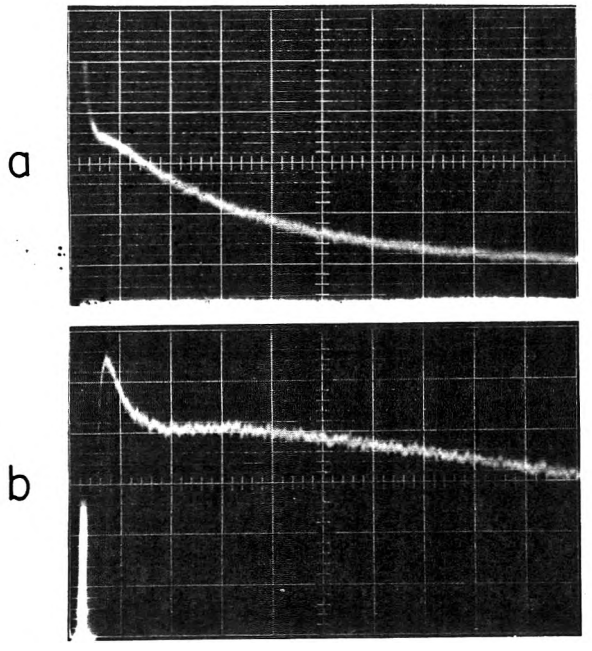

Figure 10. Optical transients observed at 560 nm; 50 μM lumiflavin solution in neutral acetonitrile: (a) 1 ms per division; (b) 200 μs per division.

ponent accounts for about 30% of the total signal, both in the presence and absence of indole. In butyronitrile the proportion of fast component is over 50%. Thus it would appear that as the polarity of the solvent is decreased the proportion of fast-decaying component is increased.

It is possible to identify the rapid decay with the recombination of the ion-radical species (i.e., $L\cdot^+ + L\cdot^-$ or $I\cdot^+ + L\cdot^-$), and the slow decays with the recombination of the cation radicals with the neutral lumiflavin radical (i.e., $L\cdot^+ + LH\cdot$ or $I\cdot^+ + LH\cdot$). This is consistent with our interpretation of the electrical conductance data (see above). An increase of $[H^+]$ in going from butyronitrile to acetonitrile to water could account for the observed changes in the relative proportions of the two components in these solvents. The growing-in of the slowly decaying transient can then be ascribed to the protonation of $L\cdot^-$. Inasmuch as we observe that the rate constant for $LH\cdot + I\cdot^+$ (k_{14}) is considerably smaller than that for $LH\cdot + L\cdot^+$ (k_5) (see Table I), the slower initial decay found in the presence of indole might be attributed to a similar disparity in the rate constants of $L\cdot^- + I\cdot^+$ and $L\cdot^- + L\cdot^+$(k_2).

On the basis of these results, and those of our earlier experiments with phenols[2] it is reasonable to conclude that radical formation in the presence of indole proceeds via the lumiflavin triplet state. However, in the absence of indole a triplet transient with a decay time of approximately 100 μs is observed. Radical formation, on the other hand, occurs within the lifetime of the flash (20 μs). Furthermore, we have done experiments which show that O_2 (4×10^{-4} M) and KI (3×10^{-4} M) completely quench radical formation, clearly implicating a triplet state.[2] This provides supporting evidence for the suggestion made on the basis of the electrical measurements that electron transfer between lumiflavin molecules occurs within preformed dimers or more complex aggregates.

ii. Effects of Acid and Base. When $HClO_4$ (up to 13 μM) is added to either lumiflavin alone or lumiflavin plus indole in acetonitrile, the flash-induced radical transient is increased by approximately a factor of 3. This is closely comparable to the maximum increase in conductance seen in the acid titration (Figure 4). Inasmuch as we are observing

mainly the neutral flavin radical in absorbance measurements at 560 nm,[2] one component of the observed increase in signal will be due to direct protonation of $L\cdot^-$, though this is essentially complete at 3 μM H^+ ($\alpha \sim 1$) and cannot account for the threefold increase of [LH·] beyond that point. The spectroscopic observation of large amounts of neutral radical in highly acidic conditions is, however, entirely compatible with the mechanism (k_7 and subsequent processes) invoked to explain the conductance behavior in this region. The effects of base (both with and without indole) on the flash transients are considerably more complex, and we have not attempted detailed analysis at this time. Comparisons between the optical and conductometric observations are made below.

iii. Comparison between the Slow Decay Processes Observed in Optical and Conductometric Measurements. Since the time resolutions of the two methods employed in these studies are so very different (optical $\geq$20 μs, electrical 0.3 μs) it is only possible to make accurate comparisons between the slowest decay processes (which occur in the millisecond region). With lumiflavin alone in acetonitrile, in neutral solution and in the presence of low (<1 μM) concentrations of acid, the final decays of the conductance and absorbance signals are both second order with approximately equal rate constants. It seems safe to state that both are due to the same process, i.e., LH· + $L\cdot^+$. In the presence of indole, however, the conductance decays by first-order kinetics ($t_{1/2}$ independent of laser power) whereas the absorbance decays according to second-order kinetics. The time scales of the two relaxations are also very different, the optical decay being very much slower. It appears certain that in this case the two methods observe different processes. The electrical decay is attributed to the loss of a proton from $I\cdot^+$ (see above) and the absorbance decay to the subsequent reaction of I· with LH·. This neutral radical recombination reaction is consistent with the slow optical decay ($k = 1 \times 10^7$ M^{-1} s^{-1}, compared to the 10^9 M^{-1} s^{-1} rate constants associated with the ion radical reactions). Comparisons are tenuous at low base concentrations (<5 μM) inasmuch as the slow decays characteristic of the optical signals cannot be accurately measured using the present apparatus.

At higher base concentrations, however, both sets of experiments (lumiflavin plus indole) give second-order kinetics with similar rate constants, implying identical mechanisms. If the decay reaction is attributed to the process $L\cdot^-$ + I·, this would be consistent with the interpretation of the conductivity data obtained in neutral and slightly acidic solutions. The rate constant obtained from the optical experiments in high base (5–14 μM) is 2×10^9 M^{-1} s^{-1}, about 100 times larger than in the neutral solutions, and this further increases confidence in the above scheme. No comparisons are possible in the absence of indole at high base because of the very small signals obtained in the optical experiments. A summary of the rate constants obtained in the present experiments is presented in Table I.

Conclusions

The phenomena described in this paper have their origins in complex electron and proton transfer reactions, some of which remain ill-defined. Our explanations of these processes are based on a number of ad-hoc hypotheses which provide a seemingly good correlation of a large body of data but which require independent studies for their verification. The primary assumption is the involvement of a polymeric (dimer or more complex aggregate) form of the flavin as the species in which photoactivated electron transfer occurs. This conclusion is indicated primarily on the basis of the true first-order kinetics of ion-radical formation ($t_{1/2}$ independent of [L_G] and laser power). This type of behavior might also arise from redox reactions involving the solvent, though we discount this possibility in the present case on the basis of the relative ion yields in water and acetonitrile. Ion-radical signals are very much smaller in water than acetonitrile in spite of the fact that the former is more easily oxidized. The observation of a long-lived triplet species whose kinetics do not correspond to the primary ionization process (itself quenched by O_2) indicates that the "normal" or monomer triplet is not involved in electron transfer but a "special" triplet is. Absolute conductance measurements suggests this latter species to comprise about 13% of the total triplet under the conditions described. Since we propose that its origin is a preformed (ground state) dimer or aggregate, studies by NMR or optical methods should confirm or deny its existence. The conductance behavior in high acid suggests that the "free" triplet can undergo electron transfer only when protonated. The exact nature of the ground state aggregate is a matter of speculation; it may consist of simple face-to-face dimers or polymeric species of higher complexity. We have not attempted detailed theorization as to why electron transfer occurs so easily in this species but not in the unprotonated monomer. It is tempting to suppose that the precise orientation provided by hydrogen bonding is responsible, or even that proton movement within the aggregate is a necessary component of the overall electron transfer process. A test of these hypotheses might be to study ion yields in N- or O-methylated flavins. Electron transfer from indole to lumiflavin appears to involve the monomer species, though ion-pair uncorrelation seems more complicated than in the undoped lumiflavin system. The second-order component (illustrated by the curvature of the plots in Figure 9) suggests that charge-separation requires the participation of additional indole molecules. The complex kinetics of the secondary reactions appear to have quantitative explanation in terms of the mechanisms proposed. These involve reasonable rate constants and do not conflict with any of the known acid–base properties of the flavins and there appears to be reasonably good correlation between the conductimetric and optical data. The proposed mechanism for the "high acid" phase involves electron transfer between protonated free triplet and ground state molecules, and gives an explanation of the major kinetic features observed, including the quenching of ion formation at high [H^+]. Similar reactions have been observed in thiazine[43] and fluorescein[44] dyes and in the porphyrins.[45]

The utility of conductimetric measurement in studying electron and proton transfer reactions is clearly demonstrated. It is highly complementary to the traditional absorbance methods, and has very great sensitivity. The complexities of the processes described in this paper are not invariably present. Porphyrins and metalloporphyrins appear to undergo clean pseudo-first-order electron transfer kinetics and accurate second-order recombination of the anion and cation radicals,[46] without the proton transfer reactions which make the photochemistry of lumiflavin so complex.

Acknowledgment. This work was supported in part by a grant from the National Institutes of Health (AM15057) to

G.T. and from the National Science Foundation (GB-33399) to D.C.M.

References and Notes

(1) G. R. Penzer and G. K. Radda, *Q. Rev. Chem. Soc.*, **21**, 43 (1967).
(2) S. P. Vaish and G. Tollin, *J. Bioenerg.*, **1**, 181 (1970).
(3) J. M. Gillard and G. Tollin, *Biochem. Biophys. Res. Commun.*, **58**, 328 (1974).
(4) K. D. Waterpaugh, L. C. Sieker, and L. H. Jensen, *Proc. Natl. Acad. Sci. U.S.A.*, **70**, 3857 (1973).
(5) R. M. Burnett, G. D. Darling, D. S. Kendall, M. E. Le Quesne, S. G. Mayhew, W. W. Smith, and M. L. Ludwig, *J. Biol. Chem.*, **249**, 4383 (1974).
(6) D. E. Edmondson and G. Tollin, *Biochemistry*, **10**, 124 (1971).
(7) D. E. Edmondson and G. Tollin, unpublished experiments with *Azotobacter* flavodoxin.
(8) W. R. Briggs in "Photophysiology" A. C. Giese, Ed., Vol. 1, 1964, p 249.
(9) G. Tollin and M. Robinson, *Photochem. Photobiol.*, **9**, 411 (1969).
(10) B. Diehn, *Biochem. Biophys. Acta*, **177**, 136 (1969).
(11) W. Haupt and I. Schonfeld, *Ber. Dtsch. Bot. Ges.*, **75**, 14 (1962).
(12) R. D. Draper and L. L. Ingraham, *Arch. Biochem. Biophys.*, **125**, 802 (1968).
(13) S. P. Vaish and G. Tollin, *J. Bioenerg.*, **2**, 61 (1971).
(14) H. S. Piloff and A. C. Albrecht, *J. Chem. Phys.*, **49**, 4891 (1968).
(15) M. Tamir and M. Ottolenghi, *Chem. Phys. Lett.*, **6**, 369 (1970).
(16) D. K. Sharma, J. Stevenson, and G. J. Hoytink, *Chem. Phys. Lett.*, **29**, 343 (1974).
(17) G. Beck and J. K. Thomas, *Chem. Phys. Lett.*, **13**, 295 (1972).
(18) J. Bullot and A. C. Albrecht, *J. Chem. Phys.*, **51**, 2220 (1969).
(19) W. M. McClain and A. C. Albrecht, *J. Chem. Phys.*, **43**, 465 (1965).
(20) K. D. Cadogan and A. C. Albrecht, *J. Chem. Phys.*, **51**, 2710 (1969).
(21) J. Lilie, S. A. Chaudhri, A. Mamou, M. Gratzel, and J. Rabani, *J. Phys. Chem.*, **77**, 597 (1973).
(22) M. Tachia and A. Mozumda, *Chem. Phys. Lett.*, **28**, 87 (1974).
(23) J. R. Miller, *Chem. Phys. Lett.*, **22**, 180 (1973).
(24) N. B. Nazhat and K. D. Asmus, *J. Phys. Chem.*, **77**, 614 (1973).
(25) Y. Taniguchi and N. Mataga, *Chem. Phys. Lett.*, **13**, 596 (1972).
(26) R. W. Bigelow, *J. Phys. Chem.*, **78**, 1395 (1974).
(27) Y. Achiba, S. Katsumata, and K. Kimura, *Chem. Phys. Lett.*, **13**, 213 (1972).
(28) J. Lilie and R. W. Fessenden, *J. Phys. Chem.*, **77**, 674 (1973).
(29) A. Kawada and R. C. Jarnagin, *J. Chem. Phys.*, **44**, 1919 (1966).
(30) Y. Taniguchi, Y. Nishina, and N. Mataga, *Bull. Chem. Soc. Jpn.*, **45**, 764 (1972).
(31) J. Feltelson and E. Hayon, *J. Phys. Chem.*, **77**, 10 (1973).
(32) K. H. Grellman and A. R. Watkins, *Chem. Phys. Lett.*, **9**, 439 (1971).
(33) M. Ottolenghi, *Chem. Phys. Lett.*, **12**, 339 (1971).
(34) A. V. Guzzo and G. Tollin, *Arch. Biochem. Biophys.*, **106**, 380 (1964).
(35) S. G. Ballard, *Rev. Sci. Instrum.*, in press.
(36) P. S. Song, T. A. Moore, and W. E. Kurtin, *Z. Naturforsch B*, **27**, 1011 (1972).
(37) F. Müller, S. G. Mayhew, and V Massey, *Biochemistry*, **12**, 4654 (1973).
(38) R. H. Sarma, P. Dannies, and N. O. Kaplan, *Biochemistry*, **7**, 4539 (1968).
(39) (a) A. C. Harkness and H. M. Daggett, Jr., *Can. J. Chem.*, **43**, 1215 (1965); (b) A. K. Covington and T. Dickinson, Ed., "Physical Chemistry of Organic Solvent Systems", Plenum Press, London, 1973, Chapter 5.
(40) S. Schriener, U. Steiner, and H. E. A. Kramer, *Photochem. Photobiol.*, **21**, 81 (1975).
(41) G. Tollin in "Molecular Associations in Biology", B. Pullman, Ed., Academic Press, New York, N.Y., 1968, p 393.
(42) J. F. Coetzee, G. P. Cunningham, D. K. McGuire, and G. R. Padmanabhan, *Anal. Chem.*, **34**, 1139 (1962).
(43) R. Bonneau, P. Fornier de Violet, and J. Joussot-Dubien, *Photochem. Photobiol.*, **19**, 129 (1974).
(44) R. Lesclaux, S.Ohayon, and J. Joussot-Dubien, *Photochem. Photobiol.*, **11**, 401 (1970).
(45) D. Mauzerall, *J. Phys. Chem.*, **66**, 2531 (1962).
(46) S. G. Ballard and D. Mauzerall, manuscript in preparation.

Transference Number and Solvation Studies in Tetramethylurea

R. C. Paul,* S. P. Johar, J. S. Banait, and S. P. Narula

Department of Chemistry, Panjab University, Chandigarh-160014, India *(Received July 28, 1975)*

Transference numbers of sodium and potassium thiocyanates have been measured in tetramethylurea at 25 °C by a modified Hittorf's method in the concentration range 1.5–9.4 × 10^{-2} M. A linear relationship is observed between the cation transference number and the square root of the concentration. Combining the limiting transference numbers and limiting equivalent conductances of these two salts, ionic mobilities of sodium, potassium, and thiocyanate ions have been found to be 16.08, 15.73, and 33.04 ohm^{-1} cm^2 mol^{-1}, respectively. From these values ionic mobilities of other univalent ions, effective ionic radii, and solvation numbers have been computed. Higher solvation of cations than of anions of comparable sizes is consistent with the aprotic nature of the solvent.

From conductance studies, Barker and Caruso[1,2] have highlighted the potentialities of tetramethylurea (TMU) as an excellent aprotic solvent for study of the transport behavior of various uni-univalent electrolytes. However, due to lack of transference number data in this solvent, they have calculated mobilities of various ions by an approximate method based on the equimobilities of triisoamylbutylammonium and tetraphenylboride ions. However, such approximations have not been found satisfactory in many solvents.[3-6] In the present work, transference numbers of sodium and potassium thiocyanates have been measured in TMU at 25 °C using a modified Hittorf's method in order to evaluate ionic mobilities accurately. Effective ionic radii and solvation numbers of various univalent ions have been calculated to throw light on the ion–solvent interactions in this solvent.

Experimental Section

Tetramethylurea (Fluka AG) was purified by storing it over sodamide for 24 h with occasional shaking, refluxed under vacuum, and then distilling. It was finally distilled under reduced pressure and the middle fraction boiling at 63.5–64.0 °C (12 mm), specific conductance[1] 2–4 × 10^{-8} ohm^{-1} cm^{-1}, d_0^1 = 0.9616 g ml^{-1}, was collected and stored under anhydrous conditions in the dark. The above solvent was freshly distilled and physical constants were checked for each experimental run.

Sodium and potassium thiocyanates (BDH AnalaR) were used as such after drying under vacuum. Transference number measurements were carried out as reported earlier.[7] The thermostat was controlled at 25 ± 0.01 °C. Be-

cause of the solubility of silver thiocyanate (formed at the anode during electrolysis) in TMU, the solutions of the cathode and the middle compartments were analyzed. The concentration of thiocyanate ions was estimated gravimetrically as silver thiocyanate. Four estimations were performed for each solution and the results agreed within ±0.0002 g/100 g. The equation for the calculation of transference number is the same as that employed by Wear and coworkers[8] and the precision was found to be within 1%. Transference of all material as far as possible was done in a nitrogen-filled drybox.

Results and Discussion

Transference numbers of sodium and potassium thiocyanates have been measured in the concentration range 1.54–5.23 × 10^{-2} and 1.76–9.39 × 10^{-2} M, respectively, in TMU at 25 °C. The results are given in Table I. The cation transference number has been found to vary linearly with the square root of the concentration ($\sqrt{c}$) and on extrapolation give a limiting transference number (t_+^0) of Na^+ and K^+ ions of 0.327 and 0.323, respectively. Combining limiting transference numbers with limiting equivalent conductances of the respective electrolytes,[1,2] the ionic mobility of the SCN^- ion has been found to be 33.04 ± 0.02 ohm^{-1} cm^2 mol^{-1}. This value differs from the value (33.44 Λ units) reported by Barker and Caruso[1] by 0.4 Λ units. Ionic mobilities obtained by the two approaches (transference measurements and equimobilities of ions of certain reference electrolytes) have been found to differ in other solvents[3-6] also. A better accuracy of the present results can be claimed as these are obtained from experimental transference number data. This value has been used to compute ionic mobilities of various univalent ions employing Kohlrausch's law of independent ion migration. All relevant data are given in Table II.

A perusal of Table II shows that limiting equivalent conductances of the alkali metal ions decrease (except Na^+) with increase in crystallographic radii. However, the mobility of Na^+ is more than that of K^+. Similar anamolous behavior is observed in *N,N*-dimethylacetamide (DMA)[9,10] also. In liquid HCN[11] and sulfolane,[12] the mobility of Li^+ is found to be more than that of Na^+. In TMU, Barker and Caruso[1] have attributed abnormal solvation of Na^+ to the stearic factors due to the size and structure of the solvent molecules.

Solvated ionic radii in TMU have been calculated using Stoke's equation as has already been reported.[5] Corrected ionic radii (r_{cor}) for the ions are then obtained from Nightingale's calibration curve constructed for tetraalkylammonium ions in this solvent. Except for the tetramethylammonium ion, all other ions lie on a straight line. This indicates that the tetramethylammonium ion is slightly solvated in TMU as in dimethyl sulfoxide,[4] DMA,[9] and hexamethylphosphoric triamide.[5] Solvation numbers of various ions have been calculated by the procedure already reported[5] using an average volume of TMU molecule (200.7 Å^3 at 25 °C). All relevant data are given in Table II.

From Table II it is clear that the solvation numbers of cations in TMU (except Na^+) decrease with increase in size of the ions. The solvation numbers of anions, on the other hand, do not follow the general pattern. The observed order is $Br^- > ClO_4^- > SCN^- > NO_3^-$.

In DMA[9] and *N,N*-dimethylformamide (DMF)[13] also, the anions show a similar behavior. A perusal of Table II further shows that the corrected radii of sodium and potassium ions are very close to that of the tetrabutylammonium ion in TMU. Whereas in other solvents such as formamide,[14] *N*-methylformamide,[15] and DMF[13] the corrected radii of sodium and potassium ions are intermediate between those of tetraethylammonium and tetrapropylammonium ions. This shows that cations form larger solvodynamic species in TMU and thus supports the aprotic nature of this solvent. The aprotic nature of this solvent is further supported by the ionic mobility–viscosity products and the chemical structure of the solvent.

TABLE I: Transference Numbers[a] of NaSCN and KSCN at Various Concentrations in Tetramethylurea at 25 °C

NaSCN			KSCN		
Concn, M	t_c (±1%)	t_a (±1%)	Concn, M	t_c (±1%)	t_a (±1%)
0.00000	0.327	0.673	0.00000	0.323	0.677
0.01542	0.310	0.690	0.01765	0.311	0.689
0.02137	0.307	0.693	0.03491	0.307	0.693
0.04533	0.299	0.701	0.04634	0.304	0.696
0.05236	0.297	0.703	0.06604	0.300	0.700
			0.09393	0.295	0.705

[a] t_c is the cation transference number and t_a is the anion transference number.

TABLE II: Ionic Mobilities ($\lambda_\pm$), Crystallographic (r_c), Solvated (r_s), and Corrected (r_{cor}) Radii, and Solvation Numbers (N) of Various Univalent Ions in Tetramethylurea at 25 °C

Ion	$\lambda_\pm$, ohm^{-1} cm^2 mol^{-1}	r_c, Å	r_s, Å	r_{cor}, Å	N
Li^+	14.47	0.60	4.04	5.10	2.8
Na^+	16.08	0.96	3.64	4.78	2.3
K^+	15.73	1.33	3.72	4.85	2.4
Rb^+	16.04	1.48	3.65	4.80	2.2
Cs^+	16.93	1.69	3.45	4.65	2.0
NH_4^+	18.01	1.44	3.25	4.45	1.9
Me_4N^+	22.57	3.47	2.59	3.95	0.4
Et_4N^+	22.07	4.00	2.65	4.00	
Pr_4N^+	16.98	4.52	3.44	4.52	
Bu_4N^+	15.49	4.94	3.78	4.94	
SCN^-	33.04	2.15	1.77	3.25	0.5
Br^-	30.12	1.95	1.94	3.40	0.7
NO_3^-	32.38	2.64	1.81	3.30	0.4
ClO_4^-	28.33	2.40	2.06	3.50	0.6

References and Notes

(1) B. J. Barker and J. A. Caruso, *J. Am. Chem. Soc.*, **93**, 1341 (1971).
(2) B. J. Barker and J. A. Caruso, *J. Phys. Chem.*, **77**, 1884 (1973).
(3) M. D. Monica, D. Masciopinto, and G. Tessari, *Trans. Faraday Soc.*, **66**, 2872 (1970).
(4) R. Gopal and J. S. Jha, *J. Phys. Chem.*, **78**, 2405 (1974).
(5) R. C. Paul, J. S. Banait, and S. P. Narula, *Z. Phys. Chem. (Frankfurt am Main)*, **94**, 199 (1975).
(6) P. Bruno, M. D. Monica, and E. Righetti, *J. Phys. Chem.*, **77**, 1258 (1973).
(7) R. C. Paul, J. P. Singla, and S. P. Narula, *J. Phys. Chem.*, **73**, 741 (1969).
(8) J. O. Wear, C. V. McNully, and E. S. Amis, *J. Inorg. Nucl. Chem.*, **18**, 48 (1961).
(9) R. C. Paul, J. S. Banait, and S. P. Narula, *Aust. J. Chem.*, **28**, 321 (1975).
(10) G. R. Lester, T. A. Gover, and P. G. Sears, *J. Phys. Chem.*, **60**, 1076 (1956).
(11) G. E. Coates and E. G. Taylor, *J. Chem. Soc.*, 1245 (1936).
(12) M. D. Monica, M. Lamanna, and L. Senatore, *J. Phys. Chem.*, **72**, 2124 (1968).
(13) R. C. Paul, J. P. Singla, D. S. Gill, and S. P. Narula, *J. Inorg. Nucl. Chem.*, **33**, 2953 (1971).
(14) R. C. Paul, J. P. Singla, D. S. Gill, and S. P. Narula, *Indian J. Chem.*, **9**, 981 (1971).
(15) R. C. Paul, D. S. Gill, J. P. Singla, and S. P. Narula, *Indian J. Chem.*, **9**, 63 (1971).

Electron Transfer in Dinucleoside Phosphate Anions

M. D. Sevilla,* R. Failor, C. Clark,

Department of Chemistry, Oakland University, Rochester, Michigan 48063

R. A. Holroyd, and M. Pettei

Department of Chemistry, Brookhaven National Laboratory, Upton, New York 11973 *(Received September 12, 1975)*

Publication costs assisted by ERDA and the Petroleum Research Fund

The electron transfer reaction within various dinucleoside phosphate radical anions has been investigated by ESR spectroscopy and pulse radiolysis. In the ESR work electrons are produced by photolysis of $K_4Fe(CN)_6$ in a 12 M LiCl glass at 77 K. Upon photobleaching the electrons react with the dinucleoside phosphate to form the anion radical. The anions of the four DNA nucleosides were also produced and their ESR spectra were appropriately weighted and summed by computer to simulate the spectra found for the dinucleoside phosphate anions. From the analysis the relative amounts of each of the nucleoside anions in the dinucleoside phosphate anion were determined. For example in thymidylyl-(3′–5′)-2′-deoxyadenosine (TdA), where the bases are likely stacked so as to allow electron transfer to the base with the greatest electron affinity, the electron is found to localize on thymine. Whereas in equal mixtures of T and dA in which the molecules are isolated in the aqueous medium anions of both nucleosides are found in approximately equal amounts. These results and those found for the other dinucleosides studied (TdC, TdG, dAdC, TT) suggest the electron affinity of the pyrimidine bases are greater than the purine bases; however, the results are not sufficient to distinguish between the individual purine or pyrimidine. When dinucleoside phosphate anions containing thymidine are warmed protonation occurs only on thymine to produce the well known "thymyl" spectrum. Pulse radiolysis experiments on individual nucleotides (TMP, dAMP), mixtures of these nucleotides and the dinucleoside phosphate, TdA, in aqueous solution at room temperature show that in the TdA anion electron transfer occurs from adenine to thymine, whereas no electron transfer is found for mixtures of individual nucleotides. Protonation is found to occur only on thymine in the TdA anion in agreement with the ESR results.

Introduction

A major initial effect of all forms of ionizing radiation on DNA is the production of positive and negative ions of the DNA bases. These ions may later react to produce biologically significant damage. Such ion radicals have been reported. Graslund, Ehrenberg, Rupprecht, and Strom report an anion radical on thymine or cytosine and a cation radical on guanine or cytosine in γ-irradiated oriented DNA at 77 K.[2] Due to the complexity of the DNA molecule, unequivocal determinations of radicals formed from these ions have not been made. However, the thymine anion has been shown to protonate to form a neutral radical in aqueous systems (reaction 1).[3–5] This reaction has been suggested to account for the formation of this radical in γ-irradiated DNA.[3,5,6]

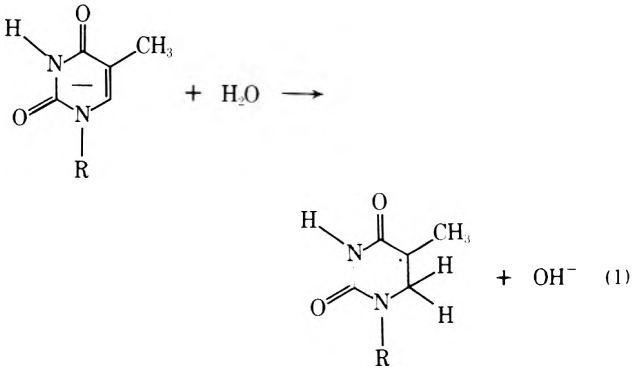

I

This electron spin resonance and pulse radiolysis study of the reaction of electrons with dinucleoside phosphates (DNPs) was begun to better understand the role of the electron in DNA radiolysis. Specifically our goals were (1) to ascertain on which DNA base the electron localized and (2) to determine what reactions occur after formation of the DNP anion.

It is important to the first goal to learn whether DNA bases in DNPs are stacked so as to make electron transfer to the more electron affinic base possible in the rigid glass used in the ESR study or in the aqueous solution used in the pulse radiolysis study. There are a number of investigations which have shown that the DNA bases in dinucleotides, or free in solution, will tend to stack.[7–12] The stacking has been found to be temperature dependent with stacking favored at lower temperatures.[7,9,10,13] Purine–purine stacking is found to be favored somewhat over pyrimidine–purine stacking.[9] In the ESR work the room temperature solutions of DNPs in 12 M LiCl are cooled to 77 K. The solution remains a liquid upon cooling to approximately 190 K where the solution becomes a glass. Thus, in this system stacking should be greatly favored. The high salt concentration in the solution might be expected to affect the stacking; however, Brahms, Maurizot, and Michelson have shown in work with a number of DNPs in 5 M KI that the ionic strength had no important effect on the stacking.[13] The work reported in this paper also suggests stacking occurs for most of the DNPs.

The abbreviations used in this paper for the nucleosides are as follows: deoxyadenosine, dA; deoxycytidine, dC; deoxyguanosine, dG; thymidine, T; thymidine-5′-monophos-

phate, TMP; deoxyadenosine-5′-monophosphate, dAMP. In the case of the dinucleoside phosphates (DNPs), the abbreviations for the component nucleosides are used: for example, TdA represents thymidylyl-(3′–5′)2′-deoxyadenosine.

Experimental Section

The nucleosides and dinucleoside phosphates used in this work were obtained from Sigma. The nucleotides were obtained from Calbiochem.

The experimental apparatus and procedure for the ESR work has been detailed in previous investigations.[4,5,14,15] In this method a solution of 12 M LiCl (D_2O) containing 2×10^{-2} M $K_4Fe(CN)_6$ and 5×10^{-4} to 1×10^{-3} M solute is cooled to 77 K. The glass formed is photolyzed with 254-nm light at 77 K. Trapped electrons formed by the photolysis of the $K_4Fe(CN)_6$ are photobleached with light from an incandescent lamp. The photobleached electrons either react with the solute or the ferricyanide formed in the photolysis. To prevent photolysis of the solute the $K_4Fe(CN)_6$ concentration was kept in at least 20-fold excess over that of the solute. In addition, photolysis times were kept short, less than 1 min, at reduced lamp intensity. Since photoionization of these solutes has been shown to be biphotonic the reduced lamp intensity helped to prevent formation of positive ions.

In order to simulate the DNP anion spectra, the spectra of the individual nucleoside anions were recorded and stored in the computer (IBM 1130) memory. Several spectra of each nucleoside and DNP anion were run, if necessary, to reduce the noise level. The resultant average was stored for later use. Since a dual cavity was employed, a second signal due to peroxylaminedisulfonate was used as a field calibration marker (A_N = 13.0G and g = 2.0056). The positions of the three components of the peroxylaminedisulfonate spectrum were simultaneously stored in the computer memory. An EAI 693 analog-digital converter was employed to digitize the data before storage. The spectra of the DNP anions were assumed to be simple sums of the spectra of the individual nucleoside anions. The program assured that the three markers from the standard aligned when summing spectra. To determine the relative weighting factors, each nucleoside anion spectrum was doubly integrated. The computed and experimental spectrum for the DNP anion were then compared and the best fit chosen.

The pulse radiolysis investigation was performed using the Van de Graaf accelerator at the Department of Chemistry of Brookhaven National Laboratory. Solutions of the nucleotides were prepared in triply distilled water containing 10% *tert*-butyl alcohol (to scavange H and OH) and 5 mM phosphate buffer and were degassed by bubbling with argon. Spectra were recorded following 5–10-μsec pulses of 1.9-MeV electrons. The ferrous sulfate dosimeter was used.

Results and Discussion

I. *ESR Results and Discussion. Individual Nucleoside Anion Radicals.* The ESR spectra of the anion radicals of the four DNA nucleosides in 12 M LiCl–D_2O at 110 K are shown in Figure 1. These spectra were used to simulate the spectra of the DNP anions discussed below. The analyses of the T, dC, adenine, and quanine anion spectra have been reported elsewhere.[5,16,17]

Below we describe the reactions of electrons with DNPs and with mixtures of their component nucleosides. These

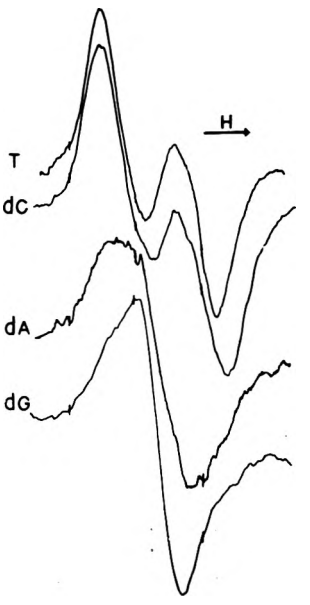

Figure 1. First derivative ESR spectra of the nucleoside anions in 12 M LiCl–D_2O at 110 K: (A) thymidine anion, (B) deoxycytidine anion, (C) deoxyadenosine anion, (D) deoxyguanosine anion. The distance in magnetic field between the markers in the spectrum is 13.0 G. The central marker is at g = 2.0056.

experiments were performed in deuterated solutions to prevent protonation reactions at carbon sites in anions such as in reaction 1. Deuteration is found to occur at a much slower rate.[15]

Reactions of Electrons with TdA and T plus dA Mixtures. In Figure 2 we show the result of electron attachment to TdA. Computer simulations show the best fit to be 100% T anion (shown in Figure 2). Simulations with as little as 10% dA anion were distinguishable. This result suggests that the DNA bases are stacked and the electron is transferred from dA to T. Another possibility is that they are not stacked and the electron reacts much more readily with T than dA in the DNP. This possibility is not in accord with the kinetics of electron reaction with thymine and adenine in aqueous solution.[18] These results show the rates of reaction to be comparable.

Since it could be argued that the rates may differ in a frozen glass of high ionic strength a test of the second explanation was performed. In these experiments equal molar mixtures of T and dA (1×10^{-3} M) were prepared. Electron addition gave the spectrum shown in Figure 3. The computer simulation gave a best fit for 60% T anion and 40% dA anion. This result is quite reasonable in light of the previous kinetic studies. The combined results for TdA and T + dA strongly suggests that electron transfer to T is occurring with the DNP.

Electron Reactions with TdG, TT, and T plus dG Mixtures. The result of electron attachment to TdG in 12 M LiCl–D_2O at 110 K is shown in the bottom curve of Figure 4. The computer simulations are for 100% T and 90% T. The depth of the switchback suggests a value between 90 and 100% T anion; however, there are clearly some differences in line shape between the simulations and that of the TdG anion. The computer simulations do not indicate that this difference is due to a small amount of dG anion.

The results of the reaction of the electron with equal molar mixtures of T and dG are shown in Figure 5. As expected the initial spectrum found at 110 K is that of an ap-

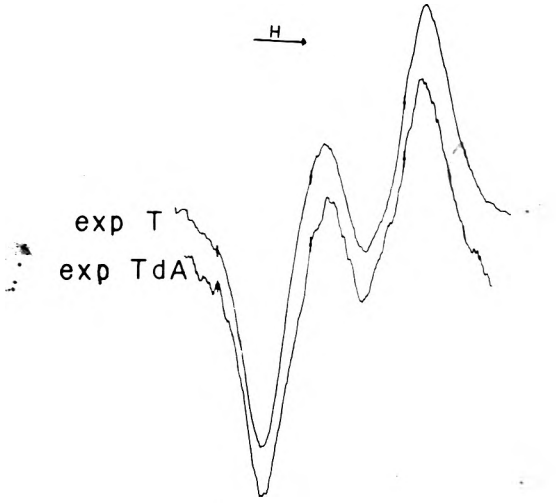

Figure 2. The ESR spectrum (lower spectrum) of the TdA anion in 12 M LiCl–D_2O at 110 K. The ESR spectrum (upper spectrum) found for T anion. Computer simulations which summed the dA anion with the T anion gave a best fit for pure T anion.

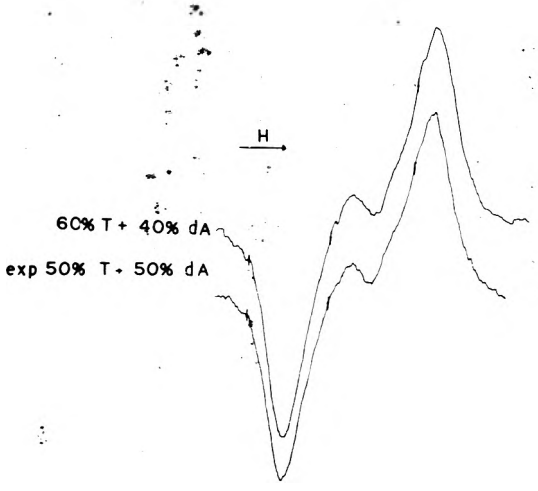

Figure 3. The ESR spectrum (lower spectrum) found after the reaction of electrons with an equal molar mixture of T and dA in 12 M LiCl at 110 K. Computer simulation (upper spectrum) of the lower curve summing T anion and dA anion in the ratio of areas 6:4.

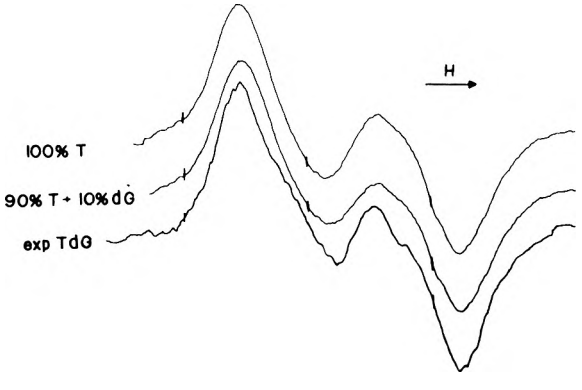

Figure 4. ESR spectrum (lower spectrum) of the TdG anion at 110 K in 12 M LiCl. Computer simulation (middle spectrum) of the TdG anion spectrum summing 90% T with 10% dG. Spectrum (upper spectrum) of T anion at 110 K in 12 M LiCl–D_2O.

proximately equal mixture of the anions. Warming the sample of 165 K (Figure 5A) results in no appreciable change in the spectrum. However, warming to 190 K where

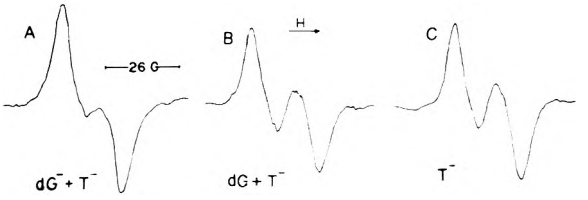

Figure 5. (A) ESR spectrum of an equal molar mixture of T and dG after electron attachment and warming to 165 K in 12 M LiCl–D_2O. In the process of warming no significant change in the spectrum occurred. (B) ESR spectrum of the mixture in A after warming to 190 K where the glass has softened sufficiently to allow for molecular diffusion. (C) ESR spectrum of T anion in 12 M LiCl–D_2O at 180 K.

the glass has softened sufficiently to allow molecular migration resulted in a spectrum (Figure 5B) essentially identical with that found for T anion at this temperature (Figure 5C). These results suggest that either (1) the electron transfer reaction 2 has occurred, or (2) the guanine anion reacts to form some other species which is less resolved. Since dG anion has a tendency to photoprotonate and since the above results were not found to repeat for T + dA mixtures we cannot at this time distinguish between these two possibilities. However, the results found at 110 K provide evidence that an electron transfer reaction to T is occurring in TdG anion as in the TdA anion.

$$T + dG^- \rightarrow T^- + dG \qquad (2)$$

The results for TdG anion suggest that T is more electron affinic than dG. The difference in computed and experimental line shapes may be a result of the stacking of the DNA bases. The stacking would be expected to place magnetic nuclei near the sites of high spin density on T, also the stacking changes the conformation of the sugar group. Both these effects could have some effect on the unresolved splittings which contribute to the line shape of the T anion in TdG.

Some support for this explanation is given by the results found after electron attachment to TT. The spectrum of TT anion in LiCl–D_2O at 110 K displays the same features that distinguish the TdG anion from the pure T anion. It is thus likely that the stacking has a small effect on the line shape and that our analysis based on the sums of the individual nucleoside anions must be considered approximate. Perhaps more importantly the results for the TT anion suggest that the electron transfer from dG to T in TdG is very nearly complete.

Electron Reactions with TdC and dAdC. In Figure 6, we show the result of electron attachment to TdC in 12 M LiCl–D_2O at 110 K. The lower spectrum in Figure 6 is a computer simulation in which the spectra of T and dC anions are added in equal proportions. The fit is excellent; however, the similarity of the spectra of T and dC anions results in approximately a 15% uncertainty in the relative concentrations. Even with this uncertainty the results may suggest that the electron affinities of the pyrimidine nucleosides are approximately equal. However, the fact that pyrimidines tend to stack somewhat less than purines may suggest an alternative explanation, i.e., that the DNA bases are not stacked and are reacting as isolated molecules. These two possibilities cannot be distinguished in this case.

In Figure 7 the result of electron attachment to dAdC in 12 M LiCl–D_2O at 110 K is shown. The lower curves show computer simulations for various relative combinations of dC and dA anions. The best fit suggests approximately 80%

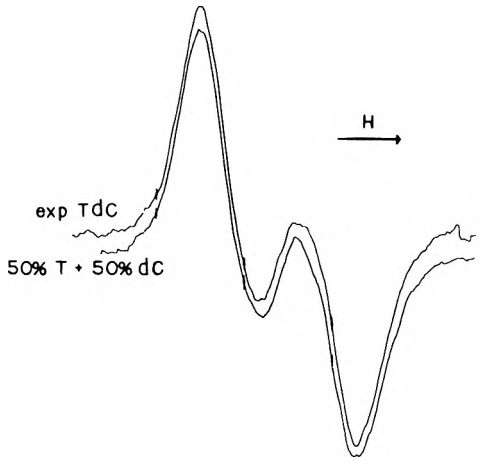

Figure 6. ESR spectrum (upper spectrum) of the TdC anion at 110 K in 12 M LiCl–D_2O. Computer simulation (lower spectrum) weighting both T anion and dC anion equally.

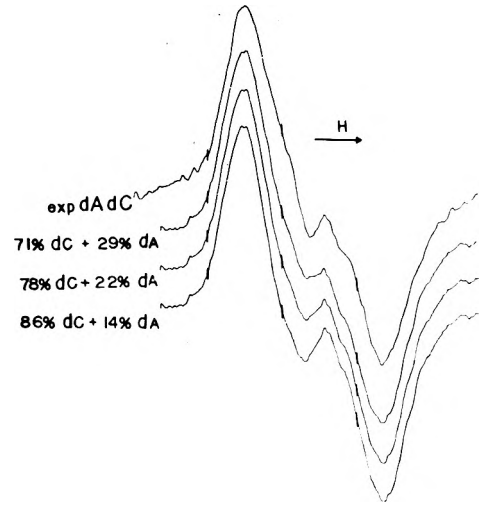

Figure 7. ESR spectrum (upper spectrum) of the AdC anion at 110 K in 12 M LiCl–D_2O. Computer simulations (lower three curves) of the dA and dC in the ratios given in the figure. The best fit is at about 80% dC and 20% dA.

dC anion and 20% dA anion in the dAdC anion. There was some variability in the experimental result. At times more resolved spectra were obtained at other times less. It may be that the amount of stacking is sensitive to the method of sample preparation such as the rate of cooling. Warming the dAdC anion to 175 K resulted in no significant change in the spectrum. These results cannot be interpreted unambiguously since stacking may not be complete.

Protonation Reactions of the TdA, TdG, TdC, and dAdC Anions. The anion radicals of TdA, TdG, TdC, dAdA, and dAdC were produced in 12 M LiCl–H_2O and warmed to 180 K. The anions of TdA and TdG protonated on the thymine base (Figure 8A) to form the expected eight-line "thymyl" radical (reaction 1). The reaction could also be induced by photolysis with long wavelength uv light (Figure 8B). For TdC only partial protonation was noted. This perhaps suggests that the bases are not stacked in TdC and electron transfer from dC to T is slowed. The dAdA and dAdC anions showed no reaction on warming.

II. *Pulse Radiolysis Results and Discussion. dAMP.* For solutions of dAMP at 20 °C the spectrum observed immediately after the pulse shows a maximum near 320 nm (ϵ ~4000) and a weaker but broad band around 560 nm (ϵ ~750), see Figure 9. This spectrum is attributed to the dAMP anion formed by electron attachment, reaction 3.[18b]

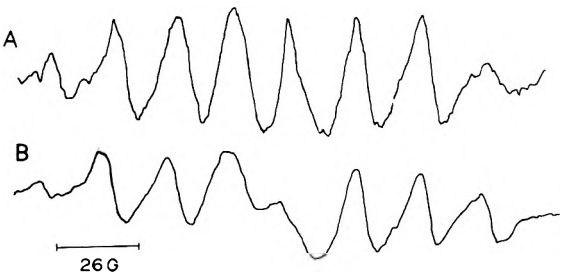

Figure 8. (A) The spectrum found after warming the TdA anion in 12 M LiCl–H_2O to 180 K for 30 min. The spectrum of the T anion has been virtually completely converted to radical I. (B) The spectrum found after uv photolysis of the TdG anion in 12 M LiCl–H_2O at 77 K with long wavelength uv >3200 Å. Only a partial conversion is found. Warming the TdG anion resulted in a nearly complete conversion of anion to radical I.

$$e_{aq}^- + \text{dAMP} \rightarrow \text{dAMP}^- \qquad (3)$$

Absorption near 320 nm is typical of nucleic acid base anions.[20,24] This spectrum rapidly transforms at pH 7 to a new spectrum with a strong, narrow peak at 355 nm (ϵ 1.1×10^4). The grow-in at 355 nm and the decay at 540 nm are both first order. The half-life of the conversion is 16 μs at pH 7. The rate of conversion is pH dependent, decreasing as the pH increases; at pH 10 the half-life is 122 μs. This first-order process (reaction 4) is suggested to yield a

$$\text{dAMP}^- \xrightarrow{H^+} \text{dAMP(H)} \qquad (4)$$

species protonated perhaps at a carbon site. Protonation of $dAMP^-$ has been observed by ESR.[19] A similar behavior is observed for adenosine but electron attachment to adenine yields only the 320-nm species. Addition of H atoms to dAMP at pH 2 yields a species with a maximum at 320 nm.

TMP. Electron attachment to TMP yields a species whose spectrum is shown in Figure 10. The absorption is weak and the maximum in this case is at 390 nm (ϵ 1400). This species is present at the end of a 10-μs pulse. Because of its similarity to the species formed by H-atom addition[20,21] it is probably a protonated species. This suggests reaction 1 occurs rapidly in this case.

Mixture of TMP and dAMP (50:50). The initial spectrum (not shown) observed immediately after a pulse for a 50:50 mixture shows absorptions at 320 and 540 nm which is characteristic of the dAMP anion. The decay at 540 nm is first order with a half-life of 13 μs which is similar to the result for pure dAMP. This indicates electron attachment to dAMP but does not exclude formation of TMP^-.

There is a rapid conversion of the spectrum and at 75 μs the spectrum is that shown in Figure 11 by the solid points. The dominant feature at this time is the strong peak at 355 nm indicating dAMP(H) is formed. The intensity of the absorption indicates 41% of the electrons form dAMP(H). The remainder react with TMP, which is shown by the following: there is more of a shoulder at 400 nm in the spectrum in Figure 11 than in Figure 9. If the contribution of dAMP(H) is subtracted the residual spectrum (open circles) is very similar to Figure 10, showing a maximum at 390 nm. The yield of the TMP adduct is about one-half the yield observed in pure TMP solutions. The observed lack

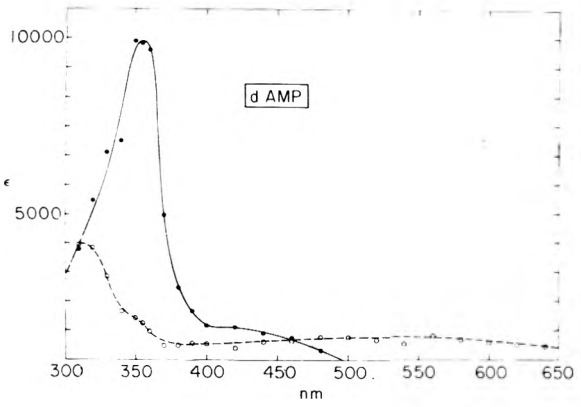

Figure 9. Uv–visible absorption spectra of species formed on electron attachment to deoxyadenosine 5′-monophosphate disodium salt (0.67 mM) at pH 7.4: (O) initial spectrum; (●) spectrum at 100 μs.

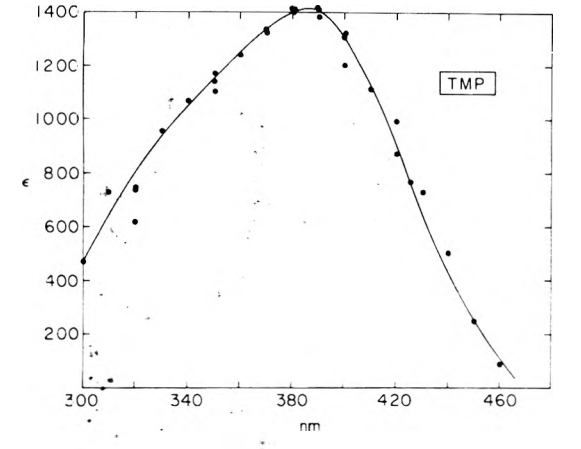

Figure 10. Absorption spectrum of species formed on electron attachment to thymidine 5′-monophosphate disodium salt (1 mM) at pH 7. This species is present immediately after a 10-μs pulse.

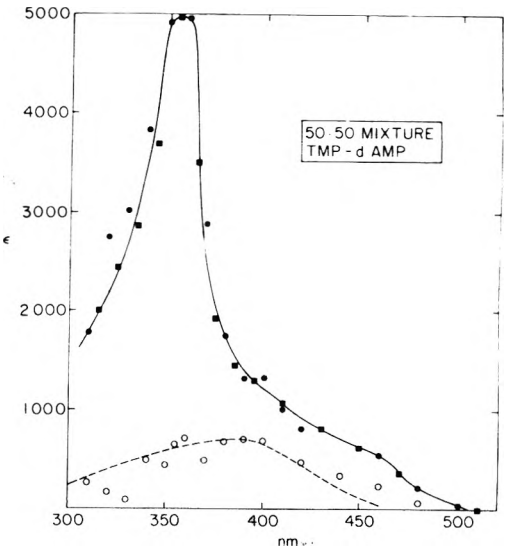

Figure 11. Absorption spectra of species formed on electron attachment to a 50:50 mixture of TMP and dAMP; absorbance vs. wavelength. Filled points are spectrum at 75 μs after pulse pH 7.2: (●) 0.4 mM of each, (■) 0.9 mM of each; (O) spectrum after subtracting 41% of 100-μs spectrum in Figure 1; (- - -) 50% of spectrum in Figure 2.

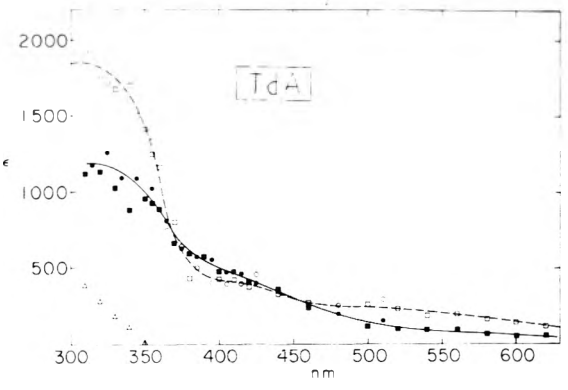

Figure 12. Absorption spectra of species formed on electron attachment to thymidylyl-(3′–5′)-2′-deoxyadenosine. Open points are initial spectrum. Filled points are spectrum at 200 μs after pulse. Circles are for 0.7 mM dinucleotide; squares are 0.4 mM. (Δ) permanent spectrum observed at 0.5 s.

of electron transfer is supported by separate experiments which show that electron transfer from these radical anions to other nucleotides does not compete with protonation.

Dinucleoside Phosphate (TdA). The initial spectrum observed following reaction of e_{aq}^- with TdA has a strong band ($\epsilon \sim 1800$) around 320 nm and a weaker absorption extending into the visible (Figure 12). This spectrum is thus very similar to that observed initially for dAMP (Figure 9) as well as for the 50/50 mixture. During the first 200 μs there is decay at wavelengths from 310 to 370 nm and from 450 to 600 nm (initial half-life ~130 μs). At wavelengths between 370 and 450 nm the absorbance either stays constant or increases slightly in this time interval; there is no grow-in at 355 nm. The decay of the final species absorbing at 400 nm follows second-order kinetics and $k = 3.3 \times 10^8$ M^{-1} s^{-1}.

There are four major results of the pulse radiolysis experiments. (1) In dAMP the anion formed by electron attachment has a weak, but characteristic band in the visible.[18b] There is no absorption in this region by the species formed from TMP. (2) The dAMP anion converts to a species absorbing at 355 nm. This spectrum (Figure 9) is sufficiently different from the spectrum obtained with TMP (λ_{max} 390 nm, see Figure 10) to allow identification of the species formed in mixtures and in a dinucleoside phosphate. (3) In the mixture electrons add to both nucleotides, there is no electron transfer from one to the other. The spectrum observed at 75 μs shows approximately equal contributions of the two secondary (protonated) species. (4) Very different results are obtained for the dinucleoside phosphate; the initial spectrum, showing absorption at 320 and 550 nm, indicates the electron is partially on adenine. Localization on thymine may also occur as is indicated by enhanced absorption around 400 nm initially. The spectral changes in the first 200 μs indicate electron transfer from A → T; this is supported by the decay at 320 and 550 nm and the grow-in at 400 nm characteristic of a protonated thymine. The lack of grow-in of a peak at 355 nm is good evidence that the electron does not stay on adenine. The slowness of the transfer is perhaps surprising since T and A are in the same molecule. It may be explained by the fact that stacking of the bases is only partial at ambient temperatures.

Conclusion

Both the ESR and pulse radiolysis results agree that

electron transfer occurs in the DNPs from the purine to the pyrimidine base. However, in the pulse radiolysis results it can be argued that the reason for electron transfer in TdA is the more rapid rate of protonation of the thymine anion, which of course would draw the electron to thymine.

Since low temperatures and deuterated solvents employed in the ESR work prevented protonation as well as induced stacking, the initial unpaired electron distribution in the DNPs is a consequence of the relative attraction of the DNA bases for an excess electron. Thus the ESR results found for the DNP anions can be used to order the four nucleosides in terms of their electron affinity in an aqueous solution. The results for TdA and TdG clearly show that the electron affinity of T is greater than dG or dA. The relative ordering of the electron affinity of dC has not been unequivocably determined. The results suggest that it is intermediate between T and the purine nucleosides. Thus, the following order of electron affinities for all the DNA nucleosides is indicated: T $\simeq$ dC > dA $\simeq$ dG. The ordering of the electron affinities of the free DNA bases would be expected to be the same as found in the DNPs.

These conclusions are in agreement with results of theoretical calculations of the electron affinity of the DNA bases.[22,23] These calculations predict the order of electron affinity to be thymine > cytosine $\gg$ quanine > adenine. Several experiments on the radiation chemistry of DNA or DNA bases lend some support to our findings. As was mentioned in the Introduction, Graslund et al. have found results that suggest free electrons generated in the γ irradiation of DNA localize on thymine or perhaps cytosine.[2] Adams et al. have found in pulse radiolysis studies that the rates of electron transfer from DNA bases to orotic acid were in the following order: thymine < cytosine < adenine.[24] The same order was found for the nucleosides and nucleotides. These results could be correlated directly with the relative electron affinity only if the reverse rate constants were also known. However, the lower rate of transfer for thymine is suggestive of a higher electron affinity. Gregoli and Bertinchamps in studies of γ-irradiated purine–pyrimidine cocrystals found that the unpaired spin transfers from the purine to the pyrimidine.[25] The authors suggested a one electron transfer mechanism to explain the results.

Both the ESR results and the pulse radiolysis results for the dinucleoside phosphate anions in H_2O solution clearly show that the T anion protonates preferentially over the other DNA base anions in the DNP anions. The localization on thymine in TdG and TdA found in the ESR work does not necessarily prohibit the pronation of dG or dA. This is because there must be some small equilibrium concentration of the purine anions. Thus if they reacted much more rapidly with H_2O than the thymine anion, they could compete effectively. However, the ESR results for nonthymine containing DNPs show that the rate of protonation of the purine base anions and cytosine anion in DNP anions is less than that of thymine anion. In agreement with these results the pulse radiolysis experiments for the individual nucleotide anions show that the TMP anion protonates more rapidly than the dAMP anion. Thus we can conclude that the rate of protonation (via reaction 1) is faster for T^- or TMP^- than for other nucleoside or nucleotide anions and that this results in preferential protonation of thymine in DNP anions. If these results are extended to a consideration of γ-irradiated DNA, we would predict localization of the excess charge on the pyrimidine bases with subsequent protonation of the thymine base only. It is interesting to note that results found for γ-irradiated DNA show this to be the case.[2]

Acknowledgment. This research was supported in the most part by the U.S. Energy Research and Development Administration. Acknowledgment is also made to the Donors of the Petroleum Research Fund, administered by the American Chemical Society, for partial support of this research. Two authors (C.C. and R.F.) were participants in the National Science Foundation Undergraduate Research Program.

References and Notes

(1) This research was supported by the United States Energy Research and Development Administration, and by the Petroleum Research Fund, administered by the American Chemical Society.
(2) N. Graslund, A. Ehrenberg, A. Rupprecht, and G. Strom, *Biochem. Biophys. Acta*, **254**, 172 (1971).
(3) R. A. Holroyd and J. Glass, *Int. J. Radiat. Biol.*, **14**, 445 (1968).
(4) M. D. Sevilla, *J. Phys. Chem.*, **74**, 3366 (1970).
(5) M. D. Sevilla, C. Van Paemel, and C. Nichols, *J. Phys. Chem.*, **76**, 3571 (1972).
(6) M. G. Ormerod, *Int. J. Radiat. Biol.*, **9**, 291 (1965).
(7) S. I. Chan and J. H. Nelson, *J. Am. Chem. Soc.*, **91**, 168 (1969).
(8) B. W. Bangester and S. I. Chan, *J. Am. Chem. Soc.*, **91**, 3910 (1969).
(9) P. O. P. Ts'o and S. I. Chan, *Biochemistry*, **8**, 997 (1969).
(10) P. M. Pitha, W. M. Hauang, and P. O. P. Ts'o, *Proc. Natl. Acad. Sci.*, **61**, 332 (1968).
(11) M. P. Schweizer, S. I. Chan, and P. O. P. Ts'o, *J. Am. Chem. Soc.*, **87**, 5241 (1965).
(12) A. D. Broom, M. P. Schweizer, and P. O. P. Ts'o, *J. Am. Chem. Soc.*, **89**, 3612 (1967).
(13) J. Brahms, J. C. Maurizot, and A. M. Michelson, *J. Mol. Biol.*, **25**, 481 (1967).
(14) M. D. Sevilla, R. Failor, and G. Zorman, *J. Phys. Chem.*, **78**, 696 (1974).
(15) C. Van Paemel, H. Frumin, V. L. Brooks, R. Failor, and M. D. Sevilla, *J. Phys. Chem.*, **79**, 839 (1975).
(16) M. D. Sevilla and C. Van Paemel, *Photochem. Photobiol.*, **15**, 407 (1972).
(17) M. D. Sevilla and P. A. Mohan, *Int. J. Radiat. Biol.*, **25**, 635 (1974).
(18) (a) E. J. Hart, S. Gordon, and J. K. Thomas, *J. Phys. Chem.*, **68**, 1271 (1964); (b) G. Scholes in "Radiation Chemistry of Aqueous Systems", G. Stein Ed., Interscience, New York, N.Y., 1968.
(19) S. Gregoli, M. Olast, and A. Bertinchamps, *Radiat. Res.*, **60**, 388 (1974).
(20) L. Theard, F. Peterson, and L. Myers, Jr., *J. Phys. Chem.*, **75**, 3815 (1971).
(21) L. S. Myers, Jr., and L. M. Theard, *J. Am. Chem. Soc.*, **92**, 2868 (1970).
(22) N. Bodor, M. J. S. Dewar, and A. J. Harget, *J. Am. Chem. Soc.*, **92**, 2929 (1970).
(23) H. Berthod, C. Gressner-Prettre, and A. Pullman, *Theor. Chim. Acta*, **5**, 53 (1966).
(24) G. E. Adams, C. L. Greenstock, J. J. van Hemmen, and R. L. Willson, *Radiat. Res.*, **49**, 85 (1972).
(25) S. Gregoli and A. Bertinchamps, *Int. J. Radiat. Biol.*, **21**, 75 (1972).

Size Effect in Transfer of Nonpolar Solutes from Gas or Solvent to Another Solvent with a View on Hydrophobic Behavior

Michel Lucas*

Département de Génie Radioactif, C.E.A., B.P. 6, 92260 Fontenay-aux-Roses, France *(Received June 4, 1975)*

Publication costs assisted by Commissariat à l Energie Atomique

The free energy of transfer for a nonpolar solute from the gaseous state to nonpolar solvents and water has been computed by means of the original scaled particle theory (SPT) and Stillinger modification of the SPT. A hypothetical water carrying the model structural features of water, but with dimensions twice as large has also been considered. The calculations make it apparent that the solvent dimensions are an important parameter in determining the sign of the free energy of transfer for a nonpolar solute from one solvent to another. The structure of the solvent determines the sign of the entropy of transfer.

I. Introduction

In the frame of the scaled particle theory (SPT) as applied to real solvents,[1,2] solvents are considered hard spheres which are related to real solvents in that the hard-sphere diameter is as close as possible to the real solvent molecular diameter. The density of the real solvent at each temperature is used in the calculation with the SPT so that some structural aspects of the solvent are implicitly taken into account.

A nonpolar solvent such as cyclohexane, neopentane, benzene, or CCl_4 is taken as a collection of hard spheres with a relatively large diameter of approximately 5.5 Å and a relatively high number density, so that the parameter y, used in the SPT and defined as $y = \pi Na^3/6V$, where N and V are respectively Avogadro's number and the molal volume of the solvent, is ca. 0.5. In addition, for enthalpy and entropy calculations the isobaric solvent expansivity coefficient $\alpha = (1/V)(\delta V/\delta T)$ is required which for the molecules considered and many other nonpolar solvents at room temperature is ca. 1.2×10^{-3} deg^{-1}.[1]

In the SPT frame, water is considered a collection of hard spheres, with $a = 2.75$ Å which is smaller than that of other usual solvents, with a relatively low number density so that y is approximately 0.38, and a small value for α which is 0.25×10^{-3} deg^{-1},[2] at 25 °C.

These small values for α and y are evidently related to the tetrahedral coordination of water, so that the SPT, as used to compute the thermodynamic properties of nonpolar solutes in water, implicitly takes somewhat into account the water structure.

The problem of hydrophobic bonding, that is, the strong tendency of hydrocarbons in water to aggregate, can be related (at least if the aggregate contains a sufficiently high number of molecules) and is intuitively related to the original problem of the transfer of nonpolar solutes to a nonpolar solvent from water[3] (e.g., transfer of C_4H_{10} from liquid C_4H_{10} to water or from cyclohexane to water), and the SPT, which has been shown to successfully predict the solubility of nonpolar rare gases or hydrocarbons into water[2] and organic solvents[1] from the gaseous state, may be used either to compute the strength of aggregates of hydrocarbons in water[3-5] (in a modified form), or the transfer of a hydrocarbon from water to its pure liquid phase. Then water is defined by its a, y, and α, and in our opinion the relative influence of these three parameters on the transfer has not been clearly assessed.

*Address correspondence to this author at Service de chimie Physique, CEN Saclay B.P. No 2, 91190 Gif sur Yvette, France.

II. Discussion

(a) *Calculations with the SPT.* In order to make apparent the relative influence of these parameters, we have computed the free energy and entropy of solution from the gaseous state for nonpolar solutes, with or without dispersion forces, into water, into a nonpolar solvent of molecular size 5.5 Å and an imaginary solvent called "hypothetical water" which has the same low y and α as water but with a diameter twice as large (5.5 Å), so that its molar volume is 144 cm^3 (8 times that of water). Then the important structural features of water are conserved (in the extent it can be so in the frame of the SPT). A nonpolar solvent is always, in our calculations, characterized by $\alpha = 1.2 \times 10^{-3}$ K^{-1} and $y = 0.5$. For the calculations the solute hard-sphere diameter a_2 is required and also the parameter necessary to compute approximately the influence of dispersion forces, that is, ϵ_{11}/k for water: 100 K (a rounded value, estimates being from 85[2] to 98 K[6]). ϵ/k for the nonpolar solvent and nonpolar solutes is given by the approximate relation[6]

$$\epsilon_{22}/k = 14\epsilon(a_2 - 2.50)$$

where a_2 is in Å and ϵ_{22}/k in K. As usual we use $\epsilon_{12} = (\epsilon_{11}\epsilon_{22})^{1/2}$. Also[1-3,7] we have $\Delta G = RT \ln K = \Delta G_{HS} + G_i$, with $G_i = -(64/3)Ry(\epsilon_{12}/k)(a + a_2)^3/8a^3$, and

$$\Delta G_{HS} = RT \ln \left(\frac{RT}{V}\right) - RT \ln (1 - y) + \frac{9}{2}RT\left[\frac{y^2}{(1-y)^2} + \frac{2y}{3(1-y)}\right]\frac{a_2^2}{a^2} + 3RT\frac{ya_2}{(1-y)a}$$

where a and a_2 are respectively the solvent and solute hard-sphere diameters, V the solvent molar volume, and K the Henry constant.

Figure 1a shows plots of the free energy of solution from the gaseous state for a nonpolar solute in the various solvents considered against solute diameter a_2. Dispersion forces are neglected and therefore ΔG is labeled ΔG_{HS}. Curve 1 is for water ($a = 2.75$ Å), curve 2 is for the "hypothetical water" ($a = 5.5$ Å, $y = 0.38$), and curve 3 is for the

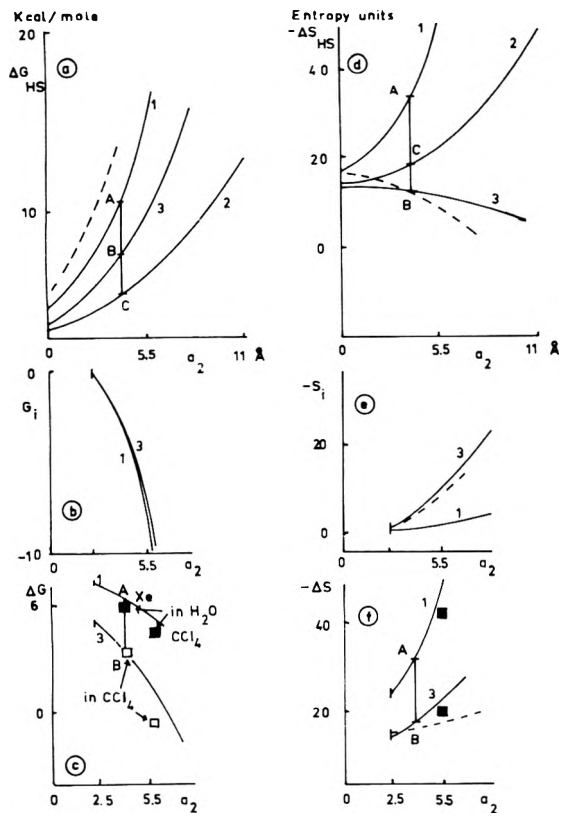

Figure 1. (a,c) Plots of the free energy of transfer from the gaseous state $\Delta G = RT \ln K$, where K is the Henry constant, against solute size: (curve 1) to SPT water with a = 2.75 Å, y = 0.38; (curve 2) hypothetical SPT water with a = 5.5 Å, y = 0.38; (curve 3) nonpolar solvent with a = 5.5 Å, y = 0.50; (dotted line) nonpolar solvent with a = 2.75 Å, y = 0.50. (d,f) Plots of the entropy of transfer. (b,e) Corrections arising from dispersion forces.

nonpolar solvent (a = 5.5 Å, y = 0.50). The vertical line AB shows that a nonpolar solute of diameter 4 Å (as Xe or C_2H_6) is more soluble in the nonpolar solvent than in water. The line BC shows that the solubility is smaller in the nonpolar solvent than in the "hypothetical water", whatever is the solute size a_2 in the range considered (from 0 to 11 Å).

Figure 1b shows the free energy correction G_i arising from dispersion forces for nonpolar solutes in water (2.75 Å) and in the nonpolar solvent (5.5 Å). These increase the solubility but are of similar magnitude in both cases.

Figure 1c shows the free energy calculated when both hard sphere effects and dispersion effects are taken into account and black squares show the experimental values for real solutes. The good fit between experimental and calculated values has evidently been already noticed by Pierotti,[1,2] but the important fact shown by the calculations is that the negative ΔG of transfer from water to a nonpolar solvent for a nonpolar solute seems to result mainly from the fact that the nonpolar solvent molecules have a larger size than water molecules.

In fact water has the smallest size of all usual solvents at room temperature except perhaps liquid HF. If one wants to consider, e.g., the transfer of butane from water to liquid butane, the calculation will involve the transfer of a nonpolar solute of about 5 Å to a nonpolar solvent of the same hard sphere size and the ΔG_{HS} will again be negative.

It is also interesting to consider the ΔG_{HS} of transfer from the gaseous state of solutes to a nonpolar solvent with a = 2.75 Å, y = 0.5 (V = 13 cm^3), and $\alpha = 1.2 \times 10^{-3}$ K. Such a solvent is purely hypothetical but has properties similar to that of other nonpolar solvents at room temperatures. The dotted line in Figure 1a shows the ΔG_{HS} for such a solvent. The influence of solvent size is again very strong, as the free energy of transfer for the nonpolar solute to another solvent with larger size is again negative. No special structural effects are involved in this negative ΔG.

Now let us consider the entropies of transfer, they are shown in Figure 1d–f. The entropy of transfer from water to a nonpolar solvent with a = 5.6 Å is shown by line AB in Figure 1d and is positive. (As previously the abscissa is the solute diameter a_2 in angstroms).

The entropy of transfer from "hypothetical water" to the same nonpolar solvent (line CB) is also positive. In contrast the entropy of transfer from a nonpolar solvent with a = 2.75 Å to a nonpolar solvent with a = 5.5 Å (line DB) is negative. Then a difference is apparent when structureless solvents are considered (the lack of structure is apparent from the high α and y used) or when structured solvents as water or "hypothetical water" are considered. Then the sign of ΔS must probably be ascribed to solvent structural effects but solvent size effects seem to play an important role in determining the magnitude of the free energy of transfer of a nonpolar solute from one solvent including water to another solvent. Of course this can be applied strictly to hydrophobic bonding in water only if the microscopic hydrocarbon aggregate has a sufficiently large size so that it can be considered a different liquid phase.

(b) *Calculations with the SPT as Modified by Stillinger.* The attempts to apply SPT to liquid water have been criticized by Stillinger, who points out that it does not take into account the strong directional interactions that operate in water to produce extensive hydrogen bonding.[8] Stillinger has improved upon Pierotti's analysis in a way that explicitly incorporates the measured radial distribution function for pure water.

It is possible to compute the ΔG of transfer for a nonpolar solute from the gaseous state to "Stillinger water" with a = 2.75 Å at 4 °C by graphical integration of the function $\lambda^2 G(\lambda)$ defined in ref 8, where the calculated $G(\lambda)$ is shown in Figure 7. Figure 2a shows plots of ΔG of transfer for a nonpolar solute at 4 °C from the gaseous state to "Stillinger water" with a = 2.75 Å, to SPT water with a = 2.75 Å. The abscissa is again the solute hard-sphere diameter a_2 in angstroms.

In order to make apparent the influence of size we have, as in the preceding section, also considered what we call "hypothetical Stillinger water", that is with a = 5.5 Å but the same $G(\lambda)$ as calculated by Stillinger in ref 8. We assume that it keeps the structural features which make water different from other solvents, but its size is increased twice.[12] It is apparent from Figure 2a that the modification by Stillinger changes significantly the ΔG of transfer. Nevertheless the main conclusions arrived at in section II.a still seem valid.

Figure 2b shows plots of the entropy of transfer for a nonpolar solute from the gaseous state to "Stillinger water" with a = 2.75 Å and "hypothetical Stillinger water" with a = 5.5 Å at 4 °C, and various other solvents. For this calculation it has been necessary to assume that $\partial G(\lambda)/\partial T$ at 4 °C is equal to $[G(\lambda)100\ °C - G(\lambda)4\ °C]/96\ °C$ that are the quantities available from Figure 7 in ref 8 (no dispersion forces have been considered in these calculations).

In the last section we shall consider the influence of non-

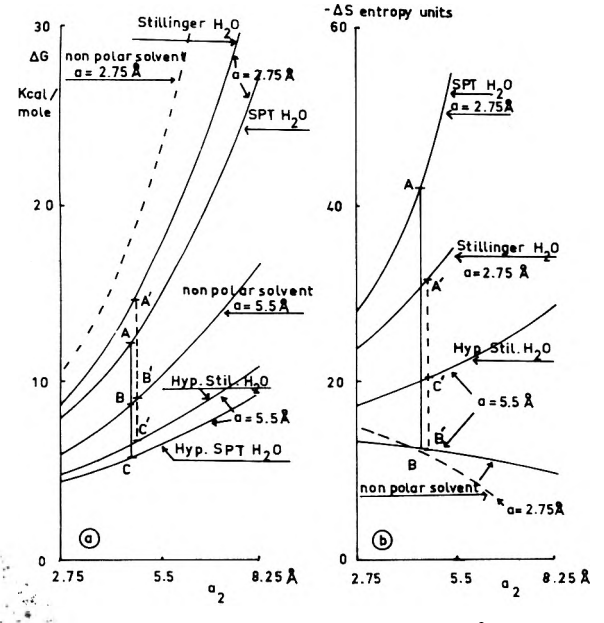

Figure 2. (a) Plots of the free energy of transfer at 4 °C, $\Delta G = RT \ln K$, against solute size. (b) Plots of the entropy of transfer. The abscissa is the solute hard-sphere diameter a_2.

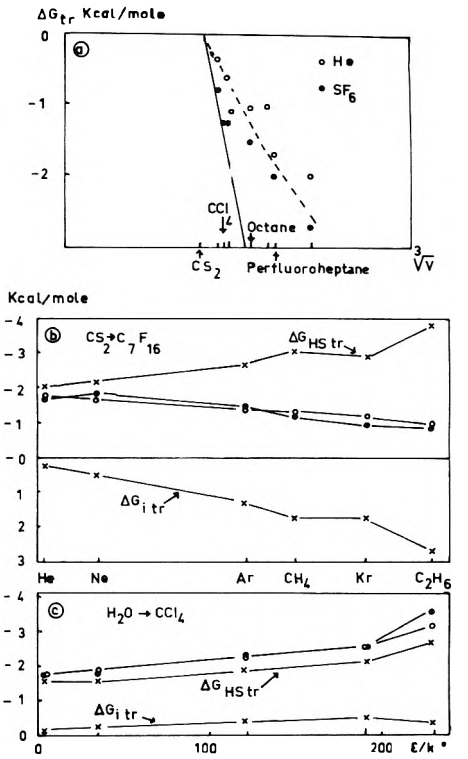

Figure 3. (a) Plots of the free energy of transfer from CS_2 to another nonpolar solvent: (open circles) solute is He, (black circles) solute is SF_6, (dotted line) calculated values from SPT for He, full line calculated values for SF_6. The abscissa is the solvent molar volume cubic root. (b) Plots of the free energy of transfer from CS_2 to perfluoroheptane for various nonpolar gases against the gas ϵ/k. (c) Plots of the free energy of transfer from H_2O to CCl_4 for various nonpolar gases against the gas ϵ/k. (b,c) black circles: experimental ΔG_{tr}; open circles: calculated $\Delta G_{tr} = \Delta G_{HS,tr} + \Delta G_{i,tr}$. All points are connected for clarity.

polar solvent size on the transfer of nonpolar solute as it is possible to compare calculated with experimental data in a few case.

(c) *Comparison between Calculated and Experimental Free Energy of Transfer of Nonpolar Solutes between Nonpolar Solvents at 25 °C.* The theory predicts that the free energy of transfer for nonpolar solutes from one nonpolar solvent to another with a larger molecular size is negative.

Although the solubility data for gases are relatively scarce it is possible to check this influence of solvent size. The experimental solubility data are taken from ref 9–11. The solvents considered are in the order of increasing molar volume V, CS_2, C_6H_6, CCl_4, cyclohexane, hexane, octane, decane, perfluoroheptane, and $(C_4F_9)_3N$. All are nonpolar except the last which is nevertheless interesting because it has the largest size of all.

The solvent hard-sphere diameter are given in ref 1, 13, and 14. The computed values for y differs slightly for the various solvents but are nearly 0.5. (They are respectively 0.53, 0.49, 0.51, 0.50, 0.51, and 0.50 for CS_2, n-C_6H_{14}, C_6H_6, CCl_4, c-C_6H_{12}, and perfluoro-n-heptane.) For $(C_4F_9)_3N$ we have assumed $y = \pi Na^3/6V = 0.50$. Dispersion forces are neglected in the calculations.

Figure 3a shows the experimental ΔG of transfer for He and SF_6 from CS_2 to other solvents considered, and the calculated ΔG. For He the comparison between calculated and experimental data is satisfactory except for the series hexane, octane, and decane, which shows an inverse size effect. In this last case it must be noticed that these molecules are far from being spherical and that the SPT is very approximate in such cases. For SF_6 the experimental ΔG is about a factor of 2 smaller than the calculated value. This may be ascribed to the influence of dispersion forces, since the importance of these dispersion forces relative to cavity energy effects increases with solute size.[15] This is shown on Figure 3b which shows the experimental ΔG of transfer for various gases from CS_2 to perfluoroheptane plotted against the gas ϵ/k. The calculated ΔG_{tr} $\Delta G = \Delta G_{HS,tr} + \Delta G_{i,tr}$ is also shown. Here $\Delta G_{HS,tr}$ is the value calculated neglecting the dispersion forces and $\Delta G_{i,tr}$ is the contribution of these dispersion forces. The parameters used in the calculations are for CS_2: $a = 4.556$ Å and $\epsilon/k = 470$ °C; and for perfluoroheptane: $a = 7.11$ Å and $\epsilon/k = 480$ °C. For the solutes, values are taken from ref 2. It is apparent that the sign of the ΔG of transfer is that of the $\Delta G_{HS,tr}$ for the gas considered, but that the possibility exists that for gases with a very large ϵ/k the process could be dominated by the influence of dispersion forces. In case of transfer of a gas from H_2O to a solvent such as CCl_4 the $\Delta G_{i,tr}$ is always small compared to the $\Delta G_{HS,tr}$, as shown by the data on Figure 3c. (The parameters used in the calculation for H_2O are $a = 2.75$ Å, $\epsilon/k = 90$ °C, and for CCl_4 $a = 5.36$ Å, $\epsilon/k = 480$ °C.)

Acknowledgments. We gratefully acknowledge the suggestion by Doctor Felix Franks to include Stillinger's theory in this paper.

References and Notes

(1) R. A. Pierotti, *J. Phys. Chem.*, **67**, 1840 (1963).
(2) R. A. Pierotti, *J. Phys. Chem.*, **69**, 281 (1965).
(3) A. Ben Naim, "Water and Aqueous Solutions", Plenum Press, New York, N.Y., 1974, Chapters 7 and 8.
(4) R. B. Hermann, *J. Phys. Chem.*, **79**, 163 (1975).
(5) R. B. Hermann in "Molecular and Quantum Pharmacology", E. Bergmann and B. Pullman, Ed., D. Reidel Publishing Company, Dorchecht, Holland, 1974, p 441.

(6) M. Lucas, *J. Phys. Chem.*, **77**, 2479 (1973).
(7) P. R. Philip and C. Jolicoeur, *J. Solution Chem.*, **4**, 105 (1975).
(8) F. H. Stillinger, *J. Solution Chem.*, **2**, 141 (1973).
(9) E. Wilhelm and R. Battino, *Chem. Rev.*, **73**, 1 (1973).
(10) S. H. Hildebrand and R. H. Lamoreaux, *Ind. Eng. Chem., Fundam.*, **13**, 110 (1974).
(11) R. J. Powel, *J. Chem. Eng. Data*, **17**, 302 (1972).
(12) As λ is a dimensionless quantity, any change in size could be fully accounted for by variation in the length *a*, F. H. Stillinger, private communication.
(13) N. Snider and T. M. Herrington, *J. Chem. Phys.*, **47**, 2248 (1967).
(14) Y. Kobatake and B. J. Alder, *J. Phys. Chem.*, **66**, 645 (1962).
(15) For the various solvents ϵ/k ranges between 300 to 500 K (ref 1, 13, 14). For He as a solute the value of G_i ranges from −0.37 to 0.56 kcal/mol, following the solvent considered. In the transfer of He from CS_2 to another solvent, there is a contribution from ΔG that amounts at maximum to 0.2 kcal/mol, so that the cavity energy is by far the more important parameter to be considered, for SF_6 the influence of dispersion forces and of the cavity energy may be of the same order of magnitude, but the process is still dominated by the latter contribution.

Hydrogen Bonding Systems Containing Hydrogen Fluoride. II. Formation Constants and Enthalpies of Complexes with Organic Compounds from Infrared Study[1]

Mitsunori Tsuda, Hidekazu Touhara, Koichiro Nakanishi,* and Nobuatsu Watanabe

Department of Industrial Chemistry, Kyoto University, Kyoto 606, Japan *(Received May 22, 1975)*

Publication costs assisted by Kyoto University

The hydrogen bonding complex of hydrogen fluoride (HF) with organic compounds having a proton-accepting group was studied by measuring the infrared F–H band of HF. Equilibrium constants (K) and enthalpies (ΔH) of complex formation were determined in a temperature range between 10 and 50 °C for the 1:1 complex of HF with the following proton acceptor molecules: acetone, acetonitrile, diethyl ether, dimethylformamide, ethanol, methanol, and tetrahydrofuran. The enthalpies of formation of these complexes are between -5.2 ± 0.5 and -9.6 ± 0.5 kcal mol^{-1}. Linear correlations were found to exist between ΔH and $\Delta\nu_{HF}$ (hydrogen bond shift), ΔH and ΔS, and log K and pK_a, except for the case when methanol or ethanol was used as the proton acceptor.

Introduction

Although thermodynamic and spectroscopic studies have been extensively made on the hydrogen bonding or charge transfer complexes, systems containing hydrogen fluoride (HF)[3-8] have received less attention at least in experimental aspects, perhaps because of technical difficulty and inaccessibility. However, theoretical studies including quantum mechanical molecular orbital calculations often concern hydrogen fluoride and its mixtures with molecules having relatively simple electronic structures. It seems thus important to establish reliable thermodynamic data for HF complexes.

In a previous paper,[2] we have reported the hydrogen bond shift (denoted hereafter as $\Delta\nu_{HF}$) for the stretching vibration mode of HF in the case when various organic compounds are added to form the hydrogen bonding complex in dilute solutions of HF in carbon tetrachloride. It has been shown that the $\Delta\nu_{HF}$ is the largest of the hydrogen bond shifts that have ever been observed with various proton donors.

We now extend our previous measurements with HF to include the determination of the equilibrium constants of formation for the hydrogen bond complexes as a function of temperature. Based on careful infrared spectral measurements, the equilibrium constants and enthalpies of complex formation have been evaluated for systems of HF with acetone, acetonitrile, diethyl ether, dimethylformamide, ethanol, methanol, or tetrahydrofuran in dilute carbon tetrachloride solution. These thermodynamic properties are discussed in terms of the Badger–Bauer relation,[9,10] correlations with the hydrogen bond shift and with the base strength of proton acceptors, and the structure of HF–alcohol complex.

Experimental Section

Materials. Hydrogen fluoride used in this study was supplied from Daikin Co. It was purified by a combination of electrolysis and distillation described below. Carbon tetrachloride used as inert solvent needed special treatment to remove trace amount of water from the commercially available spectrograde reagents. This technique was also described later. Other organic compounds used as proton acceptors were of spectrograde or guaranteed reagent. They were used without further purifications.

Purification of Hydrogen Fluoride. The purification of HF used in this study was accomplished by a combined process of electrolytic dehydration with fractional distillation. The design and operation of the electrolytic cell for the removal of water in HF were similar to those described by Rogers et al.[11] and the distillation system was the same as that used in the previous study.[2]

Unpurified HF was first electrolytically dehydrated in the electrolytic cell. The electrolysis was continued until the conductivity decreased to almost zero. With this process, trace amount of water could be completely removed from the sample liquid. However, other impurities such as

SO_2, H_4SiF_6, etc. seemed to be still present in the anhydrous hydrogen fluoride (AHF). The AHF was then transferred directly into the distillation assembly by a single step distillation. Fractional distillation was carried out after refluxing for several hours at about 20 °C. The low boiling point fraction was discarded by absorbing to a column of sodium fluoride and a middle fraction at 19.5 °C was led either to a sampler for conductivity measurement or to dehydrated carbon tetrachloride solvent placed in a cell for infrared spectral measurement.

The conductivity of distilled AHF was as small as 1.0×10^{-6} ohm^{-1} cm^{-1} at 0 °C. This is comparable to the best value obtained by Runner et al.[12] Infrared spectrum of purified AHF in dilute CCl_4 solution showed only a strong absorption at 3856 cm^{-1} due to HF monomer and no other absorption peaks due to impurities could be found.

Purification of Carbon Tetrachloride. Carbon tetrachloride is often used as an inert solvent in infrared and other spectroscopic measurements. In the studies of hydrogen bonding in alcohols, phenols, or similar proton donors, the presence of a trace amount of water may not cause much trouble. However, in the case of hydrogen bonding studies involving AHF, complete dehydration of CCl_4 becomes necessary for the following two reasons. First, the affinity of AHF with water is extremely large and may perturb the interaction of AHF with other proton acceptors. Secondly, since the solubility of AHF in CCl_4 is fairly small, a rather long optical path is needed for the infrared cell to detect the absorption of AHF and the absorptions due to a trace amount of water in the CCl_4 layer may interfere with that due to AHF.

In fact, as shown in Figure 1, even spectrograde carbon tetrachloride samples showed a remarkable absorptions due to water at 3704 and 3625 cm^{-1} when measured in a cell with an optical path length of 150 mm. This was large enough to prevent accurate determination of the absorbance of monomeric HF stretching vibration band at 3856 cm^{-1}.

We therefore developed a novel method to prepare almost completely water-free sample of CCl_4. Unpurified CCl_4 was first saturated with hydrogen fluoride by bubbling the purified AHF gas for about 30 min at room temperature. This AHF saturated solution did not show any absorption peaks except for that due to monomeric HF. This may be due to the fact that even a trace amount of water was removed with hydrogen fluoride gas which has a strong dehydrating ability. Purified CCl_4 used for dilution and preparation of reference solution in infrared measurements was then obtained by bubbling dehydrated nitrogen gas through the AHF saturated solution. With this process, hydrogen fluoride was removed with nitrogen from CCl_4 solutions.

The water content of purified CCl_4 thus obtained was determined to be less than 0.0004 M by the Karl Fischer titration method. The same titration gave 0.0044 ± 0.0005 M for the water content in unpurified spectrograde CCl_4. The spectrum of the purified CCl_4 was also given in Figure 1. As shown in a full line in the figure, no absorption band due to water was observed in the case of the purified CCl_4. This method of CCl_4 purification is very effective and yet simpler than any other methods.[13] It should be convenient and useful in other spectroscopic studies (e.g., NMR and dielectric constant measurements) in which removal of water from solvents is essential.

Infrared Measurements. Infrared measurements were made on a Shimadzu Model IR-27G grating spectrophotometer. A matched pair of cell for double path operation having an optical path of 150 mm was that used in our previous study.[2] It was now surrounded by a jacket to circulate water thermostated within ±0.5 °C. The measurements were done at temperatures between 10 and 50 °C. For measurements below room temperature, dry nitrogen was sprayed against the cell windows to prevent the condensation of moisture.

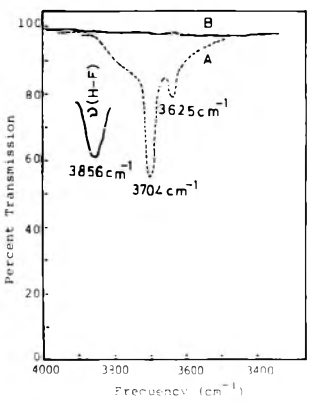

Figure 1. The ir spectrum of H_2O in CCl_4: (A) CCl_4 spectrograde; (B) CCl_4 dehydrated by AHF.

The infrared spectral diagram was obtained by the dual path technique in which HF + acceptor solution was placed in the sample cell and CCl_4 solution containing the same concentration of acceptor was placed in the reference cell. Throughout the measurements, the concentration of HF was between 0.007 and 0.016 M, where no polymeric bands due to the self-association of HF were observed. Preliminary measurements revealed that, since the interaction of HF with proton acceptors is usually very strong, the HF monomeric absorption became too small to determine its absorbance accurately when the concentration of proton acceptor greatly exceeded that of HF. Hence, the concentration of proton acceptor was selected to be about twice as much as that of HF.

The spectra were recorded with a scan speed of 80 cm^{-1} and the spectral slit width was 10 cm^{-1} at 3800 cm^{-1}. The concentration of HF in CCl_4 was determined by the photometric method with La–alizarin complexone.[14]

Calculation of Equilibrium Constant. In the analysis of spectra obtained above, it was assumed that (1) HF exists as the monomer in the concentration ranges used, that (2) the apparent molar extinction coefficient α of HF is a constant,[15] and that (3) only a 1:1 hydrogen bonding complex is formed between the HF monomer and the proton acceptor.

The validity of the first two assumptions may be confirmed by the experimental evidence given in Figures 2 and 3. Figure 2 shows the absorption peaks due to monomeric F--H stretching vibration as a function of HF concentration in CCl_4. No absorption peaks due to associated HF are observed in the concentration ranges used for the present spectral measurements. Figure 3 indicates the linear relation between the absorbance at 3856 cm^{-1} and the concentration of HF in CCl_4. Although there are negligible scatters due to the error in the determination of HF concentration, we may establish a constant value for α. The third assumption is that usually used in many infrared spectral studies. In the present case, the formation of other complexes than the 1:1 type between HF monomer and the

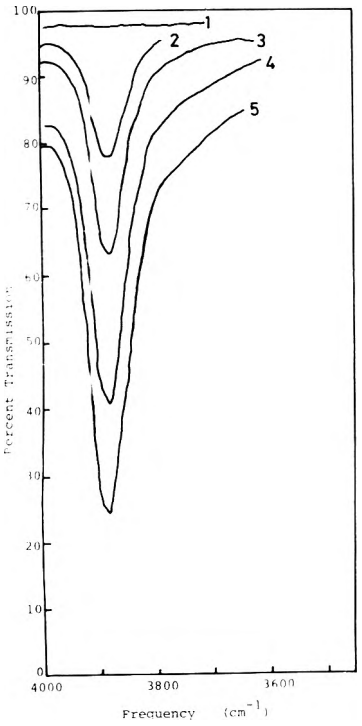

Figure 2. The variation for the 3856-cm^{-1} (monomer) band of HF in CCl_4 solution: (1) base line; (2) 3.53 × 10^{-3} M; (3) 2.26 × 10^{-3} M; (4) 1.14 × 10^{-3} M; (5) 0.61 × 10^{-3} M.

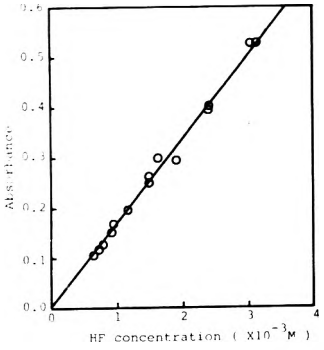

Figure 3. Plots of absorbance for the 3856-cm^{-1} (monomer) band of HF vs. HF concentration.

proton acceptor is not conceivable under the condition that an excess amount of base is added to the solution.

Under the above three assumptions, the equilibrium constant for the formation of hydrogen bonding complex K may be given by the following equation

$$K = (m_0 - m)/m(b_0 - m_0 + m) \quad (1)$$

where m_0 and b_0 are the total concentration of HF and proton acceptor, respectively, and m is the equilibrium concentration of HF monomer. The values of m were calculated from the relation

$$m = D/\alpha d \quad (2)$$

where D is the infrared optical density of the HF band and d is the cell length. It was found that the values of K calculated by eq 1 were constant for each HF–proton acceptor system, and that there was a linear relation between log K and $1/T$ (T is the temperature in K).

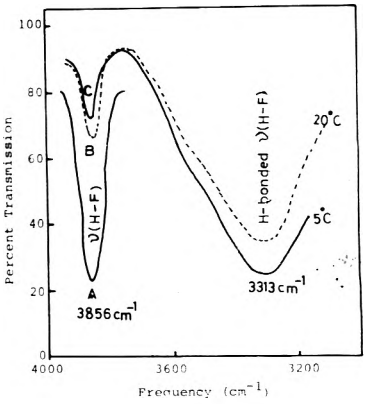

Figure 4. The ir spectra of 3.60 × 10^{-3} M HF + 3.74 × 10^{-3} M acetone in CCl_4 at 5 and 20 °C: (A) HF alone b_0 = 3.60 × 10^{-3} M; (B) b = 0.91 × 10^{-3} M (at 5°C); (C) b = 0.74 × 10^{-3} M (at 20 °C).

Results and Discussion

Spectra. The spectra of dilute solutions of HF in CCl_4 were recorded between 2400 and 4000 cm^{-1}. As seen in Figure 3 a linear relationship was obtained between the maximum absorbance at 3856 cm^{-1} and the molar concentration of HF showing that the Lambert–Beer rule is proved to hold for the concentration range studied.

The spectra of monomeric HF change remarkably with the addition of proton accepting molecules and a broad band due to complex formation appears at lower wave number region. Figure 4 shows a typical example of such spectral diagrams which was obtained with HF + acetone + CCl_4 solutions at 5 and 20 °C. From these spectral diagrams, the position of the band with each proton acceptor was obtained as ν_{HF} and the hydrogen bond shift $\Delta\nu_{HF}$ was calculated as the difference from the value of ν_{HF} in the vapor phase.[3] The equilibrium constant for the formation of the HF complex at each temperature was also estimated from the maximum absorbance.

The values for ν_{HF}, $\Delta\nu_{HF}$, and K are summarized in Table I. The temperature dependence of $\Delta\nu_{HF}$ is also given in the table. The $d\Delta\nu_{HF}/dT$ values for HF complexes are of comparable magnitude with those for other hydrogen bonding systems (e.g., MeOH, EtOH, and *tert*-butyl alcohol).[16]

Thermodynamic Properties of HF Complexes. From the temperature dependence of K, the enthalpy of complex formation ΔH may be evaluated. Table I includes the experimental values for ΔG, ΔH, and ΔS at 25 °C. Inspection of these values leads to the conclusion that the ΔH values in the HF complexes are between −5 and −10 kcal/mol and are much greater than those for other hydrogen bonding complexes. For example, the ΔH value for ethanol + acetone complex has been estimated to be −3.46 kcal/mol.[16] Most of the ΔH values for other complexes involving alcohols or phenol are also less than −5 kcal/mol. On the other hand, except for HF + alcohol complex, the ΔS values both for HF and alcohol (or phenol) complexes are in the range between −7 and −11 cal deg/mol.

It should be noted that Schepkin has obtained a value of 1.5 kcal/mol as the specific interaction between HF and CCl_4.[17] CCl_4 is certainly not absolutely inert to HF molecule. Thus the ΔH values reported in this work might be underestimated, if they are to represent the standard enthalpies of formation of hydrogen bonding complex from free molecules. The present value of ΔH, −6.9 kcal/mol, for

TABLE I: Spectral and Thermodynamic Properties

Donor	Acceptor	K,[a] M^{-1}	$-\Delta G$,[a] kcal/mol	$-\Delta H$, kcal/mol	$-\Delta S$, eu	ν_{HF},[b] cm^{-1}	$\Delta\nu_{HF}$,[b] cm^{-1}	$d(\nu_{HF})/dT$, $cm^{-1}/°C$	pK_a[d]
HF	Vapor (monomer)					3961[c]	0		
	CCl_4					3856	105	−0.30	
	Acetonitrile	141 ± 1	2.93 ± 0.01	5.2 ± 0.5	7.69 ± 1.57	3475	486	−0.67	−10.1
	Acetone	525 ± 1	3.71 ± 0.02	6.9 ± 0.5	10.61 ± 1.83	3313	648	−0.66	−7.2
	Diethyl ether	928 ± 1	4.05 ± 0.01	7.4 ± 0.2	11.17 ± 0.80	3221	740	−0.73	−3.6
	Tetrahydrofuran	1129 ± 1	4.16 ± 0.01	7.0 ± 0.4	9.68 ± 1.29	3210	751	−1.1	−2.1
	Dimethylformamide	4638 ± 1	5.00 ± 0.02	7.6 ± 0.3	8.68 ± 1.03	3148	813	−1.0	−0.01
	Methanol	596 ± 1	3.70 ± 0.01	9.6 ± 0.5	19.58 ± 1.75	3343	618	−1.0	−2.0
	Ethanol	830 ± 1	3.98 ± 0.01	8.7 ± 0.5	15.72 ± 1.66	3306	655	−0.82	

[a] Interpolated value at 25 °C. [b] Value at 20 °C. [c] Reference 3. [d] Reference 22.

HF + acetone complex is smaller than the corresponding value, −8.4 kcal/mol, reported by Schepkin.[18] At least, a part of this discrepancy may be ascribed to the above-mentioned correction to the interaction with solvent.[19]

On the other hand, Thomas[20] has obtained a value of 30 kJ mol^{-1} (≃7.2 kcal/mol) for the ΔH of the HF–diethyl ether complex in the gas phase. This is comparable with our value in CCl_4. However, if the specific interaction between HF and CCl_4 is taken into consideration, our value becomes larger and there is an nonnegligible discrepancy.

Empirical Correlations. It is well known that a roughly linear correlation has been observed between ΔH and $\Delta\nu_{HF}$ and it is often referred to as the Badger–Bauer relationship. As is shown in Figure 5, except for HF + alcohol complexes, the present data obey this correlation fairly well.

In their comprehensive review, Pimentel and McClellan[21] have collected much evidence that there is a linear relation between ΔH and ΔS for various kinds of hydrogen bonding complexes. The ΔH vs. ΔS plot for HF complexes is shown in Figure 6, where we may observe a fairly good correlation. The HF + alcohol systems are again the exception.

As a further correlation, it is interesting to examine the possible parallelism between the proton-accepting ability and the base strength of the acceptor molecules, pK_a. As shown in Figure 7, the plot of log K at 25 °C (or $\Delta\nu_{HF}$ at 20 °C) against pK_a gave a linear correlation except for the point for methanol. The values of pK_a are taken from the compilation by Arnett.[22] Although no pK_a value was available for ethanol, a similar trend may be expected for the HF + ethanol complex. While the pK_a represents the equilibrium constant of the following reaction

$$BH^+ \rightleftarrows B + H^+ \qquad (3)$$

where B is the proton acceptor, the hydrogen bond formation may be written as

$$B + HX \rightleftarrows BHX \qquad (4)$$

for which K is the equilibrium constant. Both pK_a and K involve entropy and enthalpy contributions. Since H^+ is small in size, the enthalpic and entropic anomalies due to structural origin will be larger for the reaction in eq 4 and the linearity between pK_a and K may be destroyed by such anomalies.

Anomaly in HF + Alcohol Complex. The HF + alcohol complexes show invariably an anomalous behavior in the three correlations given above. In interpreting these results, we call attention, first of all, to the fact that the entropy decrease is unusually large for the HF + alcohol complex. As given in Table I, the ΔS for HF + MeOH and HF + EtOH complexes are −19.6 and −15.7 cal deg/mol, respectively, indicating that the absolute value of the entropy change in the complex formation between HF and alcohol is almost twice as much as those for other complexes. This

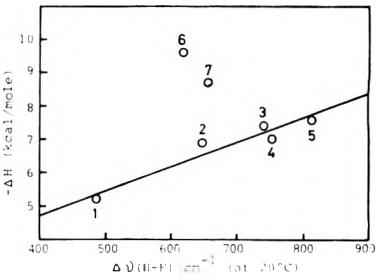

Figure 5. Enthalpy change for formation of HF–base complexes against $\Delta\nu_{HF}$: (1) acetonitrile; (2) acetone; (3) diethyl ether; (4) tetrahydrofuran; (5) dimethylformamide; (6) methanol; (7) ethanol.

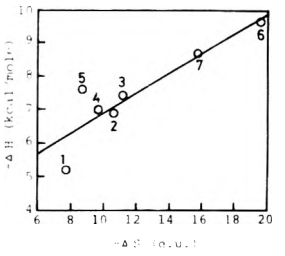

Figure 6. Plots of ΔH vs. ΔS for HF complexes. The numbering of the points is the same as that in Figure 5.

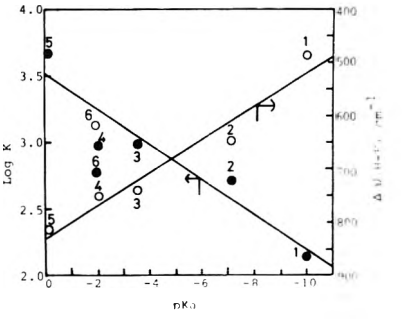

Figure 7. Plots of log K (at 25 °C) and $\Delta\nu_{HF}$ (at 20 °C) against pK_a. The numbering of the points is the same as that in Figure 5.

suggests that the structure of HF + alcohol complex may not be linear and that a cyclic structure of complex may be responsible for this greater loss of entropy.

The deviations of HF + alcohol systems from the linearity in various correlations are too large even if possible sources of scatter are considered, and structural anomaly mentioned above is strongly suggested.[23] However, evidence in favor of cyclic structure is not fully conclusive, since the decrease in the absorbance of the free OH band and the shift of the OH band could not be confirmed due to the overlapping with the broad complex band of HF. In order to obtain some clues for this problem, application of molecular orbital calculations to the HF complex should be helpful. Although preliminary calculations by the CNDO/2 method[24,25] indicated that a linear structure is more stable, optimization of geometry in the hydrogen bonding complex might not be attained and further modified calculations must be indispensable. Details of our CNDO/2 and more refined calculations will be reported later.

Acknowledgments. This work was supported by a grant from the Asahi Glass Foundation for the Promotion of Industrial Research. We thank the Daikin Co. for supplying the hydrogen fluoride.

References and Notes

(1) The first paper[2] of this series was published as a part of our thermodynamic studies on associated solutions.
(2) H. Touhara, H. Shimoda, K. Nakanishi, and N. Watanabe, *J. Phys. Chem.*, **75**, 2222 (1971).
(3) H. Hyman and J. J. Katz in "Non-Aqueous Solvent System", T. C. Waddington, Ed., Academic Press, New York, N.Y., 1965, Chapter 2.
(4) M. Kilpatrick and J. G. Jones in "Chemistry of Non-Aqueous Solvent", J. J. Lagowski, Ed., Vol. II, Academic Press, New York, N.Y., 1967.
(5) R. M. Adams and J. J. Katz, *J. Mol. Spectrosc.*, **1**, 306 (1957).
(6) M. Couzi and P. V. Huong, *J. Chem. Phys.*, **67**, 1994 (1970).
(7) M. Couzi and P. V. Huong, *J. Chem. Phys.*, **67**, 2001 (1970).
(8) M. Couzi, J. Le Calvé, P. V. Huong, and J. Lascombe, *J. Mol. Spectrosc.*, **5**, 363 (1970).
(9) R. M. Badger and S. H. Bauer, *J. Chem. Phys.*, **5**, 839 (1937).
(10) R. M. Badger, *J. Chem. Phys.*, **8**, 288 (1940).
(11) H. H. Rogers, S. Evans, and J. H. Johnson, *J. Electrochem. Soc.*, **111**, 701 (1964).
(12) M. E. Runner, G. Balog, and M. Kilpatrick, *J. Am. Chem. Soc.*, **78**, 5183 (1956).
(13) (a) U. Liddel and E. D. Becker, *Spectrochim. Acta*, **10**, 70 (1957); (b) K. W. Morcom and D. N. Travers, *Trans. Faraday Soc.*, **62**, 2063 (1967); (c) R. H. Stokes, K. N. Marsh, and R. P. Tomlins, *J. Chem. Thermodyn.*, **1**, 559 (1969).
(14) S. Hirano, H. Fujinuma, and T. Kasai, *Jpn. Anal.*, **15**, 1339 (1966).
(15) Strictly speaking, α must be a function of temperature. However, its temperature dependence is quite small and may be negligible in the following calculations.
(16) E. D. Becker, *Spectrochim. Acta*, **17**, 436 (1961).
(17) D. N. Schepkin, *Opt. Spectrosk.*, **19**, 709 (1965).
(18) D. N. Schepkin, *Teor. Eksp. Khim.*, **2**, 276 (1966).
(19) Schepkin has made a correction to the interaction of HX (X = Cl, Br, and F) with solvents by considering the change in the external rotational state of HX molecule. However, his estimation on HF is not clearly stated as far as we could judge from this paper.
(20) R. K. Thomas, *Proc. R. Soc., Ser. A*, **322**, 137 (1971).
(21) G. C. Pimentel and A. L. McClellan, "The Hydrogen Bond", W. H. Freeman, San Francisco, Calif., 1960.
(22) E. M. Arnett, *Prog. Phys. Org. Chem.*, **1**, 223 (1963).
(23) Alternatively, the deviations for HF–alcohol complexes may be ascribed to an anomaly in stoichiometry, since there is a possibility that HF and alcohol form other complex than 1:1 type. However, the facts that K was a constant for each temperature and that the temperature dependence of K could well be expressed by a van't Hoff type equation were not able to be explained by this interpretation.
(24) J. A. Pople, D. P. Santry, and G. A. Segal, *J. Chem. Phys.*, **43**, S129 (1965).
(25) J. A. Pople and G. A. Segal, *J. Chem. Phys.*, **43**, S136 (1965).

Titrimetric Applications of Multiparametric Curve Fitting. V. Acidimetric Potentiometric Titrations of Laurate Ion in Solutions of Cesium and Lithium Salts

Junryo Mino,[1] Egon Matijević, and Louis Meites*

Department of Chemistry and the Institute of Colloid and Surface Science, Clarkson College of Technology, Potsdam, New York 13676
(Received December 16, 1974; Revised Manuscript Received October 24, 1975)

This paper describes the reactions that occur when a solution of cesium (or lithium) laurate containing cesium (or lithium) chloride is titrated with a strong acid. Cesium ion behaves similarly to sodium or potassium ion in that laurate micelles may exist and either cesium hydrogen laurate or free lauric acid, or both, may precipitate during the titration. However, the solubility of lithium laurate is so low that laurate micelles cannot exist in solutions containing much lithium ion. Values of the solubility products of lithium laurate and cesium and lithium hydrogen laurates were obtained.

Introduction

An earlier paper in this series[2] described a multiparametric curve-fitting procedure for evaluating the parameters that characterize the titration curves obtained in potentiometric titrations of sodium laurate with hydrochloric acid. Such curves are complex because any, or all, of three unrelated chemical processes may occur: the disappearance of laurate micelles present initially, and the precipitation of either free lauric acid or the "acid soap" sodium hydrogen laurate, or both. All of these processes had previously been shown to be involved;[3] by applying multiparametric curve fitting to the data, we were able to evaluate the solubility products of both lauric acid and sodium hydrogen laurate and the critical micelle concentration (cmc) under the conditions of each titration in which the corresponding processes occurred. Subsequently[3] we devised a computer pro-

gram that, given the coordinates of the data points and information about the experimental conditions (such as the concentrations of laurate, acid, and alkali-metal ion in the solutions), effected machine-made identifications of the processes that actually occurred during a particular titration along with values of the parameters characterizing them. These identifications were substantially more accurate than those attained by a human chemist given the same information.

Potassium and sodium laurates had previously[4] been found to yield titration curves that were identical within experimental error, and our value[2] for the thermodynamic solubility product of sodium hydrogen laurate, $7.2\ (\pm 1.5) \times 10^{-15}$, was indistinguishable from the one (6.3×10^{-15}) given by Lucassen[5] for potassium hydrogen laurate. However, there appeared to be no information in the literature on the behaviors of the cesium and lithium systems, and these were accordingly investigated with the results reported below. Cesium, sodium, and potassium give rise to behaviors that are qualitatively and quantitatively indistinguishable but are markedly different from the behavior of lithium.

Experimental Section

Most of the solutions titrated were prepared from stock solutions of cesium or lithium laurate. The stock solutions were made by weighing out appropriate amounts of a sample of lauric acid (Nu-Chek-Prep Inc.), heating them to just above the melting point, and adding approximately 99.8% of the stoichiometric amount of a carbonate-free solution of the appropriate alkali-metal hydroxide. According to its supplier the lauric acid was at least 99.8% pure, and our assays (by potentiometric titration with standard base at elevated temperatures) agreed with this figure, which was used in calculating the stoichiometric amount of base mentioned. After stirring and dilution until a clear solution was obtained, this was transferred quantitatively to a volumetric flask and diluted to the mark. A few of the most concentrated laurate solutions were prepared individually in much the same way. Care was always taken to guard against exposure to carbon dioxide at every stage.

Titrations were performed at 26 ± 1 °C in the manner previously described.[2] The concentration of alkali-metal ion and the ionic strength were adjusted by adding cesium nitrate or lithium chloride, usually as a stock solution but occasionally as a weighed amount of solid. Reagent-grade cesium nitrate had to be recrystallized to obtain a neutral product.

Multiparametric curve fitting employed the program previously described[2] to evaluate the parameters characterizing the processes that were judged to have occurred. These fits were made in Fortran IV on an IBM 360/44 computer.

Results and Discussion

I. *Titrations in Solutions Containing Cesium Ion.* As was true for titrations made in the presence of sodium ion,[2] all but the most concentrated solutions of cesium laurate remained clear when cesium nitrate was added to them before beginning the titrations. Only if the concentration of laurate was at least 0.025 *M* did opalescence appear at this stage. It reflected micelle formation resulting from the decrease of the cmc that occurred on adding the salt.

Table I shows the results obtained. Its first two columns give the composition of the solution titrated: C_b^0 is the initial concentration of cesium laurate and $C_{MX,b}$ is the concentration of cesium nitrate added. The third and fourth columns give the composition of the reagent: C_a is the concentration of hydrochloric acid and $C_{MX,a}$ is the concentration of cesium nitrate added to it. The fifth column gives the approximate ionic strength of the titration mixture; since the acid was always much more concentrated than the base, and since the concentrations of cesium nitrate in the two solutions were always the same, the variation of the ionic strength during any one titration was insignificant. The sixth through eighth columns give the values of the concentration constants

$$K_{HL} = [H^+][L^-] \quad (1)$$

$$K_{MHL_2} = [M^+][H^+][L^-]^2 \quad (2)$$

$$\text{cmc} = [L^-] \quad \text{(in the presence of micelles)} \quad (3)$$

where L^- = laurate ion and M^+ = cesium ion in these titrations, that gave the best fits to the experimental data. The last column gives the standard deviation of the experimental points from the best-fitting curve.

Values of the thermodynamic constants K^0 were obtained from these concentration constants by employing the equation

$$pK^0 = pK + 0.511n\sqrt{\mu}/(1 + 2\sqrt{\mu}) \quad (4)$$

in which n is a stoichiometric factor equal to 2 for lauric acid and to 4 for cesium hydrogen laurate, and in which the distance of closest approach is assumed to be close to 6 Å, which is a reasonable approximation for these equilibria in view of the relatively large ions they involve. Kielland[6] gave the effective radii of hydrogen and vinylacetate ions as 9 and 6 Å, respectively.

The mean values of pK^0 obtained from eq 4 corresponded to $K^0_{HL} = (1.8 \pm 0.3) \times 10^{-10}$ M² and to $K^0_{CsHL_2} = (1.0 \pm 0.4) \times 10^{-14}$ M⁴. The value for lauric acid may be compared with that, 1.3×10^{-10} M², obtained by Lucassen[5] and with the value of $(1.4 \pm 0.2) \times 10^{-10}$ M² deduced from the data obtained in similar titrations in the presence of sodium ion. There has been no prior evaluation of the solubility product of cesium hydrogen laurate, but this result is close to the values of $(7.2 \pm 1.5) \times 10^{-15}$ for the sodium salt[2] and 6.3×10^{-15} for the potassium salt.[5] The values of the cmc show the expected decrease on adding cesium chloride, but are definitely lower in solutions containing cesium ion than in solutions containing sodium ion.[2]

II. *Titrations in Solutions Containing Lithium Ion.* If the concentrations of both lithium ion and laurate ion are very low, solid lauric acid is the only phase that separates during a titration of a mixture of lithium laurate and lithium chloride with hydrochloric acid. These are the only conditions under which the behavior of lithium ion is indistinguishable from the behaviors of sodium and cesium ions.

At higher concentrations of laurate ion and either sodium ion or cesium ion, the alkali-metal hydrogen laurate precipitates during the titration, and this process and precipitation of lauric acid occur together over a wide range of initial concentrations. With lithium ion, however, a relatively small increase of concentration leads to a sharp transition from the comparatively simple curves that correspond to precipitation of lauric acid alone to much more complex ones that have the characteristic shape shown in Figure 1. With solutions containing sodium ion, curves of this general shape were obtained when all three of the possible phase separations occurred. There the first plateau re-

TABLE I: Results of Titrations of Cesium Laurate with Hydrochloric Acid

$C_b°$, M	$C_{MX,b}$, M	C_a, M	$C_{MX,a}$, M	Approx ionic strength, M	$10^{10}K_{HL}$, M	10^{14} K_{MHL_2}, M^4	10^3cmc, M	Standard error of a single pH measurement
0.001	0.01	0.02	0.01	0.011	3.05			0.054
	0.05	0.02	0.05	0.051	1.72			0.039
0.0025	0.005	0.05	0.005	0.007	4.24			0.141
	0.05	0.05	0.05	0.052	1.93			0.065
0.025	0.075	0.5	0.075	0.1	1.72	1.54	4.09	0.233
0.05	0	1.0	0	0.05	3.06	3.30	8.80	0.205

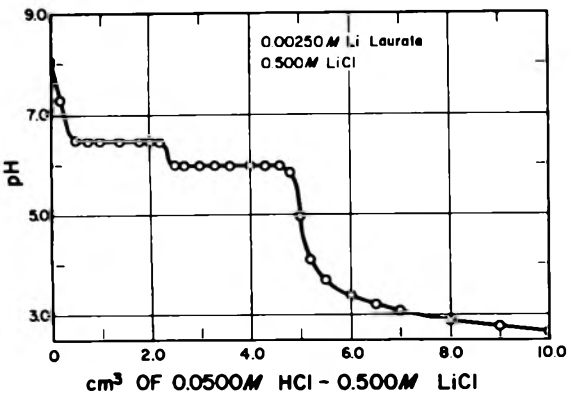

Figure 1. Open circles show the data obtained on titrating 100 cm^3 of a 2.50×10^{-3} M solution of lithium laurate containing 0.500 M lithium chloride with an 0.0500 M solution of hydrochloric acid containing 0.500 M lithium chloride. The solid curve corresponds to $K_{HL} = 2.33 \times 10^{-10}$, $K_{LiHL_2} = 2.33 \times 10^{-14}$, and $K_{LiL} = 1.78 \times 10^{-4}$.

flected the presence of micelles and solid alkali-metal hydrogen laurate, while the second reflected that of the alkali-metal hydrogen laurate and solid lauric acid. In the presence of lithium ion such curves were obtained even if the initial concentration of laurate ion was far below the cmc. In 0.05 F sodium chloride the data of Merrill and Getty[7] correspond to a cmc of 0.0133 M, and we[2] found 0.014 M by the technique used here; at the same ionic strength in lithium chloride, even 2.5×10^{-3} M laurate ion gave a curve resembling Figure 1.

Solutions containing 2.5×10^{-3} M laurate and 2.7×10^{-2} M lithium ion were clear, but with 5.2×10^{-2} M lithium ion a turbidity appeared, and it became more pronounced if the concentrations were increased further. Analyses of two samples of the solid that separated before any acid had been added gave C, 70.04 ± 0.17; H, 11.33 ± 0.02; Li 3.21 ± 0.03; calcd for $C_{11}H_{23}COOLi$: C 69.88; H, 11.24; Li 3.36. Similar analyses were obtained for the solids recovered from a number of mixtures corresponding to different stages of titrations under various conditions. At points lying on the first plateau of a curve such as the one in Figure 1, the composition of the solid always corresponded to a mixture of lithium laurate and lithium hydrogen laurate in about the proportions expected from the stoichiometry of the mixture. Once the second plateau had been attained, the lithium content always dropped below that for lithium hydrogen laurate, and the results corresponded to mixtures of this with solid lauric acid.

Thus titrations performed in the presence of lithium ion are unique in that lithium laurate precipitates from solutions in which the concentration of laurate ion is well below the cmc. In different terms, this means that the Krafft point of lithium laurate is higher than the temperature used in this work. To describe such titrations one must replace eq 3 by

$$K_{LiL}/[Li^+] = [L^-] \quad \text{(in the presence of solid LiL)} \quad (5)$$

where K_{LiL} denotes the ion-concentration product of lithium laurate. In most of these titrations the concentration of lithium ion in the hydrochloric acid used as reagent was nearly equal to the concentration of lithium ion in the solution titrated, and in all of them the concentration of acid was much larger than that of laurate. For these two reasons the concentration of lithium ion never varied by more than ±1% over the range in which solid lithium laurate was present, and therefore the left-hand side of eq 5 was constant during any one titration, though of course it varied from one titration to another as the concentration of lithium ion was changed. It was therefore possible to use the same computer program that had been employed with the sodium and cesium data, taking the constant value of $[L^-]$ to represent K_{LiL} rather than the cmc.

Table II shows the results obtained, and has the same arrangement as Table I. Combining these concentration constants with eq 4 gave $K^0_{HL} = (1.9 \pm 0.4) \times 10^{-10}$ M^2, $K^0_{LiHL_2} = (8.7 \pm 2.5) \times 10^{-15}$ M^4, and $K^0_{LiL} = (7.6 \pm 1.0) \times 10^{-5}$ M^2. The value for lauric acid is in acceptable agreement with the other values mentioned above. That for lithium hydrogen laurate is unexpectedly close to the corresponding values for the other alkali-metal ions. We have not been able to find a value of the thermodynamic solubility product of lithium laurate in the prior literature.

III. *Machine Classification.* All of the titrations performed in the presence of cesium ion were correctly classified by the machine-classification program previously described.[3] As that program was constructed to interpret virtual constancy of the laurate-ion concentration during the initial portion of the titration as reflecting the presence of micelles, it provided the message "micelles did form" whenever solid lithium laurate was present at the start, and correspondingly gave a value of the "cmc" that actually corresponded to $K_{LiL}/[Li^+]$. Automatic discrimination between behavior like that of sodium, potassium, and cesium and the behavior of lithium ion might be made by combining the numerical values obtained in different titrations with widely different concentrations of alkali-metal ion.

Conclusions

Acidimetric titrations of laurate ion in aqueous solutions at 25 ± 2 °C containing lithium, sodium, potassium, or cesium ion may involve either the precipitation of free lauric acid or that of the alkali-metal hydrogen laurate MHL_2 or both, depending on the compositions of the reacting solutions. The best current estimate of the thermodynamic sol-

TABLE II: Results of Titrations of Lithium Laurate with Hydrochloric Acid

$C_b°$, M	$C_{MX,b}$, M	C_a, M	$C_{MX,a}$, M	Approx ionic strength, M	$10^{10}K_{HL}$, M^2	10^{14} K_{MHL_2}, M^4	$10^3K_{LiL}/[Li^+]$, M	Standard error of a single pH measurement
0.0025	0.005	0.05	0	0.007	3.60			0.036
	0.025	0.05	0	0.027	4.76			0.011
	0.05	0.05	0	0.051	2.89	3.35	1.54	0.036
	0.1	0.05	0	0.10	3.42	3.08	1.37	0.132
	0.2	0.05	0.2	0.20	1.88	1.31	0.591	0.013
	0.5	0.05	0.5	0.50	2.33	2.33	0.354	0.008
	1.0	0.05	1.0	1.00	2.76	4.16	0.226	0.180
	2.0	0.05	2.0	2.00	5.86	4.27	0.0685	0.031
0.01	0.09	0.2	0.09	0.10	3.30	2.87	1.23	0.179
0.02	0.08	0.4	0.08	0.10	3.05	2.12	1.21	0.157

ubility product of lauric acid under these conditions is (1.6 ± 0.3) × 10^{-10} M^2. The solubility products of these alkali-metal hydrogen laurates appear to be independent of the identity of the alkali-metal ion, and are all equal to (8 ± 2) × 10^{-15} M^4. In solutions containing sodium, potassium, or cesium ion it is possible to attain the critical micelle concentration of laurate, but in solutions containing lithium ion this is rendered impossible by the low solubility of lithium laurate, for which the thermodynamic solubility product is equal to (7.6 ± 1.0) × 10^{-5} M^2. If the ionic strength and concentration of alkali-metal ion are kept constant during a titration, micelle formation and precipitation of a 1:1 alkali-metal laurate are algebraically indistinguishable in that titration, although the parameters that characterize them vary differently on changing the experimental conditions.

Acknowledgments. This work was supported by the Kao Soap Company, Tokyo, Japan, and by Grant No. GP-10325 from the National Science Foundation. We thank the National Science Foundation and the Eastman Kodak Company for Departmental grants that made possible the purchase and maintenance of the minicomputer system employed.

References and Notes

(1) On leave from Kao Soap Company, Tokyo, Japan.
(2) S. L. Young, E. Matijević, and L. Meites, *J. Phys. Chem.*, **78**, 2626 (1974).
(3) For a review of the prior literature see ref 2.
(4) M. E. Feinstein and H. L. Rosano, *J. Phys. Chem.*, **73**, 601 (1969).
(5) J. Lucassen, *J. Phys. Chem.*, **70**, 1824 (1966).
(6) J. Kielland, *J. Am. Chem. Soc.*, **59**, 1675 (1937).
(7) R. C. Merrill and R. Getty, *J. Phys. Colloid Chem.*, **52**, 774 (1948).

Application of the Frumkin Equation to Electrocapillary and Capacity Data of Some Aliphatic Compounds[1]

D. E. Broadhead, K. G. Baikerikar, and Robert S. Hansen*

Ames Laboratory—ERDA and Department of Chemistry, Iowa State University, Ames, Iowa 50010 *(Received February 25, 1975; Revised Manuscript Received November 6, 1975)*

Publication costs assisted by Ames Laboratory

High precision electrocapillary and capacity data for *n*-pentanoic acid, isopentyl alcohol, and primary butyl alcohol are tested against the Frumkin equation with parameters selected to minimize root-mean-square deviations from experimental data. For electrocapillary curves with maximum adsorbate coverages less than 0.9, excellent fits were obtained (average rms deviation for the three solutes 0.2 dyn/cm). Capacity–polarization curves are much more highly structured and therefore more severely test adsorption theories; deviations between experiment and theory were plainly evident in all systems and the average rms deviation for the three solutes was 1.5 $\mu F/cm^2$. Parameters chosen to best fit electrocapillary curves were in fair agreement with those chosen to best fit capacity curves but interchange of parameter sets led to noticeably poorer fits (average rms deviations about 0.6 dyn/cm and 2 $\mu F/cm^2$, respectively). Substantially poorer fits resulted if data corresponding to maximum coverages in excess of 0.9 were included.

Introduction

As early as 1956, a paper[2] from this laboratory presented a theory for the inference of amount of adsorption of organic compounds on a mercury electrode from differential double layer capacity measurements. The theory is based on an early model of the surface layer and corresponding isotherm equation due to Frumkin. In favorable cases, this theory permits establishment of adsorption isotherms (including polarization dependence), molecular areas, and normal components of dipole moments in the adsorbed state. The theory is limited (i) to monomolecular adsorption and (ii) to those classes of adsorbates which maintain a fixed orientation in the surface layer. For a successful application, the theory further requires a linear variation of surface charge with adsorbate surface excess at fixed polarization. The theory has been well tested in two subsequent papers[3,4] based upon studies of adsorption of organic compounds having different functional groups.

The fundamental equations derived in ref 2 have served as the basis for a number of investigations (pertaining to fitting electrocapillary and capacitance data) that have been carried out by the Russian electrochemists led by Damaskin. Damaskin[5,6] using Frumkin's early electrocapillary data on the adsorption of *tert*-amyl alcohol was able to fit, despite some discrepancies, the electrocapillary curves resonably well by employing the fundamental equations. However, large deviations particularly in the regions of capacitance peaks were observed when he tried to fit the experimental double layer capacity data, although the theoretical and experimental curves satisfactorily agreed in shape and position.[5-7] The differential capacitance is a much more highly structured function of polarization than the interfacial tension and greater discrepancies between the theoretical and experimental curves in the former case can be understood on this account. To improve agreement between experimental and calculated capacity curves, Damaskin[5,8,9] treated the interaction parameter in the Frumkin isotherm equation as a function of the electrode polarization, thereby introducing one or more additional adjustable parameters into the fundamental equations. Despite some discrepancies (which are sometimes large), the modified equations seem to have followed rather well electrocapillary and differential capacity curves obtained with simple aliphatic compounds.[5-7,10-15] The modified equations fail, as is to be expected, when applied to the adsorption data of organic molecules which change their orientation with the change in the electrode polarization.[16,17] Damaskin[5,18-21] has extended the theory to fit the data obtained for such compounds by proposing three condensers in parallel as a model.

Damaskin and coworkers[5-7,10-15] at no point seem to have given a quantitative measure of excellence of correspondence between the experimental and calculated electrocapillary or differential capacity curves, whether it is the original fundamental equations that were employed for fitting the data or the equations as modified by Damaskin. No mention of percentage deviation or root mean square deviation has ever been made except to present figures and to state that there was good or satisfactory quantitative agreement between the two quantities. In the case of simple aliphatic compounds, the adsorption of which is characterized by a fixed orientation in the surface layer and without any complications due to the formation of multilayers, Damaskin[5] has treated the interaction parameter as a linear function of electrode potential. These simple compounds present isotherms (surface pressure–logarithm activity curves) that have similar forms at all polarizations and thus are superimposable on a reference curve to form a composite curve. The congruency of the Frumkin isotherm with electrode potential as the independent electrical variable is thus fulfilled; the assumed linear dependence of interaction parameter on polarization is inconsistent with this result.

In the present work, complementary interfacial tension and double layer capacity investigations of the adsorption of three simple aliphatic compounds at the mercury–electrolytic solution interface have been accomplished by employing a capillary electrometer and an impedance

bridge, both of high precision. The original equations derived in ref 2 and discussed in ref 3 and 4 have been used to fit both electrocapillary and differential capacity data; the results of such fitting and the deviations observed have been presented and discussed.

Experimental Section

(1) *Electrocapillary Measurements.* Electrocapillary data were obtained by employing a capillary electrometer based on a fused quartz high-precision gauge (Texas Instruments Inc.) rather than the manometer normally employed for measurement of pressure. The details of the apparatus and the experimental details including the cleaning as well as preserving of the electrometer capillary, isolation of the saturated (NaCl solution) calomel electrode (SCE) from the experimental cell, and the care to be exercised in the maintenance of this electrode (used as reference and counterelectrode) have already been described.[22,23]

(2) *Differential Capacity Measurements.* Double layer capacities at a growing mercury drop were measured with a semiautomatic impedance bridge. The general bridge design is similar to that of Grahame's[24] except that the dc polarizing source is connected across the bridge output diagonal (i.e., dc polarization is applied between the mercury drop and the cylindrical platinum gauze electrode of large area which symmetrically surrounds the mercury drop) following Damaskin.[25] A Hewlett-Packard oscillator (4204A) energized the bridge with a low level ac signal (≈3 mV rms). General Radio Company components, precision decade capacitor (1413) with a tolerance of 0.05% and the noninductively wound precision decade resistor (1433-W) connected in series, formed part of the measuring arm of the bridge. A specially designed phase selective amplifier null detector was used and this supplied start and stop pulses corresponding to the fall of the previous drop (or the birth of a new drop) and balanced state of the bridge to the gating circuit which controlled the counter timer (Monsanto, Model 100-A). The drop time of the dropping mercury electrode could be registered with an accuracy of 0.01 s in 10 s. The satisfactory performance of the impedance bridge was established by reproducing the literature capacity data for a few electrolyte solutions.

With carefully prepared dropping mercury electrodes (siliconized capillary, drop diameter at bridge balance at least ten times larger than the capillary tip diameter) the capacity dispersion for mercury in contact with 0.1 N $HClO_4$ solution at the electrocapillary maximum (ECM), where it was maximum, was normally not more than 0.3–0.4% and was sometimes as low as 0.1% in the frequency range 400–1400 Hz. Dropping mercury electrodes with a relatively large drop time were employed (≈10 s) and capacity measurements were normally made at 80–90% of maximum drop lifetime. Capacities per unit area at fixed ac frequency measured at different times in the drop life agreed within experimental error, indicating absence of complications due to the slow diffusion of the organic adsorbate.

The saturated calomel electrode was used only as a reference electrode in the capacity measurements; this electrode was separated from the experimental cell in a similar fashion and similar care was taken in the maintenance of this electrode as discussed previously.[23]

The capacity data presented here were measured at a frequency of 400 Hz and were not extrapolated to zero frequency. The capacity curves are almost independent of frequency (at least in the range 400–1400 Hz) except in the neighborhoods of the desorption peaks.

(3) *Chemicals.* Care was taken to free the chemicals from surface active as well as oxidizable and reducible impurities. The preparation of mercury, perchloric acid, and quadruply distilled water have been previously described.[22] Primary butyl and isopentyl alcohols were analyzed reagent grade chemicals; these were purified by preparative gas chromatography. *n*-Pentanoic acid was of highest purity grade and was distilled in an all-glass assembly before use.

The solutions were degassed by bubbling through them nitrogen presaturated with vapor from adsorbate solutions.

Results and Discussion

The analysis of interfacial tension data (Figures 1–3) was carried out as described before;[22,23] briefly, each electrocapillary curve (dependence of interfacial tension γ on polarization E for a given solution) was fit by a polynomial of degree ten or less (which had no point of inflection in the region of data) with coefficients chosen to give the best least-squares fit. The root mean square (rms) deviation of data points from the polynomial representations was, averaged over all concentrations, less than 0.05 dyn/cm in all cases.

The capacitance data (Figures 4–6) were not fit with a polynomial, so no rms deviation is available for these data. Individual capacitance measurements, however, were reproducible to within 0.15%. As a check on the compatibility of the two types of measurements, the capacitance curve for the base electrolyte was twice integrated by a numerical technique, and the resulting interfacial tension data agreed within a rms deviation of 0.6 dyn/cm with the experimental electrocapillary data. Similarly, a few doubly integrated capacity curves obtained for absorbate solutions agreed with the experimental electrocapillary curves within a rms deviation of 0.7 dyn/cm. Rms deviations were markedly lower in the central regions of the curves, and greater at their extremes, for two reasons. First, the two integration constants were chosen to give agreements of positions and slopes of the curves compared at the electrocapillary maximum. Second, interfacial tension and differential capacitance data can be in slight error owing to the occurrence of small faradaic reactions at the polarization extremes.

Using the electrocapillary data, 25 constant polarization plots were made (at 50-mV intervals over the polarization range) of surface pressure π vs. logarithm of reduced concentration $\ln a$ (where $\pi = \gamma_0 - \gamma$ is the lowering of interfacial tension due to adsorption and $a = c/c_0$ where c is the solute concentration and c_0 its saturation concentration in the base electrolyte). The form of these plots was independent of polarization, as a result these plots could be superimposed on a reference plot usually taken at the electrocapillary maximum of mercury in the base electrolyte solution by abscissa translation.[22,23] The resulting composite π vs. $\ln a$ curves were fit empirically by a least-squares method with a linear combination of hyperbolas.[23] The dependence of adsorbate surface excess Γ on $\ln a$ was established by analytical differentiation of the linear combination of hyperbolas fit to the composite π vs. $\ln a$ curves.

Henceforth we shall wish to treat the quantity $a = c/c_0$ as a solute activity; for this purpose it is necessary to assume the solute activity coefficient constant over the range of concentrations covered.

The Frumkin isotherm equation can be written as

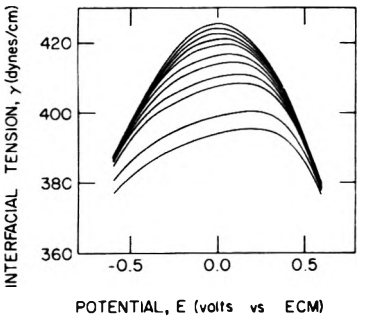

Figure 1. Electrocapillary curves for *n*-pentanoic acid in 0.1 N $HClO_4$ solution. Reduced concentrations of the adsorbate, from top to bottom, are 0, 0.01234, 0.02439, 0.03614, 0.04761, 0.06976, 0.09090, 0.1304, 0.1667, 0.3333, and 0.5000.

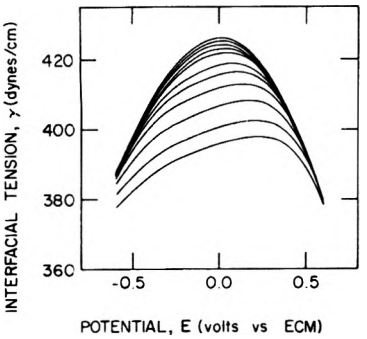

Figure 2. Electrocapillary curves for isopentyl alcohol in 0.1 N $HClO_4$ solution. Reduced concentrations of the adsorbate, from top to bottom, are 0, 0.01234, 0.02439, 0.03614, 0.04761, 0.06976, 0.09090, 0.1304, 0.2000, 0.3333, and 0.5000.

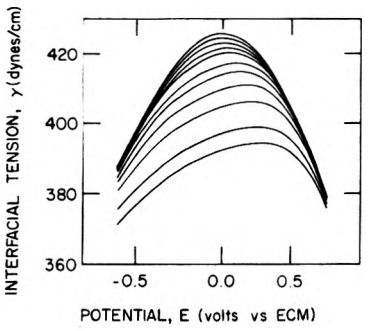

Figure 3. Electrocapillary curves for primary butyl alcohol in 0.1 N $HClO_4$ solution. Reduced concentrations of the adsorbate, from top to bottom, are 0, 0.01234, 0.02439, 0.03614, 0.04761, 0.06976, 0.09090, 0.1304, 0.2000, 0.3548, and 0.5000.

$$\theta/(1-\theta) = Bae^{2\alpha\theta} \qquad (1)$$

where surface coverage $\theta = \Gamma/\Gamma_m$, Γ_m being the limiting surface excess at full monolayer coverage; B and α are constants reflecting metal–adsorbate and adsorbate–adsorbate interactions, respectively. As discussed in the Introduction, superimposability of the π vs. ln a curves implies that α is a constant, independent of potential. B, however, is potential dependent and is a measure of the variation of standard free energy of adsorption with the change in the electrical state of the interface.

The superimposability of π vs. ln a curves further implies that surface charge varies linearly with surface excess at fixed polarization. Figure 7 provides a direct verification of this linear relationship between σ and Γ at fixed E for primary butyl alcohol and *n*-pentanoic acid. Surface ex-

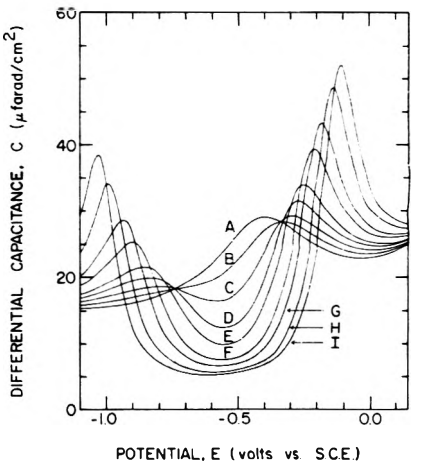

Figure 4. Differential capacitance curves for *n*-pentanoic acid in 0.1 N $HClO_4$ solution. Reduced concentrations of the adsorbate are (A) 0, (B) 0.01234, (C) 0.02439, (D) 0.03614, (E) 0.04761, (F) 0.06976, (G) 0.09090, (H) 0.1304, (I) 0.1667.

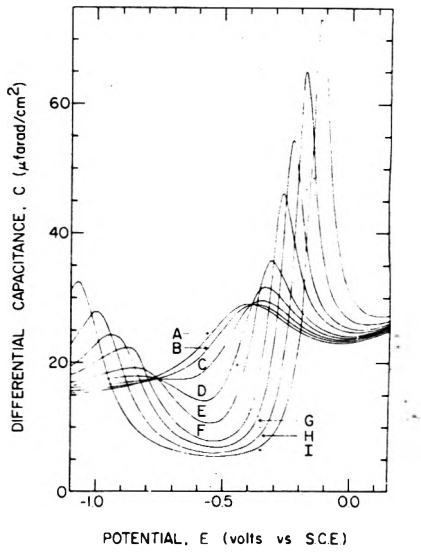

Figure 5. Differential capacitance curves for isopentyl alcohol in 0.1 N $HClO_4$ solution. Reduced concentrations of the adsorbate are (A) 0, (B) 0.01234, (C) 0.02439, (D) 0.03614, (E) 0.04761, (F) 0.06976, (G) 0.09090, (H) 0.1304, (I) 0.2000.

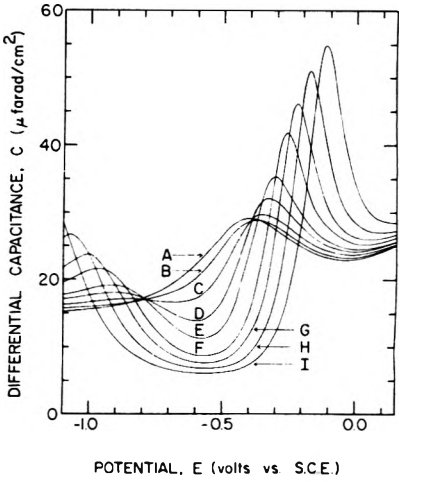

Figure 6. Differential capacitance curves for primary butyl alcohol in 0.1 N $HClO_4$ solution. Reduced concentrations of the adsorbate are the same as in Figure 5.

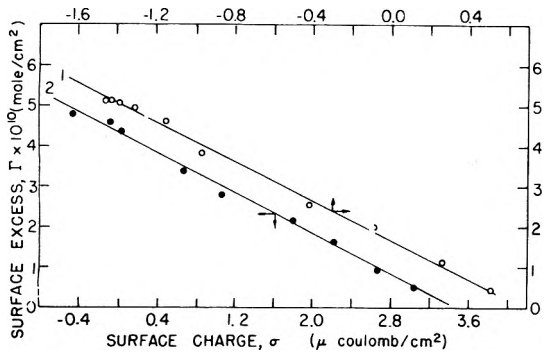

Figure 7. Surface excess vs. surface charge plots: (1) for primary butyl alcohol at −0.450 V vs. SCE, and (2) for *n*-pentanoic acid at −0.350 V vs. SCE.

cess values were obtained by analytical differentiation of the linear combination of hyperbolas fit to the individual π vs. ln a curves, and surface charge values were obtained by analytical differentiation of the polynomial fit to the electrocapillary curves. The plots shown in Figure 7 and also superimposability of π vs. ln a plots at different potentials further imply (1) that the interaction parameter α in the Frumkin isotherm equation is independent of polarization and (2) that electrode potential (as contrasted with electrode charge) is the appropriate independent electrical variable for the analysis of superimposable isotherms in these systems.

The Frumkin surface layer model consists of two condensers in parallel leading to a surface charge density given by

$$\sigma = \sigma_w(1 - \theta) + C'(E - E_N)\theta \tag{2}$$

where σ is the total surface charge per unit area, σ_w is the surface charge per unit area in the absence of adsorbate (both σ and σ_w correspond to a potential of E), C' is the capacitance (assumed constant) corresponding to $\theta = 1$, and E_N is the shift of potential of zero charge in the transition from $\theta = 0$ to $\theta = 1$. Both E and E_N are referred to the potential at the electrocapillary maximum of mercury in the base electrolyte solution.

The Gibbs adsorption theorem combined with eq 1 and 2 furnishes the expression for the generalized Frumkin isotherm[2]

$$\frac{\theta}{1 - \theta} = B_0 a e^{2\alpha\theta} e^{-(\Phi/\Gamma_m RT)} \tag{3}$$

where

$$\Phi = \int_0^E [\sigma_w - C'(E - E_N)]\, dE \tag{4}$$

On integration

$$\Phi = G(E) + C'E_N E - \frac{1}{2}C'E^2 \tag{5}$$

where $G(E) = \gamma(0, a = 0) - \gamma(E, a = 0)$ represents the lowering of interfacial tension due to polarization in the absence of organic adsorbate.

The fundamental equation derived in ref 2 for the total capacitance C is

$$C = C_w(1 - \theta) + C'\theta + \frac{[\sigma_w - C'(E - E_N)]^2}{\Gamma_m RT} \frac{\theta(1 - \theta)}{1 - 2\alpha\theta(1 - \theta)} \tag{6}$$

Many techniques are available for determining the constants Γ_m, α, B_0, C', and E_N of the Frumkin equation[5] but none of the methods uses original data to determine all the constants simultaneously. A computer program was written in an attempt to fit the five constants to the original electrocapillary data by a least-squares technique, but convergence was not obtained. It was found that if two of the constants Γ_m and C' were obtained by other means, and the other three were fit by least squares, convergence was obtained and the original data could be fit well.

Γ_m was obtained from the limiting slope of the composite π vs. ln a curve. C' was obtained from the capacitance data by extrapolation of a plot of $1/C$ vs. $1/a$ to $1/a = 0$ where C is now the capacitance at maximum adsorption. This plot is based on eq 1 and 6. Let $f = Be^{2\alpha\theta}$ in eq 1. Near the point of zero charge eq 6 reduces to $C = C_w(1 - \theta) + C'\theta$. From this and eq 1 it follows that

$$\frac{1}{C} = \frac{1 + (fa)^{-1}}{C_w(fa)^{-1} + C'} \tag{7}$$

The computer program used to fit the electrocapillary data finds the constants α, B_0, and E_N which give rise to a minimum in the sum of the squares of the deviations of the calculated surface pressures[26]

$$\pi = -\Gamma_m RT[\ln(1 - \theta) + \alpha\theta^2] \tag{8}$$

from the experimental surface pressures. For each data point θ was found from eq 3 by an iterative method.

A similar computer program was used to fit the capacitance data in which the constants α, B_0, and E_N are found which give rise to a minimum in the sum of the squares of the deviations of the calculated capacitances

$$C = C_w + \theta\left\{(C' - C_w) + \frac{[\sigma_w - C'(E - E_N)]^2}{\Gamma_m RT} \times \frac{(1 - \theta)}{1 - 2\alpha\theta(1 - \theta)}\right\} \tag{9}$$

from the experimental capacitances. θ was again found for each point by use of eq 3.

Table I compares the Frumkin equation parameters found to give best fits to electrocapillary data with those found to give best fits to double layer capacity data for each of the three adsorbates studied. The agreement of parameters for *n*-pentanoic acid and isopentyl alcohol is very good and for primary butyl alcohol fair. Figure 8 compares calculated electrocapillary curves for *n*-pentanoic acid using these two sets of parameters with experimental points. The curve using Frumkin parameters based on the electrocapillary curve appears to fit the data perfectly (actually, as Table I shows, the average rms deviation is larger than for a polynomial fit). The curve based on capacity parameters noticeably underlies the data in the electrocapillary maximum region, although its qualitative fit is nevertheless quite good. Figure 9 compares capacity curves similarly calculated with capacity data for *n*-pentanoic acid. It is immediately apparent that the more highly structured capacity–polarization data provide a much more sensitive test of the Frumkin model than do electrocapillary data. Even when the Frumkin parameters are chosen to best fit the capacity data, the average rms deviation of experimental points from Frumkin curve is (for *n*-pentanoic acid) 1.36 μF/cm^2, and the average rms deviation is about twice this value if Frumkin parameters are chosen to best fit electrocapillary data.

Table I and Figures 8 and 9 were obtained by fitting data from the seven lowest reduced concentrations studied ($a \leq$

TABLE I: Parameters of Frumkin Equation Fit to Electrocapillary and Capacitance Data

	$10^{10}\Gamma_m$, mol/cm²	C', μF/cm²	α	B_0	E_N, (V vs. ECM)	Rmsd: Frumkin fit	Rmsd: Polynomial fit
n-Pentanoic acid							
Electrocapillary data	4.799	4.444	1.06	8.54	0.241	0.14 dyn/cm	0.04 dyn/cm
Capacity data			1.13	8.70	0.259	1.36 μF/cm²	
Isopentyl alcohol							
Electrocapillary data	4.764	4.480	1.32	5.13	0.346	0.18 dyn/cm	0.03 dyn/cm
Capacity data			1.42	5.02	0.344	1.85 μF/cm²	
Primary butyl alcohol							
Electrocapillary data	5.186	4.988	1.11	6.13	0.359	0.28 dyn/cm	0.04 dyn/cm
Capacity data			1.25	5.19	0.384	1.32 μF/cm²	

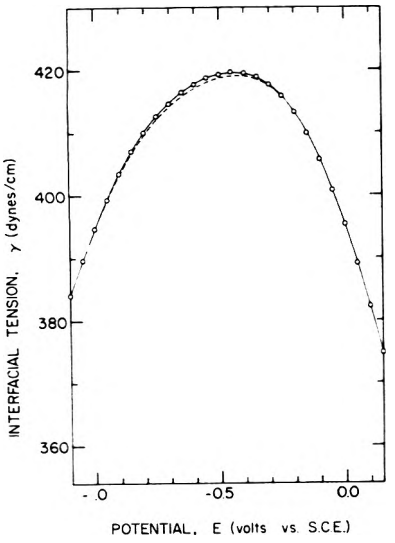

Figure 8. Electrocapillary curve for 0.1 N $HClO_4$ solution containing *n*-pentanoic acid, a = 0.04761. Points shown are experimental data. The solid curve is the Frumkin equation fit to the electrocapillary data; the dashed curve is the Frumkin equation fit to the capacitance data.

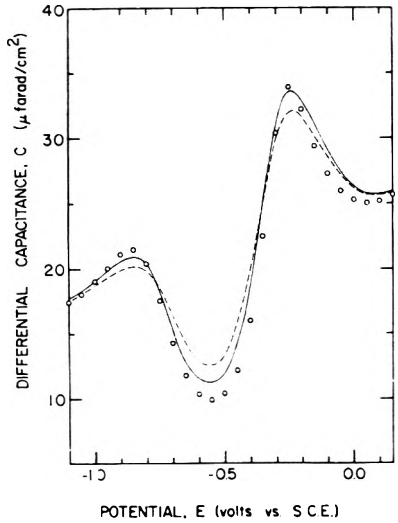

Figure 9. Differential capacitance curve for 0.1 N $HClO_4$ solution containing *n*-pentanoic acid, a = 0.04761. Points shown are representative of the experimental data (53 points were determined). The solid curve is the Frumkin equation fit to the capacitance data; the dashed curve is the Frumkin equation fit to the electrocapillary data.

0.1304). It was found that when the data for the higher reduced concentrations were included, a much larger rms deviation was obtained (e.g., 0.5 dyn/cm for the electrocapillary data in the case of *n*-pentanoic acid). Also, if the constants given in Table I were used for the higher reduced concentrations, the fit obtained was not as good as for the lower reduced concentrations. Thus, it seems that the deviations from the Frumkin equation are more severe at higher concentrations of the adsorbate.

The computer program used for fitting electrocapillary data was modified to include a sixth constant to allow for a linear variation of interaction parameter with polarization but the resulting fit was not improved.

It is difficult to compare directly our results with those of Damaskin et al.,[5-7,10-15] for their results have invariably been presented only graphically, frequently with scales making estimation of differences between experimental points and theoretical curves difficult. It appears that, in the systems we have treated, the mean deviations between experimental points and theoretical curves based on five parameters is less than obtained by Damaskin and coworkers using six. The number of adsorbate concentrations in our study (seven with maximum adsorption not greater than θ = 0.9 for each system) is greater than shown in any of their graphical presentations; further in our work, all data were used in establishing the best set of parameters in each case. Damaskin et al. do not appear to have cross-compared electrocapillary and capacity parameterizations.

Acknowledgments. Thanks are due to Mr. Wayne A. Rhinehart whose advice and active cooperation contributed greatly to the construction of the impedance bridge that was used in this work.

Supplementary Material Available: a listing of electrocapillary and capacity data employed for fitting to the Frumkin equation (25 pages). Ordering information is given on any current masthead page.

References and Notes

(1) Prepared for the U.S. Energy Research and Development Administration under Contract No. W-7405-eng-82.
(2) R. S. Hansen, R. E. Minturn, and D. A. Hickson, *J. Phys. Chem.*, **60**, 1185 (1956).
(3) R. S. Hansen, R. E. Minturn, and D. A. Hickson, *J. Phys. Chem.*, **61**, 935 (1957).
(4) R. S. Hansen, D. J. Kelsh, and D. H. Grantham, *J. Phys. Chem.*, **67**, 2316 (1963).
(5) B. B. Damaskin, O. A. Petrii, and V. V. Batrakov, "Adsorption of Organic Compounds on Electrodes", Plenum Press, New York, N.Y., 1971, pp 67-139.
(6) A. N. Frumkin and B. B. Damaskin in "Modern Aspects of Electrochemistry", Vol. 3, J. O'M. Bockris and B. E. Conway, Ed., Butterworths, London, 1964, Chapter 3.
(7) B. B. Damaskin and N. B. Grigorev, *Dokl. Akad. Nauk SSSR*, **147**, 135 (1962).
(8) B. B. Damaskin, *Usp. Khim.*, **34**, 1764 (1965).
(9) B. B. Damaskin, *Zh. Fiz. Khim.*, **37**, 2483 (1963).

(10) B. B. Damaskin, *Electrochim. Acta*, **9**, 231 (1964).
(11) R. Lerkkh and B. B. Damaskin, *Zh. Fiz. Khim.*, **38**, 1154 (1964).
(12) R. Lerkkh and B. B. Damaskin, *Zh. Fiz. Khim.*, **39**, 211 (1965).
(13) B. B. Damaskin and R. Lerkkh, *Zh. Fiz. Khim.*, **39**, 495 (1965).
(14) V. K. Venkatesan, B. B. Damaskin, and N. V. Nikolaeva-Fedorovich, *Zh. Fiz. Khim.*, **39**, 129 (1965).
(15) B. Damaskin, A. Frumkin, and A. Chizhov, *J. Electroanal. Chem.*, **28**, 93 (1970).
(16) B. B. Damaskin, I. P. Mishutushkina, V. M. Gerovich, and R. I. Kaganovich, *Zh. Fiz. Khim.*, **38**, 1797 (1964).
(17) B. B. Damaskin, V. M. Gerovich, I. P. Gladkikh, and R. I. Kaganovich, *Zh. Fiz. Khim.*, **38**, 2495 (1964).
(18) B. B. Damaskin, A. N. Frumkin, and S. L. Dyatkina, *Izv. Akad. Nauk SSSR, Ser. Khim.*, No. **10**, 2171 (1967).
(19) B. B. Damaskin, *Elektrokhimiya*, **4**, 675 (1968).
(20) B. B. Damaskin, *Elektrokhimiya*, **5**, 346 (1969).
(21) B. B. Damaskin, S. L. Dyatkina, and S. L. Petrochenko, *Elektrokhimiya*, **5**, 935 (1969).
(22) D. E. Broadhead, R. S. Hansen, and G. W. Potter, *J. Colloid Interface Sci.*, **31**, 61 (1969).
(23) K. G. Baikerikar and R. S. Hansen, *J. Colloid Interface Sci.*, accepted for publication.
(24) D. C. Grahame, *J. Am. Chem. Soc.*, **68**, 301 (1946).
(25) B. B. Damaskin, *Zh. Fiz. Khim.*, **32**, 2199 (1958).
(26) Equation 7 is the equation of state corresponding to the Frumkin isotherm and is derivable from eq 1 and the Gibbs adsorption theorem.

Solubility of Hydrogen and Deuterium in a Uranium–Molybdenum Alloy

G. Lovis Powell

Nuclear Division, Union Carbide Corporation, Oak Ridge, Tennessee 37830 *(Received May 27, 1975)*

Publication costs assisted by Nuclear Division, Union Carbide Corporation for The United States Energy Research and Development Administration

The solubility of hydrogen and of deuterium in uranium–0.222 mole fraction molybdenum alloy has been measured over the temperature range from 700 to 1350 K with a precision of ±1%. The solubility displays a minimum value near 900 K. A model, which is generally applicable to hydrogen dissolved in other metals, is presented that describes the observed phenomena, that can be extrapolated to lower temperatures, that yields the enthalpy of formation of hydrogen dissolved in the alloy at 0 K, and that suggests a quantum mechanical treatment for interstitial diffusion.

I. Introduction

Single-phase metal–hydrogen alloy systems have been studied extensively and the literature in this field has been reviewed several times.[1–3] Experimentally, the equilibrium constant (K_H) for the reaction between hydrogen gas at pressure P_{H_2} and hydrogen dissolved in a metal at concentration $[H_M]$ is determined using pressure–volume measurements yielding the relationship:

$$K_H = \frac{[H_M]}{\sqrt{P_{H_2}}} = \exp\left[-\frac{F^\circ_{H_M,T} - \frac{1}{2}F^\circ_{H_2,T}}{RT}\right] \qquad (1)$$

Here $F^\circ_{H_M,T}$ is the standard Gibbs free energy per gram atom hydrogen dissolved in the metal. Activity coefficients are usually added as $[H_M]$ becomes large. $F^\circ_{H_2,T}$ is the standard Gibbs free energy per mole for hydrogen gas. For most metals K_H either increases (Y, Ti, Nb) or decreases (Ni, Cu, W) markedly with temperature and appears to converge to approximately the same value at elevated temperatures (~1500 K). Equation 1 is known as Sievert's law.

Ebisuzaki et al.[2,4] have developed a quantitative description of the contribution of the vibrational states of a hydrogen atom in an interstitial site of a metal to K_H based on the ratio of K_H for hydrogen to that for deuterium (K_D). Qualitative correlations have been drawn between K_H and the electronic properties of some metals.[2,3] A quantitative theory generally applicable to all metals and derivable from K_H, that allow (1) the extrapolation of K_H into temperature regions inaccessible to direct measurements and (2) the direct comparison of K_H for various metals have not been reported.

The value for K_H for the high-temperature, body-centered-cubic (bccub) phase of uranium has a magnitude that is intermediate between that for niobium and that for nickel.[1] Additions of molybdenum as an alloying element broadens the temperature range over which the bccub phase is thermodynamically and kinetically stable with the maximum temperature range near 0.2 mole fraction molybdenum.[5–7]

This report describes the very precise determination of K_H and K_D for the uranium–0.222 mole fraction molybdenum alloy (U–0.222 Mo) over the temperature range from 700 to 1400 K. A minimum value was observed for K_H and K_D near 900 K. A simple model, consistent with the "isotope effect theory" of Ebisuzaki and O'Keefe,[2,4] is presented that describes the observed values of K_H and K_D and yields parameters by which K_H and K_D may be extrapolated to lower temperatures.

II. Materials

The argon (99.999% pure) was used without further purification. The hydrogen gas (99.99% pure) was filtered through UH_3 powder to remove oxygen (water).[8] The deuterium gas (99.8% D_2, 99.99% hydrogen isotopes) was filtered through UD_3 powder. The gas manifold had ultra-high-vacuum integrity and was evacuated to less than 1×10^{-10} atm before a gas was introduced.

The U–0.222 Mo alloy composition was determined from

x-ray adsorption measurements of a solution containing a dissolved aliquote of the U–0.222 Mo alloy. Major impurities were the following: 300 μg of C/g, 125 μg of Si/g, 125 μg of Fe/g, 40 μg of Ni/g, 30 μg of Cu/g, 23 μg of N/g, 23 μg of O/g. The U–0.222 Mo specimen used for this experiment weighed 102.082 g (0.4943 mol of metal atoms). To prevent contamination of the alloy by reaction with the vacuum chamber wall at temperatures near 1400 K, a yttria-lined alumina boat (1.2 cm i.d. × 7.6 cm long × 0.1 cm wall thickness) was prepared to support the sample by plasma spraying the Al_2O_3 and Y_2O_3 over a tungsten mandrel followed by sintering at 1500 K.[9]

The U–0.222 Mo alloy exists as an equilibrium bccub phase above 860 K. The alloy can retain this bccub phase indefinitely if rapidly cooled below 700 K.[5,6] This bccub phase is retained for 25 ks or longer at temperatures slightly below 860 K before transforming into a two-phase alloy consisting of a uranium-rich phase similar to α-phase uranium and a molybdenum-rich phase.[7]

III. Instrumentation

The experimental arrangement was the Sievert's apparatus shown in Figure 1. All-metal, ultra-high-vacuum equipment was used exclusively. The pressure could be reproducibly measured within 1×10^{-4} atm over the pressure range from 0.13 to 1.3 atm. At pressures below 0.13 atm, the pressure measurements were reproducible within $\pm 1 \times 10^{-5}$ atm over a 90-ks period. The reference volume (V_0 = 207.2 cm^3) was calibrated by the Oak Ridge Y-12 Plant Standards Laboratory and this calibration is traceable to the National Bureau of Standards. The working standard volume (V_1 = 52.76 ± 0.21 cm^3) was determined by argon expansions from V_0.

A proportional temperature controller maintained the sample temperature within 1 K over the temperature range from 700 to 1350 K as measured by a platinum—platinum–10% rhodium thermocouple with a precision of 0.01 mV. The sample temperature could be changed incrementally at a preset time interval by a temperature programmer that repeated itself every 26-time intervals. Another proportional temperature controller maintained V_1 and the portion of V_2 outside the high-temperature furnace at 300.3 ± 0.1 K. The sample temperature and the pressure gauge output were alternately recorded on a digital voltmeter–printer system at 60-s intervals. Thermocouples were checked against National Bureau of Standards Reference thermocouples and found to agree within 1 K.

IV. Procedure

The sample is positioned in the Mullite tube exposing only V_2 to air, evacuated, and heated to 1100 K under vacuum. Once a high vacuum is achieved, $V_3 = V_1 + V_2$ (Figure 1) is backfilled with H_2 to 0.5 atm and left undisturbed for 173 ks to reduce oxides of copper and iron on the walls of V_3. The system is then evacuated to $<1 \times 10^{-7}$ atm for 90 ks to remove residual hydrogen and water. The working standard volume V_1 was then charged with argon to 7.961×10^{-2} atm, expanded into V_2, and data were collected over an 80-ks period while the sample temperature was changed incrementally by approximately 100 K at 4-ks intervals in such a manner as to span the 700–1350-K temperature range three times. The establishment of equilibrium was indicated by no change in the recorded pressure or temperature data during the last 0.5 ks of an isothermal period. From these data the effective volume after expansion, $V_3 = V_1 + V_2$, was determined using the ideal gas law. The temperature dependence of V_3 is given by

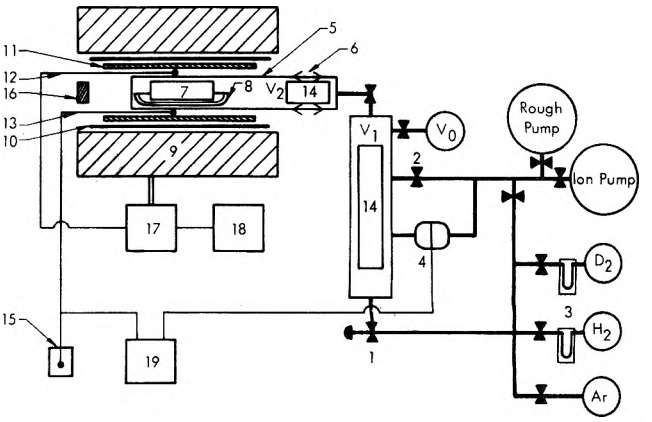

Figure 1. Sieverts apparatus used for these experiments: (1) variable leak valve (Granville-Phillips); (2) 0.75-in. all-metal valve (Varian Associates); (3) UH_3 or UD_3 powder filter; (4) pressure sensor (MKS Baratron Model 94H-1000); (5) Mullite tube (1.9 cm o.d. × 1.6 cm i.d. × 30 cm long); (6) Mullite-to-Pyrex-to-Kovar graded seal; (7) U–0.222 Mo sample (1.22 cm diameter × ~5 cm long); (8) yttria-lined alumina boat; (9) combustion tube furnace; (10) platinum cylinder for thermal and electical shielding of the sample and thermocouples; (11) Mullite thermal shield (2.54 cm o.d. × 2.20 cm i.d.); (12) temperature control thermocouple (Pt—Pt–10% Rh); (13) temperature measurement thermocouple (Pt—Pt–10% Rh); (14) alumina rod (1.27 cm diameter) to reduce the free volume of commercially available 0.75-in. vacuum hardware; (15) reference thermocouple ice bath; (16) fire brick plug; (17) proportional temperature controller; (18) temperature programmer; (19) data acquisition system.

$$V_3 = \left(79.42 + \frac{9844}{T} - \frac{1.728 \times 10^6}{T^2}\right) \text{cm}^3 \qquad (2)$$

within a precision of ±0.2 cm^3. The system was evacuated to 1×10^{-10} atm for 15 ks and V_1 was recharged with hydrogen to 7.908×10^{-2} atm. This gas was expanded into V_2, and a set of pressure–temperature data was collected over the 700–1350-K temperature range. Isothermal increments of 5.5 ks were required to achieve equilibrium. The system was reevacuated to 1×10^{-10} atm for 15 ks, V_1 was charged with deuterium, and another set of pressure–temperature data was collected. The pressure–temperature data sets for the hydrogen isotopes are plotted in Figure 2. The ideal gas law was used to calculate the difference between the number of gram atoms of hydrogen in the gas phase initially charged in V_1 and the number of gram atoms of hydrogen in the gas phase after equilibrium is achieved at some temperature (T). Thus $[H_M]$ or $[D_M]$ can be calculated at different temperatures using

$$[H_M] = 2\frac{(P_1V_1 - P_TV_3)}{R(300.3\text{ K})(M)} \qquad (3)$$

and the value $V_3(T)$ from eq 2. The equilibrium constant (K_H) can also be calculated using eq 1 with $P_{H_2} = P_T$. The term M had the value 0.4943 mol of metal.

The resulting P–T and K–T data sets for hydrogen and deuterium are shown in Figures 2 and 3. Note that the irreproducibility of the P–T measurements are greater than the uncertainties in pressure and temperature measurements. From Figures 2 and 3, $[H_M]$ and $[D_M]$ may be calculated. During both experiments $[H_M]$ was approximately

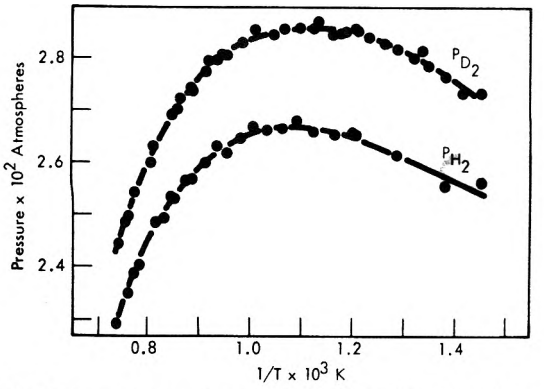

Figure 2. Pressure–temperature data sets from the Sieverts experiment: upper curve P_{D_2} ($P_1 = 7.970 \times 10^{-2}$ atm); lower curve P_{H_2} ($P_1 = 7.908 \times 10^{-2}$ atm).

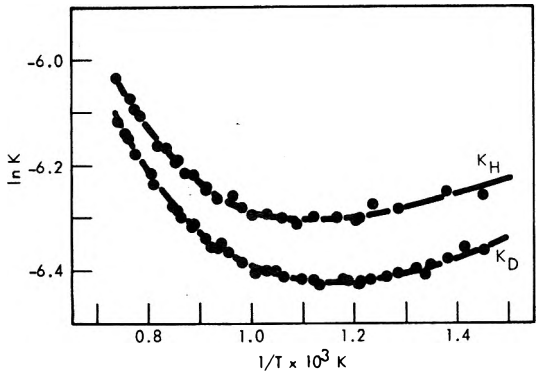

Figure 3. Equilibrium constants for the reaction of H_2 and D_2 with U–0.222 Mo alloy: upper curve K_H; lower curve K_D.

constant at 3×10^{-4} varying by less than ±10% over the 700–1350-K temperature range.

A number of preliminary experiments were carried out on a different sample of U–0.222 Mo alloy prior to installing the temperature programming capability. These experiments demonstrated the need for the initial long exposure of the system to high hydrogen pressures followed by a lengthy evacuation step.

The preliminary experiments also demonstrated that, within a precision of 5%, K_H is not a function of P_{H_2} over the range of 5×10^{-3} to 0.5 atm. The relatively poor precision in these preliminary experiments is due mainly to the irreproducibility of the pressure measurement at the pressure extremes. The pressure ranges chosen for the experiments shown in Figures 2 and 3 were chosen to minimize the effect of the error of the pressure measurement on K_H. In effect, the sample size, P_1, V_1, and V_3 were chosen such that most of the hydrogen is removed from the gas phase after the expansion step in order to achieve maximum precision in calculating $[H_M]$ (eq 3) while leaving P_{H_2} sufficiently high that it does not affect the precision of K_H.

V. Theory

A grand partition function may be written for hydrogen in the intersticies of the metal lattice as follows:[1,10,11]

$$\Xi = \sum_{N_H} \sum_{N_M} \frac{N_I!}{N_H!(N_I - N_H)!} \times (\lambda_H Z_H e^{-(E_H/RT)})^{N_H} (\lambda_M Z_M e^{-(E_M/RT)})^{N_M} \quad (4)$$

where N_I = number of interstitial positions in the lattice; N_H = number of hydrogen atoms in the metal lattice; N_M = number of metal atoms in the lattice; λ = the activity of the indicated species; Z = the canonical partition function for the indicated species; E = energy for establishing the indicated species not including energy terms explicitly included in Z.

The logarithm of the maximum term in Ξ is differentiated with respect to N_H and set equal to zero in the usual manner yielding

$$\frac{\partial \ln [\text{max term } \Xi]}{\partial N_H} = 0 = -\ln \frac{N_H}{N_I - N_H} + \ln \lambda_H + \ln Z_H - \frac{E_H}{RT} + \zeta \quad (5)$$

where

$$\zeta = \frac{\partial \ln (\lambda_M Z_M e^{-(E_M/RT)})^{N_M}}{\partial N_H}$$

The hydrogen activity in the metal at equilibrium is the same as that for the hydrogen gas which can be written as

$$\ln \lambda_H = -\frac{1}{2}\left(\frac{F^\circ_{H_2,T}}{RT} + \ln P_{H_2}\right) \quad (6)$$

Here $F^\circ_{H_2,T}$ is the standard Gibbs free energy per mole for hydrogen gas at 1 atm pressure at temperature T and P_{H_2} is the hydrogen pressure in atmospheres. The canonical partition function for hydrogen in the metal interstice, Z_H, may be written as

$$Z_H = \underbrace{\left[q_0 e^{-(E_0^e/RT)}\left(1 + \sum_{i=1}^{\infty} \frac{q_i}{q_C} e^{-(E_i^e - E_0^e/RT)}\right)\right]}_{\text{I}} \times \underbrace{\left(2 \sinh \frac{\theta_H}{2T}\right)^{-3}}_{\text{II}} \underbrace{\left(1 + \sum_{j=1}^{\infty} a_j e^{-(E_j^r/RT)}\right)^3}_{\text{III}} \quad (7)$$

Term I in eq 7 is the electronic partition function for the hydrogen atom in the metal lattice. It is expressed here as a sum over a single set of energy states. Term II is the partition function for the three normal modes of the vibrational states of the hydrogen in the metal lattice based on a simple harmonic oscillator approximation.[2,4] The term θ_H is the Einstein temperature for the vibrator and this particular form of the vibrational partition function results from choosing the reference energy as the minimum in the vibrational potential energy well. Term III is a correction term for the vibrational partition function that accounts for any additional energy levels that may be introduced by a change in shape of the vibrational potential energy well at energies comparable to the activation energy for diffusion. The term ζ (eq 5) is now redefined to include the hydrogen–hydrogen interaction energy defined by Lacher[12] as well as any changes in Z_H resulting from N_H dependent changes in λ_M, Z_M, E_M, or any of the parameters in eq 7.

Substituting eq 6 and 7 into eq 5; addition to eq 5 the terms

$$0 = \ln (N_M/N_M) \quad (8)$$

and

$$0 = H^\circ_{H,0} - H^\circ_{H,0} \quad (9)$$

where $H^\circ_{H,0}$ is the energy per mole of monatomic hydrogen gas at 0 K; and taking the antilog yields

$$\frac{[H_M]}{(N-[H_M])\sqrt{P_{H_2}}} = \frac{q_0 e^{\zeta}}{8}\left(\sinh\frac{\theta_H}{2T}\right)^{-3} \times \left(1+\sum_{j=1}^{\infty} a_j e^{-(E_j^{\nu}/RT)}\right)^3 \left(1+\sum_{i=1}^{\infty}\frac{q_i e^{-(\Delta E_i^{e}/RT)}}{q_0}\right) \times \exp\left[-\left(\frac{\epsilon}{RT}-\Phi_H\right)\right] \quad (10)$$

where N = number of interstitial positions per metal atom in the lattice (N = 3 for octahedral sites and 6 for tetrahedral sites in a bccub lattice); $\epsilon = E_0 + E_H - H^{\circ}_{H,0}$ is the energy required at 0 K to place atomic hydrogen gas in the metal lattice and allow the electrons to relax to the electronic ground state in the metal (note that the zero point vibrational energy is included in the hyperbolic sine term);

$$\Phi_H = \frac{1}{2}\left(\frac{F^{\circ}_{H_2} - H^{\circ}_{H,0}}{RT}\right) \quad (11)$$

can be calculated from thermodynamic tables[13-15]

$$\Delta E_i^{e} = E_i^{e} - E_0^{e} \quad (12)$$

An expression, similar to eq 10, can be written for deuterium. In the case of deuterium, θ_H is replaced by $\theta_D = \theta_H/\sqrt{2} = \theta/\sqrt{2}$ and Φ_H is replaced by Φ_D. Under the conditions of (a) dilute solution ($[H_M] \ll N$); (b) constant pressure ($P_{H_2} = P_{D_2}$); and (c) negligible isotopic mass dependence in E_j^{ν}; the ratio of the expression for hydrogen given in eq 9 to a similar expression for deuterium yields

$$\frac{[H_M]}{[D_M]} = \left(\frac{\sinh\dfrac{\theta}{2\sqrt{2}T}}{\sinh\dfrac{\theta}{2T}}\right)^3 \exp(\Phi_H - \Phi_D) \quad (13)$$

Equation 13 is the isotope effect described by Ebisuzaki and O'Keefe.[2,4]

In dilute solution ($[H_M] < 0.01$), ζ is probably zero since small quantities of hydrogen are not likely to significantly affect the activity or the canonical partition function for the metal. As $[H_M]$ approaches 1, ζ may well become an important factor and is a function of $[H_M]$ as well. It may also be noted that q_0 is a whole number. For diatomic hydrogen gas q_0 = 1 and for atomic hydrogen gas q_0 = 2.[13] For simplicity, one can assume that the electronic energy level spacings are large compared to RT and only a few terms in the sum

$$1+\sum_{i=0}^{\infty}\frac{q_i}{q_0}e^{-(\Delta E_i^{e}/RT)}$$

are important and then only at high temperatures. Terms of this type contribute less than 1 cal mol^{-1} to the free energy of atomic hydrogen gas at 1500 K. The activation energy for interstitial hydrogen diffusion reported for uranium and uranium alloys ranges from 7 to 13 kcal/mol[16] indicating that the contribution to K_H from term III, eq 7, will also be relatively small and then significant only at high temperatures. The magnitude of the E_j^{ν} levels is probably determined by the height of the diffusion barrier but the spacings between E_j^{ν} levels depends on the mass of the hydrogen isotope. Given the difficulties in precisely determining θ in eq 13 (K_H differs from K_D only by a few percent) and a small contribution from electronic and E_j^{ν} states, eq 10 can probably be approximated by the expressions

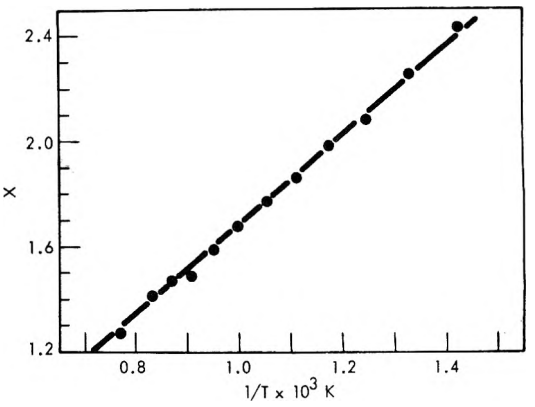

Figure 4. The Einstein temperature plot for hydrogen in U–0.222 Mo alloy calculated from Figure 3.

$$K_H = \frac{N}{8} q_0 \left(\sinh\frac{c}{2T}\right)^{-3}(1+ae^{-(b/T)})(e^{-[(\epsilon/RT)-\Phi_H]}) \quad (14a)$$

and

$$K_D = \frac{N}{8} q_0 \left(\sinh\frac{c}{2\sqrt{2}T}\right)^{-3}(1+ae^{-(b/T)})(e^{-[(\epsilon/RT)-\Phi_D]}) \quad (14b)$$

VI. Results

These experiments involved values of $[H_M]$ on the order of 3×10^{-4}, thus negligible with respect to N. Since K_H is constant at a given temperature over the range of 4×10^{-3} atm $< P_{H_2} <$ 0.4 atm, the dilute solution approximation with $\zeta = 0$ is valid.

The approximate Einstein temperature, c, was determined from Figure 3 by calculating

$$\exp\left[\frac{\ln K_H - \ln K_D - \Phi_H + \Phi_D}{3}\right] = \frac{\sinh(X/2\sqrt{2})}{\sinh(X/2)} \quad (15)$$

at various temperatures and graphically finding $X = c/T$. Equation 15 is the cube root of the ratio of eq 14a and 14b and is essentially the same as eq 13. A plot of X vs. $1/T$ is shown in Figure 4. The slope of this curve is c and was found to be 1676 K (standard deviation 18 K).

Within experimental error, the data for K_H and K_D can be described using eq 14a and 14b with the parameters shown in Table I.

Note that c is used as an adjustable parameter within the uncertainty (18 K) with which it was determined from Figure 4. Extrapolation of K_H and K_D to lower temperatures using the parameters from Table I and eq 14a and 14b is given in Figure 5. In curve fitting, the increase in K_H resulting from increasing Nq_0 is compensated by changing ϵ. In effect, the magnitude of ln K_H is increased by an increment (ln Nq_0) and this increase is then compensated by a rotation, i.e., a change in ϵ, about the origin followed by an adjustment in the parameters a and b. The rotation ($\Delta\epsilon$) required to compensate for values of Nq_0 greater than six is so large that the observed minimum in ln K_H (Figures 3 and 5) can no longer be described.

VII. Discussion

Factoring the term $e^{-(3c/2T)}$ from the hyperbolic sine term in eq 14a yields eq 16 which lends itself more readily to interpretation.

TABLE I: Parameters that Describe K_H for U-0.222 Mo using Eq 14

	$Nq_0 = 3$	$Nq_0 = 6$
a	20	143
b	4200 K	8100 K
$c(=\theta_H)$	1684 K	1676 K
ϵ	−56 589 cal (g atom)$^{-1}$	−55 532 cal (g atom)$^{-1}$
Related parameters		
$E_{HM,0}^\circ - H_{H,0}^\circ = \epsilon + {}^3/_2R\theta_H$	−51 569 (g atom)$^{-1}$	−50 535 cal (g atom)$^{-1}$
$\theta_D = c/\sqrt{2}$	1191 K	1185 K
$E_{DM}^\circ - H_{D,0}^\circ = \epsilon + {}^3/_2R\theta_D$	−53 039 cal (g atom)$^{-1}$	−51 999 cal (g atom)$^{-1}$
$E_{HM}^\circ - H_{H_2,0}^\circ$	64 cal (g atom)$^{-1}$	1 098 cal (g atom)$^{-1}$
$E_{DM,0} - H_{D_2,0}^\circ$	−504 cal (g atom)$^{-1}$	536

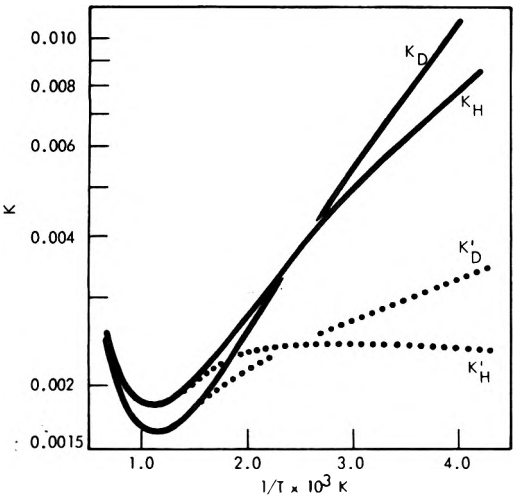

Figure 5. Extrapolation of K_H and K_D to lower temperatures using eq 14a and 14b and the parameters in Table I: (—) $q_0 = 1$; (· · · ·) $q_0 = 2$.

$$K_H = Nq_0 \left[\frac{(1 + ae^{-(b/T)})}{(1 - e^{-(c/T)})^3}\right] e^{-|(\epsilon + 3Rc/2)/RT - \Phi_H|} \quad (16)$$

In eq 16, $\epsilon + 3Rc/2 = E^\circ_{H_M,0} - H^\circ_{H,0}$ is the energy per gram atom required to dissolve atomic hydrogen gas into the metal at absolute zero. The energy of formation of H_2 gas from atomic hydrogen gas at absolute zero and 1 atm pressure is

$$E^\circ_{H_2,0} - H^\circ_{H,0} = [RT\Phi_H]_{T=0} = -51\,633 \text{ cal (g atom)}^{-1}$$
$$E^\circ_{D_2,0} - H^\circ_{D,0} = -52\,535 \text{ cal (g atom)}^{-1} \quad (17)$$

The term ϵ is primarily the energy released upon establishing the electronic bond between the free hydrogen atom and the metal. This quantity ϵ (or $\epsilon - [RT\Phi_H]_{T=0}$ when using H_2 as the reference state) should be used in comparing the electronic properties of the metal with K_H as has been attempted by Ebisuzaki and O'Keefe.[2] The difference between this quantity ($\epsilon - [RT\Phi_H]_{T=0}$) and typically reported "excess enthalpies of solution"[2,3] is dependent upon parameters a, b, and c (eq 16) and may vary by several kilocalories per mole from metal-to-metal or over a temperature range of a few hundred degrees Kelvin.

The terms enclosed by the square brackets in eq 16 represent an enhancement of the hydrogen solubility due to the existence of thermally excitable energy states. It will be shown later (eq 24) that this is an increase in the entropy of solution. Their contribution to the magnitude of K_H is an enhancement by a factor of 4.83 at 1400 K. Were the shape of the potential well such that there existed a maximum at energy Rb ≈8 kcal between intersticies over which the hydrogen atom could freely translate as drawn by Ebisuzaki, and O'Keefe,[4] the number of energy levels (a) would approach infinity resulting in K_H being orders of magnitude larger than is observed.

The potential well for c (or θ_H) = 1676 ± 18 K is quite narrow being only 0.75 × 10^{-8} cm wide at 8.3 kcal mol^{-1} (2.4 $R\theta$) compared with the 1.7 × 10^{-8} cm center-to-center distance between octahedral intersticies in U–0.222 Mo alloy.[18] The overlap of vibrational wave functions for the 8.3-kcal states of two adjacent intersticies that are described by θ_H = 1676 K is too small to predict "tunneling" between intersticies. In the case of the curve fit for which $N = 3$, $q_0 = 2$, the term $(1 + 143e^{(8100/T)})$ is best explained on the basis of 143 electronic energy states, perhaps a conduction band, 16 kcal mol^{-1} (0.7 eV) above the electronic ground state for hydrogen dissolved in the metal. For this curve fit, the present model indicates no mechanism by which diffusion may occur. This fit also describes the case for the occupancy of tetrahedral intersticies in the bccub lattice where $N = 6$ and $q_0 = 1$.

In the case of the curve fit for $N = 3$ and $q_0 = 1$, the term $1 + ae^{-(b/T)}$ may be rewritten within experimental error (1%) as

$$1 + 20e^{-(4200/T)} = (1 + 4e^{-(3800/T)})^3 \quad (18)$$

Equation 18 may be interpreted as four additional energy levels at 7.55 kcal mol^{-1} above the minimum of the vibrational potential well for each vibrational degree of freedom. These additional vibrational states are in the appropriate energy range of activation energies of diffusion. These additional vibrational states imply a broadening of the vibrational potential energy well at approximately 7.55 kcal mol^{-1} above the minimum. Figure 6 shows a single vibrational potential well for hydrogen in the metal constructed from two parabolic potential functions described by Einstein temperatures θ and θ', respectively, and separated at their minimums by the energy $R\Delta$. The energy levels and wave functions for this system are approximated by those for each potential function taken separately. Values of θ' = 350 K and Δ = 3750 K were chosen such that eq 19a and 19b were correct within 1% over the temperature range from 700 to 1300 K using θ = 1684 K, a = 20, and b = 4200 K from Table I. For H

$$\frac{(1 + ae^{-(b/T)})^{1/3}}{2\sinh\dfrac{\theta}{2T}} = e^{-(\theta/2T)} + e^{-(3\theta/2T)} + \frac{e^{-(\Delta/T)}}{2\sinh\dfrac{\theta'}{2T}} \quad (19a)$$

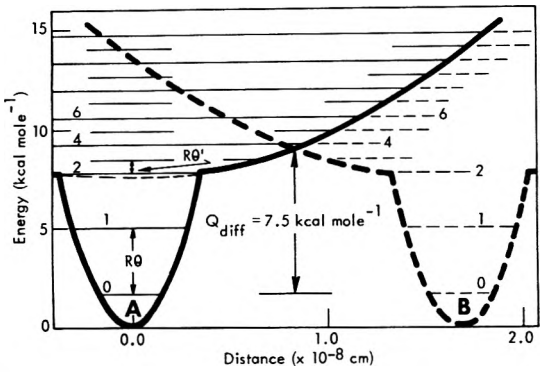

Figure 6. Vibrational potential well and energy levels for U–0.222 Mo alloy. Potential well A represents an occupied site and potential well B represents an adjacent unoccupied site.

For D

$$\frac{(1 + ae^{-(b/T)})^{1/3}}{2 \sinh \frac{\theta}{2\sqrt{2}T}} = e^{-(\theta/2\sqrt{2}T)} + e^{-(3\theta/2\sqrt{2}T)} + e^{-(5\theta/2\sqrt{2}T)} + \frac{e^{-(\Delta/T)}}{2 \sinh \frac{\theta'}{2\sqrt{2}T}} \quad (19b)$$

The terms to the right of the equal sign in eq 19a represent the partition function for potential well A shown in Figure 6, and the cube of this partition function may be substituted in place of all a, b, and c terms in eq 16. The value of Δ is independent of the mass of the hydrogen isotope so it must be attributed to some characteristic of the metal lattice. Note that the wave functions for the higher energy states overlap their complimentary states in the vibrational potential well of neighboring intersticies (B) such that vibrational overlap integrals (transition probabilities) can be calculated for diffusion. These vibrational transition probabilities are identical with the Franck–Condon factors (selection rules) that are commonly used by spectroscopists to describe radiative and nonradiative transitions between vibrational manifolds of different electronic states in complex molecules.[19-21] Comparing harmonic oscillator wave functions for a potential well characterized by $\theta' = 350$ K from Pauling and Wilson[22] with Figure 6 indicates that only such functions having even symmetry (even-numbered levels in Figure 6) would have a nonzero transition probability. The lowest energy state for which the wave function has both even symmetry and sufficient width to overlap its compliment from the adjacent intersticie is energy level number 4 (Figure 6), which is 7.5 kcal mol^{-1} above the vibrational ground state. Such a model for diffusion would be quite similar to that of Flynn and Stoneham[23] with the exception that the vibrational and electronic wave functions for hydrogen in the metal would be separated. The interaction perturbation resulting in the change of sites would be one that generates a translation of the electronic part of the wave function by one lattice site. Thus, this model predicts an activation energy for diffusion (Q_{diff}) of 7.5 kcal mol^{-1}. The only data reported in the literature that may be compared to the Q_{diff} for U–0.222 Mo alloy is for a similar alloy, U–0.166 Nb–0.056 Zr, for which $Q_{diff} = 7.3 \pm 0.4$ kcal mol^{-1}.[14] The compatibility of the data fit for $N = 3$ and $q_0 = 1$ (Table I) with interstitial diffusion argues strongly for the selection of this description as the correct expression for K_H in U–0.222 Mo alloy.

Solving eq 10 for eq 6 yields an expression for the Gibbs free energy change per gram atom hydrogen ($\frac{1}{2}F_{H_2,P,T} - H^\circ_{H,0}$) required for taking atomic hydrogen gas from 0 K and 1 atm pressure to the diatomic gas state described by P_{H_2} and T. At equilibrium, this is identical with the Gibbs free energy change per gram atom ($F_{H_M,T} - H^\circ_{H,0}$) required for taking atomic hydrogen from 0 K at 1 atm pressure to the dissolved state in the metal described by [H_M] and T. This Gibbs free energy change is expressed below within the approximations described in eq 16.

$$F_{H_M,T} - H^\circ_{H,0} = \epsilon + \tfrac{3}{2}Rc - RT \ln Nq_0 - RT \ln \left[\frac{1 + ae^{-(b/T)}}{(1 + e^{-(c/T)})^3}\right] + RT \ln \left[[H_M]\left(\frac{e^{-\xi}}{1 + \frac{[H_M]}{N}}\right)\right] \quad (20a)$$

$$F_{H_M,T} - H^\circ_{H,0} = F^\circ_{H_M,T} - H^\circ_{H,0} + RT \ln ([H_M]\gamma) \quad (20b)$$

The term $\gamma = e^{-\xi}[1 + ([H_M]/N)]^{-1}$ is an activity coefficient that approaches unity as [H_M] approaches zero. Thus, for infinite dilution, $F^\circ_{H_M,T}$ is the standard Gibbs free energy per gram atom H_M shown in eq 1.

The standard entropy ($S^\circ_{H_M,T}$) and standard enthalpy ($H^\circ_{H_M,T} - H^\circ_{H,0}$) of solution can be calculated from the thermodynamic relationships

$$F^\circ_{H_M,T} - H^\circ_{H,0} = H^\circ_{H_M,T} - H^\circ_{H,0} - TS^\circ_{H_M,T} \quad (21)$$

and

$$S^\circ_{H_M,T} = -\left[\frac{\partial F^\circ_{H_M,T} - H^\circ_{H,T}}{\partial T}\right]_P \quad (22)$$

yielding

$$H^\circ_{H_M,T} - H^\circ_{H,0} = Rb\left(\frac{e^{b/T}}{a} + 1\right)^{-1} + 3Rc(e^{c/T} - 1)^{-1} + \epsilon + \tfrac{3}{2}Rc \quad (23)$$

and

$$S^\circ_{H_M} = R \ln Nq_0 + R \ln (1 + ae^{-(b/T)}) + \frac{Rb}{T}\left(\frac{e^{b/T}}{a} + 1\right)^{-1} + 3R \ln (1 - e^{-c/T}) - \frac{3Rc}{T}(e^{c/T} - 1)^{-1} \quad (24)$$

Equations 20, 23, and 24 can now be used to calculate these thermodynamic functions based on the experimentally determined parameters. The differences between these values and similar values for diatomic hydrogen gas[15] are plotted in Figures 7 and 8. The free energy function without the contribution from the thermally excited states is also plotted in Figure 7 to emphasize the role of thermally excited states in the solubility of hydrogen in this alloy. At low temperatures, the increase with temperature of the entropy and the decrease with temperature of the enthalpy of solution relative to that for H_2 at the same temperature is dominated by the temperature dependence of $S^\circ_{H_2,T}$ and $H^\circ_{H_2,T} - H^\circ_{H,0}$, i.e., the gas phase thermodynamic functions. At higher temperatures, the temperature-dependent parts of eq 20, 23, and 24, i.e., the thermodynamic functions of hydrogen in the solid phase, change markedly with

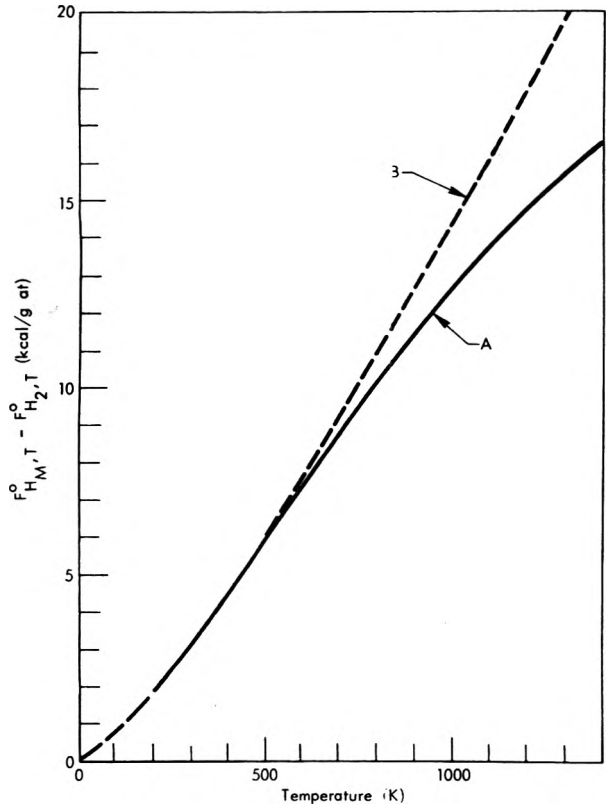

Figure 7. The standard free energy per gram atom hydrogen in U–0.222 Mo alloy referenced to diatomic hydrogen gas at the same temperature (Curve A). Curve B gives the same function without the contribution from thermally excitable energy states. The broken line below 200 K indicates that no attempt was made to consider the ortho–para effects on $F^{\circ}_{H_2,T}$.

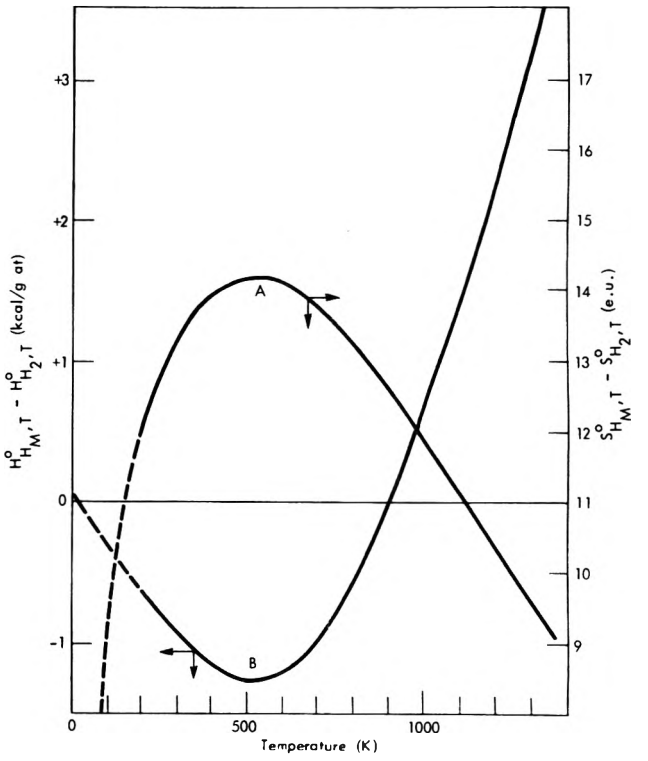

Figure 8. The standard entropy (curve A) and standard enthalpy (curve B) (per gram atom hydrogen in the metal) using the same functions for diatomic hydrogen gas at the same temperatures as the reference state. The broken line below 200 K indicates that no attempts were made to consider the ortho–para effects on the reference state.

increasing temperature resulting in the maximum in the entropy and minimum in the enthalpy shown in Figure 8.

VIII. Conclusions

The solubility of hydrogen and deuterium in the bccub alloy U–0.222 Mo at infinite dilution has been determined over the temperature range from 700 to 1350 K and a model presented describes the measurements within ±1% over the full temperature range of the measurements. For this alloy, the model implies that (1) there are three sites for hydrogen per metal atom, (2) the enthalpy of formation of hydrogen in the metal from atomic hydrogen is −51.57 kcal/g atom hydrogen at 0 K, (3) the enthalpy of formation of the electronic bond between hydrogen and the metal is −53.04 kcal/g atom hydrogen, (4) the electronic ground state of the metal hydrogen system is nondegenerate, and (5) the vibrational part of the metal–hydrogen bond can be described by a Einstein temperature of 1684 K.

For metals in general, thermally excitable energy states of hydrogen in the metal and the free energy function for H_2 contribute substantially to the temperature dependence of K_H. It would be very unusual for any metal to have a linear relationship between ln K_H and $1/T$ over a very wide temperature range.

Acknowledgments. The author is indebted to E. A. Larson who carried out the preliminary experiments, R. L. Jackson who assisted in the data analysis, and J. B. Condon for many helpful discussions. This work was carried out at the Oak Ridge Y-12 Plant for the United States Energy Research and Development Administration, Oak Ridge Operations, under Contract No. W-7405-eng-26.

References and Notes

(1) W. M. Muller, J. P. Blackledge, and G. G. Libowitz, "Metal Hydrides", Academic Press, New York, N.Y., 1968.
(2) Y. Ebisuzaki and M. O'Keefe, "Progress in Solid State Chemistry", Vol. 4, H. Reiss, Ed., Pergamon Press, New York, N.Y., 1968, Chapter 5.
(3) R. B. McLellan, "Treatise on Material Science and Technology", Vol. 5, H. Herman, Ed., Academic Press, New York, N.Y., 1974, Chapter 1.
(4) Y. Ebisuzaki, W. J. Kass, and M. O'Keeffe, *J. Chem. Phys.*, **46**, 1373 (1967).
(5) M. Hansen, "Constitution of Binary Alloys", 2nd ed, McGraw-Hill, New York, N.Y., 1958, p 978.
(6) R. P. Elliot, "Constitution of Binary Alloys", First Supplement, McGraw-Hill, New York, N.Y., 1965, p 634.
(7) P. E. Repas, R. H. Goodenow, and R. H. Heheman, Report No. ARMA CR 63-02/1 (F) (1973) (available through the National Technical Information Service, Springfield, Va.).
(8) J. B. Condon and E. A. Larson, *J. Chem. Phys.*, **59**, 855 (1973).
(9) C. E. Holcombe, Jr., and G. L. Powell, *Am. Ceram. Soc. Bull.*, **52**, 858 (1973).
(10) R. H. Fowler and E. A. Guggenheim, "Statistical Thermodynamics", Cambridge University Press, London, 1939, p 554.
(11) J. B. Condon, *J. Phys. Chem.*, **79**, 42 (1975).
(12) J. R. Lacher, *Proc. R. Soc. London, Ser. A.*, **161**, 525 (1937).
(13) D. R. Stull and H. Prophet, *Natl. Stand. Ref. Data Ser., Natl. Bur. Stand.*, **No. 37**, (1971).
(14) T. B. Douglas and C. W. Beckett, National Bureau of Standards Report No. 10904, 260 and 296 (1972).
(15) L. Haar, A. S. Friedman, and C. W. Beckett, *Natl. Bur. Stand. (U.S.), Monogr.* **No. 20**, 9 (1961).
(16) G. L. Powell and J. B. Condon, *Anal. Chem.*, **45**, 2349 (1973).
(17) G. Hertzberg, *J. Mol. Spectrosc.*, **33**, 147 (1970).
(18) A. S. Wilson and R. E. Rundle, *Acta Crystallogr.*, **2**, 126 (1949).
(19) L. Pauling and E. B. Wilson, "Introduction to Quantum Mechanics", McGraw-Hill, New York, N.Y., 1935, Chapter 11.
(20) G. W. Robinson and R. P. Frosch, *J. Chem. Phys.*, **37**, (1962).
(21) W. Siebrand, *J. Chem. Phys.*, **46**, 440 (1967).
(22) L. Pauling and E. B. Wilson, ref 19, p 75.
(23) C. P. Flynn and A. M. Stoneham, *Phys. Rev. B.*, **1**, 3966 (1970).

Investigation of Thin Surface Films and Adsorbed Molecules Using Laser Raman Spectroscopy[1]

Michael L. Howe, Kenneth L. Watters,*[2a] and Robert G. Greenler*[2b]

Laboratory for Surface Studies of the University of Wisconsin—Milwaukee, Milwaukee, Wisconsin 53201
(Received September 24, 1975)

Publication costs assisted by the Petroleum Research Fund

The sensitivities are determined experimentally for two methods of obtaining the Raman spectra of thin films on solid surfaces. The Raman spectrum of CCl_4 on high surface area silica (700 m^2/g) was obtained for surface coverages down to 4% of a monolayer. The Raman reflection method was used to obtain the spectrum of a polystyrene film on a silver mirror. With this system, a polystyrene spectrum was obtained for film thicknesses down to about 50 Å.

Introduction

Raman spectroscopy produces rather direct information on the geometric arrangement of atoms within a molecule and the nature of the bonds between atoms. When the technique is applied to molecules which are adsorbed on a solid surface, one might expect to obtain the same kind of structural information about the adsorbed molecules and to deduce some information about the bonding to the surface. A number of Raman studies have been reported of adsorption on high area powders[3-11] and a system has been described for obtaining the Raman spectrum of a thin layer on a bulk metal surface.[12] In most cases which have been reported for adsorption on high surface area oxides, the surface coverage has not been determined. So, although a strong Raman spectrum of the adsorbate may have been recorded, detection limits in terms of measured surface coverages are not known. In the reflection-Raman experiment,[12] the optimum design of the sample apparatus was carefully considered but the experimental determination of the sensitivity of the method was rather crude.

The purpose of the work reported here is to obtain an experimental measure of the sensitivity of these two methods by determining a minimum surface concentration which is detectable using standard laser-Raman equipment.

Experimental Section

The spectrometer used in this work is a Spex Ramalog 1401, 0.75 m, Czerny-Turner double monochromator used with an ITT Model FW-130 photomultiplier tube with an S-20 response. The tube is cooled to −20 °C by a thermoelectric cooler. In this work the detector system is operated in a photon-counting mode. The laser is a Coherent Radiation argon-ion gas laser. The 488-nm line gave the most intense spectra and was used in all of the spectra shown here. The laser power in this line was measured to be about 75 mW at the sample.

CCl_4-on-Silica Scattering Experiment. In this experiment we obtained the Raman spectrum of CCl_4 adsorbed on silica at a number of different pressures of CCl_4 vapor. The coverages at the different pressures were then determined from an adsorption isotherm which was established gravimetrically.

The silica gel used was type 923, supplied by W. R. Grace and Co., Davison Chemical Division. It is reported by the manufacturer to have a particle size of 100–200 mesh, a specific surface area of 700 m^2/g, and an average pore diameter of 22 Å. The CCl_4 used was spectrophotometric grade from Fisher Scientific Co. To observe the Raman spectra of adsorbed CCl_4, we put a small amount of the silica in the sample tube attached to the vacuum system as shown in Figure 1. The sample was prepared for CCl_4 adsorption by evacuating at 10^{-6} Torr for about 20 h using a cold-trapped oil-diffusion pump. The state of the surface after this treatment is poorly defined, but its description is not the object of this work.

Various pressures of CCl_4 were produced by controlling the temperature of a reservoir of CCl_4 connected to the vacuum system. The pressure is related to the reservoir temperature by the Clausius–Clapeyron expression with constants taken from the International Critical Tables.

The following procedure was used to establish varying coverages of CCl_4 on the silica gel from varying CCl_4 vapor pressure in the system. With the valve above the CCl_4 reservoir closed, the sample was pumped down to 10^{-6} Torr. The sample was then isolated from the rest of the system. With a liquid nitrogen bath surrounding the CCl_4 reservoir, the volume above the solid CCl_4 was pumped down to 10^{-5} Torr. The valves to the pump and the reservoir were then closed. The liquid nitrogen bath was replaced by a bath creating the coldest of the desired temperatures, the valves to the reservoir and sample were opened, and the system was then allowed to equilibrate. The equilibrium between the vapor and the liquid (or solid, as was the case from −78 to −23 °C) is established in a few seconds. The CCl_4 reservoir was opened to the silica sample for about 2.5 h to assure an adsorbate–adsorbent equilibrium. At this point the valves to reservoir and sample were closed and the Raman spectrum was recorded. Subsequent coverages were accomplished by changing the temperature bath and then opening the sample and reservoir valves with no intermediate pumping.

The following temperature baths were used: dry ice and acetone, −78 °C, $p < 0.1$ Torr; chloroform (slush bath), −63.5 °C, $p = 0.3$ Torr; diethylamine (slush bath), −50 °C, $p = 0.9$ Torr. Higher temperatures were produced by a thermoelectric immersion cooler.

The sample tube shown in Figure 1 is a horizontal tube of 2 mm i.d. illuminated from below by the focused laser

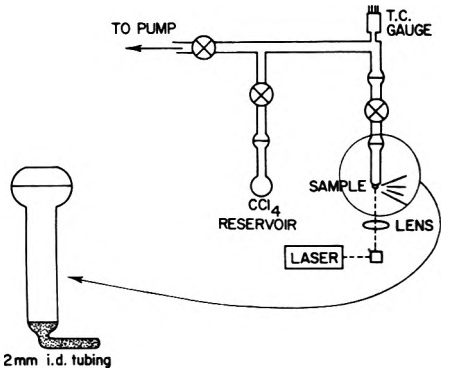

Figure 1. Sample cell and gas handling apparatus for recording the Raman spectrum of CCl_4 adsorbed on silica.

beam. The 90° scattered light is focused on the monochromator entrance slit.

The Raman spectra of the silica gel sample after exposure to various pressures of CCl_4 are shown in Figure 2. Under the operating conditions used here, it appears that the minimum vapor pressure yielding a detectable CCl_4 spectrum is about 0.3 Torr. The silica gel spectrum with zero CCl_4 coverage is also shown. There is a broad band in the 490-cm^{-1} region. Some spurious bands result from plasma lines leaking through the narrow bandpass filter. Figure 3 is the spectrum of pure liquid CCl_4 in the sample cell.

Two aspects of the spectra are of interest. The relative peak heights in the spectrum of the adsorbed CCl_4 are different than in the spectrum of liquid CCl_4. In particular, the 460-cm^{-1} peak is smaller, relative to the 314- and 218-cm^{-1} peaks. The second aspect is that the bands due to the adsorbed CCl_4 all appear to be shifted about 4 cm^{-1} higher in frequency.

The silica gel used in this experiment is in a class of porous adsorbents described as microporous. This class is characterized by having a Langmuir adsorption isotherm. The isotherm for this sample was determined in a separate experiment, in which the silica gel and CCl_4 were treated exactly as before to obtain exposures to various pressures of CCl_4 vapor. Each time, after a 2.5-h exposure, a valve to the sample chamber was closed and the sample chamber was removed and weighed. From the weighings, the amount of CCl_4 per gram of silica gel for each pressure was calculated. Figure 4 shows the resulting isotherm from which the monolayer coverage is seen to be about 0.25 cm^3/g. The minimum detectable coverage (at 0.3 Torr) represents about 0.01 cm^3/g, corresponding to a coverage of about 4% of a monolayer.

Polystyrene-on-Silica Reflection Experiment. The theory for the Raman reflection experiment has been described previously.[12] Briefly, in order to maximize the intensity of the Raman spectrum of a thin film on a reflecting metal surface, two conditions must be considered.

(1) We must choose the angle of incidence for the laser beam on the reflecting metal surface which optimizes the Raman excitation. The physical significance of the correct angle is that, at that angle, the incident and reflected beams interfere to produce the maximum amplitude of the standing electric wave in the thin film.

(2) We must choose the appropriate range of collection angles for the Raman-scattered light. The physical significance of this choice is that, at the appropriate angle, the direct Raman-scattered light and the scattered light which has been reflected from the mirror surface interfere con-

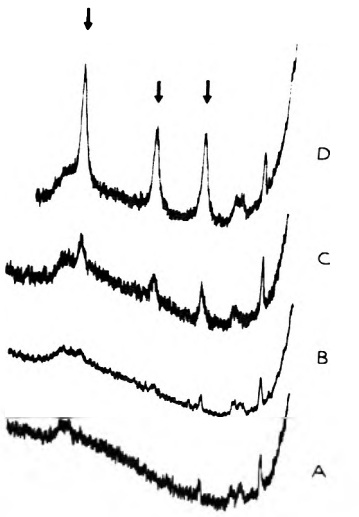

Figure 2. Raman spectra for various coverages of CCl_4 on silica gel. Bands marked with arrows are due to CCl_4 and occur at 464, 318, and 222 cm^{-1}. Instrumental parameters common to all spectra include: resolution 5 cm^{-1}; scan speed 25 cm^{-1}/min; photon counting level 3 × 10^3 Hz: (A) silica gel at 10^{-6} Torr; period setting = 5; (B) silica gel under 0.3 Torr of CCl_4 vapor; period setting = 10; (C) silica gel under 1.0 Torr of CCl_4 vapor; period setting = 5; (D) silica gel under 4.0 Torr of CCl_4 vapor; period setting = 5.

Figure 3. Spectrum of liquid CCl_4 in the sample cell: spectral resolution 5 cm^{-1}; scan speed 25 cm^{-1}/min; photon counting level 1 × 10^6 Hz; period 5.

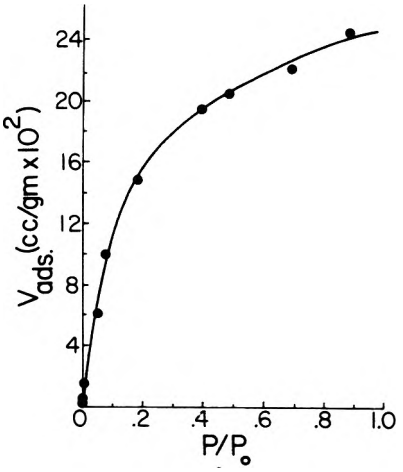

Figure 4. Gravimetric isotherm determined for CCl_4 adsorption on silica gel. P_0 is the CCl_4 vapor pressure at room temperature (115 Torr) and P is the vapor pressure of CCl_4 above the adsorbent.

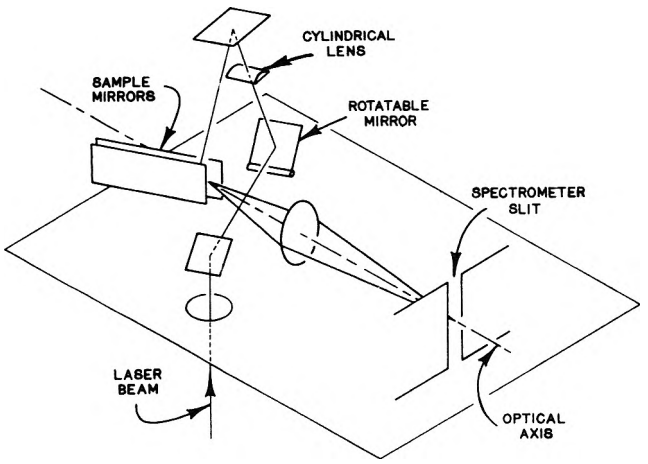

Figure 5. Schematic diagram of the reflection-Raman sample system used to record spectrum of polystyrene on silver mirrors.

structively to give a maximum in the angular distribution of Raman-scattered light. The system is shown schematically in Figure 5. The cylindrical lens focuses the laser beam to a line about 3 mm long where it enters the aperture between the sample mirrors which are spaced 0.06 mm apart. The laser beam is multiply reflected between the mirrors with an angle of incidence of 70°. The central ray of the collected, scattered light makes an angle of 50° with the mirror normal. The mirror aperture is imaged on the monochromator entrance slit with a magnification of 8, slightly overfilling the slits set at a width of 600 μm. (See ref 12 for details of the imaging geometry. The system used here is the same as described in that reference.)

The sample film is prepared by spraying a solution of polystyrene in benzene on the mirrors. The mirrors are glass plates coated with evaporated silver films. A measured volume of polystyrene solution of known concentration is sprayed with an artist's air brush. The reproducibility of the spraying is improved by placing the mirrors in the center of an area about 25 cm square and attempting to uniformly cover the layer area with a raster spray pattern which requires several passes to deposit the measured volume of solution. An effective thickness of the layer is calculated from the volume of the solution, its concentration, the area covered, and the density of polystyrene. The polystyrene was supplied by W. R. Grace and Co., Formpac Division, and the benzene was Fischer, spectrophotometric grade.

Figure 6 shows four spectra. Spectrum A is that of the silver mirrors with nothing deposited. Spectrum B is the background after being sprayed with clean benzene (which quickly evaporates) to check for the presence of a spectrum due to residual benzene or contaminants in the benzene. Spectra C and D result from polystyrene layers of 50 and 200 Å, respectively. For comparison, Figure 7 shows the Raman spectrum of bulk polystyrene. We found it difficult to obtain spectra of reproducible intensities (within a factor of 2) in the 50–200-Å range but typically we could detect the 1005-cm^{-1} line in a layer 50-Å thick.

Discussion and Summary

It is evident from the CCl_4 experiment that it is feasible to study surface species on high area adsorbents down to submonolayer coverages. In the case of CCl_4 on silica, the adsorbent does not dominate the spectrum for concentrations as low as 4% of a monolayer coverage.

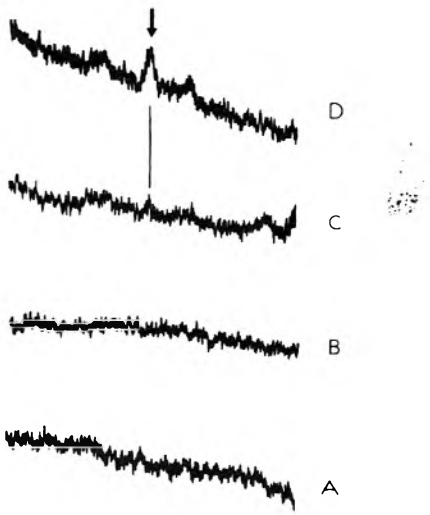

Figure 6. Raman spectra of polystyrene on silver mirrors obtained by reflection. Band marked with an arrow is due to polystyrene at 1005 cm^{-1}. Instrumental parameters include: resolution 15 cm^{-1}; scan speed 25 cm^{-1}/min; photon counting level 3×10^2 Hz; period 50: (A) spectrum of clean silver mirrors; (B) spectrum of silver mirrors, sprayed with benzene, after benzene has evaporated; (C) spectrum of 50 Å layer of polystyrene on silver mirrors; (D) spectrum of 200 Å layer of polystryene on silver mirrors.

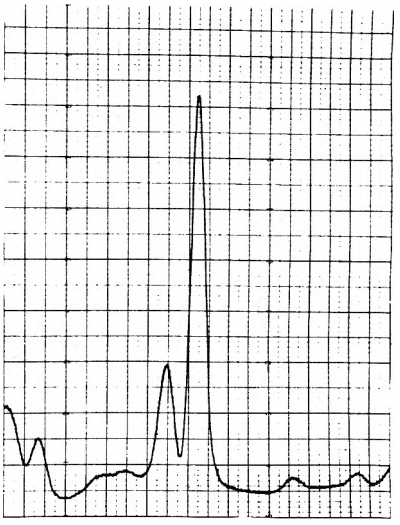

Figure 7. Spectrum of solid polystyrene. Spectrometer settings are: resolution 15 cm^{-1}; scan speed 25 cm^{-1}/min; photon counting level 3×10^5 Hz; period 5.

In this work the Raman reflection technique seems to have a sensitivity limit of about 50-Å thick film. With the current instrumentation this experimental approach would appear to be applicable to problems where layers are tens to hundreds of ångströms thick. There may be such applications in studying passivation layers used to prevent corrosion, films formed on electrodes in electrolytic cells,[13] or in biologically produced layers (such as membranes).[14]

The Raman reflection technique, as used here, appears to be an order of magnitude less sensitive than is needed to study monolayer concentrations. It is possible, however, that systems which produce a resonance Raman effect will have Raman scattering levels sufficient to observe spectra of monolayer coverages using this technique.

References and Notes

(1) This work was supported in part by the National Science Foundation (R.G.G.), in part by the donors of the Petroleum Research Fund administered by the American Chemical Society (K.L.W.), and in part by a research grant from the Graduate School, University of Wisconsin—Milwaukee.
(2) (a) Department of Chemistry, University of Wisconsin—Milwaukee. (b) Department of Physics, University of Wisconsin—Milwaukee.
(3) G. Karagounis and R. Issa, *Nature (London)*, **195**, 1196 (1962); *Z. Electrochem.*, **66**, 874 (1962).
(4) E. V. Pershina and Sh. Sh. Raskin, *Dokl. Akad. Nauk. SSSR*, **150**, 1022 (1963).
(5) P. J. Hendra and E. J. Loader, *Nature (London)*, **216**, 789 (1967).
(6) P. J. Hendra and E. J. Loader, *Nature (London)*, **217**, 637 (1968).
(7) R. O. Kagel, *J. Phys. Chem.*, **74**, 4518 (1970).
(8) P. J. Hendra and E. J. Loader, *Trans. Faraday Soc.*, **67**, 827 (1971).
(9) N. Sheppard, A. H. Hardin, T. A. Edgerton, and Y. Kogirowski, *Chem. Commun.*, **887** (1971).
(10) E. Bueckler and J. Turkevich, *J. Phys. Chem.*, **76**, 2325 (1972).
(11) C. L. Angell, *J. Phys. Chem.*, **77**, 222 (1973).
(12) R. G. Greenler and T. L. Slager, *Spectrochim. Acta, Part A*, **29**, 193 (1973).
(13) M. Fleischmann, P. J. Hendra, and A. J. McQuillan, *Chem. Phys. Lett.*, **26**, 163 (1974).
(14) L. Rimai, R. G. Kilponen, and D. J. Gill, *Biochem. Biophys. Res. Commun.*, **41**, 492 (1970).

An Investigation of Some Aspects of the Chemisorption of Carbon Monoxide on a Nickel Surface

Peter Politzer* and Stephen D. Kasten

Department of Chemistry, University of New Orleans, New Orleans, Louisiana 70122

(Received June 20, 1975)

The chemisorption of carbon monoxide on a nickel surface was investigated by computing iterative extended-Hückel wave functions for systems consisting of one CO molecule and one to nine Ni atoms in various geometrical arrangements. It was found that the number of Ni atoms involved in the interaction can be as much of a factor in determining the C–O frequency as whether the system has a linear or a bridged structure. There is a considerable transfer of electronic charge between the carbon and the nickel atoms; the carbon loses σ charge but gains π charge. These two effects occur to nearly equal extents, so that there is very little net transfer of charge between the CO and the Ni atoms. The various properties calculated for the Ni–CO systems are observed to initially change significantly as the number of Ni atoms increases, but then to level off. It appears that the interaction can be regarded as involving primarily the nearest neighbors, and in the same plane, of the site of attachment.

Introduction

This investigation was undertaken with the purpose of elucidating three specific aspects of the chemisorption of carbon monoxide on nickel. (1) What is the relationship between the structures of the Ni–CO surface complexes and the observed C–O stretching frequencies? (2) What transfers of electronic charge take place between the nickel atoms and the carbon monoxide? (3) How localized are the interactions? How many nickel atoms must be regarded as being involved to a significant extent in an interaction with a given CO molecule? Each of the points will be discussed in turn, following a brief description of the methods that were used in this study.

Procedure

Our approach was to compute semiempirical molecular orbital wave functions, using the iterative extended-Hückel method, for the systems Ni_n–CO, where n ranged from 1 to 9. The computational procedure was basically similar to that used previously to investigate the increase of the C–O stretching frequency which accompanies the chemisorption of carbon monoxide on nickel oxide.[1] Each molecular orbital, ψ_i, is written as a linear combination of the occupied valence orbitals on the various atoms:

$$\psi_i = \sum_{jk} C_{ijk}\phi_{jk} \qquad (1)$$

where ϕ_{jk} is atomic orbital j on atom k. All overlap integrals are evaluated exactly. Thus, interactions between all atoms are being taken into account. Slater-type atomic orbitals are used, the exponents being the same as in our earlier work:[1] C, 2s: 1.6083; C, 2p: 1.5679; O, 2s: 2.2458; O, 2p: 2.2266; Ni, 3d: 2.960; Ni, 4s: 1.473. The diagonal elements of the Hamiltonian matrix are set equal to the respective valence orbital ionization energies,[2] written as functions of the charges on the atoms and modified by the addition of a Madelung-type term to take account of electrostatic interactions between the atoms.[3] Atomic charges are computed by means of a population analysis over orthogonalized basis orbitals.[4] The off-diagonal elements of the Hamiltonian matrix are approximated using the Cusachs formula.[5] The final wave functions are obtained by iterating over the atomic charges until self-consistency to 0.0001 electron units is achieved for each charge.

The valence orbital ionization energies used for the nickel atoms were those corresponding to the $3d^9\ 4s^1$ configuration. This is appropriate for two reasons. First, the energy of this configuration, obtained as the weighted mean of all the multiplet energies,[2] is about 9000 cm^{-1} *lower* than that of the $3d^8\ 4s^2$ configuration.[2,6] Second, it is well-established

that the 3d band of solid nickel contains approximately 9.4 electrons per nickel atom.[7] Thus, the $3d^9\ 4s^1$ configuration is more suitable than the $3d^8\ 4s^2$ for the purpose of constructing a model of a nickel surface.

A total of 13 different Ni–CO systems was included in this investigation. They can be classified as "linear structures", in which the CO is bonded to one specific Ni atom, and "bridged structures", in which it is bonded equally to two or more Ni atoms. The various systems are shown in Figures 1 and 2. Nickel crystallizes with a face-centered cubic lattice, the shortest Ni–Ni distance being 2.492 Å.[8] All of the structures in Figures 1 and 2 correspond to the CO molecule being chemisorbed at a site on the (100) face. For the linear structures, the Ni–C bond length was taken to be the same as in $Ni(CO)_4$, 1.82 Å.[8] In the case of the bridged systems, two different values were used for the distance from the carbon to the surface plane of nickel atoms. One was again 1.82 Å; the other was 1.35 Å, which is in the neighborhood of the optimum values found for this distance in some recent CNDO calculations by Blyholder.[9] (The corresponding Ni–C bond lengths are 2.53 and 2.22 Å, respectively.) The computations for the bridged structures were carried out for both distances. In all cases, the C–O bond length was taken to be 1.15 Å, the same as in $Ni(CO)_4$.[8]

It is widely believed that CO bonds to a nickel surface through its carbon atom. In a few instances, however, the possibility of the bonding being through the oxygen was examined. Using both the sum of the occupied molecular orbitals' energies and also the total overlap population as criteria of stability,[1,10,11] bonding through the carbon was invariably found to be more stable.

C–O Stretching Frequencies

A widely used experimental approach to the problem of determining the structures of the surface complexes formed during the adsorption of CO on nickel has been infrared spectroscopy.[12,13] The absorption bands generally attributed to CO chemisorbed on nickel fall into two regions (their exact positions depending upon the state of the adsorbent and other experimental conditions). There is at least one band in a relatively narrow region between approximately 2035 and 2080 cm^{-1}, and there are one or more bands in a much broader region from about 1830 to 1970 cm^{-1}. By analogy with the transition metal carbonyls, the bands above 2000 cm^{-1} have often been assigned to structures of the linear type, while the bands below 2000 cm^{-1} have been attributed to bridged-type structures.[13,14] These assignments have been questioned, however,[13,15] especially in view of the discovery that some metal carbonyls do have linear CO ligands with frequencies well below 1900 cm^{-1}.[16] Also, the C–O stretching frequencies in carboxyhemoglobin and some other porphyrin carbonyl complexes, in which the CO is certainly not in a bridging form, are in the range 1950–1970 cm^{-1}.[17]

Since one of our goals in this work is to elucidate the structures of the surface complexes which result in the observed infrared bands, we need to be able to determine vibration frequencies from our extended-Hückel wave functions. We do this by taking the calculated C–O overlap population as a measure of the C–O force constant, which can then be related to the frequency. The overlap population, P, between atoms k and k' is defined as

$$P_{kk'} = \sum_i \sum_{jk} \sum_{j'k'} N_i C_{ijk} C_{ij'k'} \int \phi_{jk} \phi_{j'k'}\, d\tau \qquad (2)$$

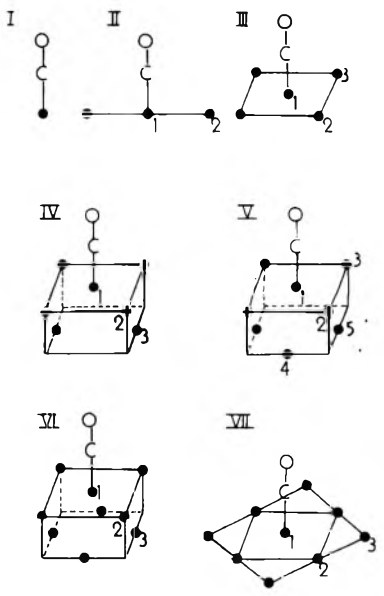

Figure 1. The "linear" structures which were included in this work. The black circles represent Ni atoms; the nonequivalent ones are numbered to permit later identification. In each structure, the distance between Ni,1 and Ni,2 is 2.49 Å. In IV–VI, the distance between the horizontal planes is 1.76 Å.

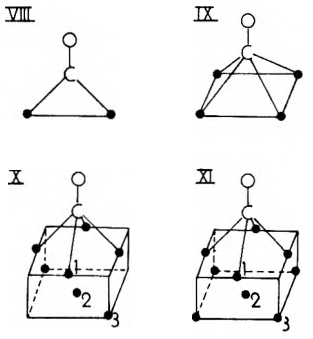

Figure 2. The "bridged" structures which were included in this work. The black circles represent Ni atoms; the nonequivalent ones are numbered to permit later identification. The shortest Ni–Ni distance in each horizontal plane is 2.49 Å. The distance between the horizontal planes X and XI is 1.76 Å.

N_i = number of electrons in ψ_i. The overlap population has often been used successfully as an indication of the strength of a given bond in a series of different systems, and has been correlated with such properties as force constants, vibration frequencies, and dissociation energies.[1,18]

In order to test the validity of using the C–O overlap population as a measure of the force constant, the experimentally determined C–O force constants of five molecules [CO, CO^+, CO_2, $Ni(CO)_4$, and H_2CO] were plotted against their calculated overlap populations.[19] Figure 3 shows that there is indeed a good correlation, extending over quite a wide range of values.

We feel justified therefore in using Figure 3, in conjunction with the C–O overlap populations of the various structures in Figures 1 and 2, to predict the C–O force constants, k_e, corresponding to each of these structures. The C–O stretching frequencies are then computed, using the harmonic oscillator approximation, by means of the formula

$$\omega_e = \frac{1}{2\pi c}\sqrt{\frac{k_e}{\mu}} \qquad (3)$$

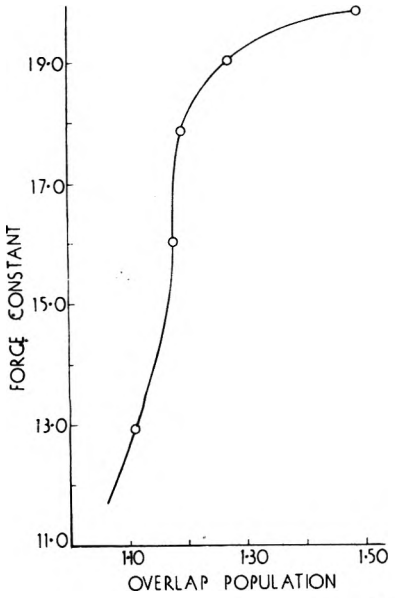

Figure 3. The relationship between the experimentally determined C–O force constants (in mdyn/Å) and the calculated C–O overlap populations for the molecules H_2CO, CO_2, $Ni(CO)_4$, CO, and CO^+ (in order of increasing force constants).

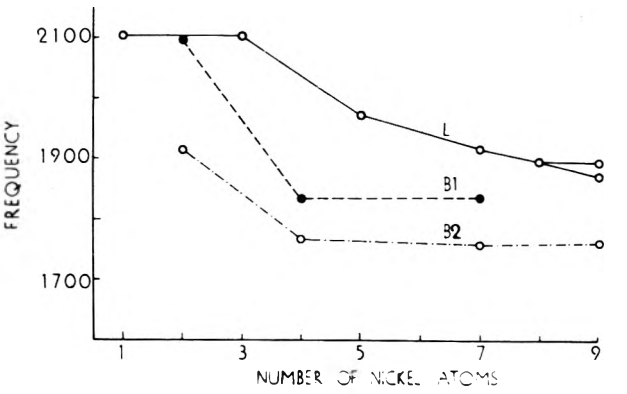

Figure 4. The calculated C–O stretching frequencies in cm^{-1} for the systems shown in Figures 1 and 2. These results do *not* include anharmonicity corrections. The points labeled L correspond to the linear structures (Figure 1), while those labeled B1 and B2 represent the bridged systems (Figure 2). B1 corresponds to the CO being farther from the surface plane of Ni atoms, B2 to the CO being closer. The upper and lower points for nine Ni atoms on the L graph are for structures VI and VII, respectively.

c = speed of light and μ = reduced mass of CO. The results are presented in Figure 4. When comparing these calculated values with those obtained experimentally, the former should be corrected for anharmonicity effects. Based on the anharmonicities observed for CO, CO^+, and $Ni(CO)_4$,[19] the correction is probably about 30 cm^{-1}, which should be subtracted from the results in Figure 4.[20]

The calculated frequencies are seen to be in the right general region of the spectrum, and as anticipated, the bridged structures tend to have lower values than the linear ones. However we do find linear systems with C–O frequencies considerably below 2000 cm^{-1}; in fact they reach the neighborhood of 1840 cm^{-1}. This is perhaps somewhat surprising, but certainly not completely unexpected in view of the previously mentioned experimental observations of low C–O frequencies in some linear carbonyl complexes.[16,17] More notable is the predicted existence of a bridged form with a frequency as high as about 2065 cm^{-1} (anharmonicity correction included). It is not known, of course, if the structure in question corresponds to anything that is actually to be found on a nickel surface; it may be that the Ni–C distance of 2.53 Å is too long to be realistic. When this distance is shortened to 2.22 Å (which is a considerable change), the predicted frequency drops to around 1890 cm^{-1}.[21]

The general pattern shown by the results in Figure 4, for *both* the linear and the bridged systems, is a sharp early decrease in the estimated C–O frequency as the number of nickel atoms increases, followed by a subsequent leveling off, in which there is relatively little further change. Figure 4 brings out the very important point that the *number* of nickel atoms involved in the interaction can be as much of a factor in determining the C–O frequency as whether the complex is of the linear or the bridged variety. Experimental support for this conclusion was recently reported by Moskovits, Ozin, and Hulse,[22] who determined infrared spectra for matrix-produced triatomic linear Ni–C–O and tetraatomic bridged Ni_2–CO. Quite similar frequencies were observed (1996 and 1969 cm^{-1}, respectively). These values differ somewhat from the results given in Figure 4 for structures I and VIII, B1, as could be expected in view of the approximate nature of the calculations and the possible differences between our input parameters, intended to correspond to a surface interaction, and those which would be appropriate for the matrix-produced species. The significant fact is that these two very simple carbonyls were found to have such similar frequencies, despite one of them being linear in structure and the other being bridged. This is in full qualitative agreement with the results for I and VIII, B1 in Figure 4, and with the conclusion that a difference in the basic structural form (linear vs. bridged) does not necessarily lead to a large difference in the C–O frequency.[23]

The leveling off which occurs for larger numbers of nickel atoms is of course closely related to the question of how localized are the interactions. It will be noted again in connection with other calculated properties.

In order to permit a more detailed analysis of the C–O overlap populations in the various systems, they have been broken down into the σ and π contributions (Table I). These should be compared with the corresponding values computed for free CO, also given in the table, to see the effects of the interactions with the nickel atoms.

The results show a definite pattern, and can readily be summarized. The σ overlap populations are somewhat greater than in free CO, and are remarkably uniform. They show almost no dependence on the number of nickel atoms, nor is there much difference between the linear and the bridged forms. The π overlap populations, on the other hand, are all considerably less than in free CO, and they initially decrease significantly as the number of nickel atoms increases. This decrease levels off after five Ni atoms for the linear structures, and after four for the bridged structures.

Transfers of Electronic Charge

In Table II are presented the calculated net charges on the atoms in the various systems. Again these should be compared to the values for free carbon monoxide. The differences are remarkably small. The net charge on the carbon is virtually unchanged by interaction with nickel atoms, regardless of the number of the latter and whether

TABLE I: Calculated C–O Overlap Populations

System[a]	No. Ni atoms	σ overlap population	π overlap population	Total overlap population
Free CO	0	0.574	0.695	1.268
I, L	1	0.618	0.573	1.191
II, L	3	0.624	0.567	1.191
III, L	5	0.626	0.547	1.173
IV, L	7	0.624	0.539	1.163
V, L	8	0.621	0.535	1.156
VI, L	9	0.619	0.536	1.156
VII, L	9	0.621	0.525	1.146
VIII, B1	2	0.597	0.589	1.187
IX, B1	4	0.602	0.527	1.129
X, B1	7	0.602	0.528	1.130
VIII, B2	2	0.612	0.549	1.161
IX, B2	4	0.624	0.472	1.095
X, B2	7	0.625	0.465	1.090
XI, B2	9	0.625	0.460	1.091

[a] The systems are identified in terms of Figures 1 and 2. The meanings of L, B1, and B2 are explained in the caption to Figure 4.

the resulting system is linear or bridged. The oxygen charges do change, but only slightly, becoming more negative; this is especially so for the bridged structures. The pattern of the charges developed on the nickel atoms is different for the linear and the bridged systems. In the former, a significant positive charge develops on the nickel to which the CO is bonded. This charge reaches a value of +0.154 for five nickel atoms, after which it changes very little as more are included. The other nickel charges are all very small and negative. In the case of the bridged structures, all of the nickel atoms have extremely small charges; those in the top plane are positive, while those in the second plane are negative.

Perhaps the most striking fact about these atomic charges is that they indicate that there is little or no *net* transfer of charge between the nickel atoms and the CO molecule. This general statement holds true for all of the systems studied. The very small net transfer that does occur in some cases is from the nickels to the CO, and it is most pronounced in the bridged form in which the CO is closer to the surface. Even there, however, the greatest net transfer calculated is only about 0.08 electrons.

It should not be inferred from these very small net charge transfers that there is essentially no movement of electronic charge. Quite the contrary is true, as can be seen when the σ and π effects are examined separately. Table II also includes the calculated numbers of σ and π electrons associated with both the carbon and the oxygen in each of the systems investigated. These data are also given for free CO, to allow comparisons. The changes in the σ and π electronic populations of the carbon and oxygen, relative to free CO, are shown graphically in Figure 5.

In each case, the carbon loses a very significant quantity of σ charge, the amount initially increasing with the number of nickel atoms but leveling off after five nickels for the linear structures and after four for the bridged ones. In each instance, however, the carbon gains a quantity of π charge which is approximately the same as the amount of σ charge that it has lost. Its net charge, therefore, remains essentially unchanged.

The oxygen atom appears to be much less involved in charge movement. It loses a very small amount of σ charge, and gains a slightly greater amount of π charge, especially in the bridged systems.

TABLE II: Calculated Numbers of Electrons and Net Charges

System[a]	Atom	No. of σ electrons	No. of π electrons	Total no. of electrons	Net charge[b]
Free CO	C	2.738	0.994	3.732	+0.268
	O	3.262	3.007	6.268	−0.268
I, L	C	2.371	1.335	3.706	+0.294
	O	3.232	3.081	6.313	−0.313
	Ni				+0.019
II, L	C	2.319	1.390	3.709	+0.291
	O	3.222	3.062	6.284	−0.284
	Ni, 1				+0.103
	Ni, 2				−0.055
III, L	C	2.266	1.451	3.717	+0.283
	O	3.213	3.064	6.277	−0.277
	Ni, 1				+0.154
	Ni, 2				−0.040
IV, L	C	2.262	1.467	3.728	+0.272
	O	3.209	3.074	6.283	−0.283
	Ni, 1				+0.165
	Ni, 2				−0.030
	Ni, 3				−0.017
V, L	C	2.270	1.466	3.736	+0.264
	O	3.210	3.082	6.292	−0.292
	Ni, 1				+0.161
	Ni, 2				−0.021
	Ni, 3				−0.021
	Ni, 4				−0.016
	Ni, 5				−0.016
VI,L	C	2.285	1.458	3.742	+0.258
	O	3.212	3.084	6.296	−0.296
	Ni, 1				+0.160
	Ni, 2				−0.013
	Ni, 3				−0.018
VIII, B1	C	2.443	1.267	3.710	+0.290
	O	3.241	3.049	6.290	−0.290
	Ni				0.000
IX, B1	C	2.286	1.423	3.709	+0.291
	O	3.224	3.095	6.319	−0.319
	Ni				+0.007
X, B1	C	2.289	1.429	3.718	+0.282
	O	3.219	3.094	6.314	−0.314
	Ni, 1				+0.026
	Ni, 2				−0.006
	Ni, 3				−0.033
VIII, B2	C	2.362	1.356	3.718	+0.282
	O	3.243	3.080	6.324	−0.324
	Ni				+0.021
IX, B2	C	2.183	1.528	3.711	+0.289
	O	3.228	3.139	6.367	−0.367
	Ni				+0.020
X, B2	C	2.165	1.558	3.723	+0.277
	O	3.216	3.144	6.360	−0.360
	Ni, 1				+0.048
	Ni, 2				−0.022
	Ni, 3				−0.043
XI, B2	C	2.167	1.561	3.729	+0.271
	O	3.212	3.144	6.357	−0.357
	Ni, 1				+0.057
	Ni, 2				−0.017
	Ni, 3				−0.032

[a] The systems are identified in terms of Figures 1 and 2, which also show the numbering of the nickel atoms. The meanings of L, B1, and B2 are explained in the caption to Figure 4. [b] The net charges on the atoms are obtained by subtracting the total number of σ and π electrons calculated for the atom in the molecule from the total number of valence electrons of the atom in the free state (four for carbon, six for oxygen, and ten for nickel).

The fact that we find so little net transfer of electronic charge between the nickel atoms and the CO molecule may seem to be at variance with the observation that the chemi-

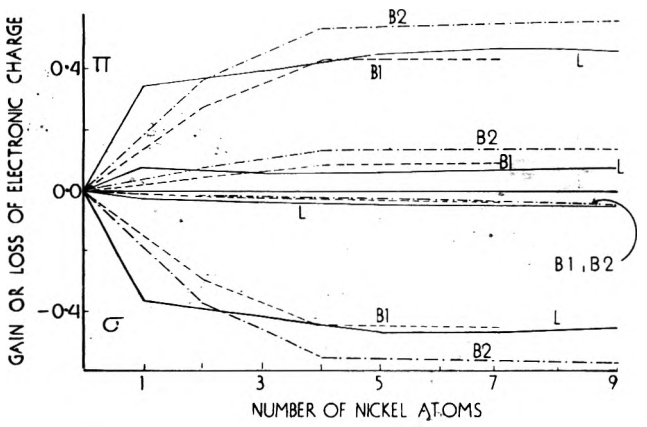

Figure 5. The changes in the numbers of σ and π electrons, relative to free CO, of the carbon and oxygen atoms in the systems shown in Figures 1 and 2. The three highest and the three lowest curves are for the carbons; the ones closer to the zero line are for the oxygens. The meanings of L, B1, and B2 are explained in the caption to Figure 4.

sorption of CO on nickel leads to a negative surface potential, of more than 1.0 eV.[24-26] It can easily be shown, however, that the observed surface potential can be satisfactorily explained in terms of the atomic charges within the CO molecule itself. The surface potential, Φ, may be estimated using the formula[27]

$$\Phi = 4\pi QRS \qquad (4)$$

in which Q represents the magnitude of the charges on the carbon and oxygen atoms, R is their separation, and S is the number of chemisorbed CO molecules per unit area of surface. The sign of Φ will be the same as the sign of the charge on the outermost atom. On the basis of a detailed analysis of a near-Hartree–Fock CO wave function,[28] the carbon and oxygen charges have been estimated to be C(+0.14), O(−0.14). These are presumably more accurate than the extended-Hückel values given in Table II. (Atomic charges calculated by the extended-Hückel method are of primarily qualitative significance.) Since this investigation has shown that the carbon and oxygen charges in the various Ni_n–CO systems differ relatively little from those in free carbon monoxide, Q in eq 4 can be approximated by 0.14. Letting R equal the bond length of carbon monoxide (1.128 Å),[8] and assuming S to be about 1.0×10^{15} molecules/cm^2,[24,25,29-31] the surface potential is estimated to be −2.9 eV. This is about twice the actual value, a discrepancy which is not surprising in view of the approximations made, such as using a point-charge model to represent the chemisorbed molecule, and assuming both the carbon and the oxygen charges to be exactly the same as in free CO. The important point is that this estimate, which is intended only as an order-of-magnitude calculation, does show that the presence of the carbon monoxide molecules on the nickel surface is in itself sufficient to account for the observed surface potential; it is not necessary to invoke charge transfer between the nickel and the chemisorbed layer.

Summary

Our results suggest that the practice of attributing the higher infrared frequencies to linearly chemisorbed CO species and the lower ones to bridged forms should be reexamined. It has been shown that the number of nickel atoms involved in the interaction, as well as the structure (linear or bridged), can be an important factor in determining the frequency. Thus, it is not inherently necessary for linear and bridged structures to have widely differing C–O frequencies, or for either one to be restricted to frequencies in just one region of the spectrum.

There appears to be a considerable amount of electronic charge transfer between the carbon and the nickel atoms; the carbon is found to lose σ charge and to gain π charge. These two effects occur to almost equal extents, however, so that there is very little *net* transfer of charge between the carbon monoxide and the nickel atoms.

Throughout this work, the various calculated properties have shown the general trend of initially changing significantly as the number of nickel atoms increases, but then tending to level off. As seen in Tables I and II and Figures 4 and 5, relatively little change occurs after five nickel atoms have been included in the linear systems and after four nickel atoms in the bridged systems. This suggests that the interactions are localized to a considerable extent, as is indicated also by other recent work, both theoretical and experimental.[9b,23,32-34] In both the linear and the bridged structures, it is primarily the nearest neighbors of the site of interaction, an in the same plane, that are involved. The lower plane of atoms seems to have little effect.[9b,33,34] To confirm that the next-nearest neighbors *in* the plane have no major effect, the C–O frequency and the σ and π overlap populations are computed for structure VII (Figure 1). The results (Figure 4 and Table I) are similar to those obtained for the other linear systems having more than five nickel atoms.

The work reported in this paper is part of a continuing study of the chemisorption of carbon monoxide on transition metals and their oxides.[1] Some further aspects of the interaction with nickel which are presently being investigated are the effects of other surface sites and crystal faces, and of additional CO molecules.

Acknowledgments. We greatly appreciate the support of the U.N.O. Research Council and the U.N.O. Computer Research Center (NSF Grant No. GJ-131).

References and Notes

(1) P. Politzer and S. D. Kasten, *Surface Sci.*, **36**, 186 (1973).
(2) H. Basch, A. Viste, and H. B. Gray, *Theor. Chim. Acta*, **3**, 458 (1965); *J. Chem. Phys.*, **44**, 10 (1966).
(3) C. K. Jorgensen, S. M. Horner, W. E. Hatfield, and S. Y. Tyree, Jr., *Int. J. Quantum Chem.*, **1**, 191 (1967).
(4) E. W. Stout, Jr., and P. Politzer, *Theor. Chim. Acta*, **12**, 379 (1968).
(5) L. C. Cusachs, *J. Chem. Phys.*, **43**, S157 (1965).
(6) J. C. Slater, "Quantum Theory of Atomic Structure", Vol. 1, McGraw-Hill, New York, N.Y., 1960, pp 195, 381.
(7) J. C. Slater, "Quantum Theory of Molecules and Solids", Vol. 2, McGraw-Hill, New York, N.Y., 1965, p 281; N. B. Hannay, "Solid-State Chemistry", Prentice-Hall, Englewood Cliffs, N.J., 1967, pp 37, 38.
(8) "Tables of Interatomic Distances and Configurations in Molecules and Ions", L. E. Sutton, Ed., Special Publications No. 11 and 18, The Chemical Society, London, 1958 and 1965.
(9) (a) G. Blyholder, *J. Vac. Sci. Technol.*, **11**, 865 (1974); (b) *J. Phys. Chem.*, **79**, 756 (1975).
(10) P. Politzer, R. K. Smith, and S. D. Kasten, *Chem. Phys. Lett.*, **15**, 226 (1972).
(11) J. Kaufman, *Int. J. Quantum Chem.*, **1S**, 485 (1967); R. Manne, *ibid.*, **2**, 69 (1968).
(12) R. P. Eischens, W. A. Pliskin, and S. A. Francis, *J. Chem. Phys.*, **22**, 1786 (1954).
(13) L. H. Little, "Infrared Spectra of Adsorbed Species", Academic Press, New York, N.Y., 1966, Chapter 3; M. L. Hair, "Infrared Spectroscopy in Surface Chemistry", Marcel Dekker, New York, N.Y., 1967, Chapter 6.
(14) R. P. Eischens, S. A. Francis, and W. A. Pliskin, *J. Phys. Chem.*, **60**, 194 (1956).
(15) G. Blyholder, *Proc. Int. Congr. Catal., 3rd, 1964*, 657 (1965); G. Blyholder, *J. Phys. Chem.*, **68**, 2772 (1964); A. M. Bradshaw and J. Pritchard, *Surface Sci.*, **17**, 372 (1969).

(16) E. W. Abel, M. A. Bennett, and G. Wilkinson, *J. Chem. Soc.*, 2323 (1959); C. S. Kraihanzel and F. A. Cotton, *Inorg. Chem.*, **2**, 533 (1963).
(17) J. H. Wang, A. Nakahara, and E. B. Fleischer, *J. Am. Chem. Soc.*, **80**, 1109 (1958); J. O. Alben and W. S. Caughey, *Biochemistry*, **7**, 175 (1968); J. P. Collman, R. R. Gagne, C. A. Reed, T. R. Halbert, G. Lang, and W. T. Robinson, *J. Am. Chem. Soc.*, **97**, 1427 (1975).
(18) E. L. Wagner, *J. Chem. Phys.*, **43**, 2728 (1965); K. G. Caulton and R. F. Fenske, *Inorg. Chem.*, **7**, 1273 (1968); A. F. Schreiner and T. L. Brown, *J. Am. Chem. Soc.*, **90**, 3366 (1968); J. Alster and M. J. Gallagher, *Mol. Phys.*, **25**, 649 (1973).
(19) The force constants were taken from the following sources: (CO, CO^+) L. H. Jones, *J. Mol. Spectrosc.*, **9**, 130 (1962); (CO_2) T. Wentink, Jr., *J. Chem. Phys.*, **30**, 105 (1959); I. Suzuki, *J. Mol. Spectrosc.*, **25**, 479 (1968); ($Ni(CO)_4$) L. H. Jones, R. S. McDowell, and M. Goldblatt, *J. Chem. Phys.*, **48**, 2663 (1968); (H_2CO) J. L. Duncan and P. D. Mallinson, *Chem. Phys. Lett.*, **23**, 597 (1973).
(20) For transition metal carbonyls, the anharmonicity correction is estimated to be 20–30 cm^{-1} (F. A. Cotton and G. Wilkinson, "Advanced Inorganic Chemistry", 3rd ed, Interscience, New York, N.Y., 1972, p 700).
(21) It is interesting to note, however, that some recent studies of the rate of desorption of CO from silica-supported nickel could be interpreted as indicating a bridged structure with a C–O frequency of about 2070 cm^{-1} (L. D. Neff, private communication).
(22) M. Moskovits, G. A. Ozin, and J. Hulse, paper presented at the Fourth North American Meeting of The Catalysis Society, Toronto, Feb 19, 1975; see also H. Huber, E. P. Kundig, M. Moskovits, and G. A. Ozin, *J. Am. Chem. Soc.*, **97**, 2097 (1975).
(23) The important role that the *number* of nickel atoms can apparently play in determining the C–O frequency may help to explain the increased intensity of the high-frequency bands of CO chemisorbed on Ni–Cu alloys that accompanies increased copper content [Y. Soma-Noto and W. M. H. Sachtler, *J. Catal.*, **34**, 162 (1974)]. Perhaps it is due in part to a decrease in the number of nickel atoms involved in some of the interactions (See Figure 4).
(24) J. C. Tracy, *J. Chem. Phys.*, **56**, 2736 (1972).
(25) K. Christmann, O. Schober, and G. Ertl, *J. Chem. Phys.*, **60**, 4719 (1974).
(26) J. E. Demuth and T. N. Rhodin, *Surface Sci.*, **45**, 249 (1974).
(27) P. M. Gundry and F. C. Tompkins in "Experimental Methods in Catalytic Research", R. B. Anderson, Ed., Academic Press, New York, N.Y., 1968, Chapter 3.
(28) P. Politzer, *Theor. Chim. Acta*, **23**, 203 (1971). In this refererence, the anomalous direction of the dipole moment of carbon monoxide, C^-O^+, is interpreted as being due to the highly localized carbon lone pair. It is not believed to reflect the actual charge distribution in carbon monoxide.
(29) R. L. Park and H. E. Farnsworth, *J. Chem. Phys.*, **43**, 2351 (1965).
(30) M. Onchi and H. E. Farnsworth, *Surface Sci.*, **11**, 203 (1968).
(31) K. Klier, A. C. Zettlemoyer, and H. Leidheiser, Jr., *J. Chem. Phys.*, **52**, 589 (1970).
(32) I. L. Sokolskaya and N. V. Mileshkina, *Surface Sci.*, **15**, 109 (1969); W. M. H. Sachtler and P. van der Plank, *Surface Sci.*, **18**, 62 (1969).
(33) J. C. Robertson and C. W. Wilmsen, *J. Vac. Sci. Technol.*, **9**, 901 (1972).
(34) G. Doyen and G. Ertl, *Surface Sci.*, **43**, (1974).

Desorption and Diffusion of Sodium Chloride Molecules Adsorbed on a Sodium Chloride (100) Crystal Surface

Paul O'Connor and Richard Schoonmaker*[1]

Department of Chemistry, Oberlin College, Oberlin, Ohio 44074 *(Received September 9, 1975)*

Publication costs assisted by Oberlin College and the Petroleum Research Fund

The energy binding adsorbed NaCl and Na_2Cl_2 molecules to a free (100) surface of a semiinfinite ideal sodium chloride lattice has been calculated by a direct computer summation of Born-type pairwise interactions between ions. The results are applied to evaluate contributions of desorption and surface diffusion to the mechanism of condensation and evaporation. The equilibrium binding energies for NaCl and Na_2Cl_2 molecules on the ideal surface are −0.425 and −0.675 eV/molecule, respectively. It is concluded that diffusion of an adsorbed NaCl molecule on the ideal sodium chloride (100) surface occurs by a hindered rotation or tumbling motion with an energy barrier of 0.133 eV/molecule. The results of these calculations suggest that an adsorbed NaCl molecule which is in thermal equilibrium with the surface at 298 K will desorb before it migrates more than a few lattice spacings. The binding energy for an NaCl molecule at a monatomic ledge is −0.706 eV/molecule.

Introduction

Several groups have recently reported results of investigations of the mechanism of condensation[2,3] and evaporation[4,5] of sodium chloride. In attempting to understand the mechanistic implications of experimental results from condensation and evaporation studies it is important to have estimates, which are not generally available, of the relative contributions of desorption and surface diffusion for adsorbed molecules. Despite the relative simplicity of ionic crystal lattices with regard to geometry and interatomic forces, the detailed theory of gas–solid interactions in such systems cannot be considered complete. In view of the increasing emphasis on understanding surface phenomena, we have attempted in the present work to apply the Born model[6] to the interaction of sodium chloride monomers, NaCl, and dimers, Na_2Cl_2, with the free (100) surface of a perfect sodium chloride lattice and to estimate some parameters which are important in the microscopic description of the mechanism of condensation and evaporation. Hove[7,8] has employed a clever Fourier series method to sum notoriously slowly convergent series in a similar study on the potassium chloride system. The principal advantage of direct summation using a high-speed digital computer is that once an elaborate computational program has been prepared it is possible to investigate any number of plausible diffusion paths to determine which has the lowest activation energy barrier.

Theory

In condensation from a molecular beam, molecules which

impinge on a crystal surface will either be back-scattered into the gas phase or trapped on the surface after inelastic energy exchange with the substrate. In the latter case it is possible for the trapped molecule to retain momentum parallel to the surface and to migrate laterally in the adsorbed state. In the precondensed, adsorbed state the molecule will diffuse across the surface until either it finds a stable site for nucleation and condensation or it desorbs. By knowing the depth and shape of the three-dimensional potential energy wells in which the molecule moves on the surface, it is possible to determine the mean time for desorption (residence time) and the mean rate of diffusion from which the mean diffusion path length can be calculated. Thus, the problem of interest is reduced to finding the potential energy surface on which the molecule moves.

Both the sodium chloride crystal and the adsorbed molecules, NaCl and Na_2Cl_2, were considered to be rigid structures. The potential energy of an ion in the adsorbed molecule resulting from all the lattice ions acting together was taken to be a sum of individual Born-type functions

$$u_i = \sum_j \left\{ \frac{q_i q_j}{r_{ij}} + A_{ij} e^{-r_{ij}/\sigma} \right\} \quad (1)$$

where u_i is the energy of the ith ion in the adsorbed molecule, q_i its charge, r_{ij} its distance from lattice ion j with charge q_j, and A_{ij} and σ are empirically determined parameters which account for the repulsion between overlapping charge clouds on neighboring ions. The sum extends over the entire three-dimensional crystal lattice of the substrate. In addition, both lattice and ad-molecule ions were considered to be polarizable with the consequence that the total energy of the system is increased by the sum of induced dipole energies, $-\vec{p}_k \cdot \vec{E}_k/2$, on all the ions. The electric field at the position of the ions constituting the adsorbed molecule was calculated from an expression first derived by Lennard-Jones and Dent[9] for the coulomb potential above the (100) face of a perfect NaCl-type lattice. From this, the induced dipoles were taken to be $\vec{p}_\pm = \alpha_\pm \vec{E}$ where $\alpha_\pm$ is the ionic polarizability of an ion of the type indicated by the appropriate subscript. A macroscopic approximation[8] was used to find the induced dipoles on the lattice ions

$$p_\pm = \frac{\alpha_\pm r_0^3}{2\pi(\alpha_+ + \alpha_-)} \left(1 - \frac{1}{K_0}\right) E$$

where E is the electric field at the lattice site owing to the ad-molecule charges, r_0 is the crystal nearest neighbor spacing, and K_0 is the optical dielectric constant of the crystal.

A computer program was written to carry out the sum in eq 1 and to evaluate the polarization energy contributions with truncation after investigation for suitable convergence which usually occurred when approximately 3×10^4 lattice positions were included in the sum (running time on the Oberlin College Xerox Sigma 9 computer was ~20 s/sum). Data used in the calculations are listed in Table I.

TABLE I: Data Used in the Calculations

NaCl internuclear distance	
Crystal, r_0	2.81 Å [a]
Gas, r_0	2.51 Å [b]
Overlap repulsion parameters [c]	
A_{++}	423.59 eV
$A_{+-} = A_{-+}$	1254.8 eV
A_{--}	3485.0 eV
ρ	0.317 Å
Polarizabilities	
Free ion [d]	
α_+	0.179 Å^3
α_-	3.66 Å^3
Crystal [e]	
α_+	0.303 Å^3
α_-	3.058 Å^3
Optical dielectric constant [d]	
K_0	2.25

[a] Reference 6. [b] Reference 10. [c] Reference 11. [d] Reference 12. [e] Reference 13.

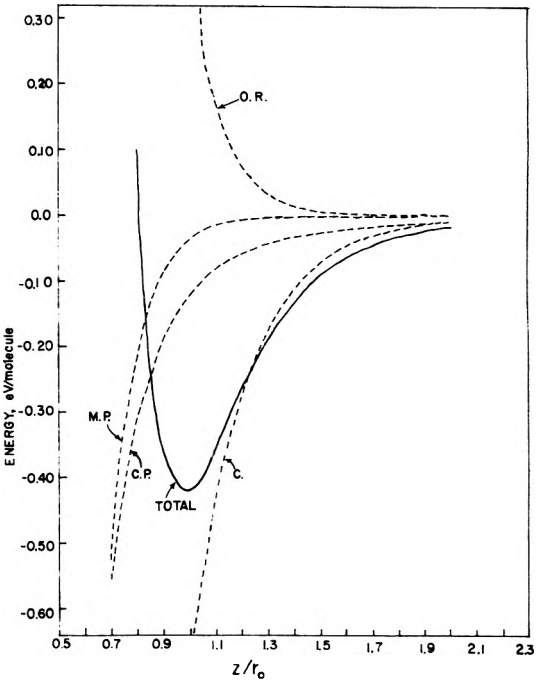

Figure 1. Energy of an adsorbed NaCl molecule as a function of distance above the surface: O.R., overlap repulsion energy; M.P., molecular polarization energy; C.P., crystal polarization energy; C., coulomb energy.

Results and Discussion

The NaCl molecule was positioned at its assumed equilibrium position on the perfect (100) NaCl crystal surface with the Na^+ ion above a surface chloride ion and the Cl^- above a neighboring surface sodium ion and the distance, z, above the surface was varied giving the curves of Figure 1 with an equilibrium binding energy of −0.425 eV/molecule at $z = 0.98r_0$. The coulomb energy at $z = r_0$ agreed to within 1% with the value found from the analytic expression given by Lennard-Jones and Dent.[9] By comparison, Hove[7,8] found an equilibrium binding energy of −0.35 eV/molecule at $z = 0.9r_0$ for a KCl molecule adsorbed on a (100) face of a potassium chloride crystal. A parabolic fit to the total energy curve of Figure 1 gave a natural frequency for vibration in the z direction of 2.74×10^{12} s^{-1}. Hove reported 1.9×10^{12} s^{-1} for the corresponding vibration frequency for adsorbed KCl.

The nature of the diffusional motion of a molecule in thermal equilibrium with the surface must be known before its migration rate can be determined. For NaCl on the (100) surface of a sodium chloride crystal at 298 K the binding between adsorbate and substrate causes lateral motion to be hindered because the energy barrier for motion from one equilibrium site to an adjacent one is greater

than the thermal energy kT. Thus, the center of mass of an adsorbed molecule will simply vibrate about its equilibrium position occasionally gaining enough energy to surmount the barrier and jump to the neighboring site. We propose that the mechanism with which surface diffusion can occur with the lowest activation energy is a hindered rotation or tumbling motion in which one ion of the molecule remains fixed at its equilibrium site while the other ion pivots about it in a plane perpendicular to the surface finally settling onto a neighboring equilibrium position, Figure 2. The result of such a diffusion jump is to displace the center of the molecular axis either r_0 or $(\sqrt{2}/2)r_0$ depending on whether the moving ion settles on a site of type A or B, the paths to which are equally favorable. The tumbling rotation of the molecule with the Na^+ ion as pivot gave the potential energy vs. angle curve shown in Figure 3 with a maximum energy occurring when the ad-molecule axis was oriented at 45° to the plane of the substrate surface. The energy barrier of 0.145 eV/molecule confirmed that this mechanism of surface diffusion is much more favorable than either in-plane rotation, which is hindered by an energy barrier greater than 0.7 eV/molecule, or translation of the entire molecule without rotation where the energy barrier is 0.68 eV/molecule. Pivoting about the Cl^- ion gives an entirely similar set of curves with a slightly lower barrier of 0.133 eV/molecule.

Absolute reaction rate theory[14] predicts that the rate constant, k_r, of a process with an activation energy E_a will be given by

$$k_r = (kT/h)(Q_2/Q_1)e^{-E_a/kT} \qquad (2)$$

where Q_1 is the partition function for the initial state and Q_2 is the partition function for the transition state including all degrees of freedom except the one corresponding to the reaction coordinate. To estimate the rates of desorption and surface diffusion of an adsorbed NaCl molecule eq 2 was used with the activation energies calculated above and with preexponential partition functions of the ad-molecule in appropriate states. The transition state for desorption is assumed to be a free gas-like molecule in accordance with evidence presented in ref 5, and the transition state for surface diffusion is taken as the ad-molecule pivoted about one ion and rotated 45° out of a plane parallel to the substrate surface.

For desorption, $Q_1 = q_x q_y q_z q_r^{(1)} q_v^{(1)}$ where q_x, q_y, and q_z are partition functions corresponding to three vibrational degrees of freedom of the center of mass, $q_r^{(1)}$ is the total rotational partition function, and $q_v^{(1)}$ is the partition function for internal vibration of the ad-molecule. $Q_2 = q_{tr}^2[q_r^{(2)}]^2 q_v^{(2)}$ where q_{tr}^2 is the translational partition function for two degrees of freedom, $[q_r^{(2)}]^2$ is the free rotational partition function in two degrees of freedom, and $q_v^{(2)}$ is the internal vibration partition function in the transition state for desorption. We assume that perturbations of the ad-molecule internal vibration owing to the presence of the surface are negligible with the consequence that $q_v^{(1)} = q_v^{(2)}$. From the harmonic oscillator approximation $q_i = e^{-h\nu_i/2kT}/(1 - e^{-h\nu_i/kT})$, $i = x, y, z$, and from our calculated vibration frequencies, ν_i, we obtain $q_z = 2.25$, $q_x = q_y = 3.56$. $q_r^{(1)}$ represents a partition function which takes account of in-plane and out-of-plane rotations of the ad-molecule. Each of these rotational motions is so hindered by high energy barriers that they are effectively vibrations which contribute numerical factors of no more than ~1–2. Thus, for desorption we estimate $k_e \approx 2.38 \times 10^{10}\ s^{-1}$.

A similar calculation using appropriate partition functions for ad-molecule and transition states for surface diffusion yields $k_d \approx 1.58 \times 10^{10}\ s^{-1}$.

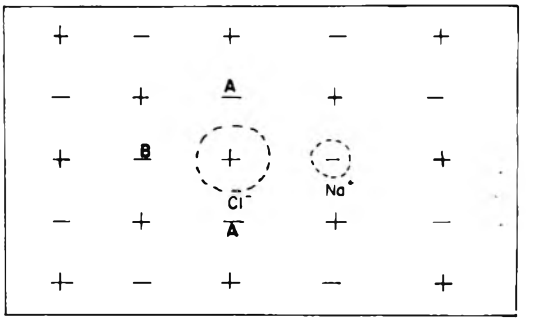

Figure 2. Top view of a (100) sodium chloride crystal surface with an adsorbed NaCl molecule on an equilibrium site. Pivoting about Cl^- produces diffusion to a new equilibrium site A or B.

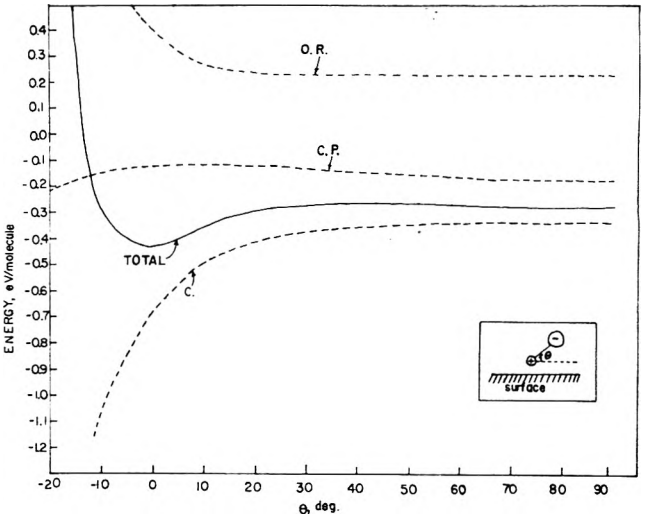

Figure 3. Energy as a function of angle for an adsorbed NaCl molecule pivoting about the Na^+ ion and rotating out of the plane of the surface: O.R., overlap repulsion energy; C.P., crystal polarization energy; C., coulomb energy.

In processes such as those being considered here the inverse of the rate constant, k_r, gives the mean time, $\tau_e = 4.2 \times 10^{-11}$ s, for desorption and $\tau_d = 6.3 \times 10^{-11}$ s for a diffusion jump. While these are approximate values for mean diffusion and desorption times in an idealized system, the relative magnitudes suggest that an NaCl molecule adsorbed on a free (100) surface of a perfect sodium chloride crystal will not migrate very far before desorption occurs. This result has been previously suggested in discussions of the mechanism of evaporation[4] and condensation[3] of sodium chloride.

Since monatomic ledges on a crystal surface may play an important role as capture sites for diffusing adsorbed molecules we have estimated the effect of a ledge as a binding site with the aid of eq 3 for the coulomb potential energy resulting from a semiinfinite planar net of point charges of alternating sign located in a square grid[15]

$$V = \frac{4q^2}{r_0} \sum_{n=0}^{\infty} \sum_{s=1}^{\infty} (-1)^s \{B_0[\pi s(2n+1)]\} \qquad (3)$$

where q is the magnitude of the charges in the grid, r_0 is the length of the square unit, and B_0 is a modified Bessel function of the second kind. Equation 3 gives the energy of a point charge in the plane of the net at a distance r_0 from a

grid point of opposite charge. The sum converges rapidly to $2V = -0.766$ eV/molecule where the factor of 2 arises to account for the presence of two ions in the NaCl molecule. The repulsive energy caused by the ions in the ledge was found by direct summation to be 0.385 eV/molecule, and the total effect of the ledge, excluding polarization, is to increase the molecular binding energy to -0.706 eV/molecule (i.e., the binding energy at a ledge is ~190% greater than the binding energy on the perfect surface). Polarization effects will make the binding energy at the ledge slightly larger than our calculated value but coulomb and repulsive energies are the dominant contributions to the total binding energy. Although ledges appear to be favorable sites for capture of adsorbed molecules it seems unlikely that they play an important role in the condensation of NaCl deposited from a molecular beam onto a room temperature UHV-cleaved sodium chloride (100) surface because the average spacing between steps[16] on the surface is 2–3 orders of magnitude or more larger than the mean diffusion distance which we have calculated for an adsorbed NaCl molecule.

For an Na_2Cl_2 molecule above its equilibrium site on the (100) sodium chloride perfect surface we calculate a binding energy of -0.675 eV/molecule at a distance r_0 above the surface. The dimer has a lower binding energy per ion than the monomer because its electric field is weaker and is thus less effective in polarizing the underlying substrate.

In assessing the validity of the calculations reported here and using them as the basis for conclusions concerning the mechanism of condensation or evaporation certain limitations must be taken into account. The rigid molecule-perfect rigid lattice model which we have used is only an approximation to the true geometry of the interacting system of crystal surface plus adsorbate. Aside from defects, impurities, contaminants, dislocations, etc. in the substrate surface there are two intrinsic effects which cause distortion of the surface layers of a real sodium chloride surface on which molecules are adsorbed. The inherent anisotropy due to the presence of an uncompensated free surface results in a relaxation of ions in the outermost layers and deviations from the regular planar arrays which are characteristic of the bulk. Furthermore, the presence of a nearby adsorbed molecule perturbs the underlying substrate causing surface ions to change position. Benson et al.[17] have reported a calculation in which relaxation of an NaCl (100) surface results in changes of ionic positions of up to 10% of bulk lattice spacings with surface chloride ions being displaced outward. This change in configuration of the surface plane would be expected to have an effect on both the binding energy and diffusion barrier for an adsorbed molecule. The general problem of taking account of relaxation of the surface is a difficult one to solve and we have no results of calculations of diffusion on a relaxed surface. A preliminary approach to desorption from a relaxed surface suggests that while the individual contributions may change from those for the relaxed surface there are compensating effects and the total binding energy may change but little from adsorption on the perfect surface to adsorption on the relaxed surface. A second effect which should lead to localized distortion of geometry is a consequence of forces of interaction between ions in the crystal and the ad-molecule. Calculations of these perturbations would be awkward to carry out particularly since the displacements of the ions would be altered as the position of the ad-molecule changes. However, it is reasonable to assume that these displacements will not be large because in the first approximation the energy of interaction is at least an order of magnitude smaller than the internal binding energies for ions in either the ad-molecule or the crystal. Deviations from ideal geometry of the type described here will increase the binding energy of the adsorbed molecule to the surface. Finally, our idealized model ignores the differences between surface ions and those in the bulk because the Born parameters were derived from compressibility data on bulk crystals. Rittner[18] has applied a modified Born model to the gas phase NaCl molecule and he has calculated the values which the repulsive parameters A_{+-} and σ must have to account for the observed equilibrium internuclear separation. He finds that the repulsive interaction must be about five times stronger and somewhat harder than in the bulk crystal. In view of the current imperfect understanding of surface conditions and gas–solid interaction potentials, the existing data on bulk crystal ions most closely approximate the true surface state in the context of the Born model.

Acknowledgment. Acknowledgment is made to the donors of the Petroleum Research Fund, administered by the American Chemical Society, for partial support of this research.

References and Notes

(1) Author to whom correspondence should be addressed.
(2) R. C. Schoonmaker and V. Lo, *J. Chem. Phys.*, **58**, 727 (1973).
(3) R. C. Schoonmaker and L. C. Tu, *J. Chem. Phys.*, **60**, 4650 (1974).
(4) J. Lester and G. Somorjai, *J. Chem. Phys.*, **49**, 2940 (1968).
(5) C. T. Ewing and K. H. Stern, *J. Phys. Chem.*, **77**, 1442 (1973); **79**, 2007 (1975).
(6) M. Born and K. Huang, "Dynamical Theory of Crystal Lattices", Oxford University Press, London, 1954.
(7) J. E. Hove, *Phys. Rev.*, **99**, 480 (1955).
(8) J. E. Hove, Ph.D. Thesis, Cornell University, 1953.
(9) J. E. Lennard-Jones and B. Dent, *Trans. Faraday Soc.*, **24**, 92 (1928).
(10) N. N. Greenwood, "Ionic Crystals, Lattice Defects, and Nonstoichiometry", Butterworths, London, 1968.
(11) M. Tosi, *Solid State Phys.*, **16**, 1 (1964).
(12) N. Mott and R. W. Gurney, "Electronic Processes in Ionic Crystals", Oxford University Press, London, 1940.
(13) A. J. Michael, *J. Chem. Phys.*, **51**, 5730 (1969).
(14) S. Glasstone, K. Laidler, and H. Eyring, "The Theory of Rate Processes", McGraw-Hill, New York, N.Y., 1941.
(15) M. Born, "Atomtheorie des Festen Zustandes", 2nd ed, Leipzig, 1923.
(16) H. Bethge, "Molecular Processes on Solid Surfaces", E. Drauglis, R. D. Gretz, and R. I. Jaffee, Ed., McGraw-Hill, New York, N.Y., 1969.
(17) G. C. Benson, P. T. Freedman, and E. Dempsey, *Adv. Chem. Sci.*, **33**, 26 (1961).
(18) E. Rittner, *J. Chem. Phys.*, **19**, 1030 (1951).

Adsorption Potential of Hydrocarbons at the Gas–Liquid Interface of Water

Claire Vidal-Madjar, Georges Guiochon,*

Laboratoire de Chimie Analytique Physique, Ecole Polytechnique, Palaiseau, France

and Barry L. Karger

Department of Chemistry, Northeastern University, Boston, Massachusetts 02115 *(Received April 3, 1975; Revised Manuscript Received October 24, 1975)*

Publication costs assisted by the National Science Foundation and Ecole Polytechnique

The adsorption potential above the gas–liquid interface of water of some n-alkanes (n-pentane, n-hexane, and n-heptane) and aromatic hydrocarbons (benzene and toluene) has been calculated. The results are in good agreement with the experimental differential energies of adsorption measured by gas chromatography at zero surface coverage, where adsorbate–adsorbate interactions are negligible. As shown from our calculations, the interaction between the n-alkanes and liquid water is mainly due to the van der Waals dispersion forces. The role and importance of the quadrupole in the adsorption energy of benzene and toluene on water is demonstrated; it represents 40% of the total adsorption potential. From our calculations, it is shown that benzene and toluene are adsorbed with a high probability on the areas of the gas–liquid interface where hydrogen atoms of the water molecules point out toward the vapor phase.

Introduction

The study of the structure and properties of water at or near interface has recently been of great interest.[1] This is in part the result of a recognition that many important processes of a biological nature occur at water interfaces. Some workers have argued that water exists in an ordered arrangement for some distance away from an interface, with a gradual change toward the structure of bulk water.[2]

In order to understand the characteristics of water at interfaces, there needs to be a close relationship between theoretical and experimental work. Both areas present difficulties. On the theoretical side, an acceptable model for the structure of water at an interface must be carefully developed, based on the structure of the bulk liquid state. Structural ordering of water molecules in the liquid over relatively long distances is possible, since four positions on the water molecule are potentially available for hydrogen bonding (e.g., the tetrahedral structure of ice Ih[3]). On the other hand, the relatively low viscosity of bulk liquid water (considering the four possible sites for H bonding) leads one to conclude that disorder must also exist in the liquid state. Thus, the structure of bulk water must be some complex compromise between order and disorder. However, the complexity of developing a correct model is such that up to now no complete picture of the structure of bulk liquid water is available.[4] Since water structure at interfaces must be related to bulk water, it is clear that a viable model for interfacial water is difficult to develop.

On the experimental side, the usual difficulties of direct measurement of properties at interfaces exist. The question must always be asked whether one is indeed measuring a true interfacial property (e.g., spectroscopic measurements). Moreover, since some of the effects measured are of such a subtle nature, much controversy exists as to whether these effects are real.[2] Indirect measurements, e.g., thermodynamics of adsorption, can be useful in inferring structure and properties of water at interfaces, but here again great care must be exercised that solute–solute interactions are minimized so that the solute can act as a probe of interfacial water properties. In addition, it must always be kept in mind that the measurements are indirect and as such that one may be unable to differentiate between several structural models. Nevertheless, it is through an accumulation of direct and indirect experimentation, matched against theoretical models, that the correct structure of interfacial water will emerge.

Recently, adsorption characteristics of nonelectrolytes at the gas–liquid interface of water in the Henry's law region has been measured by gas chromatography.[1,5,6] It has been suggested that water tends to behave as a low energy surface with the hydrogens directed toward the gas phase, in agreement with other workers.[7-9]

In this work, we shall calculate the adsorption potential of five hydrocarbons at the gas–liquid interface of water and compare the minimum value with the experimental adsorption energy obtained at zero surface coverage by gas chromatography. For three of the molecules (n-pentane, n-hexane, and n-heptane) the calculation has consisted of dispersion and induction interactions between solute and liquid adsorbent. For two aromatic molecules (benzene and toluene), we have also included an electrostatic interaction between the quadrupole moment of the adsorbate and the hydroxyl groups at the liquid surface. We have assumed a model of the water surface consisting of an expanded ice Ih structure and have been able to achieve reasonably good agreement between the calculated and experimental values. The implications of these results on the gas–liquid interfacial structure of water will be discussed.

The principles of the calculation of the thermodynamic functions of adsorption for nonpolar molecules on the homogeneous surface of graphitized carbon black have been described by Kiselev and Poshkus.[10,11] Due to the nonspecific character of this adsorbent, the adsorption process with nonpolar adsorbates only involves dispersion forces. Calculations have been simplified by adopting a semiempirical potential similar to that which describes molecular interactions.[12,13] Moreover the problems of calculation are now easily solved using a computer.[14]

A further step for a better understanding of the adsorption process has been a calculation of the thermodynamic functions of adsorption of nonpolar molecules on specific adsorbents. The minimum adsorption potential has been calculated for various adsorbents such as boron nitride,[15,16] phthalocyanines,[17] sodium chloride,[18] potassium chloride,[19] and zeolites.[20-22] In these studies, the adsorption potential has been favorably compared with the experimental adsorption energies obtained either by static or gas chromatographic techniques.

Theory

I. *Adsorption Potential.* The adsorption potential may be expressed as the sum of a dispersion energy term Φ_D, a repulsive energy term Φ_R, and an energy term due to the electrostatic forces Φ_E.[23,24]

$$\Phi = \Phi_D + \Phi_R + \Phi_E \tag{1}$$

The contribution of the nonspecific interaction ($\Phi_D + \Phi_R$) can be calculated using lattice sums of (6–12), (6 − exp), or more complicated pairwise potential. For the adsorption of nonpolar molecules on graphite, good agreement has been obtained with the experimental data in spite of the arbitrary methods employed in choosing the parameters for the potential functions.[24-27] For the calculation of the van der Waals interaction energy, we shall follow here the same treatment as the one adopted by Kiselev and coworkers[10-13,18-21] and other authors.[14,16,17]

The potential energy of the molecule due to the contribution of nonspecific interactions is taken as the sum of the adsorption potentials of its separate atoms Φ_i:

$$\Phi_D + \Phi_R = \sum_i \Phi_i \tag{2}$$

Kiselev and coworkers[12,13] have simplified the potential energy equation by introducing a semiempirical expression similar to the Lennard-Jones potential:

$$\Phi_i = -\sum_j C_{ij1} r_{ij}^{-6} - \sum_j C_{ij2} r_{ij}^{-8} + B_i \sum_j r_{ij}^{-12} \tag{3}$$

In this expression r_{ij} is the distance between the ith atom (or atom group) center of the adsorbate molecule and the jth atom (or atom group) center of the adsorbent. The potential energy is thus calculated taking into account a dipole–dipole term and a dipole–quadrupole term for the dispersion attraction forces and a term to describe the repulsion forces.

The different expressions used to estimate the attraction constants are discussed in ref 25, where it is shown that all of them can only give an approximate value of the adsorption potential. The constant C_{ij1} in eq 3 was obtained from the Kirkwood–Müller formula[25] which gave reasonably good results for the adsorption of hydrocarbons on graphite:[12]

$$C_{ij1} = -6mc^2 \left[\frac{\alpha_i \alpha_j}{\frac{\alpha_i}{\chi_i} + \frac{\alpha_j}{\chi_j}} \right] \tag{4}$$

An analogous formula was used for C_{ij2}.[12] In eq 4, m is the mass of the electron, c the velocity of light, α the polarizability, and χ the diamagnetic susceptibility. The constants for the repulsion forces are calculated for each type of atom from the equilibrium distance between the adsorbate atom and the adsorbent surface, a distance at which repulsion and attraction forces cancel.

The adsorption potential representing the electrostatic attraction forces is the sum of three different contributions:[23,28]

$$\Phi_E = -\frac{\Sigma \alpha_i}{2} F^2 - \mu F_t - \frac{1}{3}(Q_{xx}F'_x + Q_{yy}F'_y + Q_{zz}F'_z) \tag{5}$$

In this equation, F is the electric field of the adsorbent and F' its gradient. The first term represents the attraction potential caused by the electric field induced in the adsorbed molecule. It is given by the sum of all the induced attractive potential terms describing the interaction of each atom or atom group i with the electric field of the adsorbent. This procedure was used by Kiselev and coworkers[12] to calculate the interaction energy of some organic molecules with magnesia. The second term of eq 5 expresses the interaction of the dipole moment of the molecule with F_t, the component of the electric field in the direction of the dipole moment. The third term gives the interaction of the quadrupole moment of the molecule with the adsorbent. Q_{xx}, Q_{yy}, Q_{zz} are the three quadrupole moments of the molecule and F'_x, F'_y, F'_z are the field gradients along the axis Ox, Oy, Oz when the mass center of the molecule is located in O.

In the case of benzene adsorbed with its plane parallel to the adsorbent surface, the charge distribution is symmetrical around the OZ axis, so that

$$Q_{xx} = Q_{yy} = -\frac{1}{2} Q_{zz} \tag{6}$$

and eq 5 can be simplified using the Laplace's equation:

$$F'_x + F'_y + F'_z = 0 \tag{7}$$

We then can derive a relationship giving Φ_E for benzene which is similar to that previously presented.[23]

II. *The Structure Model of Water Near the Gas–Liquid Interface.* In order to be able to compute the adsorption potential from the above equations, it is necessary to know the position of the atoms which constitute the adsorbent. As we mentioned, we must assume a structure for water near the gas–liquid interface, based on a modification of a presumed bulk liquid water structure.

We first note that the basic structure of ordinary hexagonal ice (ice Ih) is well established.[31] Each oxygen atom is surrounded tetrahedrally by four other oxygen atoms, each at a distance of 2.76 Å, with every water molecule hydrogen bonded to its four nearest neighbors. Figure 1 shows the structure of hexagonal ice. The lattice consists of oxygen layers arranged perpendicular to the c-crystal axis, consisting of hexagonal rings of water molecules in the chair conformation. The hydrogen atoms are located along the axis of two adjacent oxygens, at a distance of 1.01 Å from the oxygen to which it is covalently bonded[3,32] (the hydrogen-bonded distance is then 1.75 Å).

Equation 5 assumes that the electric field is constant over the volume occupied by the molecule. We shall see later that the field gradients acting above the surface of water are large. Even for inert gases, it is thus necessary to follow the procedure introduced by Lenel[29,30] and integrate over the volume of the molecule, assuming some charge distribution. For molecules as complex as hydrocarbons we followed an approximate treatment similar to the one introduced by Kiselev and coworkers.[12] To allow for the

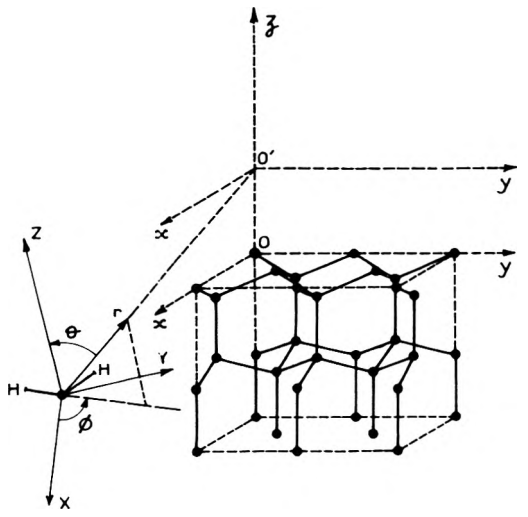

Figure 1. Basic structure of ordinary hexagonal ice (ice Ih) and coordinate systems used in the calculation of electric fields. θ is the angle between r and z axis, and ϕ is the angle between the projection of r in the X–Y plane and the X axis.

rapid spatial variations in the electric field, Φ_E is taken as the mean value of the Φ_E's for all the adsorption sites considered.

As noted previously, the structure of bulk liquid water is as yet not fully understood. Eisenberg and Kauzmann have given a useful picture of the structure, based on macroscopic properties.[32] The thermal motion in the liquid may be regarded as being of two types: rapid oscillations about temporary equilibrium positions ("the vibrationally average structure or V structure") and slower displacements of the equilibrium position ("the diffusionally average structure or D structure"). The "V structure" persists in a small region on the average, for a time τ_D of the order of 10^{-11} to 10^{-12} s, before being interrupted by the translation or reorientation of the molecule.

In the "V structure" of the liquid water, the variation in the local environment of water molecules is high compared to the relatively stable environment of an ice Ih crystal. Some nearest neighbors are as close as 2.75 Å and others may be as far apart as 3.10 Å or more. At the same time liquid water contains a large variety of hydrogen bonded molecules, but some nonhydrogen bonded OH groups may be present, as shown by the Raman studies of Walrafen.[33]

From the x-ray radial distribution function determined by Narten and coworkers,[34] it is found that in the "D structure" there are relatively high concentrations of neighbors at distances about 2.9, 4.5, and 7 Å. (At 4 °C, the average oxygen–oxygen distance is 2.84 Å, whereas at 200 °C it becomes 2.94 Å.) On the basis of these results, it seems reasonable to assume that the structure of interfacial water is a tetrahedral one, as in ice Ih, with the average distance between oxygen atoms of approximately 2.9 Å. In a theoretical model of the surface structure of water, Fletcher has suggested that any structural ordering will maintain itself for at least 10 molecular layers.[9] Consequently, we shall assume this tetrahedral structure remains roughly constant for all the layers included in the calculation of the average adsorption energy. The water molecule is considered as a whole adsorption group with a polarizability $\alpha_j = 1.5$ Å^3, and a diamagnetic susceptibility $\chi_j = -2.16 \times 10^{-5}$ Å^3.[3] The force adsorption center is located in the oxygen position.

III. *Lennard-Jones Adsorption Potential Calculation.* The dispersion forces upon adsorption are expressed by the Lennard-Jones adsorption potential of eq 3. The distances r_{ij} of this equation were calculated using a 1108 UNIVAC computer, assuming that the structure of liquid water is tetrahedral with every oxygen atom located at a distance $R = 2.9$ Å.

The adsorption energy was calculated for the equilibrium position of the adsorbent molecule. At minimum energy the molecule lies flat on the liquid surface (Oxy plane of Figure 1) at the van der Waals distance which for all the molecules in this study was $z_0 = 3.40$ Å. The exact numerical calculation of the sums of eq 3 is the same as that described for the adsorption on a graphite surface[14] and shall be briefly reviewed here for the atom arrangement of Figure 1.

Figure 2 represents the adsorption surface (Oxy plane) with the position of each oxygen atom in the surface represented by black circles and of each atom in the second layer by open circles. The locations O′, B′ . . . G′ represent possible adsorption positions for adsorbate groups at the van der Waals distance. From the origin, one can observe that two separate interaction planes exist: I and II. The coordinates of the oxygen atoms in the surface layer within the two planes are:

$$\text{I} \qquad x_j = 2R\sqrt{2}h \qquad y_j = 2R\sqrt{6}/3k \qquad z_j = 0$$

$$\text{II} \qquad x_j = R\sqrt{2}(2h + 1) \qquad y_j = R\sqrt{6}/3(2k + 1) \qquad z_j = 0 \tag{8}$$

where h and k are positive or negative integers and $R = 2.9$ Å. In the second layer, the coordinates of the oxygen atoms are:

$$\text{I} \qquad x_j = 2R\sqrt{2}h - 2R\sqrt{2}/3 \qquad y_j = 2R\sqrt{6}/3k \qquad z_j = -R/3$$

$$\text{II} \qquad x_j = R\sqrt{2}(2h + 1) - 2R\sqrt{2}/3 \qquad y_j = R\sqrt{6}/3(2k + 1) \qquad z_j = -R/3 \tag{9}$$

The atoms of the third layer have the same coordinates as those of the second except that $z_j = -4R/3$ and those of the fourth layer the same as the first layer with $z_j = -5R/3$. The sequence is the same from the fifth to the eighth layer with a translation along the Oz axis of $-8R/3$. The sums of eq 3 were calculated with a precision of 0.001 in 20 Å radius (~10 layers).

IV. *Evaluation of the Electric Field.* The electric field acting at the oxygen nucleus of a central molecule of an ice crystal has been calculated as described by Coulson and Eisenberg.[35] These authors considered contributions to the electric field out to the fourth shared nearest neighbors of oxygen atoms. They first present the expression of the electric field acting at any point and arising from an isolated H_2O molecule. In Figure 1 the H_2O molecule has its oxygen atom located at the origin of the $OXYZ$ system, with OZ as the C_2 axis and OYZ as the molecular plane. The expres-

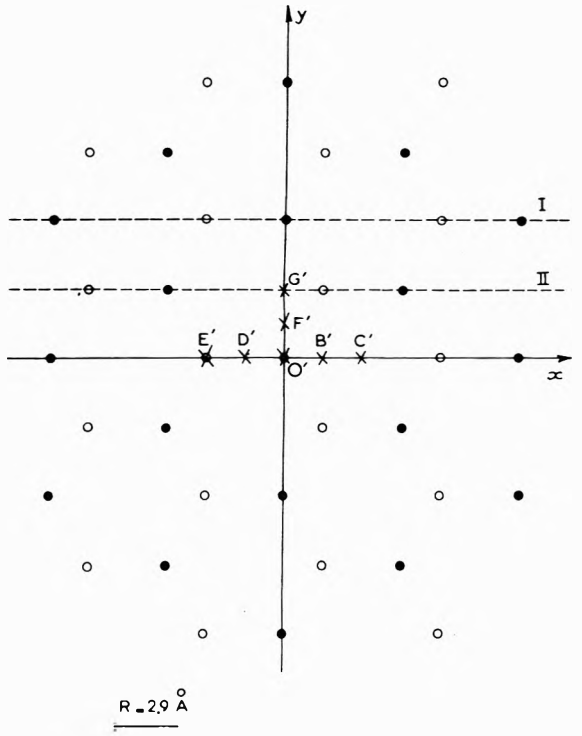

Figure 2. Surface representation of the lattice (O*xy* plane on figure 1): oxygen atoms of the first layer (black circles); oxygen atoms of the second layer (open circles); O', B', . . . G' = adsorption positions of adsorbate groups, at the distance $z = 3.40$ Å.

sion of the electric field is written in spherical coordinates E_r, E_θ, E_Φ and takes into account the dipole, the quadrupole, and the octupole moments of the H_2O molecule.

We have used the following values for the multipole moments relative to the oxygen nucleus in the $OXYZ$ axis system as defined in Figure 1: dipole moment, $\mu_Z = 1.84 \times 10^{-18}$ esu cm; quadrupole moment, $Q_{XX} = -7.482$, $Q_{YY} = -4.180$, $Q_{ZZ} = -5.680$ in units of 10^{-26} esu cm^2; octupole moments, $R_{ZZZ} = -0.849$, $R_{ZXX} = -0.597$, $R_{ZYY} = 0.920$ in units of 10^{-34} esu cm^3. The dipole moment is the experimental dipole of water vapor.[36] For the higher multipole moments we have used the data obtained from the ab initio calculations of Neumann and Moskowitz,[37] as the quadrupole moment calculated for the water molecule agree very well with the experimental one.[36]

The total electric field at a given point is then computed as the field from the given H_2O molecule along with that arising from nearest neighbors, each of whose dipoles can have six possible orientations. A computer program whose principles follow the scheme of ref 35 has been written to evaluate the probabilities of each orientation in a quasi-infinite volume, once the dipole of the central molecule is fixed. The field arising from the nearest neighbors is found to increase the total dipole moment of the H_2O molecule of liquid water to 2.82 D (from 1.84 D for an isolated H_2O molecule).

With the multipole moment values given above we have found that over 40% of the total value of the electric field is contributed by the quadrupole moment instead of 20% with the erroneous values of the quadrupole moment used by Coulson and Eisenberg[35] as the experimental one was not available at that time. The contribution of the octupole moment to the total electric field is 5% instead of 2% with the octupole values used in ref 35.

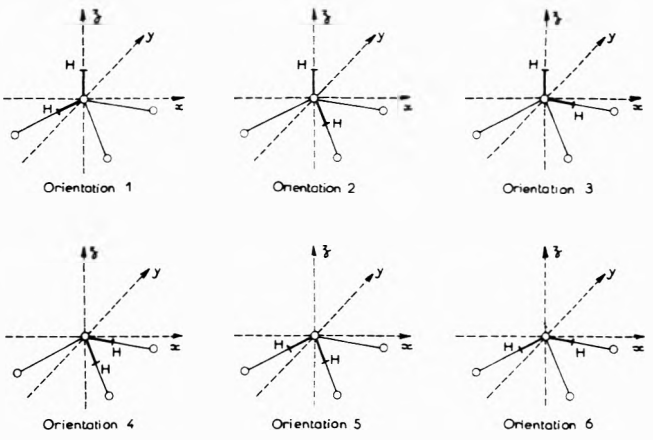

Figure 3. The six possible orientations of a water molecule on the surface of the liquid.

Consider now the case of the water molecule on the surface of liquid water. Here again there are six possible orientations of the dipole, as shown on Figure 3. For orientations 1–3, one of the hydrogen atoms is directed toward the vapor phase, whereas for 4–6 both hydrogens are directed toward the liquid state. For each orientation of the central water molecule we have first calculated the electric field F at point O' in Figure 1 (the van der Waals distance, $z_0 = 3.4$ Å) for the central molecule alone and then including all the neighboring water molecule contributions. The results are listed in Table IA and IB, along with the electric field components F_x, F_y, F_z and the gradients of the field F'_x, F'_y, F'_z along the three Cartesian axis O'x, O'y, O'z. The electric field in this table has included calculations with the aid of the computer to a precision of 0.001, requiring the inclusion of 10 nearest neighbors. The total moment of the H_2O molecule is taken as 2.82 D and the values of the quadrupole and octupole moments are those given above which are derived from ref 36.

In this procedure, we have neglected the contributions of the induced quadrupole and octupole moments to the total electric field. The contribution of the induced quadrupole may be of some importance, however, as we have seen that the quadrupole of the H_2O molecule contributes for 40% to the total electric field.

The calculation of the total fields in Table I arising from the individual fields of each molecule E_r, E_θ, and E_Φ are made in the following manner. First, E_X, E_Y, E_Z are the Cartesian coordinates of the electric field along OX, OY, OZ axis, as represented in Figure 1, and E_x, E_y, E_z and E'_x, E'_y, E'_z are the coordinates of the electric field and its gradient along O'x, O'y, O'z axis. These fields arise from each molecule of the network, with each orientation having a probability P_j calculated as indicated by Coulson and Eisenberg.[35] Hence

$$F_x = \sum_{i=1}^{n} \sum_{j=1}^{6} P_j E_x \qquad (10)$$

with equivalent relations for F_y, F_z, F'_x, F'_y, and F'_z. In eq 10, i represents each atom of the network and j the six possible orientations of the water dipole.

For each molecule and for each orientation we have

$$E_X = \sin\theta \cos\Phi E_r + \cos\theta \cos\Phi E_\theta - \sin\Phi E_\Phi$$

$$E_Y = \sin\theta \sin\Phi E_r + \cos\theta \sin\Phi E_\theta + \cos\Phi E_\Phi$$

$$E_Z = \cos\theta E_r - \sin\theta E_\theta \qquad (11)$$

TABLE I: Electric Field and Its Gradient Acting above the Central H_2O Molecule of the Surface at the Equilibrium Distance z_0 = 3.40 Å

Contribution arising from	Orientation of the central H_2O molecule of the surface (cf. Figure 3)	Electric field 10^5 esu cm^{-2}	Electric field components 10^5 esu cm^{-2}			Gradient of the electric field 10^{13} esu cm^{-3}		
			F_x	F_y	F_z	F'_x	F'_y	F'_z
(A) Central H_2O molecule	1	1.491	0.402	0.000	1.435	0.707	0.809	−1.516
	2	1.491	−0.201	−0.348	1.435	0.783	0.732	−1.516
	3	1.491	−0.201	0.348	1.435	0.783	0.732	−1.516
	4	1.113	−0.370	0.000	−1.050	−0.430	−0.519	0.948
	5	1.113	0.185	−0.321	−1.050	−0.496	−0.452	0.948
	6	1.113	0.185	0.321	−1.050	−0.496	−0.452	0.948
(B) Including neighboring H_2O molecules	1	1.841	0.189	0.000	1.831	0.842	0.888	−1.730
	2	1.841	−0.094	−0.163	1.831	0.876	0.853	−1.730
	3	1.841	−0.094	0.163	1.831	0.876	0.853	−1.730
	4	1.471	−0.157	0.000	−1.462	−0.536	−0.569	1.105
	5	1.471	0.078	−0.136	−1.462	−0.561	−0.544	1.105
	6	1.471	0.078	0.136	−1.462	−0.561	−0.544	1.105

If A is the matrix which relates the $OXYZ$ system to the $O'xyz$ system, it is then possible to write:

$$\begin{pmatrix} E_x \\ E_y \\ E_z \end{pmatrix} = A \begin{pmatrix} E_X \\ E_Y \\ E_Z \end{pmatrix} \tag{12}$$

The corresponding gradient of the electric field along the $O'z$ axis E'_z is

$$E'_z = \frac{\partial E_z}{\partial r}\frac{\partial r}{\partial z} + \frac{\partial E_z}{\partial \theta}\frac{\partial \theta}{\partial z} + \frac{\partial E_z}{\partial \Phi}\frac{\partial \Phi}{\partial z} \tag{13}$$

with similar relations for E'_x and E'_y. The solution of eq 13 is straightforward as we have the following equation which relates the spherical coordinates to the $OXYZ$ coordinates and then to the $O'xyz$ coordinates:

$$\begin{pmatrix} \frac{\partial r}{\partial x} & \frac{\partial r}{\partial y} & \frac{\partial r}{\partial z} \\ \frac{\partial \theta}{\partial x} & \frac{\partial \theta}{\partial y} & \frac{\partial \theta}{\partial z} \\ \frac{\partial \Phi}{\partial z} & \frac{\partial \Phi}{\partial y} & \frac{\partial \Phi}{\partial z} \end{pmatrix} = MA^{-1} \tag{14}$$

with

$$M = \begin{pmatrix} \sin\theta\cos\Phi & \sin\theta\sin\Phi & \cos\theta \\ \frac{\cos\theta\cos\Phi}{r} & \frac{\cos\theta\sin\Phi}{r} & \frac{-\sin\theta}{r} \\ \frac{-\sin\Phi}{r\sin\theta} & \frac{\cos\Phi}{r\sin\theta} & 0 \end{pmatrix} \tag{15}$$

V. *Comparison with Experimental Data.* The experimental thermodynamic functions of adsorption can be predicted using the classical laws of the statistical thermodynamic functions of adsorption.

For quasi-rigid molecules the adsorbate–adsorbent constant K_H (μmol/m^2) or Henry adsorption constant is related to the adsorption potential Φ according to the relation[10]

$$K_H = \frac{1}{8\pi^2 ART}\int\cdots\int [\exp(-\phi/RT) - 1] \times \sin\theta\, dx\, dy\, dz\, d\theta\, d\varphi\, d\psi \tag{16}$$

where x, y, z are the coordinates of the mass center of the molecule; θ, φ, ψ are the Euler angles of orientation to the surface; Φ is a function of these parameters; A is the surface area of the adsorbent, T the absolute temperature, and R the universal gas constant.

When both gaseous and adsorbed phases are ideal, the chromatographic retention volume, which has been measured by Karger et al.[5] and which is easily related to K_H, can be predicted, using the following equation:[38]

$$V_A = \frac{1}{8\pi^2 A}\int\cdots\int [\exp(-\phi/RT) - 1] \times \sin\theta\, dx\, dy\, dz\, d\theta\, d\varphi\, d\psi \tag{17}$$

The differential energy of adsorption at zero surface coverage is then obtained from the change of V_A with temperature

$$\overline{\Delta U} = -R\frac{d\ln V_A}{d(1/T)} \tag{18}$$

Thus $\overline{\Delta U}$ can be predicted from the value of the adsorption potential for all orientations and positions of the molecule on the adsorbent surface, according to the following relation and neglecting unity in eq 17:

$$\overline{\Delta U} = \frac{\int\cdots\int (-\phi/RT)\exp(-\phi/RT)\sin\theta\, dx\, dy\, dz\, d\theta\, d\varphi\, d\psi}{\int\cdots\int \exp(-\phi/RT)\sin\theta\, dx\, dy\, dz\, d\theta\, d\varphi\, d\psi} \tag{19}$$

The differential adsorption enthalpy or the isosteric heat of adsorption q_{st} can be predicted using analogous formulas, according to the relation:[39]

$$\overline{\Delta H} = -q_{st} = \overline{\Delta U} - RT \tag{20}$$

The rigorous way to proceed to compare adsorption potential calculations with the experimental heats of adsorption is thus to determine the adsorption potential for each position of the adsorbate molecule on the surface and to integrate eq 19.

However, these calculations are very long and tedious and would need long computer time. Moreover with straight chain alkanes, molecules which possess rotational conformers, the retention volume is given by a combination of all the equations similar to eq 17, written for each rotamer considered as a rigid molecule.[11] The differential energy of adsorption is then derived from V_A using eq 18.

TABLE II: Physical Properties of the Groups of the Adsorbate Molecules and Their Constants of Attraction and Repulsion in Eq 3

Absorbate molecule group	Polarizability, Å³	Diamagnetic susceptibility, 10^{-5} Å³	C_{ij_1}, kcal Å⁶/mol	C_{ij_2}, kcal Å⁸/mol	B_i, kcal Å¹²/mol
CH_3— (alkanes)	2.26[a]	−2.38[a]	1459	2262	1571 × 10³
CH_2— (alkanes)	1.83[a]	−1.89[a]	1168	1834	1260 × 10³
CH= (aromatics)	1.72[b]	−1.53[b]	1004	1746	827 × 10³
CH_3— (toluene)	2.25[b]	−2.12[b]	1360	2272	1480 × 10³

[a] From ref 42. [b] From ref 13.

TABLE III: Dispersion Force Contribution to the Adsorption Potential Calculated for Different Adsorption Sites (z = 3.40 Å; R = 2.9 Å)

Adsorption site (see Figure 2)	Adsorption potential (dispersion force contribution), kcal/mol: $-CH_3$ (alkanes)	$-CH_2-$ (alkanes)	−CH= (aromatics)	$-CH_3$ (toluene)
O'				
$x = 0; y = 0$	−1.07	−0.86	−0.86	−1.00
B'				
$x = R\sqrt{2}/3; y = 0$	−1.13	−0.91	−0.83	−1.06
C'				
$x = 2R\sqrt{2}/3; y = 0$	−1.10	−0.88	−0.78	−1.03
D'				
$x = -R\sqrt{2}/2; y = 0$	−1.14	−0.92	−0.84	−1.07
E'				
$x = -2R\sqrt{2}/3; y = 0$	−1.13	−0.91	−0.81	−1.06
F'				
$x = 0; y = R\sqrt{6}/6$	−1.13	−0.91	−0.85	−1.06
G'				
$x = 0; y = R\sqrt{6}/3$	−1.13	−0.90	−0.81	−1.06
Mean	−1.12	−0.90	−0.82	−1.05

TABLE IV: Comparison between the Differential Adsorption Energy (Experimental) and the Calculated Minimum Adsorption Potential on the Surface of Liquid Water

		Minimum adsorption potential, kcal/mol	Exptl differential adsorption energy, kcal/mol[a]
n-Pentane	Dispersion forces contribution	−4.94	
	Induction forces contribution	−0.98	
	Total	−5.92	−5.7
n-Hexane	Dispersion forces contribution	−5.84	
	Induction forces contribution	−1.16	
	Total	−7.00	−6.6
n-Heptane	Dispersion forces contribution	−6.74	
	Induction forces contribution	−1.34	
	Total	−8.08	−7.5
Benzene	Dispersion forces contribution	−4.92	
	Induction forces contribution	−1.12	
	Quadrupole interaction	−2.17	
	Total	−8.20	−7.5
Toluene	Dispersion forces contribution	−5.97	
	Induction forces contribution	−1.36	
	Quadrupole interaction	−2.17	
	Total	−9.50	−8.9

[a] Reference 5.

The absolute value of the minimum of the adsorption potential has been compared several times directly to the isosteric heat of adsorption.[16,17,40,41] Useful results have been obtained. Exact molecular statistical calculations of the adsorption heats of C_1–C_5 straight chain alkanes and benzene on graphite[11] have shown that the minimum adsorption potential Φ_0 is about 0.5–1.5 kcal/mol lower than the differential energy of adsorption in the temperature range where experiments are usually carried out.

For instance, for benzene on graphite[10] $\Phi_0 = -9.84$ kcal/mol while in the classical approximation (eq 19) $\overline{\Delta U}$ is −8.68 kcal/mol at 293 K. For *n*-pentane on graphite,[11] if it is assumed that all CH_3 and CH_2 groups are in contact with the surface, $\Phi_0 = -9.43$ kcal/mol, while $\overline{\Delta U} = -8.90$ kcal/mol (q_{st} = 9.42 kcal/mol).

As we use the same model to calculate the adsorption of hydrocarbons on liquid water, we can estimate with a good approximation that the calculated differential adsorption energy is 0.5–1.2 kcal/mol higher than the minimum value of the adsorption potential in the temperature range where the gas chromatographic experiments were carried out.

Results and Discussion

The minimum value of the adsorption potential has been calculated for three alkanes (*n*-pentane, *n*-hexane, *n*-heptane) and two aromatic compounds (benzene and toluene) according to eq 1. As noted previously, the adsorption potential is minimum when the molecules are adsorbed flat on the surface.

With the alkanes only dispersion forces and the induction force caused by the electric field of water are involved in the interaction between the adsorbate and the liquid surface. For benzene and toluene the quadrupole interaction with the electric field must also be included (eq 5). As the molecules studied have no dipole moment or a very low one (toluene) parallel to the adsorbent surface, we omitted the second term of eq 5.

Table II lists the values of the polarizabilities and diamagnetic susceptibilities of hydrocarbon structural units used for the calculation of the dispersion forces. The CH_3– and $-CH_2-$ groups have been considered for the alkanes, the –CH= aromatic group has been considered for toluene and benzene, and the aromatic $-CH_3$ group for toluene. Table II also presents the values of the attraction and repulsion constants of eq 3. The adsorption energy resulting

TABLE V: Electrostatic Interaction of Benzene with Liquid Water

Adsorption site = 2.9 Å	Hydrogen direction	$\overline{F}_z$ 10^5 esu cm^{-2}	$\overline{F'}_z$ 10^{13} esu cm^{-3}	Quadrupole interaction, kcal/mol	$\overline{F^2}$ 10^{10} esu cm^{-4}	Induced electrostatic interaction, kcal/mol
$x = 0$	+	1.831	−1.730	−6.98	3.389	2.52
$y = 0$	−	−1.462	1.105	4.46	2.164	1.61
$z = 3.40$ Å	Mean	0.185	−0.313	−1.26	2.777	2.07
$x = R\sqrt{2}/3$	+	1.072	−0.619	−2.50	1.745	1.30
$y = 0$	−	−1.048	0.606	2.45	1.428	1.06
$z = 3.40$ Å	Mean	0.012	−0.007	−0.03	1.587	1.18
$x = 2R\sqrt{2}/3$	+	0.315	0.066	0.26	0.448	0.33
$y = 0$	−	−0.482	0.162	0.65	0.578	0.46
$z = 3.40$ Å	Mean	−0.084	0.114	0.46	0.513	0.38
$x = -R\sqrt{2}/3$	+	1.085	−0.644	−2.60	1.753	1.30
$y = 0$	−	−1.034	0.579	2.33	1.409	1.05
$z = 3.40$ Å	Mean	0.026	−0.033	−0.13	1.581	1.18
$x = -2R\sqrt{2}/3$	+	0.344	0.028	0.11	0.457	0.34
$y = 0$	−	−0.459	0.131	0.53	0.548	0.41
$z = 3.30$ Å	Mean	−0.058	0.079	0.32	0.502	0.37
$x = 0$	+	1.220	−0.812	−3.28	2.035	1.51
$y = R\sqrt{6}/6$	−	−1.127	0.687	2.77	1.565	1.15
$z = 3.40$ Å	Mean	0.046	−0.063	−0.26	1.800	1.34
$x = 0$	+	0.477	−0.046	−0.19	0.641	0.48
$y = R\sqrt{6}/3$	−	−0.585	0.204	0.82	0.752	0.56
$z = 3.40$ Å	Mean	−0.054	0.079	0.32	0.697	0.52
Mean	+	0.906	−0.537	−2.17	1.495	1.11
	−	−0.885	0.496	2.00	1.206	0.90
	Mean	0.010	−0.021	−0.08	1.351	0.00

from the dispersion forces has been calculated from the mean value of the adsorption energies of the corresponding group located on the different adsorption positions on the water surface designed as O′, B′, ... (Figure 2), and at the equilibrium distance $z_0 = 3.40$ Å. Table III presents the dispersion force contribution for each group in each of the seven positions and the resulting mean values.

For the *n*-alkanes, the electrostatic attraction potential consists solely of the first term of eq 5, which accounts for the induction interaction between the water and the adsorbed molecule. When we include both the dispersion and the induction terms, the total minimum adsorption potentials for the *n*-alkanes on the water surface can be obtained, as shown in Table IV. Also shown in Table IV are the dispersion and induction force contributions to the adsorption potential as well as the experimental adsorption energies for zero surface coverage obtained by Karger et al.[5] When compared to the experimental differential energy, the minimum adsorption potential of *n*-alkanes calculated when all CH_3 and CH_2 groups are in contact with the surface is lower, although not as much as expected from the theoretical considerations discussed above, especially for *n*-pentane. The agreement, however, is very good if one considers the approximation made in our calculations concerning the structure of liquid water. It is also interesting to note that the induction force contribution is roughly 16% of the total adsorption potential.

For benzene and toluene the sum of the dispersion force and induction force contributions to the adsorption potential gives a value which is 1.5 kcal/mol less negative than the experimental adsorption energy, as seen in Table IV. We must include a contribution for the quadrupole interaction of the aromatic species with the water surface, in order to obtain closer agreement.

The electrostatic interaction of the benzene quadrupole moment ($Q_{zz} = -5.6 \times 10^{-26}$ esu cm^3 [36]) with the liquid field has been calculated (Table V). Included in this table is the value of the electric field F_z and its gradient along the vertical (Oz axis) for the different adsorption sites. The hydrogen direction is designated by plus sign when the hydrogen of the central molecule is oriented toward the gaseous phase and by minus sign when the hydrogens are oriented toward the liquid phase.

Table V shows that the only hypothesis which takes into account the higher experimental adsorption energy of benzene is that with the hydrogen directed toward the vapor phase. When the mean value for all orientations (+ and −) and adsorption sites is considered, a very low attraction interaction is found (−0.08 kcal/mol). The attraction potential calculated with a positive hydrogen orientation balances almost exactly the repulsion potential calculated with the hypothesis that both hydrogens are oriented toward the liquid phase.

The benzene quadrupole interaction is taken as −2.17 kcal/mol, calculated as a mean from different positions of the molecule lying flat on the surface at the equilibrium distance ($z_0 = 3.40$ Å). The toluene quadrupole interaction should be very close to that of benzene. Its value has not been calculated because no value of the quadrupole moment was available from the literature. It needs to be noted that the value of −2.17 kcal/mol is an approximation of the aromatic quadrupole interaction as the rigorous way to proceed would be to calculate the differential adsorption energy for all orientations of the molecule and on the whole surface of the adsorbent according to eq 19.

We can conclude however that benzene or toluene are adsorbed with a higher probability on the areas where the hydrogens are directed toward the vapor phase and thus where the interaction energy is higher. This result is implicit in eq 19 which gives the differential adsorption energy as an average value calculated on the whole surface, with a probability factor $e^{-\phi/RT}$.

The different contributions to the adsorption potential for benzene and toluene are reported in Table IV. The minimum value of the adsorption potential is more negative than the experimental heat of adsorption (0.7 kcal/mol for

benzene and 0.6 kcal/mol for toluene). This is in satisfactory agreement with the theory. The results of Table IV show that the contribution of the donor–acceptor type interaction similar to that occurring in the adsorption on acidic adsorbents discussed by Kiselev[38] is explained by the quadrupole interaction with the electric field of liquid water. It is the major effect of the hydrogen bonding that may occur between the protons of the liquid interface and the π electrons of the adsorbed molecule.

In contrast to adsorption on solid surfaces, the liquid water adsorbent has a significant vapor pressure at the temperatures of these experiments (~15 °C). At equilibrium we can anticipate that water molecules are continually evaporating and condensing on the surface. Thus, the assumption of no water–adsorbate interactions in the plane of the adsorbed species (or indeed above this plane) may not be correct. Hence, we decided to calculate the adsorption potential, assuming the adsorbate is surrounded by some water liquid layers (i.e., penetration of the adsorbate into the liquid surface). We observed an increasing negative adsorption potential with the number of layers of water surrounding the adsorbate molecule (e.g., about 0.5 kcal/mol for one layer of water vapor) representing the adsorbate–water vapor interaction. While this additional interaction permits a still better agreement between the adsorption potential and the experimental adsorption energy, we cannot positively state that such surface perturbation does indeed take place.

Finally, it would seem from our calculations that surface perturbation[43,44] cannot be used to explain the observed high heat of adsorption on an ice surface of an n-alkane molecule. When the calculation is carried out for ice (R = 2.76 Å), the values of the adsorption potential are not very different from the values presented in this paper, and the increase in the absolute value when the molecule is surrounded by H_2O is only 0.5–1 kcal/mol.

Conclusion

The structure model selected in this study for interfacial water assumes that oxygen atoms occupy on the average positions which are those of an expanded ice Ih structure for at least 10 layers within the surface. The adsorption potential calculated according to the above model is in reasonable agreement with the experimental differential energy of adsorption measured by gas chromatography. However, on the basis of these results no conclusive statements can be made on the structure, for other structure models may fit the experimental data as well.

Our calculations demonstrate that the relatively low heats of adsorption observed on water when compared with those obtained on solid adsorbents, such as, graphite, boron nitride, and silica gel, are due to the low density of the attractive force centers consisting of hydrogen bonded water molecules.

The interaction between n-alkanes and the water interface is mainly caused by the van der Waals dispersion forces shown by our calculations.

Considering that the n-alkanes are nonspecifically adsorbed on liquid water, as assumed by Kiselev in his classification of adsorbate–adsorbent interactions,[38] the specificity of the water interface toward benzene and toluene has been estimated to be 25% of the total adsorption potential. This specificity results from the interaction between the quadrupole of the adsorbate molecule and the electric field acting on the surface, when on the average the molecule is adsorbed on the areas where the hydrogen atoms point out toward the vapor phase at the gas–liquid interface.

Our calculations show that it is the quadrupole interaction with the electric field of liquid water which is the major effect of the OH group interaction of the adsorbent with the π electrons of the adsorbed molecule.[38]

A similar electrostatic interaction caused by the presence of OH groups on the silica surface may explain the specific adsorption of aromatic molecules on these adsorbents. The role and importance of the quadrupole in adsorption phenomenon, already stressed in ref 23, is clearly demonstrated in this work, where a general scheme for the calculation of this interaction is given. This scheme is valid even if the geometric model is partially disordered.

Acknowledgment. This work is supported in part by a grant to B.L.K. from the National Science Foundation.

References and Notes

(1) A. Hartkopf and B. L. Karger, *Acc. Chem. Res.*, **6**, 209 (1973).
(2) W. Drost-Hansen, *Ind. Eng. Chem.*, **61** (11), 10 (1969).
(3) N. H. Fletcher, "The Chemical Physics of Ice", Cambridge University Press, Cambridge, 1970.
(4) F. Franks, Ed., "Water, A Comprehensive Treatise", Vol. I, Plenum Press, New York, N.Y., 1973.
(5) B. L. Karger, R. C. Castells, P. A. Sewell, and A. Hartkopf, *J. Phys. Chem.*, **75**, 3870 (1971).
(6) J. W. King, A. Chatterjee, and B. L. Karger, *J. Phys. Chem.*, **76**, 2769 (1972).
(7) M. Blank and R. H. Ottewill, *J. Phys. Chem.*, **68**, 2206 (1964).
(8) B. Case and R. Parsons, *Trans. Faraday Soc.*, **63**, 1224 (1967).
(9) N. H. Fletcher, *Phil. Mag.*, **18**, 1287 (1968).
(10) A. V. Kiselev and D. P. Poshkus, *Trans. Faraday Soc.*, **59**, 176, 428, 1438 (1963); D. P. Poshkus, *Discuss. Faraday Soc.*, **40**, 195 (1965).
(11) A. V. Kiselev, D. P. Poshkus, and A. Y. Afreimovich, *Russ. J. Phys. Chem.*, **44**, 545 (1970).
(12) N. N. Avgul, A. A. Isirikyan, A. V. Kiselev, I. A. Lygina, and D. P. Poshkus, *Izv. Akad. Nauk SSSR, Otd. Khim. Nauk*, 1314 (1957).
(13) N. N. Avgul, A. V. Kiselev, I. A. Lygina, and D. P. Poshkus, *Izv. Akad. Nauk SSSR, Otd Khim. Nauk*, 1196 (1959).
(14) C. Vidal-Madjar, L. Jacob, and G. Guiochon, *Bull. Soc. Chim. Fr.*, 3105, 3110 (1971).
(15) A. D. Crowell and Chai Ok Chang, *J. Chem. Phys.*, **43**, 4364 (1965).
(16) G. Curthoys and P. E. Elkington, *J. Phys. Chem.*, **71**, 1477 (1967).
(17) A. V. Kouznetsov, C. Vidal-Madjar, and G. Guiochon, *Bull. Soc. Chim. Fr.*, 1440 (1969).
(18) A. V. Kiselev, A. A. Lopatkin, B. I. Lourie, and S. Shpigel, *Russ. J. Phys. Chem.*, **43**, 1498 (1969).
(19) A. V. Kiselev, A. A. Lopatkin, and E. R. Razumova, *Russ. J. Phys. Chem.*, **43**, 1004 (1969).
(20) A. V. Kiselev, A. A. Lopatkin, and L. G. Ryaboukhina, *Bull. Soc. Chim. Fr.*, 1324 (1972).
(21) A. G. Bezus, A. V. Kiselev, A. A. Lopatkin, and Pham Quang Du, *J. Colloid Interface Sci.*, **45**, 386 (1973).
(22) G. D. Mayorga and D. L. Petersor, *J. Phys. Chem.*, **76**, 1641, 1647 (1972).
(23) G. L. Kington and A. C. Macleod, *Trans. Faraday Soc.*, **55**, 1799 (1959).
(24) S. Ross and J. P. Olivier, "On Physical Adsorption", Wiley-Interscience, New York, N.Y., 1964.
(25) D. M. Young and A. D. Crowell, "Physical Adsorption of Gases", Butterworths, London, 1962.
(26) A. D. Crowell and R. B. Steele, *J. Chem. Phys.*, **34**, 1347 (1961).
(27) C. Pisani, F. Ricca, and C. Roetti, *J. Phys. Chem.*, **77**, 657 (1973).
(28) A. D. Buckingham, *Q. Rev., Chem. Soc.*, **13**, 183 (1959).
(29) F. V. Lenel, *Z. Phys. Chem.*, **B23**, 379 (1933).
(30) S. Brunauer, "The Adsorption of Gases and Vapours", Clarendon Press, Oxford and Princeton University Press, Princeton, N.J., 1945.
(31) K. Lonsdale, *Proc. R. Soc., Ser. A*, **247**, 424 (1958).
(32) D. Eisenberg and W. Kauzmann, "The Structure and Physical Properties of Water", Clarendon Press, Oxford, 1969.
(33) G. E. Walrafen, "Water, A Comprehensive Treatise", Vol. I, F. Franks, Ed., Plenum Press, New York, N.Y., 1973, Chapter 5.
(34) A. H. Narten and H. A. Levy, "Water, A Comprehensive Treatise", Vol. I, F. Franks, Ed., Plenum Press, New York, N.Y., 1973, Chapter 8.
(35) C. A. Coulson and D. Eisenberg, *Proc. R. Soc., Ser. A*, **291**, 445 (1966).
(36) T. D. Gierke, H. L. Tigelaar, and W. H. Flygare, *J. Am. Chem. Soc.*, **94**, 330 (1972).
(37) D. Neumann and J. W. Moskowitz, *J. Chem. Phys.*, **49**, 2056 (1968).
(38) A. V. Kiselev, "Gas Chromatography 1964", A. Goldup, Ed., The Institute of Petroleum, London, 1965, p 238.
(39) E. L. Pace, "The Solid Gas Interface", Vol. 1, E. A. Flood, Ed., Marcel Dekker, New York, N.Y., 1967 Chapter 4.
(40) G. M. Petov and K. D. Shcherbakova, "Gas Chromatography 1966", A. B. Littlewood, Ed., The Institute of Petroleum, London, 1967, p 50.

(41) A. V. Kiselev, A. V. Kuznetsov, I. Y. Filatova, and K. D. Shcherbakov, *Russ. J. Phys. Chem.*, **44**, 705 (1970).
(42) N. N. Avgul, A. B. Kiselev, and I. A. Lygina, *Izv. Akad. Nauk SSSR, Otd. Khim. Nauk*, 1404 (1961).
(43) A. W. Adamson, L. M. Dormant, and M. Orem, *J. Colloid Interface Sci.*, **25**, 206 (1967).
(44) M. W. Orem and A. W. Adamson, *J. Colloid Interface Sci.*, **31**, 278 (1969).

Study of the N_2O_3–H_2O–HNO_2 Equilibrium by Intensity Measurements in Microwave Spectroscopy[1]

Ravi Varma and R. F. Curl*

Chemistry Department, Rice University, Houston, Texas 77001 *(Received July 23, 1975)*

Publication costs assisted by the National Science Foundation

The energy differences between the lowest states of cis and trans conformers of HNO_2 and DNO_2 have been determined by microwave intensity measurements. The results are ΔE = 372 ± 40 cal for HNO_2 and ΔE = 488 ± 35 cal for DNO_2. Combining the results for the two isotopes, a value of 404 ± 100 cal is obtained for ΔE for HNO_2. The thermodynamic properties of HNO_2 have been recalculated and third law calculations on the equilibrium data for the reactions NO + NO_2 + H_2O ⇄ $2HNO_2$ and N_2O_3 ⇄ NO + NO_2 carried out. These calculations yield $\Delta H°_0$ = 540 (+600, − 100) cal for the reaction N_2O_3 + H_2O ⇄ $2HNO_2$. The value of $\Delta H°_0$ for this reaction has been obtained from microwave intensity measurements on the species involved in the related reactions N_2O_3 + D_2O ⇄ $2DNO_2$ and N_2O_3 + HDO ⇄ HNO_2 + DNO_2. The best value of $\Delta H°_0$ is 1050 ± 300 cal, which is in reasonable agreement with the value obtained from third law calculations.

It has been shown previously[2] that the standard enthalpy of reaction at absolute zero (ideal gas reference state) is obtained directly if the intensity of a rotational transition of each species involved in the chemical reaction is measured, providing that the rotational spectrum has been analyzed and the dipole moment components determined by Stark effect measurements. This has been used to determine the energy difference between two rotamers of the same molecule.[3]

Here we report the use of this method to determine the energy difference between the two rotamers of HNO_2

$$HNO_2(\text{cis}) \rightleftarrows HNO_2(\text{trans}) \quad (1)$$

and to determine the energy difference between the ground states of products and reactants for the reaction

$$N_2O_3 + H_2O \rightleftarrows 2HNO_2 \quad (2)$$

The System NO–NO_2–H_2O. Thermodynamics

If NO, NO_2, and H_2O are mixed, a number of chemical reactions are possible. These include

$$NO + NO_2 \rightleftarrows N_2O_3 \quad (3)$$

$$NO + NO_2 + H_2O \rightleftarrows 2HNO_2 \quad (4)$$

$$2NO_2 \rightleftarrows N_2O_4 \quad (5)$$

$$3NO_2 + H_2O \rightleftarrows 2HNO_3 + NO \quad (6)$$

and the various reactions such as (2) which can be obtained by combining these. The equilibrium for reaction 2 in the gas phase has not been directly studied. However, the equilibria for reactions 3 and 4 have been studied and reaction 2 = reaction 4 − reaction 3.

The equilibrium for reaction 3 has been studied by Abel and Proisl,[4] Verhoek and Daniels,[5] Beattie and Bell,[6] and by Solc and Pour.[7] There appear to be two sets of second law values for $\Delta H°$ at room temperature, about −10.5 kcal/mol obtained by Verhoek and Daniels[5] and Solc and Pour[7] and about −9.5 kcal/mol obtained by Abel and Proisl[4] and Beattie and Bell.[6]

The JANAF Tables[8] appear to favor the results of Beattie and Bell[6] and Abel and Proisl[4] by obtaining a third law $\Delta H°_{298}$ which agrees with the second law values found by these investigators. However, the N_2O_3 torsion is assumed to be free internal rotation and the rotational constants used, which were calculated from an assumed structure, are not in very good agreement with the more recently determined experimental values.[9]

The assignment of the vibrational frequencies of N_2O_3 has been the subject of three investigations. Devlin and Hisatsune[10] gave an assignment of the eight normal modes ν_1 to ν_8 but no assignment of the torsion ν_9. More recently, Bibart and Ewing[11] examined the gas phase infrared spectrum and revised the assignment of Devlin and Hitsatsune. Bibart and Ewing also obtained a value of 63 cm^{-1} for the torsional frequency, ν_9, from a combination band assignment. Still more recently, Bradley, Siddall, Strauss, and Varetti[12] examined the far-infrared spectrum of N_2O_3 and attempted to choose an assignment and force field which would reproduce the inertial defects found by Brittain, Cox, and Kuczkowski.[13] The three studies essentially agree on the assignment of the higher frequency in-plane models ν_1–ν_5. In the two more recent studies the assignments of ν_6 to ν_8 are rearranged and altered. The two more recent studies are close to agreement on a value of ~70 cm^{-1} for the

TABLE I: Previous Studies of NO–NO_2–H_2O Equilibria[a]

	K, atm^{-1}	Second law $\Delta H°$, kcal	Third law $\Delta H°$ JANAF[f]	Third law $\Delta H°$ Present[g]
$NO + NO_2 \rightleftarrows N_2O_3$				
Abel and Proisl[b]	0.702	−9.6	−9.86	−9.42
Verhoek and Daniels[c]	0.475	−10.3	−9.59	−9.19
Beattie and Bell[d]	0.522 ± 0.001[k]	−9.527 ± 0.096	−9.7	−9.25
Solc and Pour[e]	0.456	−10.54	−9.6	−9.16
$NO + NO_2 + H_2O \rightleftarrows 2HNO_2$				
Wayne and Yost[h]	1.74			−9.715
Ashmore and Tyler[i]	1.278	−9.057 ± 0.32		−9.533
Waldorf and Babb[j]	1.38	−9.550		−9.578

[a] K at 25 °C. $\Delta H°$ is determined by the second law method and is usually assumed constant over a range of temperatures near 25 °C. [b] Reference 4. [c] Reference 5. [d] Reference 6. [e] Reference 7. [f] Reference 8. [g] Entropy of N_2O_3 obtained from ref 15. Entropies of NO and NO_2 obtained from ref 14. Resulting $\Delta S°_{298} = -32.30$ eu for $NO + NO_2 \rightleftarrows N_2O_3$. [h] Reference 16. [i] Reference 17. [j] Reference 18. [k] Two times standard deviation listed.

torsional frequency, ν_9, which was not assigned by Devlin and Hisatsune. However, this torsional frequency had been previously estimated by Brittain, Cox, and Kuczkowski[13] as 124 ± 25 cm^{-1} from microwave relative intensity measurements.

Recently Chao, Wilhoit, and Zwolinski[14,15] have calculated the thermodynamic properties of N_2O_3. In their original calculations,[14] they used the vibrational frequencies of Devlin and Hisatsune[10] and treated N_2O_3 as a free internal rotor. In the more recent calculation,[15] they used the vibrational frequencies and internal rotation barrier height of Bibart and Ewing.[11] Since all alternate[12,13] barrier heights are higher and all alternate vibrational assignments[10,12] replace a low frequency with a higher, the values of the entropy and free energy function for N_2O_3 given by Chao, Wilhoit, and Zwolinski[15] are probably upper bounds. Using these values, a revised comparison of the third and second law $\Delta H°_{298}$ may now be made which tends to favor $\Delta H°_{298} = -9.2$ kcal. These results are shown in Table I.

The equilibrium for reaction 4 has been studied by Wayne and Yost,[16] Ashmore and Tyler,[17] and Waldorf and Babb.[18] The agreement between the results of Ashmore and Tyler[17] and Waldorf and Babb[18] is within the range of their experimental errors. The results of these investigations of equilibrium for reactions 3 and 4 are tabulated in Table I.

The entropies and free energy functions of H_2O, NO, and NO_2 at 25 °C are well known.[8,19] The entropy and free energy functions of HNO_2 are less well known. The vibrational frequencies[20,21] and rotational constants[22–24] of both cis and trans HNO_2 and various isotopic modifications are well known also. Less certain is the energy difference between the cis and trans forms. Jones, Badger, and Moore[21] give 500 ± 250 cal/mol as the difference in energy between the ground state of the two forms with the trans lower in energy, while McGraw, Bernitt, and Hisatsune[20] give 531 ± 1000 cal/mol as this difference. Both results were obtained from observations of the temperature dependence of infrared bands. We have obtained 404 ± 100 cal/mol from observation of relative intensities of rotational transitions of the two forms (vide infra). The free energy function and entropy of HNO_2 has been recalculated using this number, and the rotational constants determined by Cox, Brittain, and Finnigan,[23] and the room temperature value is listed in Table II together with these thermodynamic properties for H_2O, NO, NO_2, and N_2O_3. The thermodynamic properties of HNO_2 over a range of temperatures have been calculated and are given in Table III.

TABLE II: Thermodynamic Properties of Molecules Involved in NO–NO_2–H_2O Equilibria[a]

	$S°_{298}$, cal/mol deg	$[-(G° - H°_0)/T]_{298}$, cal/mol deg	$(H°_{298} - H°_0)$, cal/mol
H_2O[b]	45.11	37.17	2367
NO[c]	50.33	42.96	2197
NO_2[c]	57.42	49.20	2450
HNO_2[d]	60.69	51.38	2773
N_2O_3[e]	75.45	61.77	4080
			$\Delta H°_0$,[f] cal
H_2O + *trans*-$DNO_2 \rightleftarrows$ HDO + *trans*-HNO_2			256
H_2O + 2 *trans*-$DNO_2 \rightleftarrows$ D_2O + 2 *trans*-HNO_2			421
cis-HNO_2 + *trans*-$DNO_2 \rightleftarrows$ *trans*-HNO_2 + *cis*-DNO_2			52

[a] Ideal gas reference state. [b] Reference 19. [c] Reference 14. [d] Calculated from the vibrational frequencies of ref 20, the rotational constants of ref 23, and the cis-trans energy difference of 404 cal/mol obtained here. [e] Reference 15. [f] Calculated from the vibrational frequencies of ref 20 and 27.

TABLE III: Thermodynamic Properties of HNO_2

T, K	HNO_2[a] $S°$, cal/mol deg	$-(G° - H°_0)/T$, cal/mol deg	$H°_T - H°_0$, kcal/mol
100	50.28	41.85	0.84
298.15	60.69	51.38	2.77
400	64.15	54.58	3.83
600	69.59	58.74	6.51
800	73.93	62.02	9.53
1000	77.53	64.77	12.75
1500	84.53	70.26	21.41
1000	89.79	74.51	30.56

[a] Calculated from the vibrational frequencies of ref 20, the rotational constants of ref 23, and the cis–trans energy difference of 404 cal/mol obtained here.

Kinetic Considerations

This work is concerned with chemical equilibrium, not kinetics. However, one must be sure that equilibrium for the reaction 2 is established under the conditions of observation. Since we could not observe N_2O_3 at room temperature, equilibrium 2 was studied at dry ice temperature. Reaction 3 is known[16] to be rapid at room temperature. Presumably, the energy of activation is small in analogy to reaction 5. Therefore, equilibrium for reaction 3 would be rapidly achieved at dry ice temperature. On the other hand, the kinetics of reaction 4 have been the subject of

considerable study.[16,25,26] The conclusion[26] reached is that near room temperature the reaction is heterogeneous with a negative energy of activation. The rate is about second order in P_{H_2O} and first order in P_{NO} and P_{NO_2}. Presumably, N_2O_3 is reacting with adsorbed H_2O, explaining the negative energy of activation. Thus, the anomalous stability of HNO_2 at high temperature[25] is rationalized.

We have made the following observations. (1) At room temperature, if 10 mTorr of H_2O, 10 mTorr of NO, and 20 mTorr of NO_2, in that order, are introduced in the microwave absorption cell, HNO_2 lines are very weak or unobservable. (2) At room temperature, if several Torr each of H_2O, NO, and NO_2 are mixed outside the microwave absorption cell, allowed to stand several minutes, and then about 40 mTorr of the mixture is admitted to the microwave absorption cell, strong lines of HNO_2 are observed. (3) If the procedure (1) above is repeated with the absorption cell cooled with dry ice, fairly strong lines of HNO_2 are observed immediately which do not change with time. The conclusion we draw from these observations is that equilibrium for reaction 4 at a total pressure of about 50 mTorr is approached very slowly at room temperature in our apparatus and very rapidly at dry ice temperature. This rather startling result seems to be in accord with the observations of Graham and Tyler.[26]

Experimental Section

These measurements were made using a Hewlett-Packard Model 8460A MRR spectrometer in the region 26.5–40 GHz. Since HNO_2 lines could be observed at room temperature while N_2O_3 lines could not, all measurements of the cis–trans energy difference of HNO_2 (reaction 1) were made at room temperature while all measurements of the N_2O_3–HNO_2 equilibrium were made with the absorption cell packed in dry ice. The two cells of the 8460A are 92 cm in length. Both ends of each cell have to be warmed with a blower fan to prevent condensation of moisture on the windows and on the Stark connector. The dry ice pack ends about 10 cm from each end. Measurement of the temperature of the cell with a thermocouple at the middle of the cell gave −66 °C, while measurements about 12 cm from each end gave about −40 °C. The effective temperature was taken to be −49 °C. This value is a rough average over the cell. The lack of uniform temperature over the length of the cell is the principal source of misgivings about the validity of the results obtained for reaction 2. Some care had to be taken to repack the dry ice every few minutes or the temperature would drift up as a result of sublimation of a cavity through the packed dry ice. Some long term drift of the intensities of absorption lines with time remained and will be discussed further below.

In order to obtain meaningful information concerning an equilibrium with this method, it is essential that the intensity of an absorption line of every chemical species involved in the reaction be measured. There are no H_2O rotational lines found in the region 26.5–40 GHz. Therefore, the measurements were made on one HDO and two D_2O lines. Since the microwave intensity method gives the energy difference between the ground states of the products and the ground states of the reactants and the infrared deuterium isotope shifts are known for water[27] and nitrous acid,[20] the results are easily converted from one isotopic species to another.

Since all species involved in the equilibrium are observed directly, sample purity is of no concern. Commercially available samples of NO_2, NO, and H_2O were used. Similarly, pressure measurements were made only to observe whether there is any drift of total pressure with time.

Results for the Energy Difference between Rotamers of Nitrous Acid

Intensity measurements were made on several lines of *cis*-HNO_2 in comparison with *trans*-HNO_2 and several lines of *cis*-DNO_2 in comparison with *trans*-DNO_2. The basic equation for microwave intensities is

$$\gamma_0\Delta = \frac{8\pi^2\nu_0^2 |\langle J''_{\tau''}F''\|\hat{\mu}\|J'_{\tau'}F'\rangle|^2}{3\upsilon_g kT\, Q_{int}Q_{ns}} w_I N \exp(-E''/kT) \quad (7)$$

where γ_0 is the unsaturated peak absorption coefficient, Δ is the hwhm line width, ν_0 is the center frequency of the absorption, υ_g is the group velocity of light, w_I is the nuclear spin weight for any unresolved nuclear hyperfine levels, Q_{ns} is the nuclear spin partition function for these unresolved nuclear spins, Q_{int} is the internal partition function, N is the total number of molecules/unit volume of the species observed, E'' is the energy of lower level involved in the transition, T is the temperature, k is Boltzmann's constant, and $\langle J''_{\tau''}F''\|\hat{\mu}\|J'_{\tau'}F'\rangle$ is the reduced matrix element of the particular hyperfine transition observed. This reduced matrix element may be expressed[28] as

$$|\langle J''_{\tau''}F''\|\hat{\mu}\|J'_{\tau'}F'\rangle|^2 = [(2F'+1)(2F''+1)] \times \left|\begin{Bmatrix} J'' & F'' & I \\ F' & J' & 1 \end{Bmatrix}\right|^2 |\langle J''_{\tau''}\|\hat{\mu}\|J'_{\tau'}\rangle|^2 \quad (8)$$

where the symbol in curly brackets is the 6j symbol and I is the nuclear spin giving rise to the hyperfine structure.

$$|\langle J''_{\tau''}\|\hat{\mu}\|J'_{\tau'}\rangle|^2 = |\mu_\alpha|^2 S^\alpha_{J'',\tau'',J',\tau'} \quad (9)$$

where μ_a (α = a, b, or c) is the molecule fixed dipole moment giving rise to the transition and $S^\alpha_{J'',\tau'',J',\tau'}$ is the rotational line strength. If the relative intensities of two lines each belonging to a different rotamer are measured, the energy difference between the two lower levels of the transitions may be calculated

$$E_c(J''_c) - E_t(J''_t) = kT \ln\left\{\frac{(\gamma_0\Delta)_t |\langle J''_{\tau''}F''\|\hat{\mu}\|J'_{\tau'}F'\rangle_t|^2 \upsilon_g^t \nu_{oc}^2}{(\gamma_0\Delta)_c |\langle J''_{\tau''}F''\|\hat{\mu}\|J'_{\tau'}F'\rangle_t|^2 \upsilon_g^c \nu_{ot}^2}\right\} \quad (10)$$

where the label c refers to the cis rotamer and the label t refers to the trans and the spin weights w_I and nuclear spin partition functions Q_{ns} have been assumed the same for both rotamers.

The presence of hyperfine structure arising from the nitrogen nuclear quadrupole coupling causes a complicating problem. The quadrupole structure of all rotational transitions of HNO_2 and DNO_2 with $J < 25$ was predicted using the coupling constants determined by Cox, Brittain, and Finnigan.[23] Only those absorption lines which were well resolved, single, hyperfine components or which had unresolved hyperfine structure with all hyperfine components within a 0.3-MHz range were considered as possible candidates for intensity measurement. The lines actually chosen were checked for completeness of Stark modulation and freedom from overlap of nearby lines or the Stark lobes of nearby lines. The intensity was measured by recording the line and taking the product of peak height and full width at half maximum. Power saturation could not be completely avoided because relatively high microwave powers (~1 mW) were required to obtain good signal-to-noise ratios,

TABLE IV: Nitrous Acid Lines Chosen for Intensity Measurement

Line no.	Rotational transition	Hyperfine $F' \leftarrow F''$	ν_0, MHz	$\lvert\langle J'_\tau F' \rvert\lvert\mu\rvert\rvert J''_{\tau''} F''\rangle\rvert^2$ D²	$E_{J''\tau''}$, THz
trans-HNO_2					
1 Ht	$11_{2,9} \leftarrow 12_{1,12}$	$11 \leftarrow 12$	36 503.80	1.95[a]	1.854
2 Ht		$10 \leftarrow 11$ $12 \leftarrow 13$ $\Delta\nu \sim 0.2$ MHz	36 501.11	3.92[a,b]	
3 Ht	$12_{2,10} \leftarrow 13_{1,13}$	$12 \leftarrow 13$	28 924.20	1.93[a]	2.149
4 Ht		$11 \leftarrow 12$ $13 \leftarrow 14$ $\Delta\nu \sim 0.2$ MHz	28 921.41	3.89[a,b]	
cis-HNO_2					
1 Hc	$10_{1,10} \leftarrow 9_{2,7}$	$10 \leftarrow 9$	32 739.59	2.00[c]	1.368
2 Hc	$18_{4,14} \leftarrow 19_{3,17}$	$\Delta\nu < 0.07$ MHz	35 529.60	16.92[b,c]	5.322
trans-DNO_2					
1 Dt	$11_{2,9} \leftarrow 12_{1,12}$	$11 \leftarrow 12$	38 976.87	1.93[d]	1.735
2 Dt		$10 \leftarrow 11$ $12 \leftarrow 13$ $\Delta\nu \sim 0.2$ MHz	38 974.32	3.87[b,d]	
3 Dt	$12_{2,10} \leftarrow 13_{1,13}$	$11 \leftarrow 12$ $13 \leftarrow 14$ $\Delta\nu \sim 0.2$ MHz	31 139.70	3.84[b,d]	2.010
cis-DNO_2					
1 Dc	$15_{4,11} \leftarrow 16_{3,14}$	$\Delta\nu < 0.02$ MHz	30 083.5	12.51[b,e]	3.777
2 Dc	$19_{3,17} \leftarrow 18_{4,14}$	$\Delta\nu < 0.3$ MHz	35 454.84	15.07[b,e]	5.031

[a] Based on $\mu_b = 1.242$ D as determined for $HO^{15}NO$ in ref 23. [b] The reduced matrix elements of unresolved quadrupole components are summed. [c] Based on $\mu_b = 1.389$ D as determined for $HO^{15}NO$ in ref 23. [d] Based on $\mu_b = 1.208$ D as determined for DONO in ref 23. [e] Based on $\mu_b = 1.35$ D. This number is obtained by correcting the *cis*-HNO_2 dipole moment given in ref 23 for the rotation of principal axes on deuteration which gives 1.34 D and then increasing the dipole moment by 0.01 D to account for the effect of zero point vibration changes.

but was minimized by working at as high a pressure as possible without electrical discharge as a result of the Stark modulation. This pressure was about 70 mTorr as measured with a Baratron gauge. The line widths of all lines which were compared were approximately equal, implying the same relaxation times. Therefore, the difference in the amount of power saturation of the two lines being compared depends on the difference in electric dipole transition moment of the two lines. For both HNO_2 and DNO_2, the transition moments of the trans lines used for comparison are about a factor of 2 smaller than those of the cis lines used. Thus the cis lines are expected to power saturate more easily than the trans. Power saturation would, therefore, give rise to a systematic error in the direction of a higher energy for the cis rotamer relative to the trans.

If the vacuum system had been cleaned thoroughly enough, either by taking down the absorption cells and washing them or by several treatments with about 50 Torr of NO_2, the nitrous acid lines were essentially constant in intensity at room temperature for several hours. In most runs, however, there remained some residual time drift in intensity which was removed by time interpolation assuming the intensities varied linearly with time. All measurements were made at room temperature.

The lines chosen for measurement are listed in Table IV for both HNO_2 and DNO_2. Table V summarizes the results obtained for the cis–trans energy difference for HNO_2 and DNO_2. The difference between the zero point vibrational energies of HNO_2 and DNO_2 may be corrected using the known vibrational frequencies.[20] The agreement between the observations on the two isotopes is satisfactory.

Results for $\Delta H°_0$ of the Reaction $N_2O_3 + H_2O \rightleftarrows 2HNO_2$

As was mentioned previously, there are no H_2O lines in the region 26.5–40 GHz. Therefore, the equilibria of the two related reactions

$$N_2O_3 + D_2O \rightleftarrows 2DNO_2 \quad (11)$$

and

$$N_2O_3 + HDO \rightleftarrows DNO_2 + HNO_2 \quad (12)$$

were studied. For both reactions the value of $\Delta H°_0$ can be related to the intensity measurement by

$$\Delta H°_0 = -\Delta E_J - RT \ln (R_\nu R_I / R_\nu^2 R_\mu^2 R_w) + \tfrac{3}{2} RT \ln R_M \quad (13)$$

where for reaction 11, for example

$$\Delta E_J = 2(E_0 - E^{(0)})_{DNO_2} - (E_0 - E^{(0)})_{N_2O_3} - (E_0 - E^{(0)})_{D_2O} \quad (14)$$

and $(E_0 - E^{(0)})$ is the energy that the lower level involved in the transition is above the lowest level of the molecule. The R's are ratios of the same structure as the equilibrium constant for the corresponding reaction. Thus

$$R_\nu = \frac{(\upsilon_g^{DNO_2})^2}{\upsilon_g^{N_2O_3} \upsilon_g^{D_2O}} \quad (15)$$

where the υ_g's are the group velocities of light in the absorption cell at the frequencies of the corresponding rotational transitions. The quantity R_I is the ratio of the observed intensities, R_ν is the ratio of line frequencies, R_μ is the ratio of the dipole moment reduced matrix elements, R_w is the ratio of the nuclear spin weights, and R_M is the ratio of the molecular weights.

The problems involved in choosing the lines to be used for intensity measurements and the conditions of measurement have already been discussed for HNO_2 and DNO_2. For HDO there is no choice of line for measurement since there is only one HDO line in the accessible frequency region.[29] For D_2O there are two lines observable.[30] These two

TABLE V: Intensity Measurements and Cis–Trans Energy Differences in Nitrous Acid

Data label	Temp, °C	Cis line	Trans line	Peak height,[a] mm	Δ, MHz	$(E_{cis} - E_{trans})$,[b] cal/mol	Weight
				HNO_2			
A	28.8	2 Hc		131.2	0.500		
			4 Ht	43.6	0.595	264	1
B	29.0	2 Hc		159.6	0.450		
			2 Ht	106.4	0.610	452	1
			1 Ht	56.2	0.500	365	1
		2 Hc		133.3	0.575		
			4 Ht	60.0	0.675	439	0.5
		2 Hc		111.1	0.690		
			3 Ht	30.9	0.510	294	0.5
C	29.0	2 Hc		127.1	0.525		
			2 Ht	110.4	0.610	508	1
			1 Ht	55.1	0.550	455	1
D	29.5	2 Hc		129.2	0.660		
			4 Ht	58.0	0.675	356	1
E	30.0	2 Hc		132.0	0.595		
			2 Ht	94.5	0.810	500	1
		2 Hc		170.2	0.440		
			4 Ht	64.4	0.520	340	1
			3 Ht	32.8	0.515	352	0.5
F	31.0	2 Hc		141.2	0.610		
			4 Ht	53.0	0.630	249	1
		2 Hc		119.6	0.702		
			3 Ht	30.9	0.490	219	1
		2 Hc		161.6	0.490		
			4 Ht	60.1	0.555	307	1
		2 Hc		133.5	0.610		
			3 Ht	34.7	0.460	269	0.5
G	30.0	2 Hc		150.0	0.495		
			4 Ht	60.6	0.470	248	1
		2 Hc		133.8	0.565		
			3 Ht	29.7	0.430	176	1
		2 Hc		124.8	0.625		
			4 Ht	57.0	0.630	358	1
			3 Ht	31.0	0.675	456	1
H	30.1	2 Hc		80.3	0.395		
			4 Ht	36.1	0.440	409	1
		2 Hc		76.3	0.415		
			3 Ht	15.0	0.490	369	1
		2 Hc		72.3	0.435		
			2 Ht	60.0	0.485	469	1
			1 Ht	29.0	0.420	361	0.5
		2 Hc		93.0	0.480		
			4 Ht	47.0	0.475	408	1
		1 Hc		23.0	0.430		
			4 Ht	41.0	0.495	254	0.5
		1 Hc		21.5	0.460		
			2 Ht	75.0	0.630	453	1.0
			1 Ht	36.5	0.550	354	1.0
		2 Hc		79.0	0.580		
			2 Ht	75.0	0.630	534	1.0
			1 Ht	36.5	0.550	436	1.0
						Av 372 ± 40[c]	
Run no.							
				DNO_2			
I	27.8	1 Dc[c]		55	0.601		
			2 Dt	72	0.615	370	0.5
			3 Dt	46.5	0.54	319	0.5
			1 Dt	45.2	0.705	590	0.5
II	28.6	1 Dc		121	0.394		
			2 Dt	149	0.53	499	1
		1 Dc		93	0.498		
			1 Dt	77	0.515	521	1
IV	28.5	2 Dc		160	0.365		
			2 Dt	165	0.435	505	1
		2 Dc		146	0.385		
			2 Dt	165	0.435	528	1
V	29.0	1 Dc		97	0.259		
			2 Dt	113	0.405	557	1
		1 Dc		65.5	0.359		1
			3 Dt	60.5	0.425	539	
		2 Dc		81.5	0.446		
			3 Dt	60.5	0.425	463	1

TABLE V (*Continued*)

Run no.	Temp, °C	Cis line	Trans line	Peak height,[a] mm	Δ, MHz	$(E_{cis} - E_{trans})$,[b] cal/mol	Weight
VIII	27.3	2 Dc		157	0.38		
			1 Dt	81.2	0.39	417	1
		2 Dc		141	0.391		
			3 Dt	84	0.46	454	1
						Av 488 ± 35[c]	
						Cor[d] −52	
						$E_c - E_t$ (HNO_2 basis) 436 ± 35[c]	
						Av of HNO_2 and DNO_2 results 404 ± 100[e] cal/mol	

[a] Sometimes corrected for small differences in spectrometer gain setting. [b] Energy difference between lowest level of cis rotamer and lowest level of trans rotamer. [c] Two standard deviations of average. [d] Correction for the difference in the zero point energies of the deuterium as compared to the hydrogen systems. [e] Estimated uncertainty.

TABLE VI: N_2O_3 and Water Lines Chosen for Intensity Measurement

		Rotational transition	ν_0, MHz	$\lvert\langle J'\tau''\lvert\lvert\hat{\mu}\rvert\rvert J'\tau'\rangle\rvert^2$	w_I/Q_{ns}	$E_{J'',\tau''}$ THz
N_2O_3		$5_{0,5} \leftarrow 4_{0,4}$	35 137.65	20.71	1	0.072
D_2O	α	$8_{7,1} \leftarrow 9_{6,4}$	30 778.48	0.666	2/3	26.370
	β	$8_{7,2} \leftarrow 9_{6,3}$	30 182.49	0.666	1/3	26.370
HDO		$7_{1,7} \leftarrow 6_{2,4}$	26 880.38	0.468	1	12.172

TABLE VII: Summary of Equilibrium Measurements on N_2O_3–H_2O–HNO_2 Systems

Run series	Lines used	Time,[a] min	Gain, dB	Height, mm	Line width,[b] MHz	R_I	$\Delta H°_0$,[c] kcal
A. For A the sample was replaced after most measurements. A total of six measurements were made. The results cited are for measurement set 2 which gives the highest value of $\Delta H°_0$.							
DNO_2	2 Dc	38	57	92	0.450		
D_2O	α	34	66	114	0.390		
N_2O_3		46	60	88	0.710	2.46	1.47
A'. Only a single set of measurements was made for A'.							
DNO_2	2 Dc	23	44	102	0.485		
D_2O	β	26	46	102	0.340		
N_2O_3		17	60	51	0.375	29.3	0.69
B. Run B was continued for about 90 min.							
HNO_2	4 Ht	17	50	97	0.460		
DNO_2	2 Dc	13	60	109	0.380		
HDO		31	30	51	0.320		
N_2O_3		8	60	68	0.475	*d, e*	*d*
C. Run C was continued for about 90 min.							
HNO_2	4 Ht	19[f]	50	67	0.500		
DNO_2	2 Dt	5[f]	60	98	0.420		
HDO		10[f]	50	87	0.350		
N_2O_3		15[f]	50	64	0.580	*d, g*	*d*

[a] Measured from completion of introduction of sample. [b] hwhm. [c] For reaction 1. [d] No R_I or $\Delta H°_0$ calculated since time dependence was removed by graphing as in Figure 1. [e] The points plotted in Figure 1a are twice the product of height by line width without gain correction. [f] The times in Figure 1b. Sample introduction was completed at $t = -9$ min. [g] The points plotted in Figure 1b are the product of height by line width corrected to a standard gain of 60 dB.

lines are a prolate asymmetry pair with one having a spin weight, and therefore an intensity, twice the other. The more intense D_2O line was used almost exclusively. Only one N_2O_3 line was, in fact, used for measurement. For N_2O_3 the nitrogen nuclear quadrupole structure is unresolved. For all the lines the Stark voltage had to be sufficiently high for complete modulation and care had to be taken to avoid overlap with other lines or the Stark lobes of other lines. The lines of HDO, D_2O, and N_2O_3 used are listed in Table VI.

All measurements were made with the microwave absorption cells packed in dry ice. The dry ice was stirred every few minutes to avoid cavity formation. Even so, the stability of measurements with time was much poorer than was the case for the HNO_2 and DNO_2 room temperature measurements. The intensity of the N_2O_3 line decreased slowly with time, becoming roughly a factor of 2 weaker after about 1 hr. The intensity of the HDO line increased slowly with time, becoming about a factor of 2 stronger after 1 hr. No time study was made of the D_2O line. The trend of the HNO_2 and DNO_2 intensities was less clear and less pronounced. The intensities are plotted vs. time in Figure 1. The intensity ratio analogous to the equilibrium constant for reaction 12, which should be constant if the reaction is in equilibrium and if the temperature is constant, drifted significantly during a run.

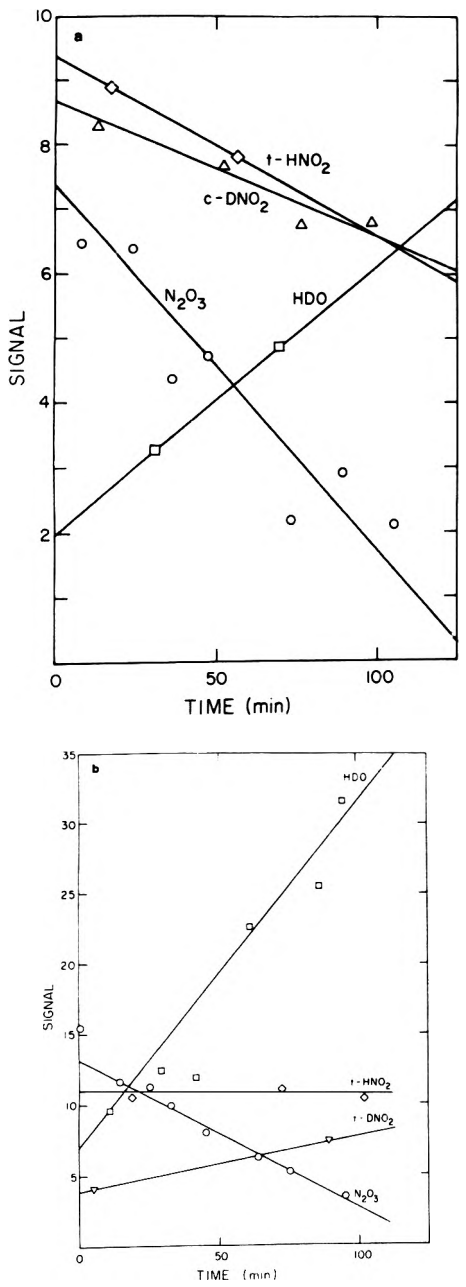

Figure 1. Time dependence of the intensities of the various species HDO, N_2O_3, HNO, and DNO_2 observed in runs B (a) and C (b) as described in Table VII.

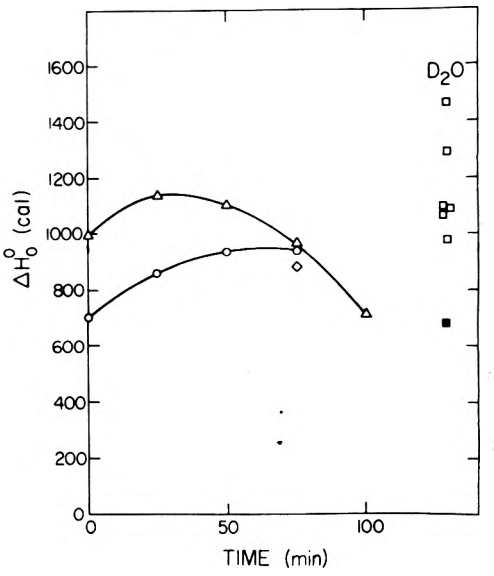

Figure 2. Summary of the information on ΔH°_0 for reaction 2 obtained from intensity measurement. The circles are obtained from run B (HDO), the triangles from run C (HDO), the squares from run A (D_2O), and the shaded square from run A′ (D_2O). The diamond at about 75 min is obtained from a measurement of *trans*-DNO_2 (2Dt) during run B.

A sample of the intensity data is given in Table VII. In Figure 2 the equilibrium data are summarized. This figure plots ΔH°_0 for reaction 2 as obtained from intensity measurements, eq 13, and the isotope dependence of zero point energy given in Table II. The ordinate is ΔH°_0, the abscissa is time. Two sets of measurements of the equilibrium of reaction 12 are plotted vs. time. The lower set involves a line of *cis*-DNO_2 while the upper set involves the trans isomers. Of course, the cis–trans energy has been removed so that the two curves should coincide. The right-hand side of the figure shows the results of a number of brief runs studying the equilibrium of reaction 11.

The equilibrium constant data of Verhoek and Daniels,[5] Beattie and Bell,[6] and Solc and Pour[7] on reaction 3, all of which agree very well, and the equilibrium constant data of Ashmore and Tyler[17] and Waldorf and Babb[18] on reaction 4, which, again, are very consistent, may be combined to give a room temperature equilibrium constant for reaction 2. The resulting equilibrium constant of reaction 2 was converted into ΔH°_0 by using the free energy functions given in Table II, giving $\Delta H^\circ_0 = 540$ cal. The most uncertain free-energy function is that of N_2O_3 because of the uncertainty in the normal mode assignments and torsional barrier of N_2O_3. As remarked earlier, the value of $-[(G_0 - H^\circ_0)/T]$ used for N_2O_3 is an upper bound, because all alternative vibrational assignments and torsional barriers give a lower number. The most plausible alternatives increase ΔH°_0 by 300–500 cal. Thus, on Figure 2, one can picture the third law results for ΔH°_0 obtained from equilibrium data[5-7,17,18] and spectroscopic calculations to fall in the region from 450 to 1150 cal.

Discussion

The intensity measurements for reaction 1 suggest $\Delta H^\circ_0 = 1050 \pm 300$ cal/mol. The previous equilibrium studies of reactions 3 and 4 suggest $\Delta H^\circ_0 = 540(+600, -100)$ cal/mol. The agreement is quite good. It is not clear which number is more accurate.

In spite of the difficulties caused by working at dry ice temperature, by nuclear quadrupole structure, by the weakness of N_2O_3 lines, and by time drifts in intensity, the results of the study of this equilibrium by microwave intensity measurements seem satisfactory. However, because the microwave intensity study of reaction 2 is subject to systematic errors arising from lack of temperature uniformity of the cell, we present the microwave results for reaction 2 with some misgivings. Although the agreement with other work is good, the possibility remains that for this system a fortuitous cancellation of errors occurs which might not occur for another system studied under the same conditions. Therefore, we regard as the principal contributions of this work the determination of the cis–trans energy difference in HNO_2, the determination of entropies and free energy functions for HNO_2, and the resolution of the dis-

crepancies between the enthalpies of reaction found by different studies previously made on this system.

It seems likely that future applications of microwave intensity measurements to the study of chemical equilibrium will be to the determination of the bond dissociation energies of weakly bound complexes. The present study has been aimed primarily at a practical evaluation of the method on an interesting chemical system. It is clear to us now that an absorption cell which can be maintained at a constant uniform temperature can be constructed and would be highly desirable for such studies.

Acknowledgment. We thank Dr. J. Chao for bringing the work of Bibart and Ewing to our attention, and Professor Ewing for bringing the work of Bradley et al. to our attention. We also thank Dr. A. P. Cox and Professors E. B. Wilson and R. L. Kuczkowski for their helpful comments.

References and Notes

(1) Supported by the National Science Foundation Grant No. MPS 71-03046.
(2) R. F. Curl, T. Ikeda, R. S. Williams, S. Leavell, and L. H. Scharpen, *J. Am. Chem. Soc.*, **95**, 6182 (1973).
(3) E. Saegebarth and E. B. Wilson, Jr., *J. Chem. Phys.*, **46**, 3088 (1967).
(4) E. Abel and J. Proisl, *Z. Elektrochem.*, **35**, 712 (1929).
(5) F. H. Verhoek and F. Daniels, *J. Am. Chem. Soc.*, **53**, 1250 (1931).
(6) I. R. Beattie and S. W. Bell, *J. Chem. Soc.*, 1681 (1957).
(7) M. Solc and V. Pour, *Collect. Czech. Chem. Commun.*, **32**, 3031 (1967).
(8) D. R. Stull and H. Prophet, *Natl. Stand. Ref. Data Ser., Natl. Bur. Stand.*, **No. 37** (1971).
(9) R. L. Kuczkowski, *J. Am. Chem. Soc.*, **87**, 5259 (1965).
(10) J. P. Devlin and I. C. Hisatsune, *Spectrochem. Acta*, **17**, 218 (1961).
(11) C. H. Bibart and G. E. Ewing, *J. Chem. Phys.*, **61**, 1293 (1974).
(12) G. M. Bradley, W. Siddall, H. L. Strauss, and E. L. Varetti, *J. Phys. Chem.*, **79**, 1949 (1975).
(13) A. H. Brittain, A. P. Cox, and R. L. Kuczkowski, *Trans. Faraday Soc.*, **65**, 1963 (1969).
(14) J. Chao, R. C. Wilhoit, and B. J. Zwolinski, *Thermochim. Acta*, **10**, 359 (1974).
(15) J. Chao, R. C. Wilhoit, and B. J. Zwolinski, "Selected Values of Properties of Chemical Compounds", Thermodynamics Research Center Data Project, Thermodynamics Research Center, Texas Engineering Experiment Station, Texas A & M University, Dec 31, 1974.
(16) L. G. Wayne and D. M. Yost, *J. Chem Phys.*, **19**, 41 (1951).
(17) P. G. Ashmore and B. J. Tyler, *J. Chem. Soc.*, 1017 (1961).
(18) D. M. Waldorf and A. L. Babb, *J. Chem. Phys.*, **39**, 432 (1963); **40**, 1165 (1964).
(19) A. S. Friedman and L. Haar, *J. Chem. Phys.*, **22**, 2051 (1954).
(20) G. E. McGraw, D. L. Bernitt, and I. C. Hisatsune, *J. Chem. Phys.*, **45**, 1392 (1966).
(21) L. H. Jones, R. M. Badger, and G. E. Moore, *J. Chem. Phys.*, **19**, 1599 (1951).
(22) A. P. Cox and R. L. Kuczkowski, *J. Am. Chem. Soc.*, **88**, 5071 (1966).
(23) A. P. Cox, A. H. Brittain, and D. J. Finnigan, *Trans. Faraday Soc.*, **67**, 2179 (1971).
(24) D. J. Finnigan, A. P. Cox, A. H. Brittain, and J. G. Smith, *J. Chem. Soc., Faraday. Trans. 2*, **68**, 548 (1972).
(25) P. L. Asquith and B. J. Tyler, *Chem. Commun.*, 744 (1970).
(26) R. F. Graham and B. J. Tyler, *J. Chem. Soc., Faraday 1*, **68**, 683 (1972).
(27) W. S. Benedict, N. Gailar, and E. K. Plyler, *J. Chem. Phys.*, **24**, 1139 (1956).
(28) A. R. Edmonds, "Angular Momentum in Quantum Mechanics", Princeton University Press, Princeton, N.J., 1957, p 111, eq 7.1.7.
(29) M. S. Cord, J. D. Petersen, M. S. Lojko, and R. H. Haas, *Natl. Bur. Stand. Monogr.*, **No. 70**, 360 (1968).
(30) J. Bellet, W. J. Lafferty, and G. Steenbeckeliers, *J. Mol. Spectrosc.*, **47**, 388 (1973).

Electron Spin Resonance Spectra of a Novel Oxyl Radical OPF_4 and Related Species[1]

A. R. Boate,[2] J. R. Morton, and K. F. Preston*

Division of Chemistry, National Research Council of Canada, Ottawa, Canada *(Received September 29, 1975)*

Publication costs assisted by the National Research Council of Canada

Intense ESR spectra observed in γ-irradiated solid solutions of OPF_3 or NSF_3 in SF_6 are ascribed to the free radicals OPF_4 and NSF_4, respectively. The radicals are believed to have a distorted trigonal bipyramidal structure in which the equatorial plane contains two fluorine nuclei, an oxygen (or nitrogen) nucleus, and the central phosphorus (or sulfur) nucleus. The magnitudes of the observed hyperfine interactions indicate that the semioccupied orbital belongs to the representation B_1 in C_{2v} symmetry and consists primarily of an oxygen (or nitrogen) 2p orbital whose nodal plane coincides with the equatorial plane of the molecule. Two derivatives of OPF_4 have been detected in γ-irradiated SF_6 containing OPF_2Cl or $OPFCl_2$. These are believed to be OPF_3Cl and OPF_2Cl_2, respectively, in which the chlorine nuclei occupy equatorial positions and show no detectable hyperfine interactions with the unpaired electron.

Introduction

Difficulties are frequently encountered in the detection and identification of oxygen-centered free radicals by the method of ESR spectroscopy, either because of their extreme reactivity, or because of the low natural abundance and high spin of the isotope ^{17}O. Oxyl radicals RO have been particularly troublesome in this respect. For example, the *tert*-butoxy radical $(CH_3)_3CO$ has twice been claimed[3,4] but each time has been disputed.[5,6] In fact, arguments have been advanced[6] suggesting that solution ESR spectra of oxyl radicals of high symmetry may not be detectable owing to a line-broadening mechanism operative in orbitally degenerate systems. This hypothesis is certainly consistent with the fact that solution ESR spectra have only been observed for oxygen-centered radicals of low symmetry, e.g., nitroxides (C_{2v} symmetry) and peroxides (C_s symmetry).

We report here the detection and characterization by ESR spectroscopy of a novel oxyl radical, OPF_4, and certain derivatives thereof. Their spectral parameters indicate that the unpaired electron essentially occupies an oxygen 2p orbital and that the disposition of the five ligands about the phosphorus atom is that of a distorted trigonal bipyramid. A related radical, NSF_4, is also described and is believed to have a similar structure.

Results

At 100 K, the ESR spectra of γ-irradiated samples of (solid) SF_6 containing dissolved OPF_3, OPF_2Cl, or $OPFCl_2$ were very similar at low resolution, consisting of six lines of relative intensities 1:1:2:2:1:1. The separation between adjacent lines indicated an analysis in terms of two equivalent spin ½ nuclei ($a_F \sim 50$ G) and a third spin ½ nucleus ($a_P \sim 40$ G). At higher resolution the spectra revealed additional hyperfine structure consisting of 2-G, 1:2:1, triplets in the case of OPF_3:SF_6 and 3-G doublets (Figure 1) in the case of OPF_2Cl:SF_6. No extra splitting could be resolved in samples of $OPFCl_2$:SF_6. The spectra were distinct from and considerably more intense than that of SF_5, which is invariably present in γ-irradiated SF_6.[7]

In the case of a sample of SF_6 containing OPF_3 enriched to ~25% in ^{17}O, a 23-G sextet of ^{17}O satellites accompanied each line of the main spectrum. These satellites were attributed to hyperfine interaction with a single ^{17}O nucleus ($I = 5/2$). There was no indication of hyperfine interaction with a second ^{17}O nucleus.

A γ-irradiated sample of thiazyl trifluoride in SF_6 exhibited at 100 K the very intense spectrum shown in Figure 2. The spectrum was interpreted in terms of hyperfine interactions with two pairs of equivalent ^{19}F nuclei (83.7 G, 9.7 G) and a single ^{14}N nucleus (8.4 G). The similarity of the ^{14}N and the smaller of the ^{19}F hyperfine interactions resulted in considerable overlapping of lines and the quintet-like appearance of each of the main groups. Second-order splittings of the expected magnitude for two equivalent spin ½ interactions of 84 G were apparent (Figure 2) in the outer lines of the central group.

The spectral parameters of all the above radicals were determined by computer diagonalization of the appropriate spin matrix;[8] results are given in Table I.

Discussion

Identification of the Radicals. It is well established that γ irradiation of SF_6 containing a dissolved solute often leads to fluorine-atom addition to the solute molecule, thereby generating a paramagnetic species detectable by ESR spectroscopy. The radicals PF_4, AsF_4, SF_5, O_2SF, and OSF_3 are but a few of the many examples which could be cited of radicals which have been produced by this technique. The possibility must therefore be considered that the radicals OPF_4, OPF_3Cl, OPF_2Cl_2, and NSF_4 have been detected as a result of fluorine-atom addition to the corresponding substrate. Our spectroscopic data support this hypothesis.

The ^{17}O hyperfine interaction in $^{17}OPF_3$:SF_6 samples (22.8 G) is similar to that in $^{17}ON(SO_3^-)_2$ (20.7 G),[9] and to that of the terminal oxygen in a variety of peroxy radicals (~23 G).[10] The latter, however, also exhibit ^{17}O hyperfine interactions with the inner oxygen, for example, CF_3O_3, 14.0 G;[11] FOO, 14.5 G;[12] O_3SOO^-, 12.8 G.[13] Since no indication of an additional (smaller) ^{17}O hyperfine interaction was discernible in our spectra we discount the possibility

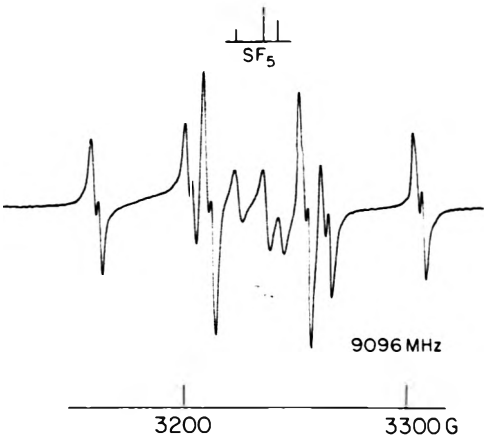

Figure 1. ESR spectrum of a γ-irradiated solid solution of OPF_2Cl in SF_6 at 100 K.

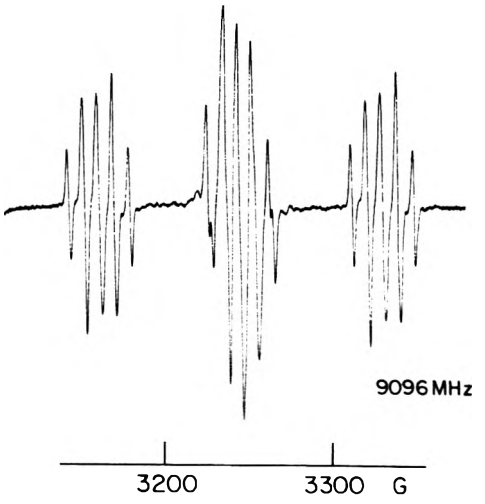

Figure 2. ESR spectrum of a γ-irradiated solid solution of NSF_3 in SF_6 at 100 K.

that our radicals are peroxy radicals (e.g., $OOPF_4$). Furthermore, organic derivatives of such species have already been detected[14] and have spectral parameters ($g \sim 2.02$, $a_P \sim 9$ G) quite different from those presently reported.

We therefore conclude that the radicals generated by γ irradiation of phosphoryl halides in SF_6 contain a single oxygen atom. In the case of the prototype radical OPF_4 the data suggest a distorted trigonal bipyramidal arrangement of ligands around the central phosphorus atom, resulting in a species having C_{2v} symmetry. Replacement of one or two

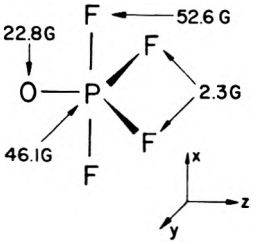

fluorine atoms by chlorine atoms evidently occurs at positions associated with the smaller ^{19}F hyperfine interactions, the resulting ^{35}Cl hyperfine interactions being unresolved. We are inclined to invoke Muetterties' rule[15] and conclude that in OPF_3Cl and OPF_2Cl_2 the chlorine atom(s)

TABLE I: ESR Parameters for Certain Phosphoranoxyl Radicals and for Thiazyl Tetrafluoride in SF_6 at 100 K

Radical	g value	Hyperfine interactions, G			
		Central atom	$^{19}F_{ap}$	$^{19}F_{eq}$	^{17}O or ^{14}N
OPF_4	2.01038(1)[a]	46.12(8)[b]	52.59(2)[b,c]	2.3(1)[c]	22.8(1)
OPF_3Cl	2.01034(1)	42.68(5)	51.90(2)[c]	3.11(5)	
OPF_2Cl_2	2.01053(2)	40.43(6)	51.32(5)[c]		
NSF_4	2.0035(1)		83.7(1)[c]	9.7(1)[c]	8.4(1)

[a] The numbers in parentheses are the estimated errors in the last significant figure quoted. [b] Very similar parameters to these have been reported for an electron-irradiated OCF_2:SF_6 sample, which presumably contained traces of OPF_3 (R. W. Fessenden and R. H. Schuler, *J. Chem. Phys.*, 45, 1845 (1966)). [c] Two equivalent ^{19}F nuclei have this hyperfine interaction.

occupy the basal (yz) plane of the radical, leaving the more electronegative fluorine atoms in the apical positions.

Thiazyl trifluoride is isoelectronic and isostructural with phosphoryl trifluoride, and a logical carrier of the spectrum in irradiated SF:NSF_3 is, therefore, the radical NSF_4, in which the unpaired electron occupies primarily the nitrogen $2p_x$ orbital. The observed ^{19}F hyperfine interactions are certainly consistent with this assignment. A ^{14}N interaction of 8 G is, furthermore, similar to that observed in iminyl radicals (e.g., $H_2C{=}N$, a_N = 10 G).[16] The alternative assignments, $FNSF_3$, or $FN{=}SF_3$, seem much less likely on comparison of the present data with those of NF_2[17] and OSF_3.[18]

Description of the Semioccupied Orbital. OPF_4 and radicals derived from it are oxyl radicals, in which the unpaired electron occupies a molecular orbital consisting primarily of an oxygen 2p atomic orbital whose nodal plane contains the phosphorus atom and the two equatorial fluorine or chlorine atoms. In C_{2v} symmetry (OPF_4) this orbital belongs to the representation B_1, and the isotropic ^{17}O hyperfine interaction of 22.8 G indicates an unpaired spin density of ~0.56 in the contributing oxygen $2p_x$ orbital.[10] Smaller contributions from the apical fluorines' 2s, $2p_x$, and $2p_z$ atomic orbitals generate the ~50-G ^{19}F hyperfine interactions.

The rather high g value of the phosphoranoxyl radicals undoubtedly reflects incomplete quenching of orbital angular momentum about z, the P–O bond direction. This implies the existence of a filled b_2 orbital, having considerable oxygen $2p_y$ character, not far below the semioccupied orbital. Molecular orbital calculations which we have carried out at the Hückel level for OPF_4 in C_{2v} geometry predicted a semioccupied orbital of B_1 symmetry lying only ~1000 cm^{-1} above the highest doubly occupied orbital of representation B_2. Such a small energy separation is certainly of the correct order of magnitude to explain the large departure of the isotropic g value of OPF_4 from that of free spin.

The disparity between the g values of the two isoelectronic radicals OPF_4 and NSF_4 may be explained on the same basis: the more normal g value of the latter species is a reflection of a more remote b_2 orbital, which is in turn the result of greater bonding between the nitrogen $2p_y$ and sulfur $3p_y$ orbitals. In terms of valence-bond theory the dominant structures in the two radicals are probably $O{-}PF_4$ and $N{=}SF_4$.

Comparison with Other Work. A spectrum similar to that which we have assigned to OPF_4 has been observed in γ-irradiated OPF_3, although the 2-G hyperfine interactions were not resolved.[19] We think that the spectrum in γ-irradiated OPF_3 is that of OPF_4, not O_2PF_2 as previously reported. The formation of OPF_4 on irradiation of OPF_3 would not be unexpected, and residual anisotropy in the larger hyperfine interactions might well mask the smaller $^{19}F_{eq}$ hyperfine interactions.

Another spectrum, observed 10 years ago in γ-irradiated ND_4PF_6, having g = 2.0108, a_P = 36.0 G, $a_F(2)$ = 60.5 G, was originally identified as PF_2.[20] More recently,[21] the formulation O_2PF_2 was suggested, but we now feel that it is probably $O_2PF_3^-$, in which two (possibly equivalent) oxygen atoms occupy the basal plane of the bipyramidal framework. A hitherto unexplained ~2-G doublet structure apparent in each line of the spectrum[20] can then be assigned to the lone equatorial ^{19}F nucleus. The presence of $O_2PF_3^-$ in irradiated ND_4PF_6 can readily be explained by partial hydrolysis to $O_2PF_2^-$ during deuteration followed by fluorine-atom attack upon γ irradiation.

Experimental Section

Phosphoryl fluoride and the phosphoryl fluoride chlorides were prepared by the fluorination of phosphoryl chloride with SbF_3.[22] Thiazyl trifluoride was obtained by the fluorination of S_4N_4 in dry CCl_4 with AgF_2.[23] The gas-phase reaction between ^{17}O labeled NO_2 and PF_3 was used to generate small amounts of $^{17}OPF_3$. Sulfur hexafluoride was purchased from Matheson Gas Products, Ind., East Rutherford, N.J. These compounds were all thoroughly degassed and subjected to trap-to-trap distillations in a high vacuum system before use.

Samples were prepared for examination by ESR as follows. Gaseous mixtures of approximately 5 mol % phosphoryl halide or thiazyl trifluoride in SF_6 were condensed rapidly into quartz ESR sample tubes at 77 K and the resulting solid solutions were exposed at that temperature for approximately 1 h to the radiation from a 9000 Ci ^{60}Co source. Spectra were recorded with a Varian E-12 spectrometer; magnetic field and microwave frequency measurements were made with the equipment described elsewhere.[24] ^{19}F NMR analyses were carried out routinely on the ESR samples to confirm that they contained sulfur hexafluoride and the desired substrate only.

References and Notes

(1) NRCC No. 15127.
(2) NRCC Research Associate.
(3) L. H. Piette and W. C. Landgraf, *J. Chem. Phys.*, **32**, 1107 (1960).
(4) S. Weiner and G. S. Hammond, *J. Am. Chem. Soc.*, **91**, 2182 (1969).
(5) K. U. Ingold and J. R. Morton, *J. Am. Chem. Soc.*, **86**, 3400 (1964).
(6) M. C. R. Symons, *J. Am. Chem. Soc.*, **91**, 5924 (1969).
(7) J. R. Morton, K. F. Preston, and J. C. Tait, *J. Chem. Phys.*, **62**, 2029 (1975).
(8) A computer program has been submitted to the Quantum Chemistry Program Exchange, Chemistry Department, Indiana University, Bloomington, Ind.
(9) Z. Luz, B. L. Silver, and C. Eden., *J. Chem. Phys.*, **44**, 4421 (1966).
(10) E. Melamud and B. L. Silver, *J. Phys. Chem.*, **77**, 1896 (1973).
(11) R. W. Fessenden, *J. Chem. Phys.*, **48**, 3725 (1968).
(12) R. W. Fessenden and R. H. Schuler, *J. Chem. Phys.*, **44**, 434 (1966).
(13) A. Reuveni, Z. Luz, and B. L. Silver, *J. Magn. Reson.*, **12**, 109 (1973).
(14) G. B. Watts and K. U. Ingold, *J. Am. Chem. Soc.*, **94**, 2528 (1972).

(15) R. Hoffmann, J. M. Howell, and E. L. Muetterties, *J. Am. Chem. Soc.*, **94**, 3047 (1972).
(16) D. Behar and R. W. Fessenden, *J. Phys. Chem.*, **76**, 3945 (1972).
(17) C. A. McDowell, H. Nakajima, and P. Raghunathan, *Can. J. Chem.*, **48**, 805 (1970).
(18) J. R. Morton and K. F. Preston, *J. Chem. Phys.*, **58**, 2657 (1973).
(19) A. Begum, S. Subramanian, and M. C. R. Symons, *J. Chem. Soc. A*, 1323 (1970).
(20) J. K. S. Wan, J. R. Morton, and H. J. Bernstein, *Can. J. Chem.*, **44**, 1957 (1966).
(21) A. J. Colussi, J. R. Morton, K. F. Preston, and R. W. Fessenden, *J. Chem. Phys.*, **61**, 1247 (1974).
(22) H. S. Booth and F. B. Dutton, *J. Am. Chem. Soc.*, **61**, 2937 (1939).
(23) O. Glemser, H. Meyer, and A. Haas, *Chem. Ber.*, **97**, 1704 (1964).
(24) A. J. Colussi, J. R. Morton, and K. F. Preston, *J. Phys. Chem.*, **79**, 651 (1975).

Nuclear Magnetic Resonance Relaxation in Lysozyme Crystals

E. Hsi, J. E. Jentoft, and R. G. Bryant*[1]

Department of Chemistry, University of Minnesota, Minneapolis, Minnesota 55455 *(Received September 5, 1975)*

Publication costs assisted by the National Institutes of Health

Nuclear magnetic resonance relaxation time measurements are reported for monoclinic lysozyme crystals. The data require three proton populations including two proton populations associated with the protein surface. One of the surface populations exchanges rapidly with the interior aqueous solution of the crystal, the other does not. The data are analyzed assuming a log normal distribution of correlation times for each unaveraged relaxation component. It is concluded that a significant fraction of the water in a protein crystal is essentially liquid and that the distances over which the protein perturbs the dynamic aspects of water structure are short.

Introduction

Water occupies a central position in the chemistry of biological processes. Recently there has been an increased effort to understand the several ways that water molecules acting singly and in concert may determine in part the properties of macromolecules or macromolecular aggregates such as enzymes and whole tissues. One of the more promising approaches to the study of water is nuclear magnetic resonance because the several possible measurements contain in various ways both structural and dynamic information. Many have reported measurements on very complex systems[2a] such as muscle, or blood cells, malignant and benign tumors; however, the complete interpretation of much of this data ultimately will rest on understanding separately the possible interactions of the several constitutents of these systems with water.

The present study of protein crystals was undertaken because the protein crystal provides a structurally well-characterized protein matrix which may serve as a model for more complex systems. At the same time a sound understanding of the water–protein interaction in the crystal is critical to structural biochemistry.

Experimental Section

Lysozyme used in this study was obtained from Worthington Biochemical Corp. Monoclinic lysozyme crystals were grown by adding sodium nitrate to 2.5% to a 1% protein solution at pH 4.7. Good crystals were usually obtained in several days at room temperature.[2b] In some instances mold growth made the crystals unusable.

Nuclear magnetic resonance measurements were made on a 30-MHz spectrometer built in this laboratory.[3] T_2 measurements were made using the Gill-Meiboom modification of the Carr-Purcell pulse sequence.[4] In most cases the signal was enhanced by signal averaging on a Varian C-1024 CAT and use of a sample and hold circuit eliminated the problems often caused by the radio-frequency transients associated with the successive 180° pulses. T_1 measurements were made using a 180–90° pulse sequence and the transient following the second pulse was often averaged for the weak samples. At low temperatures when T_2 became less than 100 μs the free induction decay or a two pulse spin echo experiment was taken as a measure of T_2. There is no discontinuity apparent in the data from making this change in experimental detail. The 90° pulse widths were less than 5 μs and the receiver recovery time is 5 μs. Errors in single component T_1 and T_2 values are estimated to be less than 5%. Errors in the relaxation times extracted from multiexponential relaxation data are less precise because of the difficulty of separating sums of exponentials.

Temperatures were regulated in the variable temperature experiments by using a Varian variable temperature controller calibrated every 10 °C using a copper–constantan thermocouple. Samples were allowed to equilibrate at each temperature for at least 30 min because of the possibility of poor thermal conduction in a sample tube not completely filled with conducting material.

Crystals approximately 0.5–1 mm long were transferred from the mother liquor by blotting on filter paper and direct deposition in the NMR tube. When reproducible moisture contents were required, the crystals were then equilibrated by connecting a reservoir containing mother liquor at the top of the tube. Crystals treated in this way always gained water over the blotted crystals. At higher tempera-

tures distillation of the water out of the crystal onto the glass tube caused problems in data analysis since the water content of the crystal was a function of temperature. This problem was overcome in part by covering the crystals with a C-12 branched fluorocarbon supplied courtesy of the 3M Co.

The NMR signal intensity associated with each proton relaxation component was determined by the following. (1) Measurement of the free induction decay amplitude at 273 K and calibration with a sample containing an H_2O–D_2O or H_2O–$(CD_3)_2CO$ mixture doped with 10 mM manganous ion. The filling factors in the samples were approximately matched by requiring the calibration volume to match the sample tube volume occupied by the crystals. In each case, the dimensions of the samples exceeded the dimensions of the radio-frequency coil. (2) Measurement of the free induction decay amplitude at temperatures below the freezing event in the crystals and comparison with the manganous ion doped H_2O–D_2O solution or H_2O–$(CD_3)_2CO$ solution. (3) Resolution of the low temperature measurement into two components was based on the relative amounts of the proton signal which relax with a long and short T_1 as determined from the extrapolated intercepts for the plot of $\log_e (A - A_\infty)$ vs. time where A is the free induction decay amplitude following the 90° pulse in the 180–90° pulse sequence. (4) Following the NMR intensity measurements the protein content of the crystal sample was determined by dissolving it in water, dilution to known volume, and measurement of the optical absorbance to obtain the protein weight from $\epsilon_{281}^{1\%} = 26.4$ independent of what inorganic solutes may be present in the crystal. The accuracy of this determination of total water content is estimated to be 5%.

Results

The continuous wave NMR spectrum of lysozyme crystals has been presented in a preliminary report.[5] The narrow component of this semisolid system which would normally be observed at moderate power levels on a high-resolution NMR spectrometer is broad by all high resolution standards and has the following characteristics. (1) The line has neither a simple Lorentzian nor Gaussian shape. (2) The signal shape may become asymmetric at high water contents. (3) The full-width at half-height is on the order of 200 Hz and is a function of spectrometer frequency. (4) The line intensity does not fall off at high radio-frequency levels in the usual way, but increases to an approximately constant value with increasing H_1. (5) The full-width at half-height does not correspond to $1/\pi T_2$ when T_2 is measured directly using pulsed methods. (6) The signal may be eliminated by exchange of the water with D_2O or by pumping the water off under vacuum.

The last observation demonstrates that the narrow component of the spectrum is directly a result of the water or exchangeable protons in the protein crystal and is not due to the hydrocarbon or nonexchangeable portions of the protein matrix. The first five observations suggest that there are several contributions to the continuous wave spectrum associated with water protons. The lack of the usual signal saturation behavior and the peculiar line shape suggests that there may be a considerable distribution of proton types in the spectrum and indicates that deductions made directly from the continuous wave data must be made with extreme caution.

Direct measurements of the proton T_2 at 30 MHz are

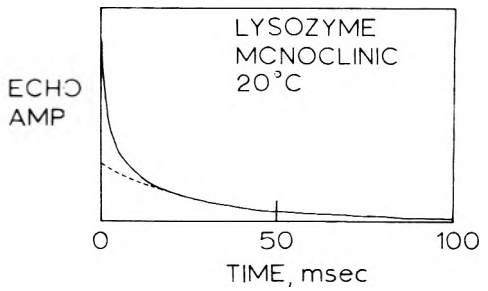

Figure 1. Proton NMR spin echo amplitude vs. time for monoclinic lysozyme crystals recorded at 20 °C and 30 MHz. The dashed line shows the extrapolation of the slower component.

shown in Figure 1 for monoclinic lysozyme crystals at 273 K. This data may be resolved into two relaxation components as shown by the dashed line. Similar behavior is observed in the T_1 data except that at room temperature approximately 14% of the signal relaxes with a T_1 of 28 ms while the remainder relaxes with a T_1 of 240 ms depending somewhat on sample preparation. The data of Figure 2 show that two T_1 values are required also at 248 K. The gross features of these plots have been observed in other systems such as water adsorbed on various surfaces or water physically partitioned between different environments.[6,7] It is important to note that partial removal of water and replacement by D_2O attenuates all the relaxation components shown uniformly. Therefore the features shown in Figures 1 and 2 are due to the water protons but may include rapidly exchanging protein protons.

The temperature dependence of the several relaxation times in the protein crystal provides direct information about the causes of relaxation. Often increasing the temperature causes an efficient chemical exchange between the two or more proton populations present in such a system with resultant mixing or averaging of the relaxation times. In the limit of rapid exchange only a single exponential is observed.[8] In the present case the two directly observable relaxation components are preserved up to temperatures of 323 K. There is no evidence that chemical exchange between the resolved relaxation components causes significant averaging of relaxation times at this temperature. The effects of decreasing temperature are less simple.

The free induction decay amplitude observed at 30 MHz is shown as a function of temperature for monoclinic lysozyme crystals in Figure 3. For monoclinic lysozyme crystals there was no evidence of supercooling or hysterisis at low temperatures. The sudden decrease in the FID amplitude may be associated with ice formation because the proton T_2 in ice is too short to contribute to the FID amplitude observed using our receiver gating conditions. Ice formation is consistent with the observation that the crystals fracture at the temperature of the transition shown in Figure 3. The fact that the FID amplitude associated with the water protons does not decrease to zero even at 215 K demonstrates that a significant fraction of the water does not freeze. This result is consistent with other studies of protein systems at low temperatures.[2a,9,10]

The freezing event shown in Figure 3 is accompanied by loss of the longest T_2 and the longest T_1 components shown in Figures 2 and 3. This loss of signal corresponds to 0.17 g of H_2O per g of protein. Only one relaxation time is required to characterize the spin echo T_2 measurements at temperatures below the freezing event. Two T_1 values are required, however. 83% of the FID relaxes with a T_1 which

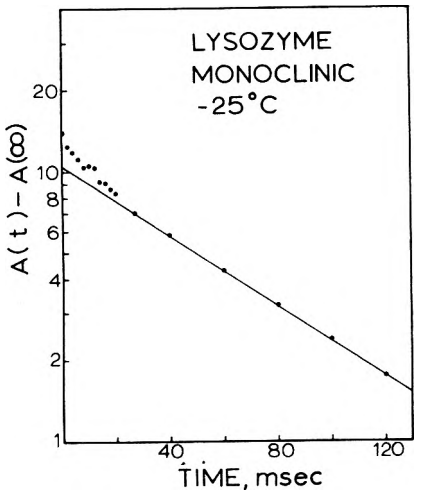

Figure 2. Proton NMR free induction decay amplitude following the 90° pulse of a 180–90° pulse sequence vs. time for monoclinic lysozyme crystals at −25 °C showing two T_1 proton relaxation components below the temperature of the transition shown in Figure 4.

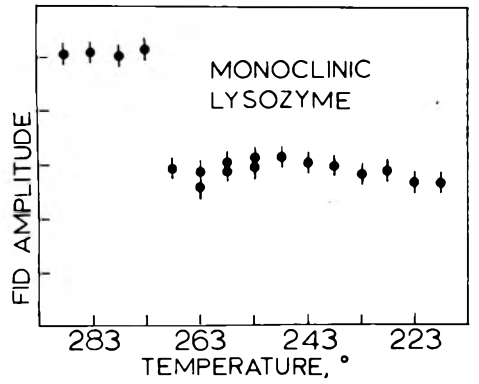

Figure 3. Proton NMR free induction decay amplitude for monoclinic lysozyme crystals as a function of temperature at 30 MHz

is 68 ms at 230 K while 17% of the signal relaxes with a T_1 which is 2 ms at 230 K. These two populations correspond to 0.20 and 0.03 g of H_2O per g of protein, respectively. The total water content of the crystals above the freezing event was found to be 0.40 g of H_2O per g protein in excellent agreement with the x-ray data.[11]

The temperature dependence for both T_1 and the T_2 relaxation times are shown in Figure 4. The activation energy for the reorientation process monitored by T_2 is 7.2 kcal mol^{-1} which is considerably higher than that observed in pure water, but is similar to activation energies reported for transport properties in supercooled water.[12,13] There is no evidence for shoulders or plateaus in the T_2 data unless it is masked by the freezing event just below 273 K.

Several additional observations are important. (1) If crystals are allowed to dry partially, the fraction of the total observed proton population which relaxes with the longest T_1 and T_2 decreases and the values of T_1 and T_2 for this fraction decrease. On the other hand, the T_1 and T_2 values for the fraction of the total observed proton population relaxing with the shorter T_1 and T_2 shown in Figures 1 and 2 are essentially constant as long as any of the more slowly relaxing protons are observed. (2) The relaxation behavior observed below the temperature of the freezing event is independent of water content as long as the crystals are sufficiently wet to display a freezing event. (3) Only

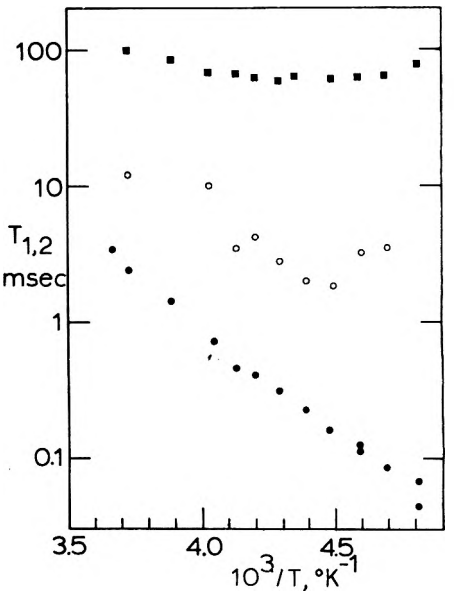

Figure 4. Proton T_1 and T_2 as a function of reciprocal temperature for monoclinic lysozyme crystals at 30 MHz: (■) component I T_1, (●) component I, II T_2, (O) component II T_1.

a single proton T_1 and T_2 was resolved if the protein sample is first cooked in water at 80 °C for 20 min or denatured by concentrated urea. (4) Perfussion of manganous ion into cross-linked lysozyme[14] crystals cause the anticipated decrease in proton relaxation rates. Concentrations of manganous ion in excess of 0.1 M are required to affect the proton population relaxing with a T_2 of 3 ms at room temperature. The important features of the data cannot therefore be caused by paramagnetic impurities.

Discussion

For convenience of discussion the observed protons in the lysozyme crystals may be divided into three groups based on their contributions to the relaxation rates observed. 83% of the protons observed at temperatures below the freezing event relax with a T_1 of 68 ms at 230 K. This group corresponds to 0.20 g of H_2O per g of protein and will be called component I. The other 17% of the protons observed below the temperature of the freezing event relax with a T_1 which is 2 ms at 230 K and corresponds to 0.03 g of H_2O per g of protein. This group will be referred to as component II. The protons which are observed above the freezing event, but which are not observed below the temperature of the freezing event will be called component III.

The appearance of two transverse and two longitudinal relaxation rates in the relaxation of the water protons in the lysozyme crystals studied requires that there be two populations of protons which do not exchange rapidly on the time scale of the relaxation times involved.[8] The loss of both signals on exchange of the water for deuterium oxide further requires that these protons are associated with water molecules or protein protons which exchange with the water protons.

The values of T_1 and T_2 for the protons relaxing with the longest relaxation times above the freezing event imply that this group of protons represents an essentially liquid environment. For a simple liquid the ratio of T_1 to T_2 is expected to be 1.6[14] and for these slowly relaxing protons this ratio is only slightly larger. That the T_1:T_2 ratio is slightly larger than 1.6 suggests that some chemical exchange may

contribute to the relaxation process. Such exchange has often been postulated.[2a,9,10] An independent measure of the fluidity of the crystal interior is provided by observations of the ESR spectrum of ionic nitroxides perfused into the crystal. These experiments support the conclusion that a portion of the crystal interior is liquid in that the rotational correlation time for the nitroxide species is similar to that of the mother liquor.[16]

Two conclusions are therefore possible. (1) Since the spaces in a protein crystal are small and an essentially liquid component to the relaxation rates is observed, the spatial extent of any significant perturbations caused by the water–protein interface on the dynamic behavior of the water is very limited. (2) Since a separate and short T_1 for what we have called component II is observed above the temperature of the freezing event, this group of protons apparently does not exchange chemically with the protons of components I or III on the time scale of tens of milliseconds.

It is difficult to determine whether the group of protons relaxing with the slowest rate above the freezing event is characterized by one or more relaxation times because of the errors inherent in the analysis of multiexponential relaxation. The protons which are identified as component I below the freezing event will have T_1 values very similar to those of component III above the freezing event. It is also likely that these T_1 relaxation rates are partially averaged by chemical exchange events. An additional complication is provided by the possibility that the nature of the spaces between protein molecules may differ in detail depending on how the molecules pack in the unit cell.[17] A distribution in the sizes of the solution pool which may exchange with protons in component I, caused by packing constraints, would lead to different relaxation rates in different areas of the crystal provided that diffusion between these domains is not rapid.

An apparent discrepancy exists in that Figure 1 clearly shows considerably greater than 10% of the protons relax with a short T_2 value above the freezing event, but only 10% of the protons relax with a short T_1. This may be resolved by recognizing that if the rate of proton exchange between component I and component III is slow compared with 3 ms, but rapid compared with hundreds of milliseconds, then all of components I and III will appear as the group of protons relaxing with the long T_1 above the freezing event, but I and III will be resolved on the faster time scale of the T_2 experiment. Since subfreezing measurement show that the T_2 value for components I and II are very similar, the same is expected above the freezing event. Therefore the group of protons with the short T_2 above the freezing event corresponds to components I and II. Failure to fully appreciate this difficulty has led to confusion about the populations reported earlier.[5]

Below the freezing event the protons associated with the protein surface are easily resolved. The ratio T_1:T_2 for the protons of component I is very large. Similar observations have been reported for earlier measurements on complex systems such as whole tissue or liquids adsorbed on various surfaces.[6,7] Interpretations have focused on the necessity of postulating a distribution of correlation times in the system.[19,20] Most often this idea is incorporated as a normal distribution of activation energies leading to a log normal distribution of correlation times. To within the approximations discussed elsewhere[19] the present data for component I require a distribution in correlation times. A log normal distribution will be assumed in the present case without further justification. This procedure may represent simply a parameterization of the data; however, the basic conclusions which will be drawn are not particularly sensitive to this choice of model.

The data of Figure 4 permit evaluation of the parameters required to fit the relaxation data for component I.[19] The mode of the correlation time distribution is at 3.3×10^{-9} s at 230 K, the temperature of the T_1 minimum. The distribution has a width, β, of 4.2 and a second moment of 1.5×10^{10} radian^2 s^{-2}. If the data are corrected using the method outlined by Resing[21] and the distribution corrected for a slow motion cut-off, a width, β, of 5.7 and a second moment of 2.0×10^{10} radian^2 s^{-2} is obtained. This second moment is close to that of 2.63×10^{10} radian^2 s^{-2} reported for ice.[22] These values correspond closely to those reported for other protein systems such as wool.[23] The activation energy for the T_2 relaxation process obtained from Figure 4 is 7.2 kcal/mol which is in agreement with values obtained in earlier work.[23] It is possible to calculate from these numbers that the center of the distribution of correlation times will be at 2.9×10^{-11} s at room temperature provided that the activation energy remains constant, which is a questionable assumption.

It is of considerable interest to estimate the origin of the reorientation causing the NMR relaxation. It has been suggested that the dominant contribution to the relaxation of "protein bound" water originates in the slow rotation of the protein molecule in solution.[24] However, the rotation of the whole protein molecule is impossible in the crystal and protein motions are restricted to side chains. If these motions were rapid, on the order of 10^{-11} s, then it should be possible to resolve proton resonances for the protein side chains in protein crystals which have not been observed to date.[25] In addition the activation energy for the T_2 process is high enough to question the suggestion that the correlation time describes a purely rotational process. For water in contact with other materials, it has been suggested that the correlation time corresponds to a translational diffusion on a surface.[6]

Although identification of the correlation time with a translational jump time must be taken as tentative, it does lead to interesting consequences. If the measured correlation time represents a three-dimensional translational jump time on the protein surface, a self-diffusion coefficient for water on the surface may be estimated provided a reasonable value for the jump length is assumed. If it is assumed that the jump length is 3.7 Å, which has been estimated for pure water, and that the surface diffusion constant is approximated by

$$D = l^2/4\tau$$

then at the temperature of the T_1 minimum or 230 K the diffusion coefficient would then be 8.3×10^{-8} cm^2 s^{-1}. Extrapolation of data reported for supercooled water indicates that the protein surface diffusion coefficient calculated in this manner is approximately 10% that of water at this temperature.[12,13] This is a striking consequence of the assumptions above because the value of the water self-diffusion coefficient in tissue systems is rarely reported to be less than 10% that of pure water under the same conditions.[2a]

The data shown for component II in Figure 4 have considerable scatter, however, the ratio T_1:T_2 would again require a distribution of correlation times or significant con-

tributions from chemical exchange events. Although it may be said that the width of the distribution required would be significantly narrower than that for component I, the data are not sufficiently precise to warrant more detailed discussion.

If we may apply the theory of Zimmerman and Brittin[8] which assumes that relaxation in each of several groups of protons is characterized by different but exponential behavior, a requirement of the separation of relaxation components is that the water molecules comprising component II exchange slowly with those of components I and III on the time scale of tens of milliseconds. There are several reasons to believe that the same situation should obtain in aqueous solution. (1) Similar behavior is observed in protein powders and a variety of protein crystals.[10] (2) The major fraction of protein surface in the crystal is not involved in protein–protein contacts so that the bulk of the surface experiences the immediate proximity of the aqueous component III. (3) Component III is similar to mother liquor as measured by its dynamic properties. We therefore suggest that the rapid exchange of water in a protein solution with the protein surface would occur only with some or all of component I which is approximately 80% of the total signal associated with the surface. The observable effects of such an exchange on the water proton T_2 would be very small because of the short correlation time of the water in component I and the dominant effects of the excess water in the solution.

The conclusion that there is a surface "phase" of water associated with protein molecules certainly has precedent. Only a few reports implying dynamic information will be mentioned. Pennock and Schwan[26] have interpreted dielectric dispersion measurements on protein solutions by postulating a bound phase of water amounting to about 0.2 g of H_2O per g of dry protein. This water had an activation energy for the reorientation process of about 7 kcal/mol. Tomaselli and Shamos[27] have suggested that in the case of collagen there are two processes important in determining relaxation at higher temperatures and implicate a chemical exchange event as one of them. Harvey and Hoekstra[28] have studied lysozyme powder and indicate that with increasing hydration of the dry powder there is more than one relaxation component which may be ascribed to water. It appears that the second components observed in these experiments corresponds to component III.

Although NMR measurements on whole tissues have been reported where relaxation times have displayed multicomponent behavior, there is difficulty in comparing these directly with the present data due to the possibility that physical partitions between the several parts of the tissue generate additional distinct proton populations.

Conclusions

This work permits several direct conclusions concerning the nature of water in lysozyme crystals. (1) A significant amount of water in the lysozyme crystals studied has the properties of an only moderately viscous liquid. For monoclinic lysozyme crystals this amounts to 0.17 g of H_2O per g of protein of 132 water molecules per protein molecule. (2) There are two types of proton associated with the protein surface which may be distinguished based on their lifetime in the surface region and by their relaxation behavior below the freezing event in the crystal. The two proton populations correspond to 0.20 g of H_2O per g of protein or 161 water molecules per protein molecule and 0.03 g of water per g of protein or 24 water molecules per protein molecule. These groups may include exchangeable protein protons. (3) If we apply the usual theoretical treatments, both proton populations associated with the protein surface may be described by a distribution of correlation times, but the details of the distributions differ. (4) The average motion of the water molecules at the protein surface as monitored by the proton relaxation rates is rapid, however, the distributions or correlation times which describe the data are sufficiently wide that some water molecules would reorient with correlation times on the order of protein rotational correlation times in solution.

Acknowledgment. This work was supported by the National Institutes of Health (GM-18719; GM-21335), The Graduate School and the Chemistry Department, University of Minnesota, The Research Corporation, and the Merck Company. Helpful discussions with D. E. Woessner, H. A. Resing, and R. Lumry are gratefully acknowledged.

References and Notes

(1) Camille and Henry Dreyfus Teacher-Scholar.
(2) (a) R. Cooke and I. D. Kuntz, *Ann. Rev. Biophys. Bioeng.*, **3**, 95 (1974); (b) M. Sundaralingam, private communication.
(3) E. Hsi, Ph.D. Thesis, University of Minnesota, Minneapolis, Minn., 1975.
(4) S. Meiboom and D. Gill, *Rev. Sci. Instrum.*, **29**, 688 (1958).
(5) J. E. Jentoft and R. G. Bryant, *J. Am. Chem. Soc.*, **96**, 299 (1974).
(6) H. A. Resing, *Adv. Mol. Relaxation Processes*, **1**, 109 (1967–1968).
(7) H. Pfeifer, *Nucl. Magn. Reson.*, **7**, 68 (1973).
(8) J. R. Zimmerman and W. E. Brittin, *J. Phys. Chem.*, **61**, 1328 (1957).
(9) J. A. Walter and A. B. Hope, *Prog. Biophys.*, **23**, 3 (1971).
(10) F. Noack, *Nucl. Magn. Reson.*, **3**, 83 (1971).
(11) K. T. Gillen, D. C. Douglass, and M. J. R. Hoch, *J. Chem. Phys.*, **57**, 5117 (1972).
(12) B. W. Matthews, *J. Mol. Biol.*, **33**, 491 (1968).
(13) J. C. Hindman and A. Svirmickas, *J. Phys. Chem.*, **77**, 2487 (1973).
(14) F. A. Quiocho and F. M. Richards, *Biochemistry*, **5**, 4062 (1966).
(15) N. Bloembergen, E. M. Purcell, and R. V. Pound, *Phys. Rev.*, **73**, 679 (1948).
(16) R. P. Mason and R. G. Bryant, unpublished results.
(17) R. L. Vandelen and A. Tulinsky, *Biochemistry*, **12**, 4193 (1973).
(18) E. Hsi and R. G. Bryant, unpublished data.
(19) L. J. Lynch, K. H. Marsden, and E. P. George, *J. Chem. Phys.*, **51**, 5673 (1969).
(20) A. Odajima, *Prog. Theor. Phys. (Kyoto)*, Suppl. 10, 142 (1959).
(21) H. A. Resing, *J. Chem. Phys.*, **43**, 669 (1965).
(22) K. Kume, *J. Phys. Soc. Jpn.*, **15**, 1493 (1960).
(23) L. J. Lynch and K. H. Marsden, *J. Chem. Phys.*, **51**, 5681 (1969).
(24) S. H. Koenig and W. E. Schillinger, *J. Biol. Chem.*, **244**, 3283 (1969).
(25) J. E. Jentoft and R. G. Bryant, unpublished results.
(26) B. Pennock and H. P. Schwan, *J. Phys. Chem.*, **73**, 3600 (1969).
(27) V. P. Tomaselli and M. H. Shamos, *Biopolymers*, **12**, 353 (1973).
(28) S. C. Harvey and P. Hoekstra, *J. Phys. Chem.*, **76**, 2987 (1972).

Intermolecular and Intramolecular Motions in the Solvation Spheres of Some Ions in Methyl and Ethyl Alcohol

H. G. Hertz,* R. Tutsch, and N. S. Bowman[1]

Institut für physikalische Chemie und Elektrochemie der Universität Karlsruhe, Karlsruhe, West Germany *(Received July 2, 1975)*

Proton relaxation rates in solutions $MnCl_2$–CD_3OH and $MnCl_2$–C_2D_5OH are reported and from these data rotational correlation times for the solvation complexes are determined. Proton and deuteron relaxation rates for the hydroxyl, methylene, and methyl group in solutions of $Mg(ClO_4)_2$, $CaCl_2$, $NaClO_4$, NaI, and KI in methyl alcohol and ethyl alcohol are reported, and correlation times for the various groups are determined. The various correlation times are compared with one another and, in those cases where they differ for a given solvation complex, intermolecular or intramolecular motions are postulated. The results are also compared with predictions derived from pertinent theories currently available. It is found that the description of the internal motions by the theory is not satisfactory in all cases.

1. Introduction

In a number of previous studies it has been concluded from nuclear magnetic relaxation measurements[2-8] that in the first hydration sphere of certain ions the water molecules rotate about an axis given by their electric dipole moment which is at the same time the axis M–O (M = metal ion). The mean time after which such a rotation about the dipolar axis has occurred is of the order 10^{-11} s. Among the ions having this property are the structure forming ions Na^+, Li^+, F^-, Ba^{2+}, Sr^{2+}, Ca^{2+}, and even such strongly hydrated ions as Mg^{2+} and Ga^{3+}.[8] This finding implies that for these ions the first hydration sphere is not a strictly rigid arrangement of water molecules during a time range of $\approx 10^{-11}$ s. It should be mentioned that for Al^{3+} absence of water rotation about the M–O axis has been established.[8]

In the work performed at this laboratory the evidence for rotation about the M–O axis is based on a comparison of the reorientation time of the vector connecting the central ion with one of the protons of the first hydration waters (M–H vector) with the reorientation time of the vector connecting the two water protons inside the H_2O molecule (H–H vector). In all relevant examples it was found that the latter vector reorients faster than the former vector which proves internal rotation in the hydration shell.

It is generally known that the structure stabilization effects of ions are comparatively weak in aqueous electrolyte solutions. This is due to the fact that the solvent water has a strong tendency to form its own structure, so part of the force exerted by the ion electric field is needed to break down the proper structure of water which reduces the efficiency in stabilizing a new solvent structure around the ion. Consequently solvation structure stabilization is known to be stronger in nonaqueous solvents where proper solvent structures are absent or less developed. We quote three typical observations which give support to this statement: (I) the dynamical structure breaking effect (the increase of fluidity accompanying the dissolution of large low charge ions) is unique for the solvent water, see, e.g., ref 9. (There are very few exceptions known.[9]); (II) the viscosity B coefficients are larger in nonaqueous solvents than in water, see, e.g., ref 9; and (III) the heat of transfer and the entropy of transfer for the transfer of simple salts from water to organic solvents usually are negative, see, e.g., ref 9 and 10. Furthermore, the exchange of solvent molecules from the solvation shell is faster in aqueous solution than in nonaqueous solution, for literature see ref 10. We cite but one special example which is of importance for the present article, namely, the slower methanol exchange from the solvation shell of Mg^{2+} as compared with the water exchange from the Mg^{2+} hydration in aqueous solution.[11,12]

This stronger fixation of solvent molecules around ions in nonaqueous solvents induced us to examine whether rotation about an axis which leaves the electric dipole moment unchanged is absent or not. As solvents we chose methanol and ethanol. The strongly solvated cations were Mg^{2+} and Ca^{2+}; some data for the more weakly solvated cation Na^+ will also be presented for comparison. Mg^{2+} was chosen since, first in CH_3OH slow solvent exchange from the solvation shell is known for this ion,[11,12] and secondly, the reorientation time of the M–H vector can be determined directly for Mn^{2+} dissolved in these solvents[13] which permits comparison of the reorientation times for two different vectors in the solvation sphere. The ions Mn^{2+} and Mg^{2+} are so similar that results for Mn^{2+} may well be used for Mg^{2+}. For Ca^{2+} this equality is valid to a lesser degree; here one should consider the Mn^{2+} correlation time to be an upper limit.

In the systems to be investigated here we chose the proton of the alcohol OH group to be the proton of the M–H vector. The second vector whose reorientation time was studied in order to be compared with the reorientation time of the M–H vector was the O–D vector in MeOD and EtOD. In a rigid solvation complex in the sense to be understood here, the reorientation times of the M–H vector and the O–D vector should be equal. On the other hand, if "internal" rotation of the OD groups with respect to the solvation complex occurs, then we should find that the reorientation time of the OD vector is shorter than that of the M–H vector (which is identical with that of the M–D vector).

There is another interesting aspect connected with the study of the solvents methanol and ethanol. This is the fact that in the methanol molecule itself for instance, internal rotation occurs, i.e., the methyl group rotates about the C–O axis. This has been concluded from nuclear magnetic relaxation measurements.[14-16] The rotational correlation time of a vector connecting two protons in the methyl

group (H–H vector) is found to be shorter than the rotational correlation time of the OH vector in the hydroxyl group of the same molecule. The same is true for another vector in the methyl group, namely, the C–H vector (or the C–D vector in the corresponding deuterated compound). Likewise it has been observed that the correlation time of the H–H and C–D vectors in the ethyl group of ethanol are shorter than the correlation time of the O–H vector in the same molecule.[14-17] The correlation time of the methyl H–H vector of methanol is roughly five times shorter than that of the polar group of the molecule.[14-17] The reason for this inequality of correlation times is rather obvious. For the methyl group of methanol the rotational potential barriers exerted by the neighbor molecules and the intramolecular rotational barrier about the C–O axis are comparatively flat whereas for the OH group there is a strong intermolecular potential well due to the hydrogen bond which hinders the rotation of one OH group relative to the OH group of a bonded neighbor molecule. In ethanol the situation is similar though somewhat more complicated because in this case one has also to consider the possibility of internal rotations about the C–C axis connecting the methylene group with the methyl group (see also ref 18).

Thus, one point of interest is the question whether the internal rotation in the alcohol molecule is also slowed down or even entirely removed when the molecule is strongly attracted by the electric field of the cation and thereby tightly pressed toward the ion. Such a force could have the effect of producing a sufficiently deep potential well even for the internal rotation of the methyl group which stops its motion in the time range to be considered here, i.e., $\approx 10^{-11}$ s.

Furthermore, we are not sure whether we have a correct understanding at the present time of the interconnection between the various correlation times of different groups or vectors in the molecule. Probably part of the difficulty involved regards the problem of independent diffusional motion of the parts of a molecule and the knowledge of the axes in the molecule with respect to which the rotational motion is isotropic, i.e., of such a nature as to produce a single exponential decay of the correlation function of the second-order spherical harmonics.

Thus, in the course of the discussion of our experimental results we shall always compare these results with the predictions given by the pertinent formulas which are available at the present time. Indeed we shall find that these expressions seem not to be suitable to give a proper description in all cases.

2. Basic Formulas

In the (paramagnetic) solutions containing $MnCl_2$ or similar paramagnetic salts the relaxation rate of the solvent proton is (in good approximation) given by the formula:[19-21]

$$\frac{1}{T_1} = \frac{2}{5}\frac{\gamma^2\gamma_s^2\hbar^2 S(S+1)n_2 n_c^+}{n_1 R_0^6}\left[\tau_c^{**} + \frac{(7/3)\tau_c^{**}}{1+\omega_s^2(\tau_c^{**})^2}\right] \quad (1)$$

γ and γ_s are the gyromagnetic ratios of the proton and the paramagnetic ion (Mn^{2+}), respectively, S is the spin of Mn^{2+} ($S = 5/2$), n_2 and n_1 are the total numbers of moles of Mn^{2+} ions and of solvent molecules, respectively, in the solution, n_c^+ is the first solvation number of Mn^{2+}, R_0 is the distance between the center of the cation and the solvent proton in the first solvation sphere whose relaxation is studied, τ_c^{**} is the rotational correlation time of the vector $\vec{R}_0$ connecting the center of the cation with this proton, $R_0 = |\vec{R}_0|$, ω_s is the electron spin resonance frequency, i.e.

$$\omega_s = \gamma_s H_0$$

where H_0 denotes the static magnetic field. On the other hand, the nuclear magnetic resonance frequency ω_I is

$$\omega_I = \gamma_I H_0$$

whence

$$\omega_s = \frac{\gamma_s}{\gamma_I}\omega_I$$

According to eq I τ_c^{**} is the only parameter which determines the frequency dependence of $1/T_1$. Thus measurement of $1/T_1$ as a function of ω_I allows the determination of τ_c^{**}.

In diamagnetic electrolyte solutions under usual conditions the experimental proton magnetic relaxation rate $1/T_1$ consists of an intramolecular contribution $(1/T_1)_{intra}$ and an intermolecular contribution $(1/T_1)_{inter}$, i.e.

$$\left(\frac{1}{T_1}\right)^H = \left(\frac{1}{T_1}\right)^H_{intra} + \left(\frac{1}{T_1}\right)^H_{inter}$$

Most of the information we are seeking is contained in the intramolecular relaxation rate. In the systems under investigation here, the total concentration of solvent protons is approximately constant. In such a situation we are allowed to use the approximation that the intermolecular contribution is proportional to the intramolecular relaxation rate which implies that with variation of the salt concentration the rotational diffusion coefficient and the translational diffusion coefficient vary roughly in the same way.[3] Thus we have

$$\left(\frac{1}{T_1}\right)^H_{inter} = \alpha\left(\frac{1}{T_1}\right)^H_{intra} \quad (2)$$

$\alpha \approx$ constant, and we may write for the intramolecular relaxation rate:

$$\left(\frac{1}{T_1}\right)^H_{intra} = \left(\frac{1}{T_1}\right)^H(1+\alpha)^{-1}$$

where $(1/T_1)^H$ is the quantity obtained by experiment. Since we shall only be interested in changes of $(1/T_1)^H_{intra}$ relative to the pure solvent, precise knowledge of the factor α is not needed ($\alpha \approx 1$). $(1/T_1)^H_{intra}$ may be written in the following form:[16,19]

$$\left(\frac{1}{T_1}\right)^H_{intra} = F\tau_c \quad (3)$$

with

$$F = \frac{3}{2}\frac{\hbar^2\gamma^4}{n}\sum_{i=1}^{n}\sum_{\substack{j=1\\ i\neq j}}^{n}\frac{1}{r_{ij}^6} \quad (4)$$

n is the number of protons in the molecule (or group of molecule) considered, r_{ij} is the distance between the ith and the jth proton. τ_c is the rotational correlation time for the magnetic dipole–dipole interaction, that is, as the theory shows,[19,20] for the spherical harmonics of second order. In an electrolyte solution the division of the solvent in regions corresponding to the free solvent (mole fraction x^0) and nonoverlapping regions corresponding to the solvation spheres of the cation (x^+) and anion (x^-), respectively, leads to the expression:[3,21,22]

$$\left(\frac{1}{T_1}\right)^{H}_{intra} = F^+x^+\tau_c^+ + F^-x^-\tau_c^- + F^0x^0\tau_c^0 \quad (5)$$

The interaction factors $F^{\pm}$, F^0 and the correlation times $\tau_c^{\pm}$, τ_c^0 are the quantities referring to the respective regions. For the solutions we are studying in first approximation we may write

$$\tau_c^- = \tau_c^0 \quad (6)$$

furthermore

$$F^+ = F^- = F^0$$

$$x^+ = n_c^+c^*/55.5$$

n_c^+ = first coordination number of the cation, c^* = salt concentration in aquamolality, i.e., c^* = moles salt/55.5 moles of solvent. From these relations we obtain

$$\frac{\tau_c^+}{\tau_c^0} = 1 + B''\frac{55.5}{n_c} \quad (7)$$

where

$$B'' = \lim_{c^*\to 0}\frac{(1/T_1)^H_{intra}(c^*) - (1/T_1)^H_{intra}(0)}{(1/T_1)^H_{intra}(0)c^*} \approx$$

$$B' = \lim_{c^*\to 0}\frac{(1/T_1)^H(c^*) - (1/T_1)^H(0)}{(1/T_1)^H(0)c^*} \quad (8)$$

In this paper our interest concerns the relative changes of the correlation time in the cation solvation sphere and we see from eq 7 and 8 that in order to obtain this quantity we have to measure the slope of $(1/T_1)(c^*)$ as $c^* \to 0$.

Part of the measurements presented are deuteron relaxation times. The deuteron magnetic relaxation process occurs via electric quadrupole interaction.[19-22] Now the relaxation rate is always of intramolecular nature, and is given by the formula ($I = 1$):[19]

$$\left(\frac{1}{T_1}\right)^{D}_{intra} = \left(\frac{1}{T_1}\right)^{D} = \frac{3}{8}\left(\frac{eQq}{\hbar}\right)^2\tau_q = \frac{3}{2}\pi^2K^2\tau_q \quad (9)$$

$K = eQq/h$ is the quadrupole coupling constant, τ_q is the correlation time of the quadrupole interaction. As before, it is a correlation time of the spherical harmonics of second order, but in general the vector within the molecule defining the orientational arguments of the spherical harmonics differs from that corresponding to the magnetic dipole–dipole interaction. In the case of deuteron relaxation this is the C–D or O–D vector, in the case of dipole interaction it is the proton–proton vector (H–H vector). All other relations and denotations correspond to those given for the case of magnetic dipole–dipole interaction, thus

$$\left(\frac{1}{T_1}\right)^{D} = \frac{3}{2}\pi^2\left\{\left(\frac{eqQ}{h}\right)^2_0 x^0\tau_q^0 + \left(\frac{eqQ}{h}\right)^2_+ x^+\tau_q^+ + \left(\frac{eqQ}{h}\right)^2_- x^-\tau_q^-\right\} \quad (5a)$$

and if all quadrupole coupling constants are the same, i.e.

$$\left(\frac{eqQ}{h}\right)_0 = \left(\frac{eqQ}{h}\right)_+ = \left(\frac{eqQ}{h}\right)_- \quad (5b)$$

one obtains

$$\frac{\tau_q^+}{\tau_q^0} = 1 + B''\frac{55.5}{n_cc^*} \quad (7a)$$

$$B'' = \lim_{c^*\to 0}\frac{(1/T_1)^D(c^*) - (1/T_1)^D(0)}{(1/T_1)^D(0)c^*} \quad (8a)$$

Next we quote some formulas given in the literature[17,23-27] to interconnect different correlation times τ_1, τ_2 of different vectors in the same molecule when internal rotation occurs. These formulas are based on the assumption of an independent superposition of the rotational diffusion of an axis and the rotational diffusion of a group or vector around this axis. For one particular situation the formula is

$$\tau_2 = \frac{\tau_1}{4}\left|(3\cos^2\theta - 1)^2 + 3\sin^2 2\theta\left(\frac{1}{\tau_1/\tau_i + 1}\right) + 3\sin^4\theta\left(\frac{1}{4\tau_1/\tau_i + 1}\right)\right\} \quad (10)$$

Here τ_1 is the correlation time of the axis, and it is assumed that the axis performs *isotropic rotational* diffusion, τ_2 is the correlation time of the vector which may perform rotational diffusion about the axis, $\tau_i = 1/D_i$ is the time constant describing the rotational diffusion of the vector (or group) as seen from a coordinate system in the molecule which performs the same isotropic rotational diffusion as the axis. θ is the angle between the axis and the vector.

However, the motion of the axis may not be describable as isotropic diffusion. Rather, its rotational diffusion is also anisotropic. It may be describable by the two rotational diffusion coefficients: $D_\perp$ and $D_\parallel$. Then let β be the angle which the axis forms with the direction whose rotational diffusion is described by $D_\perp$. In this situation the formula may be derived:

$$\tau_2 = \sum_{n,j=-2}^{+2}\frac{[D_{0j}^{(2)}(0,\theta,0)D_{jn}^{(2)}(0,\beta,0)]^2}{6D_\perp + (D_\parallel - D_\perp)n^2 + j^2\,1/\tau_i} \quad (11)$$

where we may also write

$$\frac{1}{\tau_1} = 6D_\perp; \frac{1}{\tau_{11}} = D_\parallel - D_\perp$$

The quantities $D_{jn}^{(L)}(\alpha,\beta,\gamma)$ are the matrix elements of the Wigner rotation matrix.[28,29] It may be seen from eq 11 that anisotropy of the motion of the axis leads to a rather complicated formula. In the appendix (supplementary material) we present eq 9 together with eq 11 written as a function of simple trigonometric functions.

In the other model the motion of the vector or group as seen from a coordinate system diffusing with the axis consists of "jumps" leading from one of the trigonal equilibrium positions to another. Now we have

$$\tau_2 = \frac{\tau_1}{4}\left\{(3\cos^2\theta - 1)^2 + [4 - (3\cos^2\theta - 1)^2]\frac{1}{1 + \tau_1/\tau_i}\right\} \quad (12)$$

if the axis performs isotropic rotational diffusion, and

$$\tau_2 = \sum_{j,n=-2}^{+2}\frac{[D_{0j}^{(2)}(0,\theta,0)D_{jn}^{(2)}(0,\beta,0)]^2}{6D_\perp + (D_\parallel - D_\perp)n^2 + 1/\tau_j} \quad (13)$$

with $1/\tau_j = 0$ for $j = 0$ and $1/\tau_j = 1/\tau_i$ for $j = \pm 1, 2$, if the axis performs anisotropic rotational diffusion. Equation 13 is only approximately valid; the dependence of τ_2 on the orientation of the trigonal equilibrium positions relative to the axes defining $D_\perp$ and $D_\parallel$ has been neglected.[30] In the Appendix (see paragraph at end of text regarding supplementary material) we present eq 13 in terms of ordinary trigonometric functions. In Figure 1 τ_2 as a function of τ_1, τ_{11}, and τ_i is given for a number of typical examples.

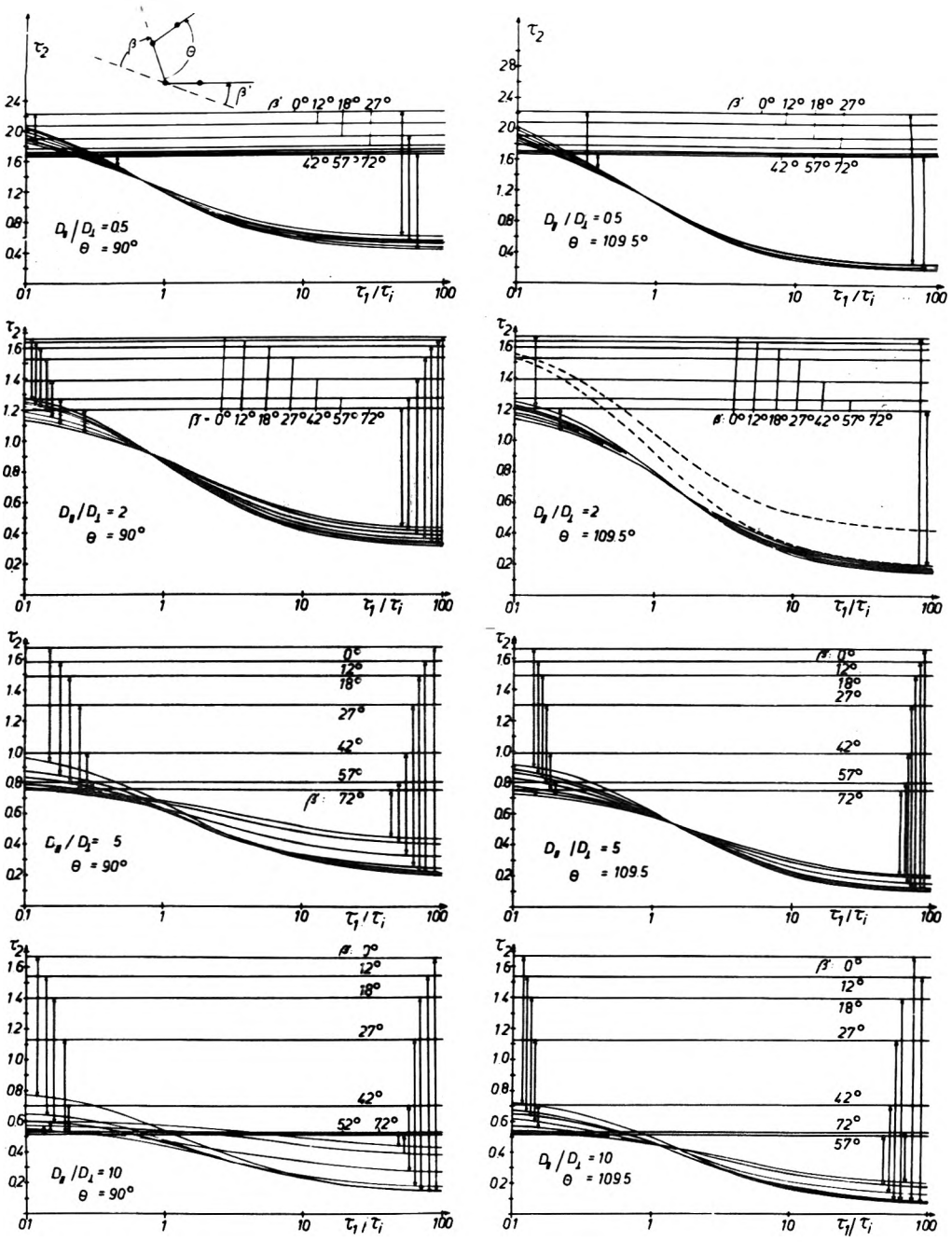

Figure 1. Effective correlation times τ_2 in the case of anisotropic motion of axis as a function of the ratio τ_1/τ_i describing the degree of internal rotation. The horizontal lines correspond to the angles $\delta = 0$ and β', i.e., they give the correlation time of an axis itself. The double arrows connect the curve for a given β with that horizontal line to which it corresponds according to the geometry of the methanol molecule, i.e., $\beta' = 180-(109.5 + \beta)$. The dashed curves give the correlation time τ_2 if the motion of the axis is isotropic. We have set $D_\perp = 1 \times 10^{11}$ s^{-1}. Then τ_2 is given in ps.

3. Experimental Section

In the diamagnetic solutions proton and deuteron relaxation times were measured with the 90°–90° pulse sequence method at 20 and 12 MHz, respectively. The spectrometers were home-built and of various forms. The paramagnetic solutions were measured with a variable-frequency Bruker spectrometer SXP 4-100, again the 90°–90° technique was applied. The temperature was 25 ± 0.2 °C, and was controlled by pumping water through the probe head and a Colora Ultra thermostat. The solvents methanol and ethanol in their various deuterated forms were purchased from Sharp and Dohme, Munich. The degree of deuteration in the respective position was >99 atom %. The salts were p.a. substances obtained from Merck, Darmstadt. $Mg(ClO_4)_2$ was freed from crystal water by heating it to 200 °C, $CaCl_2$ was supplied as "water free" from the manufacturer, and was dried. The salt concentrations were determined by weighing, the accuracy was ±1%. With the usual freeze–pump method the samples were freed from oxygen. The experimental error of our relaxation rates is estimated to be ±5%. The uncertainty of the B' coefficients is ±20% if B' is relatively small, otherwise the accuracy is better.

4. Results and Evaluation for Pure Solvents

4.1 Intramolecular Proton and Deuteron Relaxation

Times in Methanol. We were able to reproduce the relaxation rates of the methyl and hydroxyl deuterons and the methyl protons, respectively previously reported from this laboratory.[14,31,32] In all our evaluations according to eq 9, 3, and 4 we chose the quadrupole coupling constant K_{OD} = 222 kHz in the liquid state.[32] For the methyl group, F = 5.28×10^{10} s^{-2} and a quadrupole coupling constant K_{CD} = 170 kHz[14] has been used. The dynamical data thus derived are collected in Table 1 (supplementary material). The calculated ratios $(\tau_j/\tau_k)_{calcd}$ j,k: OD, CD_3 ... were obtained with eq 10 or eq 12 and $\tau_i \ll \tau_1$.

It may be seen from Table 1 line 1 that $(\tau_{OD}/\tau_{CD_3})_{obsd}$ is greater than it should be in the limit of very fast internal rotation. This is surprising because we have no reason to assume very fast rotation, $\tau_i < 10^{-13}$ s, in a molecule such as methanol. In Figure 1, we present some numerical results obtained for the case of anisotropic diffusion of the axis. We have used the model for stepwise internal rotation, i.e., eq 13 or A2 was applied. It may be seen that with $D_\parallel/D_\perp = 2$, that is $\tau_1/\tau_{11} = 1/6$ and $\tau_1/\tau_i = 100$, the experimental correlion time ratio can be accounted for. The same is true, e.g., for the combination $D_\parallel/D_\perp = 5(\tau_1/\tau_{11} = 2/3)$ and $\tau_1/\tau_i = 16$. In both cases $\beta' = 0$, i.e., the OD vector is the direction with the longest correlation time τ_1. Still, even with this anisotropic model the resulting motions around the axis (τ_i) and around the OD vector ($D_\parallel$) are very fast and we may question whether eq 10–13 give an adequate description of the physical situation.

4.2 The OH Relaxation Rate in Pure Methanol and Ethanol. In our previous work[31] the proton relaxation times of CD_3OH and C_2D_5OH were found to be T_1 = 11.3 s and T_1 = 5.9 s, respectively. In the conventional sense these relaxation times are produced by the *intermolecular* magnetic dipole–dipole interaction because there are no other protons in the same molecule. The interactions with the deuterons may be ignored. However we may consider a hydrogen bonded dimer or polymer as a molecular species and then the OH relaxation rate represents an intramolecular relaxation rate with respect to the hydrogen bonded species. Now eq 3 and 4 can again be applied. This implies that the lifetime of the dimer is longer than the correlation time τ_c. From the geometry of the hydrogen bonds in the association chain we estimate a proton–proton distance between nearest neighbors b = 2.3 Å. With this figure from eq 3 and 4 one calculates a correlation time $\tau_c = 7.8 \times 10^{-12}$ s for methanol and $\tau_c = 1.4 \times 10^{-11}$ s for ethanol.[34] The agreement of these times with those derived from the OD and ^{17}O relaxation[32] is satisfactory and by taking account of the influence of next nearest neighbors could be improved.

4.3 Intramolecular Proton and Deuteron Relaxation Times in Ethanol. In the C_2H_5 group the potential energy barrier corresponding to the rotation of the methyl group relative to the methylene group is about $E_A \approx 3.5$ kcal/mol,[35] with $\tau = \tau_0 e^{E_A/RT}$ and $\tau_0 \approx 10^{-13}$ s, $\tau \approx 10^{-11}$ s. This is of the order of the reorientation time of the ethanol molecule and thus we may consider the ethyl group to be rigid in the time range to be considered here. Therefore, internal rotation should be of such a kind that the whole C_2H_5 group rotates about the CO axis (see also ref 17). The experimental data regarding pure ethanol are to be reported in more detail elsewhere;[36] for convenience some pertinent results are listed in Table 2 (supplementary material). The dynamical data derived from these results are presented in Table 1. We see from these values that the ratios τ_{OD}/τ_{CD_2} and τ_{CD_2}/τ_{CH_2} corresponding to the methylene group are closer to unity than the "theoretical" values for $\tau_i \ll \tau_1$. This would mean that internal motion is not very fast compared with the correlation time of the OH group. From Figure 1, we find $\tau_1/\tau_i = 6$ if we assume isotropic reorientation of the O–C axis, and $\tau_1/\tau_i = 4$ if we assume anisotropic motion of the O–C axis with $D_\parallel/D_\perp = 2$, i.e., $\tau_1/\tau_{11} = 1/6$, and the vector for which $D = D_\perp$ pointing in the O–H direction ($\beta' = 0°$). These numbers then give τ_i = 1.7 ps and 2.5 ps for the rotation of the C_2H_5 around the O–C axis, in the first and second case, respectively, certainly still a fast motion.

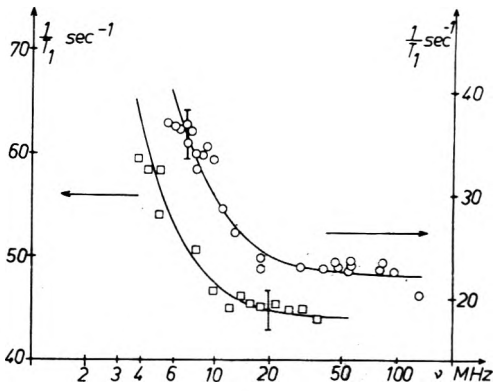

Figure 2. Proton relaxation rate in the systems 3×10^{-3} M $MnCl_2$ + CD_3OH (O, right-hand ordinate) and 3×10^{-3} M $MnCl_2$ + C_2D_5OH (□, left-hand ordinate) as a function of the proton resonance frequency ν. The temperature is 25 °C. The solid lines are calculated from eq 1 with τ_c^{**} = 130 ps and τ_c^{**} = 57 ps for ethanol and methanol, respectively.

Regarding the methyl group, the experimental ratio τ_{OD}/τ_{CD_3} is greater than it should be theoretically even for very fast rotation $\tau_1/\tau_i \gg 1$. Thus clearly this finding conflicts with the model of a rigid C_2H_5 group. On the other hand, the experimental ratio $\tau_{CD_3}/\tau_{CH_3} > 1$ as expected. One might propose that, contrary to our original assumption, the CH_3 rotates relative to the CH_2 group. Let us assume that we can describe the motion of the CH_2 group and the C–C axis by two time constants τ_1 and τ_{11}. Then we might apply eq 13 (or eq A3) to the description of the rotational motion of CH_3 relative to CH_2. However, since now we are concerned with the angles θ = 109.5 and 90° inspection of the Figure 1 shows that in such a situation we must necessarily have $\tau_{CD_3}/\tau_{CH_3} < 1$ which is in contradiction with the experimental finding. No simple explanation of this discrepancy can be offered.

5. Experimental Results Regarding Electrolyte Solutions

Figure 2 gives the OH-proton relaxation rates in the systems $CD_3OH + 3 \times 10^{-3}$ M $MnCl_2$ and $C_2D_5OH + 3 \times 10^{-3}$ M $MnCl_2$ (M: molarity scale, moles of salt/liter of solution). It will be seen that the relaxation rate increases with decreasing frequency when the frequency is sufficiently low. Since, according to eq 1 such an increase occurs if $(\tau_c^{**})^{-1}$ is of the order of $\gamma_s 2\pi\nu$, it is immediately evident that the correlation time τ_c^{**} is markedly longer in ethanol than in methanol. Figure 3 shows the relaxation rates of solutions of various salts in methanol. The much stronger increase of $1/T_1$ caused by Mg^{2+} than that due to the univalent ions is striking. In Figure 4 corresponding data are given for the deuteron relaxation rates, the qualitative behavior is simi-

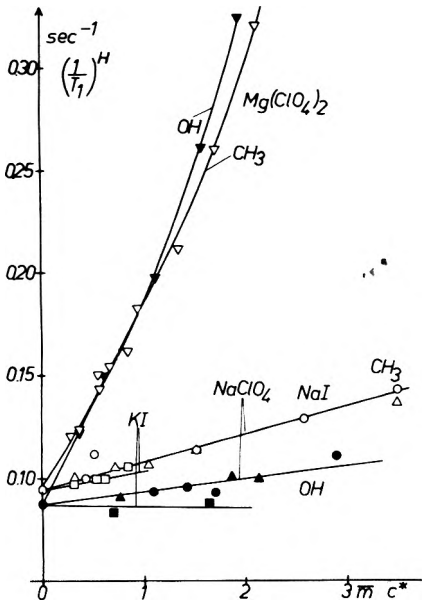

Figure 3. Proton relaxation rates of solutions of various salts in methanol as a function of the salt concentration c^*. c^* is given as aquamolality $\bar{m}$ (moles salt/55.5 moles of alcohol). Full symbols represent OH relaxation rates. Along a given curve the hydrogen nuclei of the molecule, whose relaxation rate is not shown, are deuterons (25 °C).

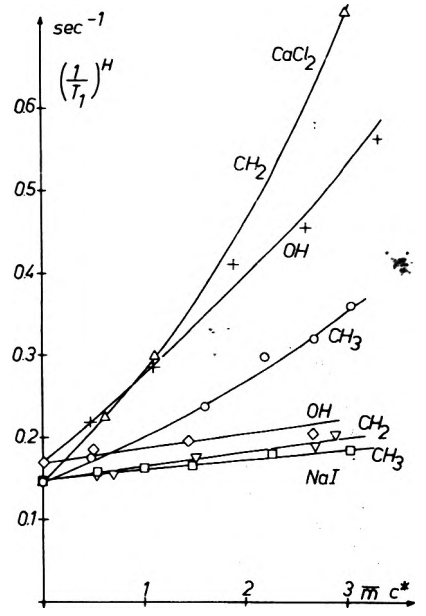

Figure 5. Proton relaxation rates of solutions of $CaCl_2$ and NaI in ethanol as a function of the salt concentration (aquamolality scale). Along a given curve the hydrogen nuclei of the molecule, whose relaxation data are not shown, are deuterons (25 °C).

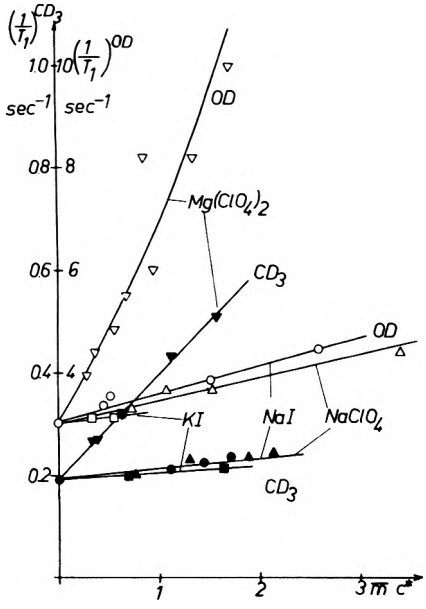

Figure 4. Deuteron relaxation rates of solutions of various salts in methanol as a function of the salt concentration c^* (aquamolality scale). Along a given curve the hydrogen nuclei of a molecule, whose relaxation data are not shown, are protons (25 °C).

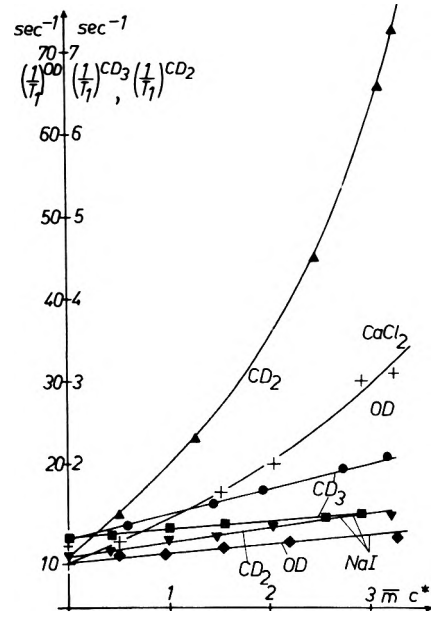

Figure 6. Deuteron relaxation rates of solutions of $CaCl_2$ and NaI in ethanol as a function of the salt concentration (aquamolality scale). Along a given curve the hydrogen nuclei of the molecule, whose relaxation data are not shown, are protons (25 °C).

lar to that found for the proton rates. Figures 5 and 6 give the relaxation rates for protons and deuterons, respectively, for solutions of $CaCl_2$ and NaI in ethanol. The qualitative information which is immediately available from these diagrams is the surprising fact that the methylene nuclei show the strongest increase of their relaxation rates whereas the methyl nuclei approach fairly close toward the relaxation behavior of the solution containing the more weakly solvated salt NaI.

6. Evaluation of Experimental Results for Electrolyte Solutions

All dynamical parameters for the solvation shells derived for the diamagnetic electrolyte solutions (Figures 3–6) are collected in Table 3 (supplementary material).

The anions have been chosen in such a way that their contribution to the B' coefficients is as small as possible. Of course, there is no rigorous theoretical or experimental procedure available by which a separation of the B' coefficient of the salt into ionic contributions can be accomplished.

Therefore, partly to remain in agreement with previous work and partly by intuition, we adopt the following values: in methanol, CH_3, CD_3, OD: $B' = 0.02\ m^{-1}$ for ClO_4^- and $B' = 0.03\ m^{-1}$ for I^-; OH: $B' = 0$ for ClO_4^- and I^-; in ethanol, CH_2, CD_2, OD: $B' = 0.02$ m for I^- and $0.07\ m^{-1}$ for Cl^-; CH_3, CD_3: $B' = 0$ for I^-, $B' = 0.03\ m^{-1}$ for Cl^-; OH: $B' = 0$ for I^- and Cl^-.

6.1 Rotational Correlation Time of the Vector Connecting the Center of the Mn^{2+} Ion with OH Protons in the First Solvation Sphere. Evaluation of the experimental data shown in Figure 2 with eq 1 yields for Mn^{2+} (as chloride) $\tau_c^{**} = 5.7 \times 10^{-11}$ s. This is markedly longer than the value $\tau_c^{**} = 2.4 \times 10^{-11}$ s reported by Sperling and Pfeifer.[37] The result of these authors was obtained from measurements with CH_3OH. Thus the superposition of the signals due to the CH_3 and OH protons was observed. Furthermore, direct evaluation of the frequency dependence was not possible. The correlation time quoted by Sperling and Pfeifer is based on the assumption that the distance from center to center of Mn^{2+}–CH_3 protons is 3.7 Å. From the relaxation rate at high frequencies and eq 1 we derived a Mn^{2+}–HO separation of $R_0 = 3.4$ Å. Since Mg^{2+} is somewhat smaller than Mn^{2+} ($r_{Mg^{2+}} = 0.66$ Å, $r_{Mn^{2+}} = 0.8$ Å), for Mg^{2+} $R_0 = 3.2$ Å may be more suitable.

Correspondingly, for the Mn^{2+} solution in ethanol (as chloride) we find from Figure 2 with eq 1 $\tau_c^{**} = 1.3 \times 10^{-10}$ s and a Mn^{2+}–HO separation of $R_0 = 3.7$ Å.

6.2 The Relaxation of the Hydroxyl Hydrogen Nuclei and the Rigidity of the Solvation Complex. 6.2.1 The Deuteron Relaxation Rate in the System $Mg(ClO_4)_2$ + CH_3OD. The results given in Table 3 line 1 were obtained with the assumption that the OD quadrupole coupling constant in the solvation sphere is the same as in the bulk (see eq 5b).

Usually the trend is such that the quadrupole coupling constant decreases as the molecule passes from the gaseous phase via the liquid phase to the solid phase.[38] Since the solvation sphere is "more solid" than the bulk, one would expect that the corresponding decrease of the quadrupole coupling constant occurs here as well. Considering various spectroscopic observations[11,39-45] we estimate that the quadrupole coupling constant in the Mg^{2+} solvation sphere suffers a decrease of ≈5% relative to the bulk. This then gives a 10% increase of the correlation time, i.e., we have $\tau_q^+ = 5.2 \times 10^{-11}$ s. Thus from a comparison of τ_c^{**} as given in section 6.1 we get

$$\tau_q^+ \approx \tau_c^{**}$$

which is the criterion of a rigid solvation sphere. However, it should be kept in mind that in the evaluation of the diamagnetic solution a contribution from the second coordination sphere of Mg^{2+} has been neglected[6,8,21,22] (which would somewhat reduce τ_q^+) and that Mn^{2+} and Mg^{2+} are not strictly identical ions.

From all these facts we conclude that around Mg^{2+} in methanol a rapid rotation of the OH groups about the dipole vector (M–O vector) can be ruled out; however, a slow motion of this type cannot be excluded.

6.2.2 The Proton Relaxation Rate in the System $Mg(ClO_4)_2$ + CD_3OH. Since now the factors $F^{\pm}$, F^0 in eq 5 are of intermolecular origin, these quantities need a particular consideration. It is reasonable to assume that $\tau_c^- F^- \approx \tau_c^0 F^0$ (see below). Then, instead of eq 7 we have

$$\frac{\tau_c^+}{\tau_c^0} = \frac{F^0}{F^+}\left(B'\frac{55.5}{n_s} + 1\right) \qquad (14)$$

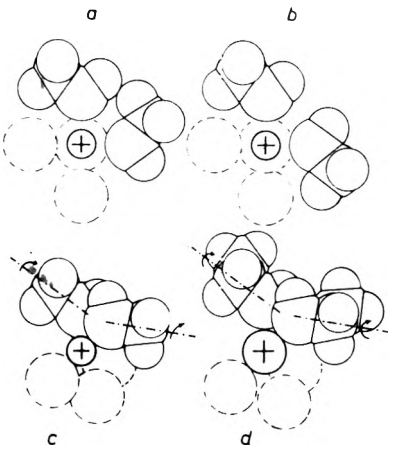

Figure 7. Models for the solvation sphere in alcohols: (a) and (b) O atoms at octahedral positions and dipole moments oriented radially; (c) Mg^{2+} in methanol, proposed configuration. Tilting around axes – · – · – · – leads to varying intermediate configurations between radial dipole orientation and H bonding. (d) Ca^{2+} in ethanol. Dashed circles: O atoms of three other alcohol molecules. Thus the sixth solvation molecule is not shown in order to render visible the central cation.

What is the geometry of the solvation complex? Since the chemical shift of the OH proton in methanolic solutions is upfield for weakly solvated ions,[43,46,47] in the ionic field the hydrogen bond configuration between two methanol molecules is at least partly distorted. Let us assume that the solvation complex consists of three pairs of methanol molecules. Then, in the pair configuration of Figure 7a the two OH protons are separated by a distance of 4.5 Å. This leads to $F^0/F^+ \approx 50$ and consequently τ_c^+/τ_c^0 would come out much too large. In the configuration Figure 7b the smallest OH-proton–proton separation is still ≈3 Å, which would lead to an unrealistic τ_c^+/τ_c^0 ratio (>50). We see that the octahedral O positions with radial dipole orientations of Figure 7a,b do not give hydroxyl H–H distances which are smaller than that corresponding to the H bond, i.e., 2.3 Å. The actual pair of molecules probably is somewhat distorted from the planar configuration shown in Figure 7a,b, such as to give the H–H separation of ≳2.3 Å. Figure 7c gives a proposed pair configuration. Having thus excluded that $F^0/F^+ < 1$, we arrive at the result for τ_c^+/τ_c^0 given in Table 3, that is $\tau_c^+ \gtrsim 5 \times 10^{-11}$ s. This is in reasonable agreement with the figures obtained from the deuteron relaxation and the Mn^{2+} system and thus confirms the model of a fairly rigid OH skeleton of the solvation complex.

6.2.3 The Deuteron and Proton Relaxation Rates in the Systems $CaCl_2$ + C_2H_5OD and $CaCl_2$ + C_2D_5OH. From line 3 of Table 3 we derive $\tau_q^+ = 5.8 \times 10^{-11}$ s. This value is to be compared with the correlation time of the vector connecting the center of the Ca^{2+} ion with the OH proton in the first solvation sphere. For Mn^{2+} in ethanol we found $\tau_c^{**} = 1.3 \times 10^{-10}$ s (see section 6.1). However, since the radius of Ca^{2+} is greater than that of Mn^{2+} by 0.2 Å ($r_{Ca^{2+}} = 1.0$ Å), this is an upper limit. Let us estimate $\tau_c^{**} = 1 \times 10^{-10}$ s for Ca^{2+} in EtOH. Then the conclusion is that the OH group of the ethanol molecules performs rotational motion about the M–O axis.[48] If we assume the solvation configuration consisting of three pairs as shown in Figure 7d, the OH–OH proton–proton separation should not differ very much from the H bond value of 2.3 Å, thus $F^0/F^+ \approx 1$ and $\tau_c^+/\tau_c^0 \approx 6.5$. This ratio is in reasonable agreement with the previous value; it suggests that the lifetime of the

distorted H bond in the first solvation sphere is of the order of the reorientation time of the M–O vector, i.e., $\approx 10^{-10}$ s.

Summarizing the results of this section and of section 6.1 we state that the solvation sphere of Ca^{2+} in EtOH is not rigid, that is, rearrangements of the OH vectors occur within a time range of the rotational correlation time of the M–O vector, i.e., 10^{-10} s.

6.3 The Rotation of the Methyl and Methylene Group in the Solvation Complex. 6.3.1 Mg^{2+} in Methanol. In the system $Mg(ClO_4)_2$ + CH_3OD the experimental quantity is the total proton relaxation rate. However we are interested in the intramolecular relaxation rate. Here and below eq 2 is assumed to be a sufficiently good approximation. The data in line 5 of Table 3 give $\tau_q^+ = 4.7$ ps, a value which implies very fast rotation of the methyl group around the C–O axis. This is true even if the methyl group should be distorted such that θ comes closer to the magic angle 125.6°. The same result follows from the CH_3 data (line 6). Such a fast internal motion in the solvation complex is surprising because all particles should be strongly pressed together due to electrostriction effects. More than this, since in the solvation sphere of Mg^{2+} anisotropic motion of the C–O vector is to be excluded, the large experimental ratios τ_{OD}/τ_{CD_3} and τ_{CD_3}/τ_{CH_3} are in conflict with the theoretical prediction for $\tau_i/\tau_1 \to 0$ (see Table 1).

6.3.2 Ca^{2+} in Ethanol. We discuss the desired information regarding the internal motions of the ethanol molecule in the first solvation sphere of Ca^{2+}. First we consider τ_{OD}/τ_{CD_2}. In the solvation sphere this ratio is less than the corresponding ratio found for the pure liquid (see Table 1). We conclude that there is still rotation about the C–O axis, but that rotation has become slower. The same result follows from the experimental ratio τ_{CD_2}/τ_{CH_2}. This yields a ratio of the correlation times $\tau_1/\tau_i = 2$, that is, as seen from the OH group the methylene group has a reorientation time of ≈20–30 ps. In the pure liquid the corresponding numbers were $\tau_1/\tau_i = 4$, and $\tau_i = 2.5$ ps. Of course, the character of anisotropy has changed now, we expect $\beta \approx 50°$ (see Figure 7d).

However, for the methyl group the ratio τ_{OD}/τ_{CH_3} exceeds the theoretical value for the very fast rotation of the entire ethyl group by almost a factor 3 (see Table 1). Clearly this is not consistent with the relatively slow rotation of the methylene group postulated above. The only way out of this difficulty is the intuitive statement that now the methyl group rotates relative to the methylene group. In pure ethanol we assumed that the ethyl group is rigid because the internal rotation barrier is high compared with the intermolecular barriers effective for the ethyl group, however, it should be kept in mind that also in that case a satisfactory explanation of all details was not possible. In the solvation sphere of Ca^{2+} the methylene group comes in the direct influence of the strong electrostatic intermolecular potential which is deeper than the intramolecular potential for the CH_3–CH_2 rotation. As a consequence, the rotation of the CH_3 group relative to the CH_2 occurs more frequently than the reorientation of the methylene group relative to the ion. A similar observation was made by Versmold[17] who added glycerol to ethanol. Here as well the strong interaction of glycerol with the CH_2–CO end of ethanol caused the CH_3 rotation to be more frequent than the reorientation of the remainder of the molecule. However, as with pure ethanol, if we try to understand the methyl correlation times as being due to a rotation of CH_3 about the C–C axis, we must in any case have $\tau_{CD_3}/\tau_{CH_3} < 1$ which is in contradiction to our experimental finding $\tau_{CD_3}/\tau_{CH_3} \approx 1.2$. It should be mentioned that the quadrupole coupling constant of the deuteron is not expected to suffer any change in the solvation sphere; however, the intermolecular contribution to the CH_3 proton relaxation rate is very likely to be reduced relative to the intramolecular contribution. Thus, we have in fact $\tau_{CD_3}/\tau_{CH_3} > 1$. Summarizing, the only statement which can be made so far is to point out that there is qualitative evidence that in the solvation sphere of Ca^{2+} CH_3 rotates distinctly relative to CH_2, but that the formulas available at the present time are not sufficient to give a quantitative description of the mechanism.

6.4 The Solvation Sphere of the Na^+ Ion. From $(1/T_1)^{OD}$ of the $NaClO_4$ and NaI solutions in methanol we derive $\tau_q^+ \approx 9$ ps and the OH relaxation yields $\tau_c^+ \gtrsim 7$ ps ($n_c^+ = 6$). Regarding τ_c^{**}, the correlation time of the M–H vector, we are dependent on an estimate. The correlation time τ_c^{**} of the Na^+–H vector in aqueous solution has been found to be ≈10 ps.[49,50] Now, the correlation time of the Mn^{2+}–H vector in aqueous solution is $\tau_c^{**} = 31$ ps.[13,20,21] Since for Mn^{2+}–methanol we have found $\tau_c^{**} = 57$ ps, it is reasonable to multiply the Na^+–HOH result by the factor 5.7/3.1 in order to get the desired correlation time for the Na^+–HO–CD_3 vector. The result is $\tau_c^{**} = 18$ ps. Thus, as expected, we see that the O–H vector rotates about the M–O axis in the solvation sphere of Na^+ in MeOH. The same conclusion may also be derived for the solvation of Na^+ in ethanol. Furthermore, the rotation of the CH_3 group of methanol is still very fast and the ratio $\tau_{OD}/\tau_{CD_3} = 11$ is still greater than it should be theoretically, this in spite of the fact that anisotropy of motion should be reduced in the solvation sphere of Na^+. Again, eq 10–13 seem not to be fully satisfactory. The methylene rotation relative to the OH group is somewhat slowed down in the solvation sphere, however, the ethanol CH_3 rotation with respect to OH is slightly accelerated. The general discrepancies which are met with ethanol in the pure liquid and in the Ca^{2+} solvation sphere are still persisting.

Acknowledgments. We wish to thank Dr. C. Yoon and Dr. M. Holz for performing a number of measurements. Financial support by the Fonds der Chemischen Industrie is gratefully acknowledged. One of us (N.S.B.) is grateful for a Fulbright Lectureship during which time a portion of this work was conducted.

Supplementary Material Available: an Appendix and Tables 1–3 (5 pages). Ordering information is given on any current masthead page.

References and Notes

(1) On leave from The University of Tennessee.
(2) H. G. Hertz and M. D. Zeidler, *Ber. Bunsenges. Phys. Chem.*, **67**, 774 (1963).
(3) L. Endom, H. G. Hertz, B. Thül, and M. D. Zeidler, *Ber. Bunsenges. Phys. Chem.*, **71**, 1008 (1967).
(4) B. P. Fabricand and S. S. Goldberg, *Mol. Phys.*, **13**, 323 (1967).
(5) H. G. Hertz, *Mol. Phys.*, **14**, 291 (1968).
(6) H. G. Hertz, G. Keller, and H. Versmold, *Ber. Bunsenges. Phys. Chem.*, **73**, 549 (1969).
(7) R. E. Connick and K. Wüthrich, *J. Chem. Phys.*, **51**, 4506 (1969).
(8) H. G. Hertz, R. Tutsch, and H. Versmold, *Ber. Bunsenges. Phys. Chem.*, **75**, 1177 (1971).
(9) G. Engel and H. G. Hertz, *Ber. Bunsenges. Phys. Chem.*, **72**, 808 (1968).
(10) H. G. Hertz, *Angew. Chem.*, **82**, 91 (1970); *Angew. Chem., Int. Ed. Engl.*, **82**, 124 (1970).
(11) S. Nakamura and S. Meiboom, *J. Am. Chem. Soc.*, **89**, 1765 (1967).
(12) N. A. Matwiyoff and H. Taube, *J. Am. Chem. Soc.*, **90**, 2796 (1968).

(13) N. Bloembergen and L. O. Morgan, *J. Chem. Phys.*, **34**, 842 (1961).
(14) E. V. Goldammer and M. D. Zeidler, *Ber. Bunsenges. Phys. Chem.*, **73**, 4 (1969).
(15) M. Gruner, Thesis, Karlsruhe, 1969.
(16) E. v. Goldammer and H. G. Hertz, *J. Phys. Chem.*, **74**, 3734 (1970).
(17) H. Versmold, *Ber. Bunsenges. Phys. Chem.*, **78**, 1318 (1974).
(18) R. O. W. Howarth, *Chem. Commun.*, 286 (1974).
(19) A. Abragam, "The Principles of Nuclear Magnetism", Oxford University Press, London, 1961.
(20) H. G. Hertz, *Prog. Nucl. Magn. Reson. Spectrosc.*, **3**, 159 (1967).
(21) H. G. Hertz, *Water: Compr. Treatise 1973*, **3**, 301 (1973).
(22) H. G. Hertz, *Ber. Bunsenges. Phys. Chem.*, **71**, 1008 (1967).
(23) D. E. Woessner, *J. Chem. Phys.*, **36**, 1 (1962).
(24) D. E. Woessner, *J. Chem. Phys.*, **37**, 647 (1962).
(25) D. E. Woessner, B. S. Snowden, and G. H. Meyer, *J. Chem. Phys.*, **56**, 719 (1969).
(26) D. Wallach, *J. Chem. Phys.*, **47**, 8258 (1967).
(27) H. Versmold, *Z. Naturforsch. A*, **25**, 367 (1970).
(28) A. R. Edmonds, "Angular Momentum in Quantum Mechanics", German translation, Bibliographisches Institut, Mannheim, 1964.
(29) M. E. Rose, "Elementary Theory of Angular Momentum", Wiley, New York, N.Y., 1957.
(30) H. Versmold, *J. Chem. Phys.*, **58**, 5649 (1973).
(31) M. Gruner and H. G. Hertz, *Adv. Mol. Relaxation Processes*, **3**, 75 (1972).
(32) H. G. Hertz and M. D. Zeidler, "The Hydrogen Bond. Recent Development in Theory and Experiments", North-Holland Publishing Co., Amsterdam, 1975.
(33) J. R. Lyerla, Jr., and D. M. Grant, *Phys. Chem., Ser. One, 1972–1973*, **4**, 155 (1972).
(34) R. Goller, H. G. Hertz, and R. Tutsch, *Pure Appl. Chem.*, **32**, 149 (1972).
(35) D. R. Herschbach, *J. Chem. Phys.*, **25**, 358 (1956).
(36) H. G. Hertz and R. Tutsch, to be submitted for publication.
(37) R. Sperling and H. Pfeifer, *Z. Naturforsch. A*, **19**, 1342 (1964).
(38) E. A. C. Lucken, "Nuclear Quadrupole Coupling Constants", Academic Press, London, 1969.
(39) R. E. Verrall, *Water: Compr. Treatise 1973*, **3**, 211 (1973).
(40) D. E. Irish in "Structure of Water and Aqueous Solutions", Verlag Chemie, Weinheim, 1974.
(41) H. Hartmann and E. Muller, *Z. Naturforsch. A*, **18**, 1024 (1963).
(42) T. Chiba, *J. Chem. Phys.*, **41**, 1352 (1964).
(43) R. M. Hammaker and R. M. Clegg, *J. Mol. Spectrosc.*, **22**, 109 (1967).
(44) J. A. Pople, W. G. Schneider, and H. J. Bernstein, "High-Resolution Nuclear Magnetic Resonance", New York, N.Y., 1959.
(45) J. R. Homes, D. Kivelson, and W. C. Drinkard, *J. Am. Chem. Soc.*, **84**, 4677 (1962).
(46) C. Franconi, C. Dejak, and F. Conti, "Nuclear Magnetic Resonance in Chemistry", Academic Press, New York, N.Y., 1965, p 363.
(47) Z. Kecki, *Rocz. Chem., Ann. Soc. Chim. Polonium*, **44**, 213 (1970).
(48) Here and in the following second coordination sphere corrections are omitted, because such a neglect never effects the qualitative conclusions to be drawn.
(49) H. Langer, private communication.
(50) This result was obtained from the proton–Na^+ intermolecular relaxation rate. A corresponding experiment can also be performed in MeOH. (D. S. Gill, H. G. Hertz, and R. Tutsch, to be submitted for publication.)

Kinetics of Endothermic Decomposition Reactions. I. Steady-State Chemical Steps

Alan W. Searcy* and Dario Beruto

Inorganic Materials Research Division, Lawrence Berkeley Laboratory and Department of Materials Science and Engineering, College of Engineering, University of California, Berkeley, California 94720 and Istituto di Technologie, Facoltà di Ingegneria, Universita di Genova, Italy *(Received October 31, 1974; Revised Manuscript Received November 14, 1975)*

Publication costs assisted by the U.S. Energy Research and Development Administration

When the solid product of an endothermic decomposition reaction is porous, the rate-limiting chemical step is usually assumed to be a surface step of the gaseous product or of a precursor of that product. It is shown here that the rate of such a reaction may also depend upon (a) rates of diffusion in the reactant phase, (b) the rate of transfer of the solid reaction product at the reactant–product interface, and/or (c) the thermodynamic stability of the solid product. Rate equations are derived for the six possible limiting cases when either a single step or a coupled pair of steps of a decomposition reaction significantly influence its rate. Data for calcite ($CaCO_3$) decomposition are shown to be most simply explained as reflecting formation of a known metastable modification of calcium oxide with near equilibrium conditions maintained for each reaction step except desorption of carbon dioxide. If this explanation is correct the free energy of formation of the metastable oxide from the stable oxide should be found to be about $+7500 - 5T$ cal/mol.

I. Introduction

Reactions in which a solid reactant yields a new solid phase plus a gaseous product, that is, reactions which can be described by the general equation

$$AB(solid) = A(solid) + B(gas) \qquad (1)$$

are usually called decomposition reactions.[1] When the solid decomposition product is porous, the rate-limiting chemical step is usually assumed to be a surface step of the eventual gaseous reaction product.[2–4]

This assumption may often be wrong. During steady-state decomposition, such as characterizes calcium carbonate[5] and barium sulfate[6] single crystals heated under vacuum, the solid reactant is converted at a constant rate to the solid product plus pores through the solid product. Decomposition at a constant rate is only possible if four different steps occur at the same rate (see Figure 1). (a) A flux j_B formed from that portion of chemical component B that is at an interface between the solid reactant phase AB and the solid product phase must undergo solid state diffusion to the surface at a pore. (b) A flux J_B of component B must transfer from the AB surface to the gas phase. (c) A flux j_A formed from that portion of chemical component A that is at the AB surface fronted by a pore must undergo diffusion on or in the AB phase to a particle of the solid product

* Address correspondence to this author the University of California.

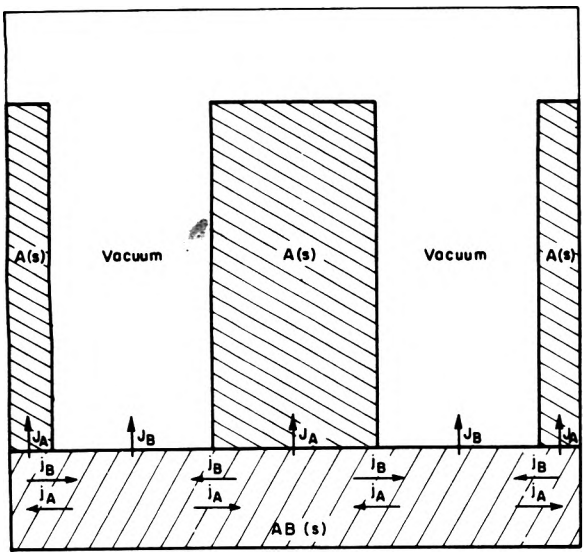

Figure 1. Schematic cross-sectional drawing of the spatial relations for the steady state reaction AB(solid) → A(solid) + B(gas). j_B is a diffusional flux of chemical component B from interfaces between solid AB phase and the solid product phase to the AB surface fronted by pores, and j_A is the oppositely directed diffusional flux of component A. J_A is the flux of A across the interface between AB and the solid product phase, and J_B is the flux of B from the AB surface to the gas phase.

phase A. (d) A flux J_A must transfer from the AB phase across the interface to the solid product phase. Using the symbols i for interface, s for surface, and g for gas, these four reaction steps can be written in the order described as

$$B_i \rightleftharpoons B_s \tag{2}$$

$$B_s \rightarrow B_g \tag{3}$$

$$A_s \rightleftharpoons A_i \tag{4}$$

$$A_i \rightleftharpoons A_p \tag{5}$$

The central purpose of this paper is to derive rate equations which describe the kinetics of steady-state decomposition reactions under vacuum when any of the four steps (2–5) is slow enough to influence the rate. Application of the analysis is illustrated in the Discussion section with data for calcite.[5]

II. Thermodynamic Considerations

Darken[7] showed that rate equations for highly nonideal systems are better expressed in terms of activity gradients than of concentration gradients. An important advantage will be gained by writing the rate equations of the four coupled steps of a decomposition reaction in terms of activity gradients. The activities of one of the two chemical components of a binary (or pseudobinary) phase can be calculated from the integral free energy of the phase and a measured activity of the other component even though the variations of composition that produce the changes in activity are too small to measure.[8,9] It is, for example, thermodynamically meaningful to calculate the activity of calcium oxide, viewed as one component of a system, in a calcium carbonate phase from the activity of the other component, carbon dioxide, at pressures different from the dissociation pressure.

Consider the reaction between a solid and a gas in their standard states to form a solid of a particular composition $A_{1+\delta}B_{1-\delta}$

$$(1+\delta)A(s) + (1-\delta)B(g) = A_{1+\delta}B_{1-\delta}(s) \tag{6}$$

The integral free energy change in reaction 6, ΔG_6, can be written as a function of the partial molar free energy changes of the two components, and the partial free energy changes can be expressed in terms of activity or fugacity changes:[10]

$$\Delta G_6 = (1+\delta)RT \ln a_A + (1-\delta)RT \ln f_b \tag{7}$$

where the activity a_A and fugacity f_B are those for components A and B in the AB phase of the composition described in reaction 6.

For phases of narrow composition limits, the integral free energies of formation, unlike the partial free energies of formation, usually vary by negligible amounts with composition. Therefore, $-\Delta G_6$ is for practical purposes equal to $\Delta G_1°$, the standard free energy change for reaction 1, independent of composition. With this substitution and neglecting the small δ, eq 7 yields

$$a_A P_B = \exp(-\Delta G_1°/RT) \tag{8}$$

in the experimental range where the partial pressure of B can be substituted for its fugacity.

For the purposes of this paper it is convenient to define the activity of B for any particular composition of the AB phase, not in the usual way, but as the ratio of the partial pressure of B for that composition, P_B, to the equilibrium decomposition pressure $P_B(d)$ for each temperature. This definition combined with eq 8 yields $a_A a_B = 1$ for the AB phase at any composition when it is at internal equilibrium.

A decomposition reaction can proceed at a finite rate only if the AB phase is supersaturated with respect to component A so that the activity of component A in the AB phase is greater than 1. For supersaturated solutions, provided that internal equilibrium is maintained, the relationship $a_A a_B = 1$ should be essentially as good an approximation as it is for the thermodynamically stable composition range because the phase boundary does not reflect any discontinuity in properties of the AB phase but only the coincidence in activities of the chemical components in phase AB and in solid phase A. However during decomposition, local equilibrium may not be maintained if one of the chemical components is much less mobile than the other. The less mobile component may not be able to rearrange locally under the steady-state reaction conditions to produce the atomic coordinations and distances characteristic of the equilibrium phase of the particular local composition. If local equilibrium is not maintained the local products $a_A a_B$ at surfaces and at interfaces (which will be called K_s and K_i) will be greater than unity.

Decomposition reactions often yield as the direct solid product a metastable crystal modification or an amorphous form of the solid.[1,3] In either event, the activity of the product, which can be called a_{Ap}, is not unity but

$$a_{Ap} = \exp(\Delta G_p/RT) \tag{9}$$

where ΔG_p is the positive free energy of formation of the metastable form of solid A from the stable form. When the interphase transfer of component A (eq 5) is a near equilibrium process, the activity of component A on the AB side of the interface, which can be called a_{Ai}, approaches as a limit a_{Ap}. Then, if local equilibrium is attained in the AB phase at its interface with the solid product so that $K_i = 1$

$$a_{Bi}a_{Ai} = a_{Bi} \exp(\Delta G_p/RT) = 1 \tag{10}$$

where a_{Bi} is the activity of B on the reactant side of the interface. Equation 10 shows that, when the solid reaction product is metastable, the maximum activity that can be attained by component B, regardless of reaction mechanism, is not unity but $\exp(-\Delta G_p/RT)$, which has a value less than unity.

III. The Rate Equations for Steady-State Decomposition

The average diffusion distances that must be traversed by particular atoms or molecules are functions of their initial positions relative to the advancing pores and particles of the solid reaction product. For example, an A atom or molecule originally located in a volume element of the AB phase that is swept through by a growing particle of the solid reaction product need not diffuse at all, and the minimum distance over which an A atom or molecule that is originally under a pore must diffuse is its distance to the boundary between the pore and the solid product phase.

Suppose that the flux of component A that must diffuse per unit area of that part of the surface of AB which is fronted by pores is j_A. That flux is

$$j_A = \sum_n (d_n a_{Asn} - d_n' a_{Ain}) \tag{11}$$

where, for example, d_n is the rate constant for movement in the forward direction over one of the characteristic steady-state paths, d_n' is the rate constant for the reverse direction over the same path, a_{Asn} is the activity of component A at the particular point of the AB phase surface at which the nth diffusion path is initiated, and a_{Ain} is the activity of A at the point in the interface between the solid reactant and solid product at which the nth path is terminated.

To simplify eq 11, it will be assumed that each activity of the kinds a_{Asn} and a_{Ain} can be replaced by average activities at the surface, a_{As}, and interface, a_{Ai}, respectively. The summation Σd_n can be called k_4 and the summation $\Sigma d_n'$ can be called k_4'. Then the diffusion flux of component A is $j_A = k_4 a_{As} - k_4' a_{Ai}$. Similarly, if j_B is defined as the flux of component B that must diffuse per unit area of interface between the solid product phase A and the reactant then $j_B = k_2 a_{Bi} - k_2' a_{Bs}$ where k_2 and k_2' are similar summations for diffusion reaction 2.

The flux in the surface step for component B (reaction 3) can be written $J_B = k_3 a_{Bs}$ where J_B is the total flux of B leaving each unit area of AB phase. The net flux of component A that leaves each unit area of the AB phase is $J_A = k_5 a_{Ai} - k_5' a_{Ap}$ where k_5 and k_5' are the forward and reverse rate constants for step 5.

The steady-state decomposition of AB is thus characterized by four interdependent rate equations, which are for steps 2–5 of the overall reaction respectively:

$$j_B = k_2 a_{Bi} - k_2' a_{Bs} \tag{12}$$

$$J_B = k_3 a_{Bs} \tag{13}$$

$$j_A = k_4 a_{As} - k_4' a_{Ai} \tag{14}$$

$$J_A = k_5 a_{Ai} - k_5' a_{Ap} \tag{15}$$

There are important restrictions on the steady-state reaction:

$$J_A = J_B \tag{16}$$

$$j_A = j_B \tag{17}$$

$$a_{Ai} a_{Bi} = K_i \geq 1 \tag{18}$$

$$a_{As} a_{Bs} = K_s \geq 1 \tag{19}$$

Equation 16 expresses the restriction that the total fluxes of A and B must be equal during steady-state decomposition. Equation 17 is a similar restriction on the steady-state diffusion fluxes in or on the AB phase. Furthermore, since j_B is the flux that diffuses per unit area of AB-solid product interface and j_A is the flux per unit area of AB fronted by pores, $j_B = J_B$ numerically and $j_A = J_A$ numerically.

The four restrictions on the steady-state system can be used to obtain a general solution in which all the activities other than the activity of the product phase have been eliminated.[11] Here we derive rate equations for the six limiting cases possible for these four steps. Setting eq 12 equal to eq 13

$$k_2 a_{Bi} - k_2' a_{Bs} = k_3 a_{Bs}$$

so that

$$a_{Bs} = k_2 a_{Bi}/(k_2' + k_3)$$

and from (13)

$$J_B = k_2 k_3 a_{Bi}/(k_2' + k_3) \tag{20}$$

For an elementary (single step) reaction the rate constant at any particular composition for the foreward direction divided by the rate constant at the same composition for the reverse direction equals the equilibrium constant, even if the rate constants are functions of composition.[12] The equilibrium constants for steps 2 and 4 are both unity. However, as explained in the discussion that follows eq 11, the constants k_2, k_4, and k_4' are not rate constants for elementary reactions, so we do not know that $k_2 = k_2'$ or that $k_4 = k_4'$. We expect each k' to be of the same magnitude as the corresponding k and assume the equalities to simplify eq 20. When component A in the reactant phase is at equilibrium with both component B and with the solid product phase A, $a_{Bi} = 1/a_{Ap}$ and eq 20 yields two limiting solutions. For $k_2 = k_2' \gg k_3$, that is when the rate constant for diffusion of component B is large relative to its rate constant for desorption

$$J_B = k_3/a_{Ap} = k_3 \exp(-\Delta G_p/RT) \tag{21}$$

When $k_2' \ll k_3$

$$J_B = k_2/a_{Ap} = k_2 \exp(-\Delta G_p/RT) \tag{22}$$

When transfer of component A to the product phase by step 5 is assumed to be irreversible so that $k_5' a_{Ap}$ can be neglected relative to $k_5 a_{Ai}$, substitution of eq 18 and 15 into 20 yields

$$J_A J_B = k_2 k_3 k_5 K_i/(k_2' + k_3)$$

At steady state, $J_A = J_B$, and this expression has two solutions

$$J_B = (k_3 k_5 K_i)^{1/2} \tag{23}$$

when $k_2' = k_2 \gg k_3$, or

$$J_B = (k_2 k_5 K_i)^{1/2} \tag{24}$$

when $k_2' \ll k_3$.

When diffusion of component A and desorption of component B are assumed to be slow, the product $J_A J_B$ is $(k_4 a_{As} - k_4' a_{Ai})(k_3 a_{Bs})$. Then if $k_4' a_{Ai} \ll k_4 a_{As}$

$$J_A = J_B = (k_4 k_3 K_s)^{1/2} \quad (25)$$

The sixth limiting expression is obtained by use of eq 17–19 to eliminate unknown activities in the two diffusion equations, eq 12 and 14. The result is a quadratic equation in a_{Bs} and a_{Bi}

$$a_{Bs}^2 - a_{Bs}\left[\frac{k_2}{k_2'}a_{Bi} + \frac{k_4' K_i}{k_2' a_{Bi}}\right] + \frac{k_4 K_s}{k_2'} = 0 \quad (26)$$

If $K_s \simeq K_i \simeq K$, $k_2 \simeq k_2'$, and $k_4 \simeq k_4'$, eq 26 has two solutions

$$a_{Bs} = a_{Bi} \quad (27)$$

and

$$a_{Bs} = \frac{k_4 K}{k_2 a_{Bi}} = \frac{k_4 a_{Ai}}{k_2} \quad (28)$$

Equation 27 describes the limit that is approached when diffusion in the AB phase is so rapid relative to other steps that activity gradients in the reactant phase are negligible; then diffusion is not rate limiting. Equation 28 can be physically meaningful only when $k_4 a_{Ai} < k_2$ because the maximum value possible for a_B is one. Also, because the minimum value for a_{Ai} is one, $k_4 < k_2$. Substitution of eq 28 into 13 with $a_{Ai} \simeq a_{Ap}$ yields

$$J_B = k_3 k_4 a_{Ap}/k_2 \quad (29)$$

for the flux when diffusion of component B is slow and the rate constant for diffusion of component A is smaller than that for component B.

IV. Discussion

Previous studies of decomposition reaction kinetics have usually assumed that the slowest chemical step is a surface step for the gaseous component.[2–4] Equation 21 shows that if the surface step is indeed the slowest of the four necessary steps in steady-state decomposition, the rate also depends on whether the solid reaction product is stable or metastable. Equation 22 shows that if the rate for solid state diffusion of the gaseous component is smaller than the rate for the surface step, the rate depends on the rate constant for diffusion of the gaseous component and on the activity of the solid product phase.

If one of the rate constants for the solid component is smaller than both rate constants for the gaseous component, three limiting cases arise in which the steady-state rate is the geometric mean of the product of the rate constants for the slowest step of each of the two components and a product of their activities (eq 23–25). When solid state diffusion of the solid component is the slowest step and solid state diffusion of the gaseous component is slower than its surface step, eq 29 gives the steady state flux. These four relatively complex equations result because, when a step of the solid component is slower than a step of the gas, the activity of the gaseous component decreases in the AB phase and that of the solid increases until the fluxes of the two components are equal.

The utility of one of the limiting rate equations can be illustrated by its application to rate data that we recently obtained for decomposition of calcite[5] (calcium carbonate) single crystals under vacuum. A crystallographically distorted, metastable form of calcium oxide was showed in that study to be present as a 30-μ thick layer between the undercomposed calcite and the growing layer of calcium oxide. The stable oxide must have formed by an irreversible transformation of the distorted oxide when its strain energy became sufficient to overcome an energy barrier to the transformation. The stable oxide could not have been in equilibrium with the calcite because, if it were in equilibrium, the metastable oxide would not have been present between the stable oxide and the calcite.

We showed in the experimental paper on calcite decomposition that a decomposition reaction is characterized by a maximum possible flux J_{max} which can be calculated by means of the Hertz–Knudsen–Langmuir equation

$$J_{max} = P_B(d)/(2\pi MRT)^{1/2} \quad (30)$$

where $P_B(d)$ is the equilibrium dissociation pressure, M is the molecular weight, and R is the gas constant. This maximum flux would only be obtained if there is no energy barrier for condensation of the gaseous reaction product on the reactant surface and if the activity of the gaseous component on the reactant surface is the equilibrium value for the dissociation reaction to the stable solid reaction product,[5,13,14] that is if a_B as defined in this paper is unity.

However, for calcite decomposition, the stable oxide is certainly not at equilibrium with the calcite phase. The metastable oxide may or may not be. If the metastable oxide is at equilibrium with calcium carbonate, the activity of carbon dioxide is $a_{CO_2} = 1/a_{CaO^\bullet}$ where $a_{CaO^\bullet}$ is the activity of the metastable oxide. If the metastable oxide is not at equilibrium with the carbonate, the activity of carbon dioxide must be less than $1/a_{CaO^\bullet}$. The maximum flux produced by decomposition to the metastable oxide is

$$J_{max} = \frac{P(d)}{(2\pi MRT)^{1/2} a_{CaO^\bullet}} \quad (31)$$

Equation 31 is a special case of eq 21 in which k_3 is identified as $P(d)/(2\pi MRT)^{1/2}$.

The observed flux J_o may be equal to or less than J_{max}. Solving the inequality gives

$$\exp(\Delta G_{CaO^\bullet}/RT) = a_{CaO^\bullet} \leq \frac{P_B(d)}{(2MRT)^{1/2} J_o} \quad (32)$$

Substitution of known values of the dissociation pressure of calcite and values of J_o from our experimental paper into (32) yields $\Delta G_{CaO^\bullet} \leq 7500 - 5T$.

An entropy change of the order of +5 cal/deg is reasonable for formation of a metastable solid from its stable modification. A positive heat of formation at least as large as 7500 cal is consistent with the x-ray evidence that interionic distances are 7% greater in the metastable oxide than in the stable form.[5] We suggest, therefore, that the calculated maximum free energy of formation probably is close to the actual value, and that all steps of the decomposition reaction to the metastable oxide are close to equilibrium. This interpretation could be tested by measuring the enthalpy of formation of the metastable oxide calorimetrically or by measuring its equilibrium dissociation pressure.

Other decomposition reactions that have been recently studied at Berkeley do not fit the simple interpretation proposed from calcite.[6,15] In a second theoretical paper we will show that the effect on decomposition rates of pressures of the product gas and of the porous product layers can be used to determine for these more complex cases whether or not a step of the component that forms the solid product is slow enough to influence the reaction rates.

Acknowledgment. We appreciate advice on this study by Alfred Büchler and David J. Meschi. This work was supported by the U.S. Energy Research and Development Administration.

References and Notes

(1) See, for example, "Chemistry of the Solid State", W. E. Garner, Ed., Butterworths, London, 1955.
(2) R. D. Shannon, *Trans. Faraday Soc.*, **60**, 1902 (1964).
(3) D. A. Young, "Decomposition of Solids", Pergamon Press, Oxford, 1966.
(4) K. H. Stern and E. L. Weise, *Natl. Stand. Ref. Data Ser., Natl. Bur. Stand.*, **No. 30** (1969).
(5) D. Beruto and A. W. Searcy, *J. Chem. Soc., Faraday Trans. 1*, **70**, 2145 (1974).
(6) P. Mohazzabi and A. W. Searcy, *J. Chem. Soc., Faraday Trans. 1*, **72**, 290 (1976).
(7) L. S. Darken, *Trans. AIME*, **180**, 430 (1949).
(8) A. W. Searcy, "Proceedings of the Second International High Temperature Chemistry Symposium", Asilomar, Calif., Oct 1959, Wiley, New York, N.Y., 1960, p 157.
(9) A. W. Searcy in "Chemical and Mechanical Behavior of Inorganic Materials", A. W. Searcy, D. V. Ragone, and U. Colombo, Ed., Wiley-Interscience, New York, N.Y., 1970, p 2.
(10) See, for example, K. S. Pitzer and L. Brewer, "Thermodynamics", McGraw-Hill, New York, N.Y., 1961 Chapters 14, 17, and 20.
(11) A general solution of the rate equation and an alphabitical list of symbols are available in "Appendices to The Kinetics of Endothermic Decomposition Reaction: I Steady State Chemical Steps" by A. W. Searcy and D. Beruto, LBL-3137 Review Supplement.
(12) A. W. Searcy, A. Büchler, and D. Beruto, *High Temp. Sci.*, **6**, 64 (1974).
(13) A. W. Searcy in ref 8, Chapter 6.
(14) A. W. Searcy and D. Beruto, *J. Phys. Chem.*, **78**, 1298 (1974).
(15) T. K. Basu and A. W. Searcy, submitted for publication.

COMMUNICATIONS TO THE EDITOR

Electron Paramagnetic Resonance Study of the Diphenylketyl Radical at Low Temperatures

Sir: The diphenylketyl radical is known to be an important intermediate in the photochemistry of benzophenone.[1-3] We have recently reported the formation mechanisms of aromatic ketyl radicals in the ultraviolet photolysis of benzaldehyde, acetophenone, and benzophenone at low temperatures.[4] In this paper, intensive EPR studies of the diphenylketyl radical have been carried out using benzophenone-*carbonyl*-^{13}C at temperatures from 77 to 140 K. The reversible temperature dependence of the EPR spectrum was observed. The isotropic and anisotropic ^{13}C hyperfine coupling parameters have been estimated from analysis of the EPR spectra.

The EPR spectrometer used was a conventional X-band type (JEOL JES-3BS-X) operated with 100-kHz modulation. Methanol was mainly used as solvent, and ethanol, 2-propanol, and EPA were also used. Benzophenone (natural abundance of isotopes) and benzophenone-*carbonyl*-^{13}C (91.9 atom % ^{13}C) were used as solute. The concentration of benzophenone was $10^{-2} \sim 10^{-4}$ M. The solutions were degassed with a high vacuum system. The irradiation source was a high-intensity high-pressure mercury lamp and a Halio glass filter which transmitted light of wavelength longer than 300 nm was used.

Diphenylketyl radicals were formed in the following ways. (1) At ~130 K, the radicals were produced by light irradiation of wavelength longer than 300 nm. Under this condition, diphenylketyl radicals were easily formed by the hydrogen abstraction reaction through the lowest triplet state ($^3n,\pi^*$) of benzophenone. Stopping the irradiation, the second-order decay of the ketyl radical disappearance was observed at temperatures higher than 140 K, which was expected from the combination reaction of two ketyl radicals to form pinacol.[2] In this method, no solvent radical was observed. (2) At 77 K, diphenylketyl radicals and solvent radicals were obtained by high intensity light irradiation ($\lambda > 300$ nm). This process is thought to be a biphotonic process through the higher excited triplet state of benzophenone. By raising the sample temperature to ~130 K, the solvent radicals disappeared, and the EPR spectrum of the ketyl radical remained. Both these reaction paths 1 and 2 were previously discussed in detail.[4]

When benzophenone-*carbonyl*-^{13}C in methanol was photolyzed, the EPR spectrum of the diphenylketyl radical with carbon-13 hyperfine splitting was obtained in both methods 1 and 2. The spectrum was transformed reversibly by changing the temperature between 77 and 138 K, which is shown in Figure 1. However in the case of benzophenone-*carbonyl*-^{12}C, only a broad singlet spectrum was obtained and a significant spectrum transformation by temperature was not observed. Similar results were also obtained in the cases of ethanol, 2-propanol, and EPA solvents. The triplet spectrum at 77 K shown in Figure 1 is understood by assuming the anisotropy of $Ph_2{}^{13}COH$ radicals in rigid solvent. From this spectrum, $a_\parallel(^{13}C)$ was estimated at about 50 G and $a_\perp(^{13}C)$ was thought to be below 15 G. There exists an interesting phenomenon. In spite of the averaging of the anisotropic spectrum by raising the sample temperature, the interval between both side peaks of the first derivative of the EPR absorption spectra did not apparently show a remarkable change. The ketyl radical does not show the spectrum of complete free motion under this condition,

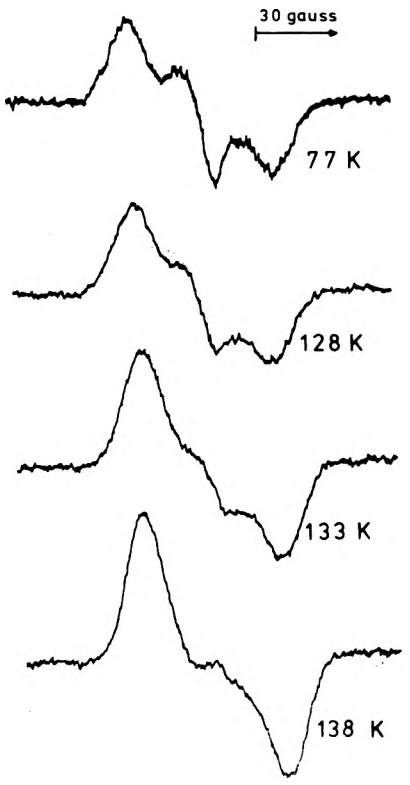

Figure 1. EPR spectra of ketyl radical ($Ph_2{}^{13}COH$) in methanol solution at various temperatures.

since this type of radical is too large and complicated to move freely in methanol solution in this temperature range. The value of $a_{iso}(^{13}C)$ of the diphenylketyl radical was estimated at 17–27 G from the values of $a_{\parallel}(^{13}C)$ and $a_{\perp}(^{13}C)$. The EPR spectrum at 138 K is explicable using this value. In the cases of H_2COH,[5] H(OH)CCOOH, and $(HO)_2C$-COOH,[6] $a_{iso}(^{13}C)$ was reported to be 47.4, 33, and 29 G, respectively. In comparison with those results, the value of a_{iso} estimated above is reasonable. The spin densities on ^{13}C are $\rho_s \sim 0.02$ and $0.4 < \rho_p < 0.5$ assuming literature values for atomic orbital couplings.[7] This result shows that the contribution of an unpaired electron to the s orbital is very small; that is, the bonds of the α carbon of the diphenylketyl radical in rigid media are almost sp^2 hybridized.

Acknowledgments. We are very grateful to Professor I. Tanaka for support and encouragement. We also acknowledge with pleasure the useful discussion with Dr. K. Shimokoshi in particular.

References and Notes

(1) G. Porter and F. Wilkinson, *Trans. Faraday Soc.*, **57**, 1686 (1961).
(2) A. Beckett and G. Porter, *Trans. Faraday Soc.*, **59**, 2038 (1963).
(3) R. Wilson, *J. Chem. Soc. B*, **84**, 1581 (1968).
(4) H. Murai and K. Obi, *J. Phys. Chem.*, **79**, 2446 (1975).
(5) A. J. Dobbs, B. C. Gilbert, and R. O. C. Norman, *J. Chem. Soc. A*, 124 (1971).
(6) L. Bonazzola, C. Hesse-Bezot, and J. Roncin, *Chem. Phys. Lett.*, **20**, 479 (1973).
(7) P. B. Ayscough, "Electron Spin Resonance in Chemistry", Methuen, London, 1967, p 438.

Department of Chemistry
Tokyo Institute of Technology
Ohokayama, Meguro-ku
Tokyo, Japan

Hisao Murai
Mamoru Jinguji
Kinichi Obi*

Received October 6, 1975

Mechanism of Catalytic Reaction between NO and NH_3 on V_2O_5 in the Presence of Oxygen

Publication costs assisted by the Department of Chemistry, The University of Tokyo

Sir: The catalytic reduction of NO to form nitrogen offers a significant issue for environmental sciences and many varieties of reaction systems have already been studied.

Otto and Shelef proposed the mechanism of the reduction of NO by NH_3 over Pt and CuO, in which ammonia is dissociatively adsorbed on the catalyst as NH_2(ad) and H(ad) reacting with adsorbed NO(ad) via the Langmuir–Hinshelwood mechanism.[1,2] It is generally accepted that the reaction between nitric oxide and ammonia is markedly accelerated by the addition of oxygen. To explain this fact, Markvart and Pour conjectured that the effect may be due to the acceleration of the dissociative adsorption of ammonia by oxygen.[3] The mechanism of this reaction, however, has not been established. In this communication we will propose a new mechanism of the reduction of nitric oxide by ammonia on V_2O_5 in the presence of oxygen. V_2O_5 has a very high activity as well as selectivity to form N_2 molecule and is not easily poisoned by gases such as SO_2 which are frequently contained in the reacting gas in practical use. For elucidating the reaction mechanism, we separately studied the elementary steps of the reaction, by using volumetric, infrared, x-ray photoelectron spectroscopy, and mass spectrometry techniques.

A commercial V_2O_5 (Nakarai Chemical, special grade) and alumina supported V_2O_5 (V_2O_5/Al_2O_3) were used as catalysts. The V_2O_5/Al_2O_3 was prepared by impregnating alumina with a V_2O_5 saturated solution of oxalic acid, heated under vacuum at 400 °C for 2 h and then oxidized in 100 Torr of oxygen at 400 °C for 1 h before use. The x-ray photoelectron spectra of these catalysts after pretreatment showed only V and O for V_2O_5 and Al, V, and O for V_2O_5/Al_2O_3 (V^{5+}, O^{2-}). No contaminants that would influence the reaction were observed on the catalyst surface except for a small amount of carbon. The infrared measurements of the adsorbed species were carried out by means of a circulating system equipped with an ir cell as described previously.[4]

The ir spectra after adsorption of ammonia on V_2O_5, Al_2O_3, and supported V_2O_5 (V_2O_5/Al_2O_3) are shown in Figure 1a–c. The adsorbed ammonia on the V_2O_5 surface exhibited a strong absorption band at 1413 cm^{-1}. This band was assigned to adsorbed $NH_4{}^+$(ad) on V_2O_5, since the infrared spectrum of meta ammonium vanadate (NH_4VO_3) also showed a very strong band at 1410 cm^{-1} due to $NH_4{}^+$ and the binding energy of nitrogen 1s electron in the adsorbed ammonia on the V_2O_5 surface obtained by x-ray photoelectron spectroscopy was exactly the same as that of NH_4VO_3. The other two bands at 1610 and 1275 cm^{-1} in the ir spectrum are due to adsorbed NH_3(ad) on γ-Al_2O_3, as Eischens et al. have already reported.[5]

When oxygen was introduced onto the ammonia adsorbed V_2O_5/Al_2O_3 surface, the absorption band of NH_3(ad) on γ-Al_2O_3 decreased in intensity, while $NH_4{}^+$(ad) on V_2O_5 increased. This indicates that NH_3(ad) on γ-Al_2O_3 was expelled from Al_2O_3 and was adsorbed on the V_2O_5 surface as $NH_4{}^+$(ad) by the introduction of oxygen.

No adsorption of NO was observed on the V_2O_5 catalyst surface, even when the surface was oxidized by oxygen or

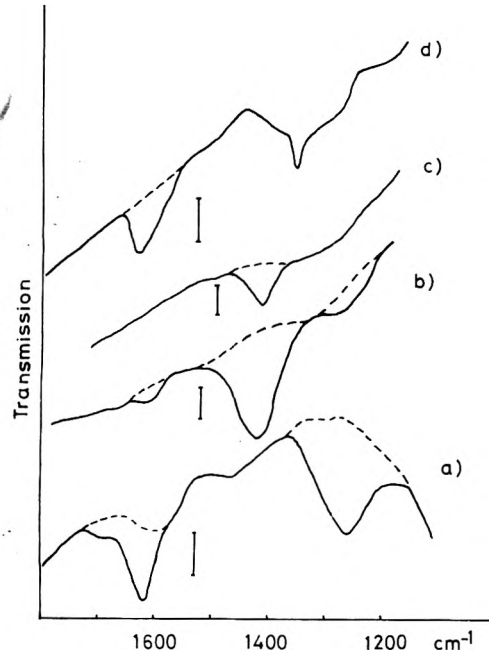

Figure 1. Ir spectra of adsorbed species at room temperature. Adsorbed ammonia on Al_2O_3 (a), alumina supported V_2O_5 (b) and V_2O_5 (c), and adsorbed species given by NO + O_2 on V_2O_5/Al_2O_3 (d). Dotted lines represent the background spectra, and bars show the transmission range of 10%.

reduced by hydrogen. When a gas mixture of NO and O_2 was introduced onto the V_2O_5 surface, however, adsorption took place and the infrared spectrum of the adsorbed species exhibited a band at 1632 cm^{-1} as shown in Figure 1d. An absorption band at the same position (1632 cm^{-1}) was observed when only NO_2 gas was introduced onto the V_2O_5 surface. The absorption band at 1632 cm^{-1} may be assigned to the antisymmetric stretching of NO_2(ad),[6] which suggests that NO is adsorbed on V_2O_5 as NO_2(ad) in the molecular form in the presence of oxygen. The absorption band at 1355 cm^{-1} was assigned to the NO_3^- ion on the NaCl window of the ir cell.

When NO_2 gas was introduced onto the ammonia preadsorbed V_2O_5 or V_2O_5/Al_2O_3 at room temperature, the ir spectrum of the adsorbate NH_4^+(ad) on V_2O_5 decreased in intensity, and N_2 and H_2O were detected in the reaction system. The decrease of adsorbate NH_4^+(ad) did not occur when only NO was introduced onto the surface. When ammonia was introduced onto the NO_2 preadsorbed V_2O_5 surface, on the other hand, the ir peak of adsorbed NO_2(ad) decreased and N_2 was also detected as the reaction product. These results indicate that NO_2(ad) from gaseous NO with oxygen, and NH_4^+(ad), produced by the reactant NH_3, are both very reactive surface species in the reduction of NO by NH_3.

The reaction between NO_2(ad) and NH_4^+(ad) was separately studied by the infrared technique. After adsorbing ammonia and NO_2, the gas-phase species were removed, and the two absorption bands (1410 and 1630 cm^{-1}) due to each adsorbate, NH_4^+ and NO_2, were examined. Both bands were decreased and almost dissappeared in 30 min at room temperature, while in the absence of one of these two adsorbed species, the absorption band of the other remained unchanged. This demonstrates that NO_2(ad) reacts readily with NH_4^+(ad) on the V_2O_5/Al_2O_3 surface at room temperature. In this manner NO reacts with NH_3 in the presence of oxygen via NO_2(ad) and NH_4^+(ad) on the V_2O_5 catalyst, where a marked accelerating effect of oxygen is observed.

No N_2O was detected after introduction of NO gas onto the reduced V_2O_5 surface, which shows that the surface reaction on V_2O_5

$$2NO \rightarrow N_2O + O(ad)$$

does not take place. This process is an indispensable elementary process in the so-called "redox mechanism" reaction.[7]

On the basis of the results we have obtained, it was concluded that the marked oxygen effect on the reaction between NO and NH_3 may be explained by the following mechanism. As a first step, NO oxidized by ambient O_2 is adsorbed as NO_2(ad) on V_2O_5, and NH_3 as NH_4^+(ad), respectively. Then both adsorbates react to form the product N_2.

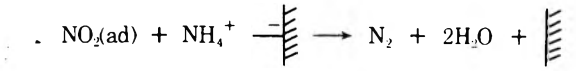

This mechanism explains well the effect of oxygen upon the reaction.

References and Notes

(1) K. Otto and M. Shelef, *J. Phys. Chem.*, **76**, 37 (1972).
(2) K. Otto and M. Shelef, *J. Phys. Chem.*, **74**, 2690 (1970).
(3) M. Markvart and VL. Pour, *J. Catal.*, **7**, 279 (1967).
(4) Y. Noto, K. Fukuda, T. Onishi, and K. Tamaru, *Trans. Faraday Soc.*, **63**, 2300 (1967).
(5) L. H. Little, "Infrared Spectra of Adsorbed Species", Academic Press, London, 1966.
(6) N. D. Parkyns, *Proc. Fifth Int. Congr. Catal., 5th*, **12**, 255 (1972).
(7) J. W. London and A. T. Bell, *J. Catal.*, **31**, 96 (1973).

Department of Chemistry
The University of Tokyo
Bunkyo-ku, Tokyo, 113 Japan

Maki Takagi
Tomoji Kawai
Mitsuyuki Soma
Takaharu Onishi*
Kenzi Tamaru

Received October 14, 1975

Effects of Manitol and Sorbitol on Water at 25 °C

Publication costs assisted by the National Science Foundation

Sir: Stern and O'Connor[1] reported in this journal the enthalpies of transfer of NaCl from water to aqueous solutions of two stereoisomer alcohols, mannitol and sorbitol. According to them, the enthalpies of transfer from pure water to dilute mannitol are first positive while those to sorbitol are negative, indicating opposing effects for the two alcohols. We have repeated the measurements and obtained results in serious disagreement from those of Stern and O'Connor; no opposing effects for the two alcohols were found.

Our calorimeter and calorimetric method with the details on standardization and precision have been described previously.[2-4] Our enthalpy of solution of NaCl at infinite dilution is 928 ± 5 cal/mol which is in excellent agreement with the "best" values selected by Parker.[5] The materials used were sodium chloride (Baker AR); mannitol (Mallinckrodt AR Mannite and also Matheson Coleman Bell

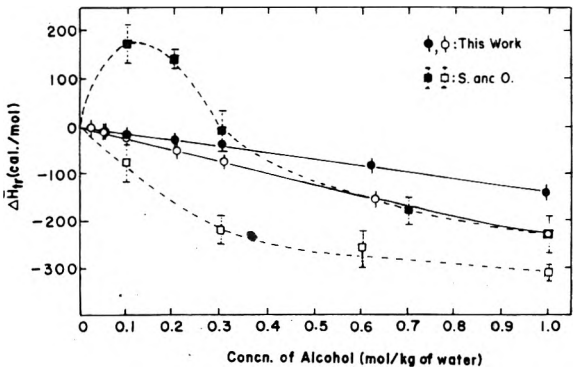

Figure 1. Enthalpies of transfer of NaCl from water to aqueous mannitol and sorbitol at 25 °C: – ● – ● –, data of this work for mannitol; – O – O –, data of this work for sorbitol; – □ – □ –, data for mannitol from ref 1; – ■ – ■ –, data for sorbitol from ref 1.

Reagent Mannitol); sorbitol (MCB Reagent Sorbitol and also J. T. Baker Baker Grade D-Sorbitol Hydrate). These polyols were used either without further purification or recrystallized from deionized water, water–ethanol mixture, or ethanol, but yielding the consistent results within experimental uncertainty.

The enthalpy of transfer, $\Delta\bar{H}_{tr}(B \leftarrow A)$, of a salt from a state of infinite dilution in solvent A to a state of infinite dilution in solvent B is given by

$$\Delta\bar{H}_{tr}(B \leftarrow A) = \Delta\bar{H}_s\left(\frac{1}{\infty},B\right) - \Delta\bar{H}_s\left(\frac{1}{\infty},A\right)$$

where $\Delta\bar{H}_s$ is the enthalpy of solution at infinite dilution and solvent A or B may be mixed solvents. The enthalpies of solution of NaCl were extrapolated to infinite dilution with the Debye–Hückel limiting law using the dielectric constant data of aqueous mannitol reported by Akerlöf.[6] Since the dielectric constants of aqueous sorbitol were not available, they were assumed to be identical with those of aqueous mannitol. For the study of dilute aqueous solutions containing 0 to 15 wt % alcohols, the small change in dielectric constant does not seem to affect the limiting slope appreciably. Our enthalpies of transfer of NaCl from pure water to aqueous mannitol and sorbitol are given in Table I and they are compared with those reported by Stern and O'Connor in Figure 1. We fail to reproduce the endothermic peak for the enthalpies of transfer in mannitol. For sorbitol, the negative enthalpies of transfer are confirmed qualitatively but not quantitatively. Enthalpies of transfer of NaCl from water to aqueous solutions of the two polyols are found to be both monotonically negative over the entire concentration range studied.

At our request, Franks[7] carried out two measurements on the transfer of NaCl from water to aqueous mannitol with LKB batch and flow calorimeters. The results of Franks for mannitol agree with ours within experimental errors.

The order of exothermic curves indicates that sorbitol is a stronger structure breaker than mannitol. Jeffrey[8] has found that sorbitol and mannitol adopt different conformations in aqueous solution. It seems that mannitol can be more easily adopted into the hydrogen-bonded structure than sorbitol.

Acknowledgments. The financial assistance of the National Science Foundation is gratefully acknowledged.

Supplementary Material Available: (Table I) a listing of enthalpies of solution and transfer of NaCl from H_2O to aqueous mannitol and sorbitol at 25 °C (2 pages). Ordering information is available on any current masthead page.

References and Notes

(1) J. H. Stern and M. E. O'Connor, *J. Phys. Chem.*, **76**, 3077 (1972).
(2) D. P. Wilson and W.-Y. Wen, *J. Phys. Chem.*, **79**, 1527 (1975).
(3) R. B. Cassel and W.-Y. Wen, *J. Phys. Chem.*, **76**, 1369 (1972).
(4) D. P. Wilson, Ph.D. Thesis, Clark University, 1974.
(5) V. B. Parker, *Natl. Stand. Ref. Data Ser., Natl. Bur. Stand.*, **No. 2** (1965).
(6) G. Akerlöf, *J. Am. Chem. Soc.*, **54**, 4125 (1932).
(7) F. Franks, private communications.
(8) See discussion of E. M. Arnett and G. A. Jeffrey in *J. Solution Chem.*, **2**, 114 (1973).

(Professor Stern indicates that he is in agreement with the above communication.—Ed.)

Jeppson Laboratory
Department of Chemistry
Clark University
Worcester, Massachusetts 01610

David P. Wilson
Wen-Yang Wen*

Received November 3, 1975

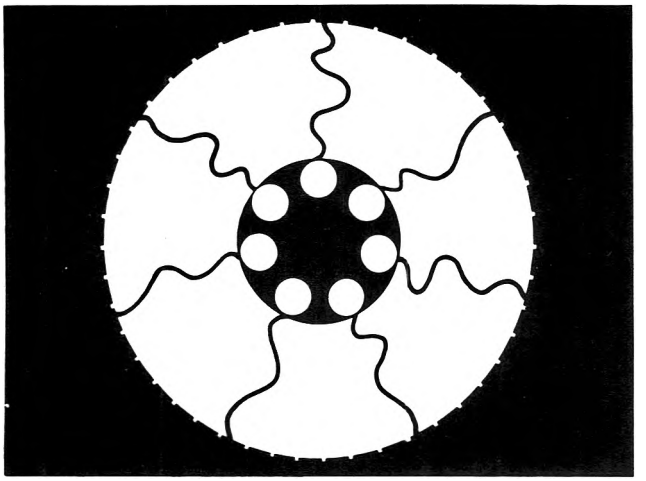

A two-volume symposium honoring Robert D. Vold and Marjorie J. Vold sponsored by the Division of Colloid and Surface Chemistry of the American Chemical Society, edited by K. L. Mittal.

Adsorption at Interfaces

ACS Symposium Series No. 8

Twenty papers examine thermodynamics of adsorption and interparticle forces; isolated chain molecules; equilibrium film pressure; Gibbs surface excess; water in porous glass; contact angles; nickel hydroxide; adhesion of ice; surface behavior of carbons; olfaction; low interfacial tension; and much more.

290 pages (1975) $12.95 clothbound (ISBN 0-8412-0249-4).

Colloidal Dispersions and Micellar Behavior

ACS Symposium Series No. 9

Twenty-four papers discuss colloid chemistry history; ultracentrifugal techniques; electric emulsification; macromolecular emulgents; emulsion polymerization; micelles; phase equilibria and structure; water soluble polymers; surfactant-protein interactions; anticoagulant drugs; and other topics.

353 pages (1975) $13.95 clothbound (ISBN 0-8412-0250-8). Nos. 8 & 9 ordered together $25.00. Postpaid in U.S. and Canada, plus 40 cents elsewhere.

Order from:
Special Issues Sales
American Chemical Society
1155 Sixteenth St., N.W.
Washington, D.C. 20036

From Wiley-Interscience.

Topics in Carbon-13 NMR Spectroscopy, Vol. 2
Edited by George C. Levy, **Florida State University**
Contents: Conformation and Structure of Peptides. Carbon-13 Nuclear Magnetic Resonance Spectroscopy of Naturally Occurring Substances. ^{13}C NMR Biosynthetic Studies. ^{13}C NMR Studies of Biopolymers. Carbon-13 Nuclear Magnetic Resonance Studies of Organometallic and Transition Metal Complex Compounds. Organic Structure Assignments Using ^{13}C Spin-Relaxation Data. The Computer in Fourier Transform NMR. Theory of Indirect Spin-Spin Coupling.
1976 Approx. 496 pp. $27.50

Techniques of Chemistry, Vol. 8
Parts 1 & 2: Solutions and Solubilities
Edited by Michael R. J. Dack, **CSIRO, Central Communications Unit, Australia**
The most recent experimental procedures in solutions and solubilities. A volume in the Wiley Techniques of Chemistry series.
Part 1: 1975 475 pp. $29.50
Part 2: Feb. 1976 Approx. 528 pp. $34.50

Organic Electronic Spectral Data, Vol. XI, 1969
Edited by John P. Phillips, **University of Louisville,** Henry Feuer, **Purdue University,** Paul M. Laughton, **Carleton University,** & B. S. Thyagarajan, **University of Texas at San Antonio**
Contains spectral maxims, extinction coefficients, and source references for ultraviolet and visible spectra of organic compounds published in 1970. Indexed for easy reference.
1975 1072 pp. $42.00

Classical Field Theory
Davison E. Soper, **Princeton University**
Application of the "principle of least action" to a wide range of theories in continuous systems, fluids, elastic solids, electric/magnetic fields, more.
1976 Approx. 288 pp. $19.95

The Physics of Liquid and Solid Helium, Part 1
Edited by K. H. Bennemann, **University of Berlin** & J. B. Ketterson, **Argonne National Laboratory, Illinois**
A multiple authored work which presents physics of solid and liquid Helium, reflecting important theoretical and experimental advances.
1976 608 pp. $29.95

Fourier Analysis of Time Series:
An Introduction
Peter Bloomfield, **Princeton University**
An elementary account of fourier analysis of time series beginning with examples and developing theory only as far as is necessary to follow examples.
1976 288 pp. $13.50

The Structures of the Elements
Jerry Donohue, **University of Pennsylvania**
Collection of complete descriptions of the structures of all of the elements in solid state, and includes latice constants, positional parameters, interatomic distances, bond and torsion angles.
1974 436 pp. $23.75

Theory and Applications of Molecular Paramagnetism
E. A. Boudreaux, **University of New Orleans,** & L. N. Mulay, **The Pennsylvania State University**
A lucid treatment of the basic theory of paramagnetic phenomena from both classical and quantum mechanical viewpoints.
1976 Approx. 512 pp. $35.50

Available at your bookstore or write to Robert Badger, Dept. 5483.

WILEY-INTERSCIENCE
a division of John Wiley & Sons, Inc.
605 Third Avenue, New York, N.Y. 10016
In Canada: 22 Worcester Road, Rexdale, Ontario
Prices subject to change without notice.
092 A5483-WI

PHASE DIAGRAMS

Materials Science and Technology

VOLUME 4: The Use of Phase Diagrams in Technical Materials

edited by ALLEN M. ALPER

A Volume in the REFRACTORY MATERIALS Series

CONTENTS: *A. Reisman and T. O. Sedgwick,* Chemical Vapor Deposition and Solid-Vapor Equilibria. *K. E. Spear,* Phase Behavior and Related Properties of Rare-Earth Borides. *C. F. Chenot,* The Use of Phase Diagrams in the Research and Development of Phosphor Materials. *H. J. Van Hook,* Phase Equilibria in Magnetic Oxide Materials. *J. White,* Recent Applications of Phase Diagrams to Problems in the Field of Refractory Materials.

1976, 320 pp., $28.00/£14.55

ADVANCES IN MAGNETIC RESONANCE, Volume 8

edited by JOHN S. WAUGH

CONTENTS: *J. H. Freed and J. B. Pedersen,* The Theory of Chemically-Induced Dynamic Spin Polarization. *K. H. Hausser and H. C. Wolf,* Optical Spin Polarization in Molecular Crystals. *D. W. Jones and T. F. Child,* NMR in Flowing Systems. *L. R. Dalton, et al.,* Saturation Transfer Spectroscopy.

1976, 288 pp., $25.50/£13.25; also available in Library Edition with Microfiche, $33.00/£17.15; Microfiche only, $18.00/£9.35

MACROMOLECULAR PHYSICS

VOLUME 2: Crystal Nucleation, Growth, Annealing

by BERNHARD WUNDERLICH

This book presents an in-depth summary of the last twenty years of research on macromolecular crystal nucleation, growth, and annealing, designed to bring the reader up-to-date in this rapidly developing field. It not only covers crystallization of macromolecules, but also summarizes the reaction of monomers to macromolecular crystals. The topic of crystallization during polymerization, which has been the subject of serious research only in the last few years, represents the major present research interest of the author. The book features extensive references to the original literature, as well as 165 photographs and diagrams and 27 tables.

1976, 476 pp., $46.50/£24.05

HIGHER EXCITED STATES OF POLYATOMIC MOLECULES, Volume 2

by M. B. ROBIN

This two-volume monograph presents an encyclopedic description of the vacuum-ultraviolet spectra of all basic classes of molecules, and a unified interpretation of them. Volume 1 begins with a brief introduction to the theories used in later chapters, a synopsis of methods for calculating the properties of the higher states of polyatomic molecules, and a brief section on recent experimental advances. The remainder of the volume considers the experimental spectra of sixteen classes of saturated polyatomic molecules, their relationship to their photoelectron spectra, and their interpretation. Volume 2 applies this unified approach to twenty-two classes of molecules bearing pi-electrons, and to biological and inorganic systems.

CONTENTS OF VOLUME 2: Two-Center Unsaturates. Nonaromatic Unsaturates. Aromatic Compounds. Inorganic Systems. Biochemical Systems. Addendum. References.

1975, 432 pp., $39.50/£18.95

Now Complete in Eight Volumes

SILICATE SCIENCE

VOLUME 8: Industrial Glass Glazes, Enamels

by WILHELM EITEL

Complete in eight volumes, this authoritative treatise provides a valuable repository of information on the basic chemistry of silicates and their applications in glass, ceramic, and construction technology. Covering the entire international literature, *Silicate Science* is encyclopedic in scope, with a numbering system for paragraphs which facilitates easy cross-referencing, as well as extensive indices. As the only comprehensive reference work of its type, this monumental treatise will remain indispensable to students, teachers, researchers, and workers in silicate science and related fields.

CONTENTS OF VOLUME 8: General Introduction. Reactions of Glass Batch Mixtures at Elevated Temperatures. Reactions in Batches and Their Kinetics. Fining of Molten Glass. Requirements Which Must Be Fulfilled by the Fined Glass before Working. Technologically Important Physical and Chemical Properties of Glass. Physical Properties of Glass as a Function of the Chemical Composition. Chemical Durability of Glass. Spontaneous and Controlled Crystallization in Glass.

1976, in preparation

REDUCED DENSITY MATRICES IN QUANTUM CHEMISTRY

by ERNEST R. DAVIDSON

This is perhaps the first text to deal with the topic of density matrices. It provides elements of reduced density matrices needed to understand the electronic structure of atoms and molecules. The text elucidates the analytical and physical properties of the one- and two-body reduced density matrices.

Analytical properties covered in detail include spin, symmetry, and asymptotic behavior. The text describes, without explicit use of the wavefunction, the mathematical and physical principles needed for describing the electronic charge and spin distribution in a molecule, with emphasis on N-representability conditions. Physical properties presented in detail include the use of the density in interpretation of the bond-order and orbital population. The text reviews use of natural orbitals in molecular calculations and clarifies problems in interpretation and direct calculation of the two-body density. Insights on unsolved problems in the theory of density matrices are offered throughout the text.

1976, 152 pp., $17.00/£8.85

N.B.: Postage plus 50¢ handling charge on all orders not accompanied by payment.
Prices subject to change without notice.

ACADEMIC PRESS, INC.

A Subsidiary of Harcourt Brace Jovanovich, Publishers

111 FIFTH AVENUE, NEW YORK, N.Y. 10003/24-28 OVAL ROAD, LONDON NW1 7DX